

ROBUST MAGNETIC RESONANCE IMAGING OF SHORT T2 TISSUES

A Thesis Submitted to the
College of Graduate and Postdoctoral Studies
In Partial Fulfillment of the Requirements
For the Degree of Doctor of Philosophy
In the Division of Biomedical Engineering
University of Saskatchewan
Saskatoon

By

LUMENG CUI

© Copyright Lumeng Cui, December 2021. All rights reserved.
Unless otherwise noted, copyright of the material in this thesis belongs to the author

PERMISSION TO USE

In presenting this thesis/dissertation in partial fulfillment of the requirements for a Postgraduate degree from the University of Saskatchewan, I agree that the Libraries of this University may make it freely available for inspection. I further agree that permission for copying of this thesis/dissertation in any manner, in whole or in part, for scholarly purposes may be granted by the professor or professors who supervised my thesis/dissertation work or, in their absence, by the Head of the Department or the Dean of the College in which my thesis work was done. It is understood that any copying or publication or use of this thesis/dissertation or parts thereof for financial gain shall not be allowed without my written permission. It is also understood that due recognition shall be given to me and to the University of Saskatchewan in any scholarly use which may be made of any material in my thesis/dissertation.

DISCLAIMER

Reference in this thesis/dissertation to any specific commercial products, process, or service by trade name, trademark, manufacturer, or otherwise, does not constitute or imply its endorsement, recommendation, or favoring by the University of Saskatchewan. The views and opinions of the author expressed herein do not state or reflect those of the University of Saskatchewan and shall not be used for advertising or product endorsement purposes.

Requests for permission to copy or to make other uses of materials in this thesis/dissertation in whole or part should be addressed to:

Head of the Division of Biomedical Engineering
57 Campus Drive
University of Saskatchewan
Saskatoon, Saskatchewan S7N 5A9 Canada

OR

Dean
College of Graduate and Postdoctoral Studies
University of Saskatchewan
116 Thorvaldson Building, 110 Science Place
Saskatoon, Saskatchewan S7N 5C9 Canada

Abstract

Tissues with short transverse relaxation times are defined as ‘short T2 tissues’, and short T2 tissues often appear dark on images generated by conventional magnetic resonance imaging techniques. Common short T2 tissues include tendons, meniscus, and cortical bone. Ultrashort Echo Time (UTE) pulse sequences can provide morphologic contrasts and quantitative maps for short T2 tissues by reducing time-of-echo to the system minimum (e.g., less than 100 μ s). Therefore, UTE sequences have become a powerful imaging tool for visualizing and quantifying short T2 tissues in many applications. In this work, we developed a new **F**lexible **U**ltra **S**hort time **E**cho (FUSE) pulse sequence employing a total of thirteen acquisition features with adjustable parameters, including optimized radiofrequency pulses, trajectories, choice of two or three dimensions, and multiple long-T2 suppression techniques. Together with the FUSE sequence, an improved analytical density correction and an auto-deblurring algorithm were incorporated as part of a novel reconstruction pipeline for reducing imaging artifacts. Firstly, we evaluated the FUSE sequence using a phantom containing short T2 components. The results demonstrated that differing UTE acquisition methods, improving the density correction functions and improving the deblurring algorithm could reduce the various artifacts, improve the overall signal, and enhance short T2 contrast. Secondly, we applied the FUSE sequence in bovine stifle joints (similar to the human knee) for morphologic imaging and quantitative assessment. The results showed that it was feasible to use the FUSE sequence to create morphologic images that isolate signals from the various knee joint tissues and carry out comprehensive quantitative assessments, using the meniscus as a model, including the mappings of longitudinal relaxation (T1) times, quantitative magnetization transfer parameters, and effective transverse relaxation (T2*) times. Lastly, we utilized the FUSE sequence to image the human skull for evaluating its feasibility in synthetic computed tomography (CT) generation and radiation treatment planning. The results demonstrated that the radiation treatment plans created using the FUSE-based synthetic CT and traditional CT data were able to present comparable dose calculations with the dose difference of mean less than a percent. In summary, this thesis clearly demonstrated the need for the FUSE sequence and its potential for robustly imaging short T2 tissues in various applications.

Acknowledgements

Undoubtedly, obtaining a Ph.D. has never been easy for anyone, but it does get easier when you have good company.

I would like to express my appreciation to the best supervisors in the world, Dr. Emily McWalter and Dr. Niranjana Venugopal. I want to thank them for offering me this Ph.D. opportunity four and half years ago and for unconditional supports for the whole time. Emily and Niranjana are not only good mentors but also wonderful friends. I have never questioned their professionalism, integrity, academic principles, and care for students, including me. The honours are all mine for being their student.

I would also like to show my gratitude to Dr. Gerald Moran. Jerry plays another mentoring role during my Ph.D. Through the Mitacs-Siemens internship program, he has never hesitated to help me and my research with any support and resources. It is my honour to get to know him during my Ph.D. and develop another mentor/friend relationship. He will always have my respect.

I am also grateful for having wonderful researchers and professionals in my committee, Drs. Gerald Moran, Andrew Alexander, Sheldon Wiebe, and Gordon Sarty. They have been giving me invaluable advice and encouragement for my research over the past four years. I can never make this far without their guidance and recognition.

I also want to sincerely thank Dr. Michael D. Noseworthy from McMaster University for agreeing to be my external examiner and taking the time to read my thesis. The discussion we had in my defence was truly educational and inspirational. I would also like to thank him for his encouraging comments and enlightening advice on my thesis.

I would also like to thank my lab members, Kirstin Olsen, Brennan Berryman, Álvaro Espinosa, and Shiva Mostafavi. They are terrific lab partners. You will never feel lonely when you have nice people to help you or laugh about our small setbacks on research. I will miss our group meetings and our happy, peaceful, hilarious lab culture.

I also owe tons of thanks to Dr. Giles Santyr and Dr. Brandon Zanette from Sickkids for providing me with their supports and resources during my stay in Toronto and introducing their fantastic lab

members to me. Without their help, I would never be able to finish my research during this unprecedented COVID-19 pandemic.

I also want to thank the staff from the Royal University Hospital (RUH). They have been giving me endless help and support ever since my Master's study. I will never forget the wonderful, nice people and their kindness. The RUH will always be my home base.

I also want to extend my thanks to my funding sources, Mitacs-Accelerate IT10545 and IT19172, Arthritis Society Young Investigator Operating Grant. I also want to show my appreciation to Siemens Healthineers for their technical supports.

At last, I want to make this space and give my special thanks to my beloved family and close friends and ‘bros’ in Canada, Mom and Dad, Grandma and Grandpa, my in-laws who have become my other ‘Mom and Dad’ and younger ‘brother’, Tao, Denson and Jenifer, Liangliang, Young, Yuzhu and Boen, Mingming, and LaoWang. They have been giving me endless encouragement, laughter, and emotional supports. They get me through many dark stages of my life and have become the most important part of my life.

At the very end, I want to express my greatest appreciation to my wife, best friend, and soul mate, Shuyu, and my fluffy, four-legged ‘sons/friends’, Hupi (cute grey tabby cat) and Ramen (cute red Shiba Inu dog). Over the last four and half years, they have been sharing my joy and satisfaction but also the frustration and pain. They witness my personal growth, success, and any tiny achievement. I owe them the biggest thanks and apologies. To all of the three, thank you for being my family, and you are the reason I live with courage.

Lumeng Cui

2021-12-23

Table of Contents

<i>PERMISSION TO USE</i>	<i>i</i>
<i>Abstract</i>	<i>ii</i>
<i>Acknowledgements</i>	<i>iii</i>
<i>List of Tables</i>	<i>ix</i>
<i>List of Figures</i>	<i>x</i>
<i>List of Abbreviations</i>	<i>xiii</i>
Chapter 1 Introduction	1
1.1. Background	1
1.2. Literature Review	10
1.2.1. UTE Techniques	10
1.2.1.1. Excitation Pulses	11
1.2.1.1.1. <i>Half-Pulse and Variable-Rate Selective Excitation (VERSE)</i>	11
1.2.1.1.2. <i>Rectangular Pulse</i>	12
1.2.1.2. Trajectories	12
1.2.1.2.1. <i>Radial</i>	13
1.2.1.2.2. <i>Spiral</i>	14
1.2.1.3. Reconstruction Techniques	15
1.2.1.4. Summary of UTE techniques	16
1.2.2. Qualitative UTE Imaging	17
1.2.2.1. Dual-Echo Subtraction	17
1.2.2.2. Long T2 Saturation Pulses	19
1.2.2.3. Long T2 Inversion Recovery Pulses	21
1.2.2.4. Off Resonance Saturation	23
1.2.2.5. Summary of Qualitative UTE Imaging	24
1.2.3. Quantitative UTE Imaging	24
1.2.3.1. T1 Relaxation Time Mapping	25

1.2.3.2.	T2* Relaxation Time Mapping	27
1.2.3.3.	Magnetization Transfer Ratio (MTR)	28
1.2.3.4.	Quantitative Magnetization Transfer (QMT)	30
1.2.3.5.	Summary of Quantitative UTE Imaging	33
1.2.4.	UTE Applications	33
1.2.4.1.	The Musculoskeletal System	33
1.2.4.2.	Radiation Treatment Planning	41
1.2.4.3.	Other Applications	42
1.2.4.4.	Summary of UTE Applications	42
1.2.5.	Conclusion	42
1.3.	Research Motivations and Thesis Objectives	42
1.4.	Thesis Organization	43
	<i>Chapter 2 Design and development of a novel Flexible Ultra Short Echo time sequence (FUSE)</i>	45
2.1.	Introduction	45
2.2.	Materials and Methods	47
2.2.1.	Development of a Flexible Ultra Short Echo Time Sequence (FUSE)	47
2.2.1.1.	RF Pulse Design	50
2.2.1.2.	Implementation of Multiple K-Space Trajectories	50
2.2.1.3.	Implementation of Various Long T2 Suppression Techniques	52
2.2.2.	UTE Reconstruction Pipeline	54
2.2.2.1.	K-Space Trajectory Correction	55
2.2.2.2.	K-Space Density Correction	56
2.2.2.3.	Automatic Off-Resonance Correction Algorithm	59
2.2.3.	Phantom Evaluation of the FUSE	59
2.3.	Results	63
2.3.1.	Density Correction	63
2.3.2.	Off-Resonance Artifact Correction	66
2.3.3.	Direct Comparison between Combinations of RF Pulses and Trajectories	69
2.3.4.	The Effect of Echo Time Minimization	71

2.3.5. Effective Long T2 Suppression Techniques.....	73
2.4. Discussion	76
2.5. Conclusion	81
<i>Chapter 3 Morphological and quantitative musculoskeletal (MSK) imaging of the bovine knee using a novel flexible ultrashort echo time (FUSE) sequence</i>	<i>82</i>
3.1. Introduction	82
3.2. Materials and Methods	86
3.2.1. Bovine Specimen Study.....	86
3.2.2. FUSE Sequence.....	88
3.2.3. Morphological Imaging.....	88
3.2.4. Quantitative Imaging	89
3.2.4.1. B1 Mapping.....	89
3.2.4.2. T1 Mapping.....	90
3.2.4.3. Quantitative magnetization transfer (QMT) Mapping	90
3.2.4.4. T2* Mapping.....	93
3.2.5. Data Evaluation.....	94
3.3. Results.....	95
3.3.1. Qualitative Imaging.....	95
3.3.2. T1 Mapping.....	98
3.3.3. QMT Mapping.....	103
3.3.4. T2* Mapping.....	108
3.4. Discussion	113
3.5. Conclusion	119
<i>Chapter 4 Improving cortical bone imaging using the FUSE sequence for optimal synthetic CT generation</i>	<i>120</i>
4.1. Introduction	120
4.2. Materials and Methods	123
4.2.1. Phantom and Human Skull	123

4.2.2.	FUSE Sequence.....	124
4.2.3.	MR and CT Image Acquisitions	124
4.2.4.	Image processing and Evaluation	128
4.2.5.	Dose Calculation Using Synthetic CT.....	128
4.3.	Results.....	129
4.3.1.	Optimization of the Use of the FUSE Sequence	129
4.3.2.	Improved Cortical Bone Imaging Using the FUSE.....	133
4.3.3.	Morphological Comparison between the FUSE and CT	135
4.3.4.	Dose Calculation Results	138
4.4.	Discussion	140
4.5.	Conclusion	143
<i>Chapter 5 Integrated Discussions and Future Considerations</i>		<i>144</i>
5.1.	Summary of Findings	144
5.2.	General Discussion	146
5.2.1.	Why is UTE important?	146
5.2.2.	What makes our UTE pulse sequence different?	147
5.2.3.	How can we take advantage of our flexible UTE sequence?	148
5.3.	Scientific Contributions	149
5.4.	Overall Strengths and Limitations.....	152
5.4.1.	Strengths	152
5.4.2.	Limitations and Challenges.....	153
5.5.	Future Work	153
5.6.	Conclusion	154
<i>References.....</i>		<i>156</i>
<i>Appendix A</i>		<i>175</i>

List of Tables

Table 2.1. Scan parameters for the systematic evaluation of 1) the methods for k-space density correction (Experiment 1); 2) the approaches for off-resonance artifact correction (Experiment 2-4); 3) the combinations of the various RF pulses and trajectories (Experiment5); 4) 3D RF pulses with the shortest TEs (Experiment 6); 5) the comprehensive long-T2 suppression techniques (Experiment 7).	62
Table 3.1. Scan parameters for the morphological and quantitative imaging in the knee joint.	87
Table 3.2. Statistic of the T1 maps without and with B1 correction for the intra- and inter-specimen in both menisci.	100
Table 3.3. Descriptive statistics of the QMT maps using two lineshapes and with and without B1 correction for the intra- and inter-specimen in both menisci.	105
Table 3.4. Statistic of the T2* maps using the mono-exponential fit and the T2I*, T2s*, F1, and Fs maps using the bi-exponential fit for the intra- and inter-specimen in both menisci.	110
Table 4.1. MRI scan parameters for the systematic optimization using the phantom.	126
Table 4.2. MRI scan parameters for the human skull.	127

List of Figures

Figure 1.1. The process of excitation using a radiofrequency (RF) pulse with a flip angle of α.	3
Figure 1.2. Longitudinal T1 relaxation, transverse T2 relaxation, and transverse T2* relaxation.	3
Figure 1.3. Diagram of a conventional pulse sequence (gradient-recalled echo) using a Cartesian trajectory.	5
Figure 1.4. K-space and reconstruction.	6
Figure 1.5. Common UTE data-filling trajectories in k-space and the corresponding pulse sequences.	9
Figure 1.6. Example of axial tibia UTE imaging using various dual-echo subtraction methods.	19
Figure 1.7. Example of a comparison between various suppression techniques on axial mid-tibia images.	21
Figure 1.8. Example of a comparison between various long-T2 inversion pulses used in a phantom.	23
Figure 1.9. Example of a comparison between the dual-echo subtraction and off-resonance saturation technique used in a phantom.	24
Figure 1.10. Example of T1-related maps of an agarose bone phantom.	26
Figure 1.11. Example of the mono- and bi-component T2* fit.	28
Figure 1.12. Example of a magnetization transfer ratio map of human tibial cortical bone in vivo.	30
Figure 1.13. Example of the UTE-QMT modelling used in the porosity assessment of the bone.	32
Figure 1.14. Knee anatomy illustrated using a sagittal MR image.	34
Figure 1.15. Structure of the articular cartilage.	37
Figure 1.16. Structure of the meniscus.	39
Figure 1.17. Menisci scanned by fat-saturated UTE-MRI with TE varying from 0.012 to 12 ms.	40
Figure 2.1. The feature tree of the FUSE sequence.	49

Figure 2.2. Proposed UTE reconstruction pipeline.	55
Figure 2.3. In-house short-T2 phantom.	61
Figure 2.4. Comparison between the traditional and new analytical density correction functions.	64
Figure 2.5. Comparison of the density correction techniques used in the 3D radial and spiral.	65
Figure 2.6. The off-resonance artifact improved with the deblurring algorithm.	67
Figure 2.7. The off-resonance artifact improved with increases of the bandwidth-per-pixel (BWP) and spiral interleaves.	68
Figure 2.8. Qualitative and quantitative evaluations of the various combinations of the implemented RF pulses and trajectories.	70
Figure 2.9. Comparison of the implemented RF excitation schemes including VERSE-modified half-Sinc pulse (VHSP), regular half-Sinc pulse (RHSP), and rectangular pulse (RP) with the TE variation.	72
Figure 2.10. Direct qualitative and quantitative comparisons between the implemented long-T2 suppression techniques.	75
Figure 3.1. Multiple morphological contrasts generated by the FUSE sequence.	97
Figure 3.2. B1 map and T1 maps of the menisci.	99
Figure 3.3. Signal measurements and T1 fitting of the menisci.	101
Figure 3.4. Distribution plots of the T1 maps for all meniscus specimens (S01-S06).	102
Figure 3.5. QMT maps of the menisci superimposed on an MT-weighted volume.	104
Figure 3.6. Signal measurements and QMT fittings of the menisci.	106
Figure 3.7. Distribution plots of the QMT maps for all meniscus specimens (S01-S06).	107
Figure 3.8. T2* maps of the menisci.	109
Figure 3.9. Signal measurements and T2* fitting of the menisci.	111
Figure 3.10. Distribution plots of the T2* maps for all meniscus specimens (S01-S06).	112
Figure 4.1. Variations of the artifacts, SNRs, and times with the increase of in-plane trajectory lines for the radial and spiral trajectory.	131
Figure 4.2. Variations of the artifacts, SNRs, and times with the increase of out-of-plane trajectory lines for the Spiral-Cones trajectory.	132
Figure 4.3. Comparison between T2-SPACE, PETRA, and FUSE.	134

Figure 4.4. Comparison between CT and FUSE.136
Figure 4.5. Geometrical evaluation between CT and FUSE.137
Figure 4.6. Comparison of the dose calculation between two radiation treatment plans using CT and FUSE-derived sCT.139

List of Abbreviations

ADC	Analog-to-Digital Converter
AFI	Actual Flip-angle Imaging
BWP	Bandwidth-per-Pixel
CNR	Contrast-to-Noise Ratio
CT	Computed Tomography
CWPE	Continuous-Wave-Power-Equivalent
DA	Double-Angle
DC	Density Correction
DCF	Density Correction Function
DRR	Digitally Reconstructed Radiograph
FBP	Filtered Back Projection Reconstruction
FFT	Fast Fourier Transform
FID	Free Induction Decay
FLASH	Fast Low Angle SHot
FLORET	Fermat Looped, Orthogonally Encoded Trajectories
FOV	Field-of-View
FS	Fat Saturation
GoF	Goodness-of-Fit
Hz	Hertz
iFFT	Inverse Fast Fourier Transform
iFT	Inverse Fourier Transform
IQR	Interquartile Range
MMF	Macromolecular Fraction
MR	Magnetic Resonance
MRI	Magnetic Resonance Imaging

ms	Milliseconds
MSK	Musculoskeletal
MT	Magnetization Transfer
MTR	Magnetization Transfer Ratio
NUFFT	Non-Uniform Fast Fourier Transform
OA	Osteoarthritis
OS	Off-resonance Saturation
QMT	Quantitative Magnetization Transfer
RF	Radiofrequency
RHSP	Regular Half-Sinc Pulse
ROI	Region-of-Interest
RP	Rectangular Pulse
RT	Radiation Therapy
SAR	Specific Absorption Rate
sCT	Synthetic Computed Tomography
SNR	Signal-to-Noise Ratio
SPGR	Spoiled Gradient-Recalled
SR	Saturation-Recovery
Std. Dev.	Standard Deviation
TE	Time-of-Echo
TI	Time-of-Inversion
TPI	Twisted Projection Imaging
TR	Time-of-Repetition
TSR	Time of Saturation Recovery
UTE	Ultrashort Echo Time
VERSE	Variable-Rate Selective Excitation
VFA	Variable-Flip-Angle

VHSP	VERSE-modified Half-Sinc Pulse
VTE	Variable-Time-of-Echo
VTR	Variable-Time-of-Repetition
1D	1-Dimensional
2D	2-Dimensional
3D	3-Dimensional

Chapter 1 Introduction

Synopsis: Tissues with short T2 relaxation times are defined as ‘short T2 tissues’, and they normally are not visible or dark on conventional Magnetic Resonance (MR) images. Ultrashort Echo Time (UTE) can provide qualitative and quantitative contrast for short T2 tissues by drastically reducing time-of-echo (TE) to low as 8 μ s. As such, UTE sequences have become a promising imaging tool for short T2 tissues in many applications. This chapter introduces the research background of magnetic resonance imaging (MRI) physics, then provides a comprehensive literature review of UTE, identifies gaps in the literature and finally states the objectives of this thesis.

1.1. Background

MRI is a non-invasive medical imaging modality that uses a strong static magnetic field, magnetic gradient fields, and radiofrequency (RF) waves to form a visible image. MRI can provide superior contrast for soft tissues and delivers no ionizing radiation, as compared to other imaging modalities, e.g., X-ray, computed tomography (CT), and positron emission tomography (PET).

The differences in tissue relaxation processes under the influence of a changing magnetic field are the underlying mechanism in achieving contrast in MRI. MR scans rely on the abundance of hydrogen-containing tissues enriched in the body (e.g., muscles, fat, and bone marrow) (1). The protons (^1_1H), each of which carries a magnetic moment due to its spin (angular momentum), are randomly directed in the body in the natural state; however, when they are placed in the strong external magnetic field of MRI (i.e., B_0), some of their magnetic moments will align with the field and form a net magnetization, M_0 , along the longitudinal B_0 direction without transverse components (1). The protons, described as the net magnetization M_0 , rotate about the B_0 direction at a constant frequency, called the Larmor frequency, which is dependent on the gyromagnetic ratio of the nucleus and the magnetic field strength; this rotation is termed precession (1). The precession continuously carries on in a dynamic equilibrium state where there is no transverse component

due to the dephasing. MRI uses RF radiation, an electromagnetic wave, carrying a frequency set to the Larmor frequency to disturb this dynamic equilibrium, triggering resonance. For further explanation, this RF wave, produced by a transmitter coil, can generate a magnetic field B_1 perpendicular to B_0 , which can tip M_0 away from the longitudinal direction to the transverse plane. This process is described as an excitation. The angle that B_1 rotates M_0 away from the longitudinal direction with is called the flip angle, α , regulated by the time and strength of the excitation (Figure 1.1). During the excitation, M_0 has a reduced longitudinal component M_z and an increased transverse component M_{xy} (Figure 1.1). When the excitation is complete, the longitudinal component M_z will recover back to its original state M_0 , while the transverse component M_{xy} will decay to zero. These two individual processes are described as longitudinal relaxation and transverse relaxation, also known as the T1 relaxation and T2 relaxation, respectively (Figure 1.2). T1 is a time constant that describes the longitudinal relaxation formalized as exponential recovery

$$M_z(t) = M_0 \cos(\alpha) e^{-t/T1} + M_0(1 - e^{-t/T1}) \quad [1.1]$$

Where $M_z(t)$ is the longitudinal component with respect to the time variable t ; M_0 is the original magnetization; α is the flip angle of the RF wave; $T1$ is the longitudinal relaxation time (1). Likewise, T2 is a time constant that describes the transverse relaxation formalized as an exponential decay:

$$M_{xy}(t) = M_0 \sin(\alpha) e^{-t/T2} \quad [1.2]$$

Where $M_{xy}(t)$ is the transverse component with respect to the time variable t ; M_0 is the original magnetization; α is the flip angle of the RF wave; $T2$ is the transverse relaxation time (1).

During the T1 and T2 relaxation process, both the longitudinal component M_z and transverse component M_{xy} maintain the precession at the Larmor frequency. One can use a rotating reference frame with this base frequency to consider both relaxation processes occurring without rotation. T2* relaxation time is a different but related term that is important in gradient echo and ultrashort echo time imaging. Compared to the relaxation time T2, T2* relaxation time describes the transverse relaxation but includes the consideration of inhomogeneous main magnetic field and different magnetic susceptibilities of various tissues, thus it is always smaller than T2 (Figure 1.2) (2). If these inhomogeneities are not addressed by MRI scans, the T2* relaxation time is the ‘effective’ transverse relaxation time as opposed to the ‘true’ transverse relaxation time T2 (2). The relaxation times T1, T2, and T2* are tissues properties and vary with tissue type.

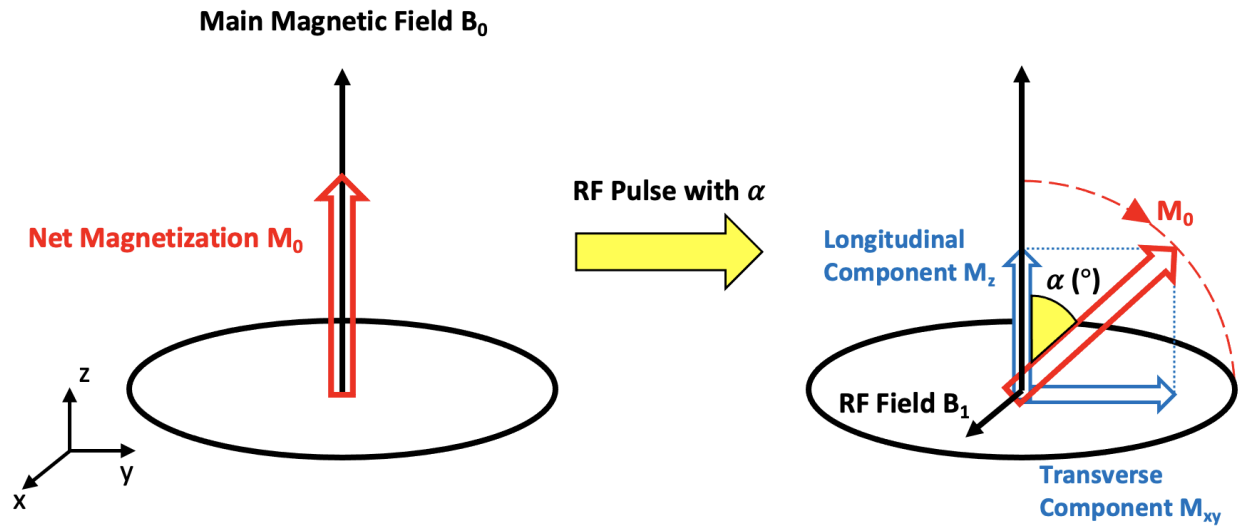


Figure 1.1. The process of excitation using a radiofrequency (RF) pulse with a flip angle of α .

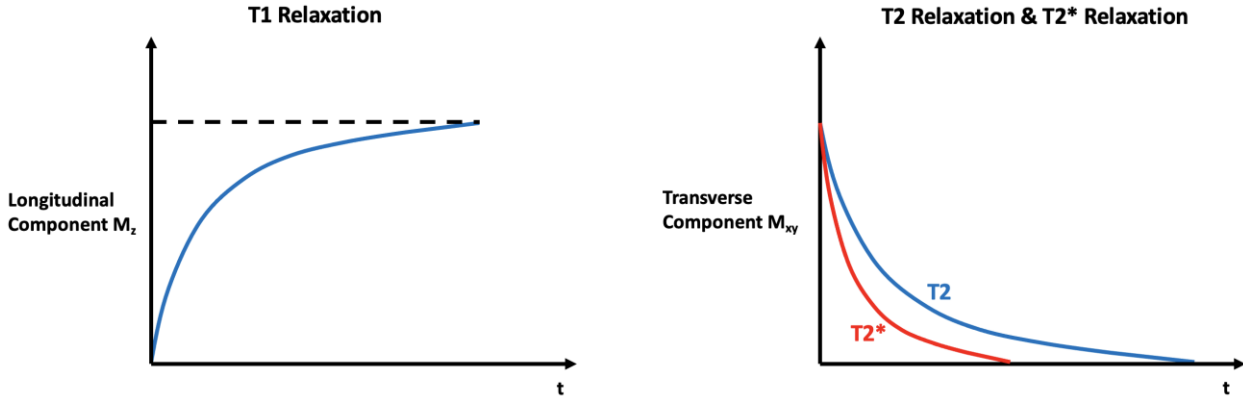


Figure 1.2. Longitudinal T1 relaxation, transverse T2 relaxation, and transverse T2* relaxation.

Modern MRI imaging methods are developed by employing computer programming codes that are specific to the hardware vendor. The developed code, termed Pulse Sequence, typically includes a set of RF pulses, encoding gradients, and raw MR signal collection using analog-to-digital converters (ADC). During RF excitation, the pulse sequences first transmit an RF wave (pulse) with the Larmor frequency to flip the magnetization fully or partially into the transverse plane and initiate the longitudinal (T1) and transverse (T2) relaxation process simultaneously (1). Then, during the relaxation processes, the pulse sequences use magnetic gradient fields (superimposed on the main magnetic field) to spatially encode the magnetization at every position with different phases and frequencies into k-space (1). Last, before the relaxation processes are complete, the

pulse sequences control a receiver coil to pick up the raw MR signal during the frequency encoding process (i.e., data readout) from the transverse component of the position-encoded magnetization (according to Faraday's law of induction) and digitally samples the raw signal with an ADC (1). This full procedure involving the excitation, position encoding, and raw MR signal collection is a repeated process varied by the gradient fields, and each repetition provides a raw MR signal uniquely encoded with position information (Figure 1.3). By following a specific strategy, all position-encoded raw MR signals can fill to a matrix called k-space, and the strategy to fill k-space is described as a trajectory (Figure 1.4). The Cartesian trajectory is the most common and robust k-space-filling strategy adopted by many conventional pulse sequences. The raw MR signals, aligned by the trajectory in k-space, are defined in the Fourier domain and need to be reconstructed by an inverse Fourier transform (iFT) into the final MR image (Figure 1.4).

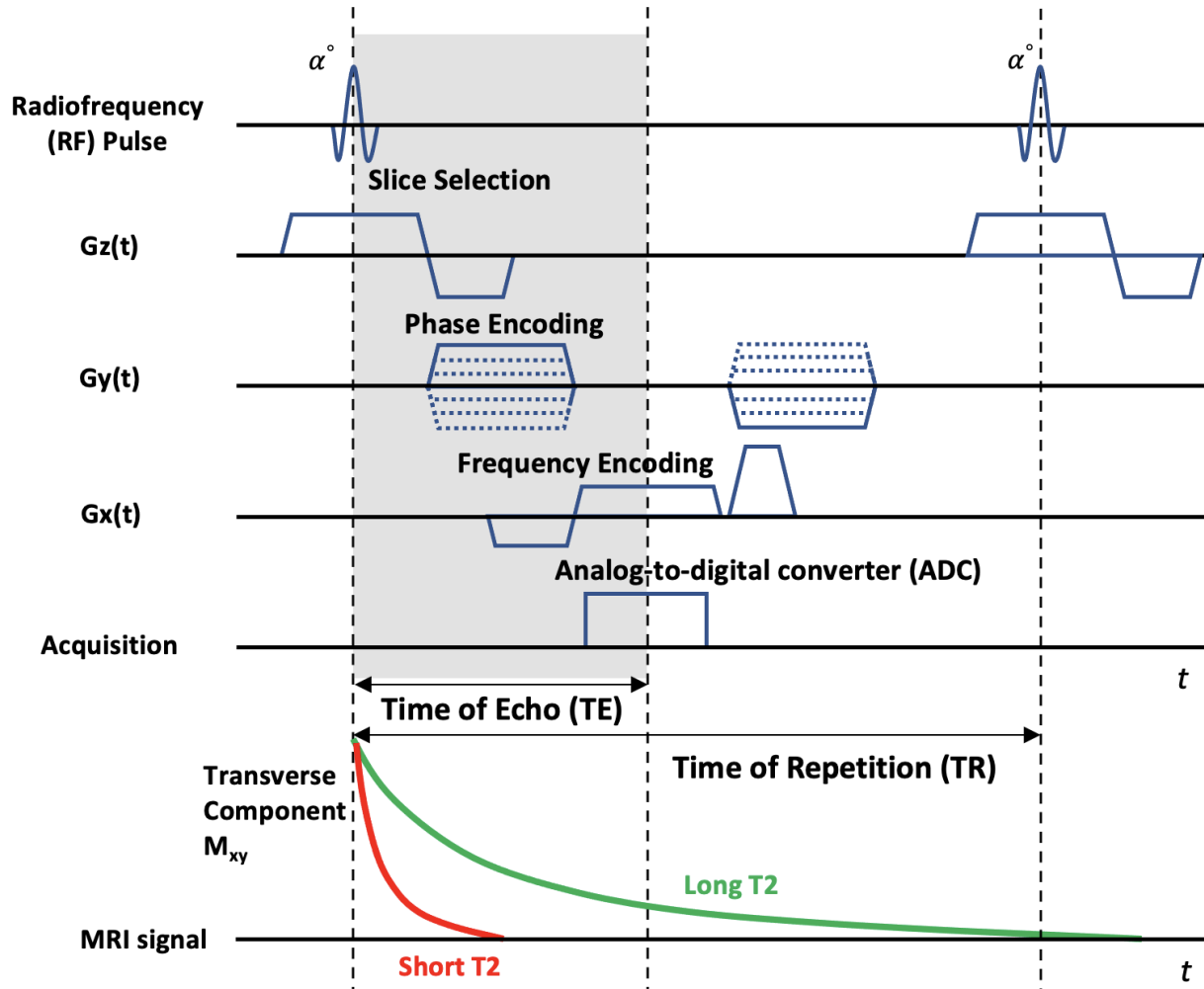


Figure 1.3. Diagram of a conventional pulse sequence (gradient-recalled echo) using a Cartesian trajectory.

Unlike the transverse relaxation with a long T2 time, the transverse relaxation with a short T2 time could be fully decayed before the starting of acquisition.

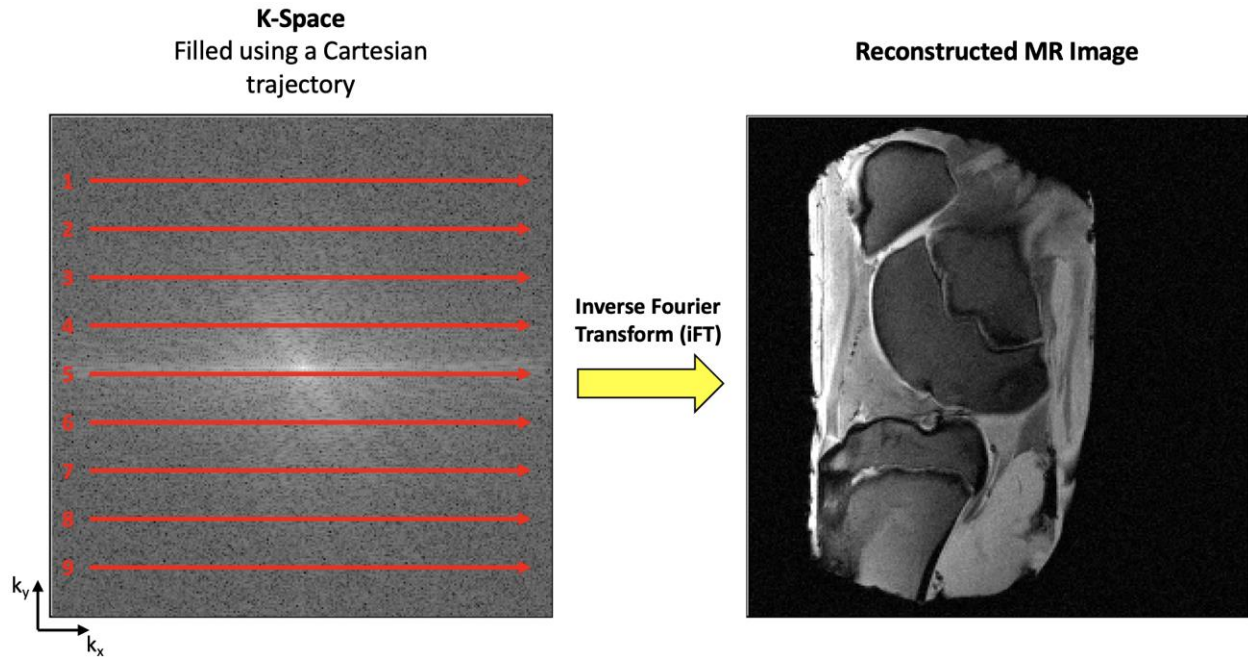


Figure 1.4. K-space and reconstruction.

K-space can be filled using a Cartesian trajectory (the red lines). Processed by an inverse Fourier Transform (IFT), raw MR signals in k-space can be reconstructed to a final MR image.

Generating contrast from a collection of tissues can be manipulated by purposely changing two important parameters of pulse sequences, time-of-echo (TE) and time-of-repetition (TR) (Other determining parameters can also include the time-of-inversion and flip angle) (1). TR is the time interval for each repeating cycle of pulse sequences. In pulse sequences, TR decides the initial magnetization, restored from the longitudinal relaxation of the last repetition, for each excitation and then the excited transverse component of the net magnetization for each acquisition. For example, if after an RF pulse with a flip angle (α) of 90° , the transverse component of the net magnetization for the acquisition is (combining Eq. [1.1] and Eq. [1.2]),

$$M_{xy}(t) = M_0(1 - e^{-TR/T1})e^{-t/T2} \quad [1.3]$$

TE defines the time interval between the starting of T2 relaxation and the moment the received raw MR signal reaches the maximum during the T2 relaxation decay (i.e., arriving at the k-space centre). For example, in the Cartesian trajectory that fills k-space from left to right for every acquisition line, TE is presented as the time interval between the middle of the excitation and the middle of the acquisition; while, in non-Cartesian trajectories that use k-space centre-out data filling strategies (e.g., the radial or spiral trajectory), TE appears as the time interval between the middle of the

excitation and the beginning of the acquisition. In both cases, the TE indicates the moment when the data filling is at k-space centre.

In MRI, short-T2 tissues can lead to a rapid signal decay due to their very short T2 relaxation times and may not be detectable using conventional pulse sequences. Although MRI can provide well-defined anatomical details for many soft tissues, conventional MR images still cannot visualize a subset of tissues with adequate brightness or high contrast. These tissues often appear ‘black’ or as ‘signal void’ on MR images because their signal decays too quickly to capture; using MRI terminology, this is due to their quick T2 relaxation times. Usually, tissues with T2 relaxation times less than ~10 ms are defined as short T2 tissues (3,4). Common short-T2 tissues may include tendons (T2 ~ 6 ms), ligaments (T2 ~ 4-10 ms), cortical bone (T2 ~ 0.4-0.5 ms), meniscus (T2 ~ 5-8 ms), and deep layers of cartilage (T2 ~ 5-10 ms) (5–8). Relatively, tissues with more free protons (i.e., water) usually possess longer T2 relaxation times, over 10 ms, and are detectable with standard sequences (9,10); for example, at 3.0 T, the liver has a T2 relaxation time of 42 ± 3 ms, the skeletal muscle has a T2 relaxation time of 50 ± 4 ms, and blood has a T2 relaxation time of 275 ± 50 ms (measured at a blood oxygen level of 95%) (6). For comparison, short T2 tissues, such as deep layers of articular cartilage or cortical bone, have relaxations times less than a few milliseconds (4,11). The reason for this is that these tissues contain protons that are bound to macromolecules, which results in the rapid signal decay that conventional MRI sequences fail to detect (9,10,12). This is a result of the fact that many tissues have complex biological structures that contain multiple components with varying T2 times. Even tissues visible with standard MRI may have interesting short-T2 components, which are relatively unknown and understudied. For example, the articular cartilage in knee joints has a long-T2 component (the superficial layer) and a short-T2 component (the deep layer) (13); further the middle layer contains both free water and bound water which can also result in multiple T2 components.

Consequently, Ultrashort Echo Time (UTE) pulse sequences have been developed to image the short-T2 tissues and short-T2 components with short TEs (14,15). The overall goal of UTE sequences is to reduce TE as much as possible. The ultrashort TE is achieved by short RF pulses (e.g., half-Sinc pulse, half-Sinc pulse with Variable-Rate Selective Excitation (VERSE) modification, or short rectangular pulse) and non-Cartesian centre-out trajectories (e.g., radial and

spiral) (14–20). Compared to the Cartesian trajectory (Figure 1.4), the non-Cartesian centre-out trajectories can fill up k-space (i.e., accomplishing the entire data readout) in an efficient way by only using frequency encoding (without phase encoding); the centre-out frequency encoding collects the MR signal as free induction decay (FID). Also, UTE signals are collected from T2* relaxation decay instead of T2 relaxation decay due to the lack of an inversion pulse and refocusing gradient; these two pulse sequence events can remedy the magnetic field's inhomogeneity and the susceptibility of various materials, but they are not adopted intentionally in UTE pulse sequences in order to achieve the shortest possible TE. UTE sequences are capable of two-dimension (2D) or three-dimension (3D) acquisitions by adopting combinations of various short RF pulses and non-Cartesian centre-out trajectories (Figure 1.5). It must be noted that in UTE pulse sequences, TE is the time interval between either the end (half-Sinc) or middle (rectangular) of an excitation pulse and the beginning of an ADC event, which looks different from the conventional sequence (Figure 1.3 vs. Figure 1.5). While it may appear that UTE sequences violate TE's definition, in fact, because UTE sequences usually use half (or full) pulses and non-Cartesian centre-out trajectories, TE in the context of UTE does comply with the conventional definition of being the time from the centre of the RF pulse to when the centre of k-space is filled (further detail of the half sinc RF pulse is provided in section 2.1.1.1). By this definition TEs of UTE sequences can be less than 0.1 ms (4). On most MRI systems, the smallest allowable TE is related to the receiver deadtime, $\sim 8 \mu\text{s}$ (21,22). Given that routine MRI techniques cannot effectively obtain any signal from the tissues with T2 times less than 10 ms, UTE imaging is an important innovation in order to distinguish between short T2 tissues (9,23).

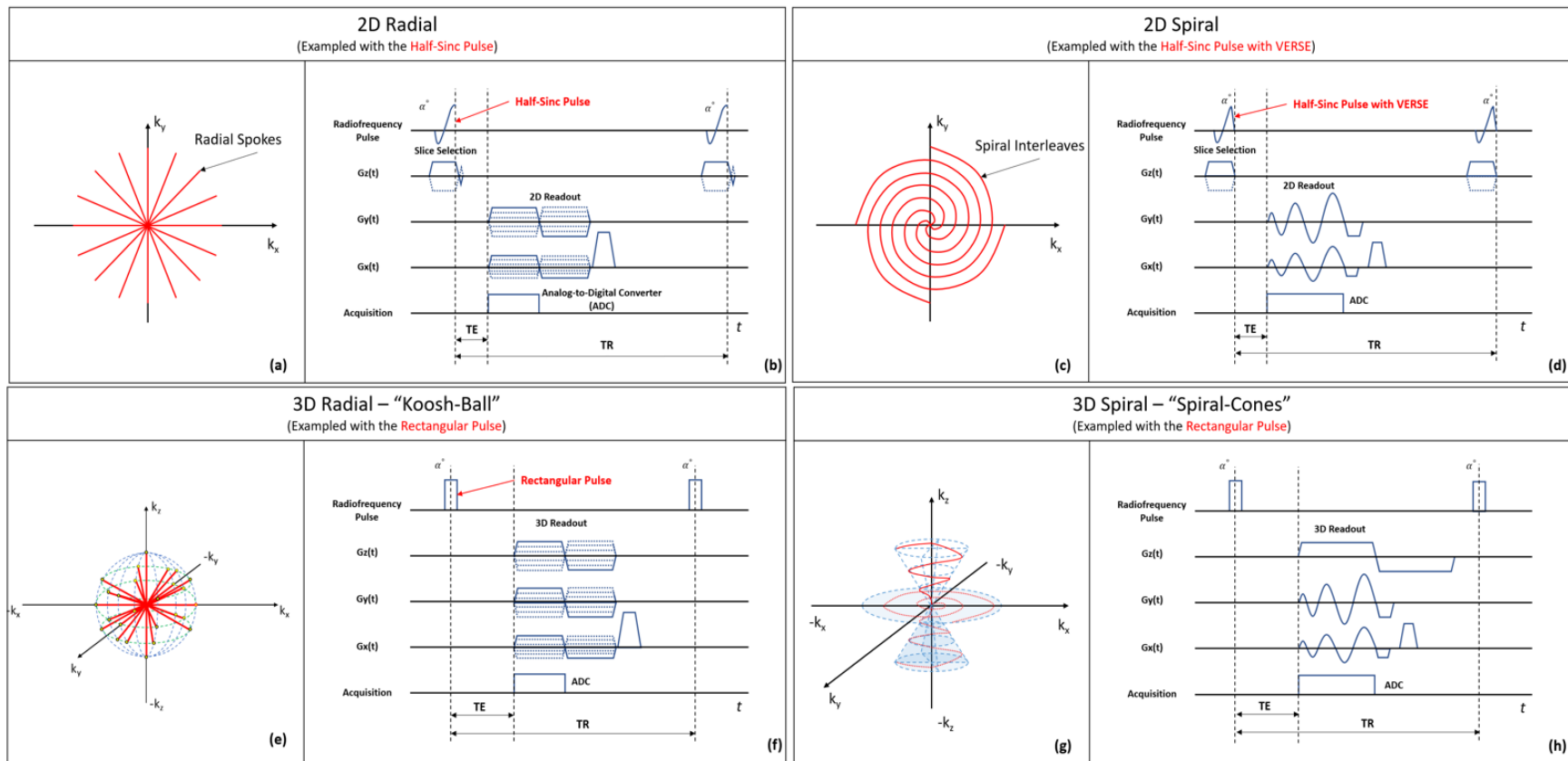


Figure 1.5. Common UTE data-filling trajectories in k-space and the corresponding pulse sequences.

(a) 2D radial trajectory with the radial spokes as the trajectory lines (red); (b) the pulse sequence diagram of the 2D radial trajectory; (c) 2D spiral trajectory with the spiral interleaves as the trajectory lines (red); (d) the pulse sequence diagram of the 2D spiral trajectory; (e) 3D radial trajectory (“Koosh-Ball”) with the radial spokes (the red trajectory lines) extended to a sphere space; (f) the pulse sequence diagram of the 3D radial trajectory; (g) 3D spiral trajectory (“Spiral-Cones”) with the spiral trajectory lines (red) extended to multiple cone-shaped spaces; (h) the pulse sequence diagram of the 3D spiral.

For better qualitative and quantitative characterization of short T2 tissues, many UTE techniques have been continuously developed and improved, including the excitation pulses, k-space trajectories, long-T2 suppression techniques for enhanced morphological imaging, and quantification techniques with data modelling. Due to these developments and improvements, UTE sequences have a broad scope of applications from musculoskeletal (MSK) imaging to lung imaging to radiation therapy (RT) planning. Despite the various developments and improvements, it is still unclear which particular UTE technique is the most appropriate for each specific application. For example, differing approaches might be necessary to obtain a high-resolution image of skull cortical bone morphology for synthetic CT generation versus to carry out a quantitative magnetization transfer (MT) modelling in a musculoskeletal tissue, such as the menisci. Therefore, it is essential that we understand the differences between the various UTE techniques via direct comparisons, in order to optimize our acquisitions for specific applications. However, there currently exists no sequence that combines different UTE features so that this type of comparison can be made; instead, research groups tend to use one particular approach depending on the sequence(s) they have access to.

1.2. Literature Review

This section reviews the existing literature on UTE, scoping from sequences and reconstruction techniques to imaging methods (qualitative and quantitative) to applications.

1.2.1. UTE Techniques

UTE is a class of MRI pulse sequences that can visualize and quantify short-T2 tissues (typically invisible in conventional MR images). To reveal the component of short T2 tissues in MR images, researchers have developed many novel RF excitation pulses and centre-out trajectories to achieve an ultrashort TE (24). Additionally, due to the necessary non-Cartesian trajectories required for UTE acquisitions, special reconstruction techniques are needed to adapt the acquired data to the Cartesian coordinate system to accommodate the iFT to image space (25–27). This section will review the existing RF excitation pulses, k-space trajectories, and reconstruction methods implemented in UTE sequences.

1.2.1.1. Excitation Pulses

As with other conventional MRI pulse sequences, UTE sequences control coils to transmit RF pulses to excite protons (resonance) for acquisition. However, for achieving an ultrashort TE less than 0.1 ms, UTE sequences require half-Sinc, VERSE-modified half-Sinc, or short rectangular RF pulses to minimize the excitation time. These three common excitation pulses adopted in UTE are reviewed in this section.

1.2.1.1.1. Half-Pulse and Variable-Rate Selective Excitation (VERSE)

Half-Sinc excitation pulses are used in UTE techniques to reduce TE. Two half-Sinc pulses paired with opposite slice selection gradients are employed in two TR repetition cycles, respectively (Figures 1.5.a and b) (15,28). By adding the MR signals from these two cycles, the resultant slice selection profile is equivalent to the one from an intact ‘Sinc’ excitation. In other words, the summation of the signals resulted from a pair of half-Sinc excitations is mathematically analogous to the signal originating from a conventional full-Sinc excitation (14,29). With two first halves of a Sinc pulse (and a slice selection gradient), this arrangement achieves a reduction of TE without jeopardizing the slice selection profile. As an improvement to this approach, a variable-rate selective excitation (VERSE) technique has been used. In the VERSE pulse, the ramp-down of the slice selection gradient can become a part of the half-Sinc excitation process that ends up at the beginning of TE (Figure 1.5.c and d) (14). By combining a time-varying gradient and a modified RF pulse, the VERSE technique can excite a slice profile comparable to a regular selective excitation (16). The application of the VERSE technique can help reduce the specific absorption rate (SAR) of RF pulse and, more importantly in this context, the duration of excitation (30). For UTE implementation, with a reconfigured half-Sinc pulse playing simultaneously with the slice selection gradient’s plateau and ramp-down, the VERSE-based half-Sinc excitation can accomplish the selective excitation without a gradient ramp-down and refocusing gradient. For these reasons, the VERSE-based half-Sinc excitation has been widely adopted in UTE applications for its superiority in reducing minimal TE (31–33).

There are also some challenges for implementing the half-Sinc pulses in UTE sequences. Most applications involving half-Sinc excitation utilize 2D UTE imaging with a minimal TE of 8 μ s (14,33–36), but there are a few implementations of 3D half-Sinc excitation combining with a stack-

of-radial-spokes technique, which only allows for one 'authentic' ultrashort TE acquisition (at $k_z=0$ in the k space) (22,37). One problem with the VERSE-modified pulse is that it can only accurately create the slice profile for on-resonance spins (water); it causes profile distortion for off-resonance spins, such as fat (16,30). The profile distorts more drastically when the strength of the slice selection gradient increases (16). A simple half-Sinc excitation without VERSE can also be implemented in UTE imaging with a refocusing gradient (38,39). This measure can theoretically avoid off-resonance distortion brought by the VERSE technique but potentially prolong the minimal TE due to the need for a refocusing gradient. However, the trade-off between the off-resonance distortion and the minimal TE has not been well studied in the literature.

1.2.1.1.2. Rectangular Pulse

The rectangular pulse is a more popular choice in 3D UTE imaging. Compared to a standard slab-selective pulse in 3D, a rectangular pulse has a shorter duration without a need for a slab selection gradient and a corresponding refocusing gradient (Figure 1.5.e and f). Given the complexity of the half-Sinc pulse implemented with VERSE and the doubled acquisition time, the rectangular pulse is better solution in 3D UTE imaging to obtain a minimal TE of less than 0.1 ms (40,41). Regarding patient safety, a rectangular pulse is prone to lead to a higher SAR and increased transmitter bandwidth as compared to a slab-selective Sinc pulse, as the former uses a shorter pulse duration to carry out a non-selective excitation. However, nearly without any applications of half-Sinc pulses in 3D UTE imaging, there has been no thorough study for the direct comparisons to the rectangular pulse in terms of signal, contrast, Signal-to-Noise Ratio (SNR), and SAR.

1.2.1.2. Trajectories

In UTE imaging, Cartesian trajectories are replaced by non-Cartesian to achieve an ultrashort TE. This is accomplished by manipulating the amplitude and waveform of the readout gradients. Radial- and spiral-based trajectories are two common k-space filling strategies used in UTE 2D and 3D imaging. This section will give an overview of the radial trajectory, the spiral trajectory and their variants.

1.2.1.2.1. Radial

In UTE imaging, radial trajectory fills k-space with the collected free induction decay (FID) signals beginning from the centre and moving radially outwards (Figure 1.5.a). Different from the Cartesian trajectory that is achieved by a phase-encoding gradient linearly varied from TR to TR and a constant readout gradient, the radial trajectory discards the phase-encoding gradient and (only) varies the readout gradient's amplitude with a cosine and sine function along the x and the y axis, respectively (Figure 1.5.a and b):

$$G_x = G \cos(\theta) \quad [1.4]$$

$$G_y = G \sin(\theta) \quad [1.5]$$

where G is the readout gradient amplitude determined by the field-of-view (FOV) and readout bandwidth, θ is an azimuthal angle, describing the radial line's (spoke) angle from the x axis with a range of $[0, 2\pi)$, and G_x and G_y are the resultant gradient amplitudes along the x axis and the y axis. As a UTE sequence acquisition starts nearly immediately after the RF-excitation, the ADC for the radial trajectory usually begins from the ramp-up of readout gradient instead of waiting for the arrival of the plateau as done in Cartesian trajectory (Figure 1.5b). The ramp-up acquisition portion oversamples the FID signal in k-space, which must be accounted for in the k-space filling and reconstruction. Although the centre-out radial trajectory, also known as projection acquisition (PA), was the first acquisition strategy invented for MRI in 1973 (42), the combination of a 2D radial trajectory and a half-Sinc (VERSE) excitation was the first UTE implementation for investigating short T2 components in 1991, and it has been widely applied in the 2D UTE imaging ever since (14).

For UTE, the radial trajectory has also been extended to 3D imaging using a Stack-of-Stars or Koosh-Ball approach (43). Stack-of-Stars stacks a pile of 2D planes of radial spokes (projections), forming a cylinder in the 3D k-space (37,44). Stack-of-Stars uses a 2D radial trajectory in each plane while using a phase-encoding gradient along the third dimension, the slice selection direction (e.g., the z -axis). The introduction of phase encoding gradient in the Stack-of-Stars approach potentially prolongs minimal TE. To further reduce the minimal TE, one can employ a VERSE-modified half-Sinc pulse along with a variable TE strategy (22,37). The variable TE strategy minimizes TE to $8 \mu\text{s}$ at $k_z=0$, the exact middle radial plane at the z -axis of the k-space, as the phase encoding gradient is zero at this point. The TE of $8 \mu\text{s}$ at $k_z=0$ is regarded as the effective TE since

this radial plane carries the most signal energy in the k-space. The Koosh-Ball approach fills the 3D k-space in a sphere-like manner by radial spokes extending from the origin at the centre of k-space in all three dimensions (45). Besides the azimuthal angle θ used in the 2D radial trajectory, Koosh-Ball introduces the polar angle φ from 0 to π to constitute a 3D radial trajectory by varying the readout gradient in each direction (Figure 1.5.e and f):

$$G_x = G \sin(\varphi) \cos(\theta) \quad [1.6]$$

$$G_y = G \sin(\varphi) \sin(\theta) \quad [1.7]$$

$$G_z = G \cos(\varphi) \quad [1.8]$$

where G is the readout gradient amplitude determined by FOV and readout bandwidth, θ is the azimuthal angle ranging from 0 to 2π , φ is the polar angle ranging from 0 to π , and G_x , G_y and G_z are the resultant gradient amplitudes along the x , y , and z axis. Even though sometimes a non-isotropic result and shorter scan time are more desired with the help of phase encoding gradients in Stack-of-Stars (22,43), Koosh-Ball can achieve shorter TEs for all its FID signals because it does not employ phase encoding and provides an isotropic image volume (39,43).

1.2.1.2.2. *Spiral*

The spiral trajectory is another popular centre-out non-Cartesian trajectory; it achieves UTE scans by varying the readout gradient waveform with time. There are different techniques to design spiral trajectories, as introduced in by several groups (17,18,46,47). A well-known drawback of spiral trajectories with long data readouts is that they are sensitive to the inhomogeneity of gradient fields and susceptibility. Therefore, a common practice is to apply the spiral trajectory in an interleaved fashion (multi-shots) by breaking up a long spiral waveform (with ADC) into multiple segments and radially filling them to the k-space plane. This method borrows the radial trajectory's approach except the radial spokes are replaced with segmented spirals. Combined with half-Sinc pulses, the spiral trajectory can serve as an alternative to the radial for 2D UTE imaging (Figure 1.5.c and d) (33,48). There are various forms of 3D spiral trajectories and are known as Stack-of-Spirals, Twisted Projection Imaging (TPI), Fermat looped, orthogonally encoded trajectories (FLORET), or Spiral-Cones (Figure 1.5.g and h) (49–53). Similar to Stack-of-Stars, Stack-of-Spirals fills the 3D k space by piling up 2D planar spiral into a cylinder; this trajectory also utilizes a variable duration of phase encoding gradient along the z -axis (49,51,54,55). The UTE imaging using Stack-of-Spirals has been often applied in lung imaging where the shorter scan time is required; however,

with a non-isotropic resolution and a variable short TE in return. TPI is a hybrid of a radial and spiral trajectory: TPI starts with a Koosh-Ball style trajectory to fill the centre of k-space and then twists the radial spokes into spiral shape in the peripheral k-space (52). This method can help compensate for the sampling inefficiency observed in the periphery of k-space (52). However, an abrupt transition can occur from the radial to the spiral gradient portion, which must then be smoothed (50). Recently, another spiral-based trajectory, FLORET, has gained some attention in UTE imaging. FLORET fills 3D k-space using two or three orthogonal “hubs”; each hub comprises a group of cones with different angles from the z-axis; each cone is composed of a Fermat’s spiral trajectory (56,57). The FLORET trajectory uses only one spiral leaf in each cone to achieve a highly efficient 3D k-space filling (56). The Spiral-Cones trajectory also uses a series of cones to fill 3D k-space, but each cone typically consists of multiple interleaved spirals (Figure 1.5.g). The Spiral-Cones trajectory carries out spiral gradients along the in-plane direction (e.g., the x-y plane) and a radial gradient along the out-of-plane direction (e.g., the z-axis) (Figure 1.5.h). As an advantage, the Spiral-Cones can provide a shorter data acquisition window due to the application of multi-interleaved spirals despite longer scan time. This characteristic will become very valuable in MSK imaging as a shorter data acquisition window can maximally alleviate short T2 signal and resolution losses expected during readout (19). Also, the design of Spiral-Cones gradient waveforms is subject to the maximal amplitude and slew rate of the gradient system. Last, the Spiral-Cones trajectory can also provide an isotropic resolution with a consistent TE for all collected FID signals.

1.2.1.3. Reconstruction Techniques

Unlike the Cartesian-acquired MR data, UTE sequences, using non-Cartesian trajectories, do not distribute k-space data uniformly in a grid, so reconstruction methods that support non-Cartesian trajectories are required. Three main methods of non-Cartesian reconstruction are Filtered Back Projection Reconstruction (FBP), the gridding algorithm, and Non-Uniform Fast Fourier Transform (NUFFT).

The FBP method is only applicable to non-Cartesian k-space data collected by pure radial-based trajectories. This method first uses a 1D inverse Fast Fourier Transform (FFT) to process each radial spoke defined in the non-Cartesian coordinate system. Then, all transformed spokes form a

2D plane based on each radial angle. Lastly, an inverse Radon transform is applied to the 2D plane to complete the MR reconstruction. Due to the incompatibility with other non-Cartesian trajectories, FBP is less preferred than the gridding algorithm and NUFFT.

As a universal method, the gridding algorithm can adapt to any arbitrary trajectory for reconstruction. This method uses a Kaiser–Bessel window, which is a low-pass filter, to convolute with the k-space data collected by the non-Cartesian trajectory and then re-grid it to a Cartesian coordinate system (25,26). The re-gridded data in k-space is then treated as Cartesian collected data and processed by an inverse FFT to complete the reconstruction of MR images. This method has been widely adopted for various trajectories and applications (40,43,50,51,57,58).

Last, NUFFT is another popular method for the non-Cartesian reconstruction in UTE imaging. NUFFT can accommodate the non-uniformity in non-Cartesian trajectories, allowing for direct reconstruction of non-Cartesian k-space data (59,60). However, in essence, NUFFT is equivalent to the gridding algorithm that uses a Gaussian convolution window (instead of the Kaiser–Bessel window) (60). As acknowledged, NUFFT has become another effective method for the non-Cartesian reconstruction of UTE sequences (43,61–63).

1.2.1.4. Summary of UTE techniques

Although various techniques have been developed with their unique features for achieving UTE imaging, as reviewed above, there are still some gaps in the literature regarding the UTE techniques.

- Nearly no application of half-Sinc pulse or its VERSE modification has been applied in 3D UTE imaging for excitation.
- There is no direct comparison between the rectangular pulse, half-Sinc pulse, and half-Sinc pulse with the VERSE modification regarding the contrast or SNR.
- It is relatively unknown what trajectory is better regarding the SNR in 2D and 3D UTE imaging.
- It is also unclear what combination of the RF pulse and trajectory can yield higher SNR images.
- It is relatively unclear what reconstruction technique is superior and if they can be improved regarding artifact reduction.

- It has not been well studied whether differing UTE acquisition techniques can improve the images by reducing or removing artifacts.
- Likewise, it has not been well studied whether differing UTE acquisition techniques can improve the SNR of images.

1.2.2. Qualitative UTE Imaging

One main application of UTE is to provide signal directly to short-T2 tissues for morphological imaging. UTE sequences can create a contrast between short-T2 tissue and also other tissues. One example is that UTE sequences allow for a discernible contrast between the deep layer of cartilage and the subchondral cortical bone due to their different short-T2 relaxation times, but they both appear as a merged, indistinguishable signal void on conventional MR images (64,65). As another example, UTE sequences can also create a noticeable contrast between the cortical bone (short-T2) and bone marrow (long-T2) by directly supplying the brightness to the cortical bone on UTE images (64). However, in some cases, the stronger long T2 signal can severely obscure the short T2 signal in UTE images without providing a well-emphasized contrast between the short-T2 and long-T2 tissue. For example, the deep radial, calcified cartilage and subchondral bone (short-T2) is positioned between the middle layer of cartilage and bone marrow fat, both of which have long T2 relaxation times; and if without a simultaneous signal suppression for both the middle layer of cartilage and bone marrow fat, the contrast of the deep radial, calcified cartilage and subchondral bone is difficult to distinguish from either of the long-T2 tissues (66). Hence, the long-T2 suppression techniques, including the dual-echo subtraction methods, saturation pulses, or inversion nulling pulses, are essential for UTE sequences to selectively suppress the signals from various long-T2 tissues while enhancing the contrast for short-T2 tissues.

1.2.2.1. Dual-Echo Subtraction

Adopted by many UTE sequences, the dual-echo subtraction method achieves a short T2 contrast enhancement with great simplicity. The procedure is to acquire two images using a UTE sequence first with an ultrashort TE and next with a longer TE, and then subtract the later signal from the former to obtain the difference image. Because the short T2 components are experiencing a much faster signal decay than the long T2 components over the short interval between two TEs, the former should generally present predominant contrast in the resultant image. However, different

TE pairs and subtraction methods will cast a varied impact on the contrast enhancement for short T2 components. Typically, the longer TE is chosen for the minimal time for fat and water to be in-phase (i.e. 2.2 ms for a 3 Tesla system) or the multiples of this value (e.g., 4.4 or 6.6 ms for a 3 Tesla system), while the shorter TE is the UTE lower limit - usually less than 100 μ s (67). Because the minimum TE (of UTE) is approximately zero, i.e., the initial state of fat and water is in-phase, the subsequent in-phase times (longer TEs) can help offset the long T2 signals from both water and fat simultaneously (67,68). For the subtraction methods, the most common approach is to use the second echo to directly subtract from the first echo to obtain the enhanced details of short T2 components (Figure 1.6.a-c) (69,70). Alternatively, the second (or the first) echo can be rescaled linearly or exponentially to higher (or lower) intensities before the subtraction, which can further dim the contrast for long T2 components (even to negative values) while highlighting the details for short T2 components (e.g., Bone) (Figure 1.6.d-h) (67,70,71). These linear or exponential weighting factors can be determined experimentally by optimizing the SNR and contrast-to-noise ratio (CNR) (70,71).

Even though the dual-echo subtraction can efficiently suppress the signal from long-T2 tissues in UTE imaging, it has some deficiencies—i.e., degrading SNR and increased vulnerability to susceptibility artifact (67,68). Also, in combination with saturation or inversion recovery pulses, the dual-echo subtraction can be further improved, which will be covered in subsequent sections (66,72).

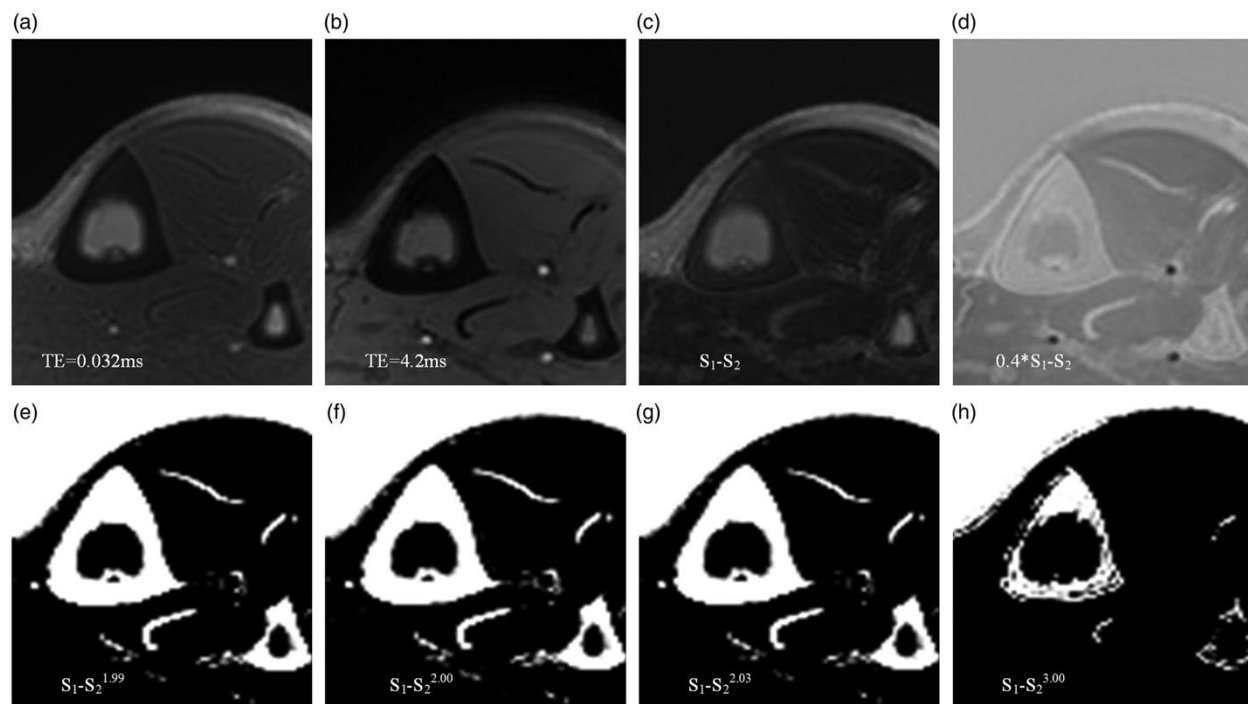


Figure 1.6. Example of axial tibia UTE imaging using various dual-echo subtraction methods.

(a, b) show images of the tibia acquired with a TE of 0.032 ms and 4.2 ms, respectively. The cortical bone has the lowest brightness, the bone marrow fat demonstrates the highest brightness, and the muscle presents the intermediate brightness. (c) The direct subtraction without any rescaling where the muscle's signal was heavily suppressed. (d) The linearly weighted subtraction with the first echo rescaled by 0.4 where the cortical bone's contrast was enhanced with bright signal. (e–h) The exponential subtraction methods with the second echo exponentially rescaled with different factors (i.e., 1.99, 2.00, 2.03, and 3.00) where the cortical bone's contrast (bright) was isolated from the suppressed bone marrow fat and muscle (dark). Reprinted from (70) (DOI link: <https://doi.org/10.1177/0284185119877797>). Permission is granted by SAGE Publications for gratis reuse in a thesis/dissertation.

1.2.2.2. Long T2 Saturation Pulses

Saturation pulses can also help highlight the short-T2 contrast in UTE imaging by directly suppressing the long-T2 signal during the acquisition. The saturation pulses usually require a long duration (e.g., 9-24 ms) and a flip angle of 90° to selectively saturate the long-T2 components while sparing the short-T2 components (15,68). Long T2 saturation pulses are usually implemented prior to gradient spoilers. Saturation pulses can address the limitations of the subtraction method described above (67,68). For water saturation, one can utilize a long 90° rectangular pulse followed by a spoiling gradient to tip the long T2 magnetizations to the transverse plane first, and the spoilers can subsequently destroy the net magnetization through dephasing (15). However, given the chemical shift between two peaks of water and fat in the spectrum (about 440 Hz in 3.0 Tesla), a

90° long rectangular pulse can only effectively eliminate the water signal with limited influence on fat. As a remedy for this, two long rectangular pulses, centred at the water (90°) and fat (120°) frequencies (each with a gradient spoiler), can be sequentially applied, which allows for selective suppression for both water and fat (which is known as T2-selective RF Excitation-TELEX) (34). However, the long rectangular pulse is very sensitive to off-resonance effects due to its narrow spectral bandwidths. Thus, an equivalent Gaussian or Sinc pulse, with a wider bandwidth, can be adopted alternatively for a more stable saturation (67,69). As an improvement, the single-and dual-band saturation pulses produced by the Shinnar–Le Roux transform can provide a better suppression profile (73). Finally, due to the different relaxation times and bandwidths between water and fat, the optimal flip angles for the saturation pulses are usually slightly larger than 90°; for example, one needs to use a flip angle of 100° for water and 110° for fat when using a dual-band pulse (68). Specifically, these optimized saturation pulses can slightly invert water's and fat's magnetizations to the longitudinal direction. Given the delay between the magnetization preparation and RF excitation, this setup forces the inverted longitudinal magnetizations to be returning to zero when the excitation occurs (68). The dual-band saturation pulse can suppress the fat and water signal and highlight the short-T2 contrast, e.g., the cortical bone (Figure 1.7.c-d) (68). Furthermore, the saturation pulses can also be assisted with the dual-echo subtraction method to suppress the residual long T2 signal resulted from an imperfect saturation (Figure 1.7.d) (67,68).

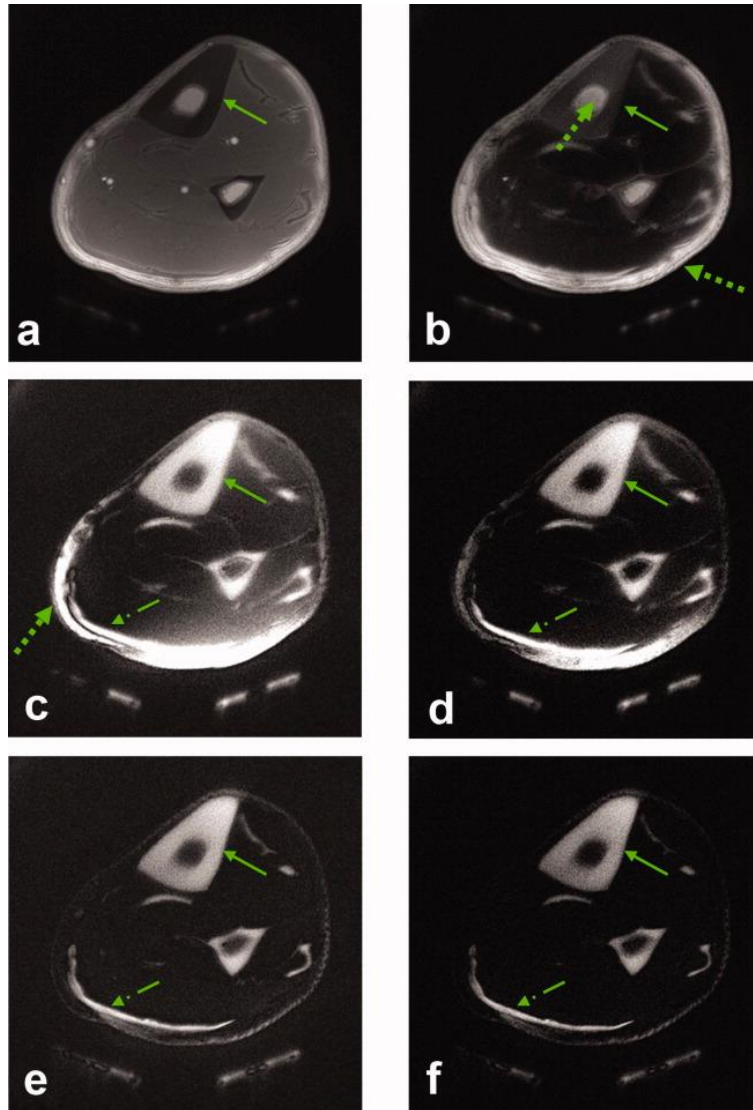


Figure 1.7. Example of a comparison between various suppression techniques on axial mid-tibia images.

The solid arrow indicates the cortical bone, the dotted arrow indicates the fat, including the bone marrow, and the dotted-dashed arrow indicates the tendon. (a) UTE's first echo; (b) the subtracted image using dual-echo UTE scans; (c) dual-band UTE's first echo; (d) the subtracted image using dual-band UTE's two echoes; (e) inversion recovery UTE (IR-UTE)'s first echo; (f) the subtracted image using with IR-UTE's two echoes. Notably, the fat signal was suppressed by dual-band UTE and IR-UTE better than dual-echo UTE. Also, dual-echo UTE can further improve the long-T2 suppression carried out by dual-band UTE and IR-UTE. Reprinted from (68) (DOI link: <https://doi.org/10.1002/mrm.23267>). Permission is granted by John Wiley and Sons for reuse in a thesis/dissertation.

1.2.2.3. Long T2 Inversion Recovery Pulses

Long-T2 suppression in UTE imaging can also utilize long adiabatic inversion recovery pulses. Because the long adiabatic inversion pulses are insensitive to B1 field inhomogeneity, they can

uniformly invert the long T2 components 180° and pose little influence on the short T2 components. As the reversed longitudinal magnetizations will grow back to their original states after the inversion pulse is delivered, the time of inversion (TI) is used to describe the time that indicates how much magnetization has recovered from the inversion before data acquisition. Therefore, a proper choice of TI forces the inverted, longitudinal magnetization of long-T2 components to be fully nulled at the time the UTE sequence begins. Similar to the long-T2 saturation, this method can also effectively preserve most of the short T2 signal while suppressing the long T2 signal. To null the signals from both water and fat, one can choose a single adiabatic inversion pulse with a broad bandwidth (e.g., 1kHz) and centre frequency (around -440 Hz in 3 Tesla) that can cover both water and fat (67,68). However, since the inverted water and fat magnetizations have significantly different TI times for nulling, it is challenging to create an optimal suppression for one without jeopardizing the other. Practically, one can address this issue by applying two inversion pulses with two TI times (Figure 1.8): here two adiabatic inversion pulses, centred at the water and fat, were applied sequentially (35,67,74). Due to the sufficiently different TI times between water and fat, an optimized combination of the TI times can force both materials to reach a concurrent null point (35,74). Compared to the saturation pulse, the adiabatic inversion pulse can achieve a superior suppression of the long T2 components due to its robustness to B1 inhomogeneity but at the cost of longer scan time and degraded SNR for the short T2 components (Figure 1.7.c-f) (67,68). The inversion pulses can also work alongside the dual-echo subtraction method to achieve improved long T2 suppression (67).

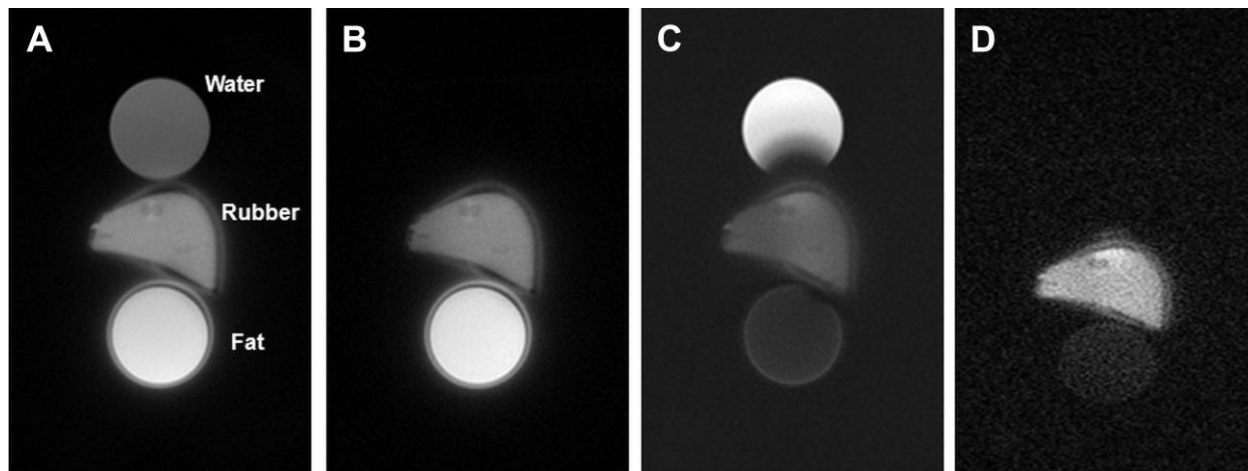


Figure 1.8. Example of a comparison between various long-T2 inversion pulses used in a phantom. (a) UTE imaging of a phantom comprising water, fat, and rubber (short T2 material) without any long-T2 suppression. (b) With the adiabatic inversion pulse centred at the water peak, the UTE image shows a complete void on water and high intensity for fat. (c) With the adiabatic inversion pulse centred at the fat peak, the UTE image shows a heavily suppressed signal for fat and still bright contrast for water. (d) With the dual inversion recovery (DIR) technique, the UTE image shows a simultaneous suppression for both water and fat, leaving enhanced rubber contrast. Reprinted from (35) (DOI link: <https://doi.org/10.1016/j.joca.2012.09.009>). Permission is granted by Elsevier for reuse in a thesis/dissertation.

1.2.2.4. *Off Resonance Saturation*

Off-resonance saturation pulses followed by spoiler gradients can also suppress the long-T2 signal but does so indirectly. Short T2 components have a much broader spectral bandwidth than long T2 components. Therefore, an off-resonance pulse with a frequency offset far away from water/fat frequencies can selectively saturate the short T2 components and minimize the impact on long T2 components. Additionally, the off-resonance pulse can affect the short T2 components in two ways: direct saturation and MT. Therefore, one can use two UTE images, acquired with and without the off-resonance saturation, to create a contrast difference reflecting these two effects (72,75). As the off-resonance saturation pulse nearly has no impact on the long T2 components, the difference image will cancel out the signal from water and fat and only highlight the contrast of short T2 components. The off-resonance saturation pulse can provide excellent suppression for long T2 components indirectly with an optimized combination of flip angle, duration, and frequency offset (Figure 1.9) (72).

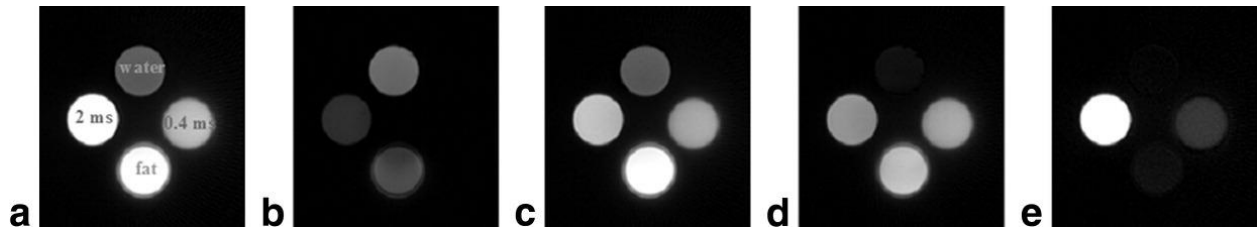


Figure 1.9. Example of a comparison between the dual-echo subtraction and off-resonance saturation technique used in a phantom.

The phantom comprises distilled water, plant oil, MnCl₂ solution possessing two short T₂ times of 2 ms and 0.4 ms, respectively. From (a-c), the UTE imaging settings are as follows: (a) TE = 8 μs, (b) TE = 4.4 ms, and (c) TE = 8 μs and Fermi off-resonance saturation pulse with duration = 16 ms and flip angle = 2400°. (d) The dual-echo subtraction method, i.e., (a) minus (b), producing a bright signal for the short-T₂ tubes but poor contrast over the plant oil tube. (e) Off-Resonance Saturation Contrast (UTE-OSC), i.e., (a) minus (c), providing high contrast for short-T₂ tubes and excellent suppression for long-T₂ water and plant oil tubes. Reprinted from (72) (DOI link: <https://doi.org/10.1002/mrm.22007>). Permission is granted by John Wiley and Sons for reuse in a thesis/dissertation.

1.2.2.5. Summary of Qualitative UTE Imaging

Long-T₂ suppression techniques are important in UTE scans for providing enhanced contrast for short-T₂ tissues.

- The efficacy of the off-resonance saturation method (i.e., using MT pulse) using UTE sequences has not been widely studied and utilized.
- Especially, there are not thorough studies that directly compare the off-resonance saturation method with other long-T₂ suppression methods regarding contrast and SNR.
- For suppression performance evaluation, if the long-T₂ suppression scans use the same sequence with other imaging parameters identical, it is unclear how one long-T₂ suppression technique compares to another regarding the contrasts and SNR produced by various materials (e.g., water or oil).

1.2.3. Quantitative UTE Imaging

Besides the morphological contrast, UTE sequences can be used quantitatively to produce parametric maps, such as T₁ or T₂* relaxation times, for short-T₂ components. This can be particularly important in studies of disease, for example, UTE-T₂* relaxation time increases with meniscal degeneration (76,77). This section will review the methods that have been widely or newly implemented in UTE imaging for quantifying short-T₂ components, specifically T₁ relaxation time mapping, T₂* relaxation time mapping with a mono- or bi-exponential analysis,

evaluation of magnetization transfer ratio (MTR), and analysis of quantitative MT (QMT) parameters using a two-pool model (78).

1.2.3.1. T1 Relaxation Time Mapping

T1 relaxation time mapping for short-T2 tissues can be carried out by using UTE sequences. Saturation-recovery (SR), variable-flip-angle (VFA), and variable-time-of-repetition (VTR) are three widely available T1 mapping methods in UTE imaging (79–81). Even though the inversion recovery technique is the gold standard for T1 measurement, the inversion pulses cannot effectively invert short T2 components, as they can easily do for long T2 components (6,81). Therefore, this method is impractical for T1 quantification using UTE sequences (12,82). Instead, short saturation pulses (e.g., a 90° rectangular pulse with 256 us) followed by spoiling gradients have been used to saturate both the short and long T2 components. As a result, one can obtain T1 mapping by varying the time of saturation recovery (TSR) and fitting the collected UTE signals to an exponential model (79). However, the saturation recovery method for T1 mapping is usually adopted in 2D imaging because it is not time-efficient to add the saturation block to each TR cycle required for 3D imaging. For the T1 mapping in 3D UTE imaging, the VFA or VTR method can serve as a better alternative (80,81,83). However, VFA and VTR are sensitive to B1 field inhomogeneity, so one might need to use B1 mapping or actual flip angle imaging for correction to improve T1 quantification (Figure 1.10) (81).

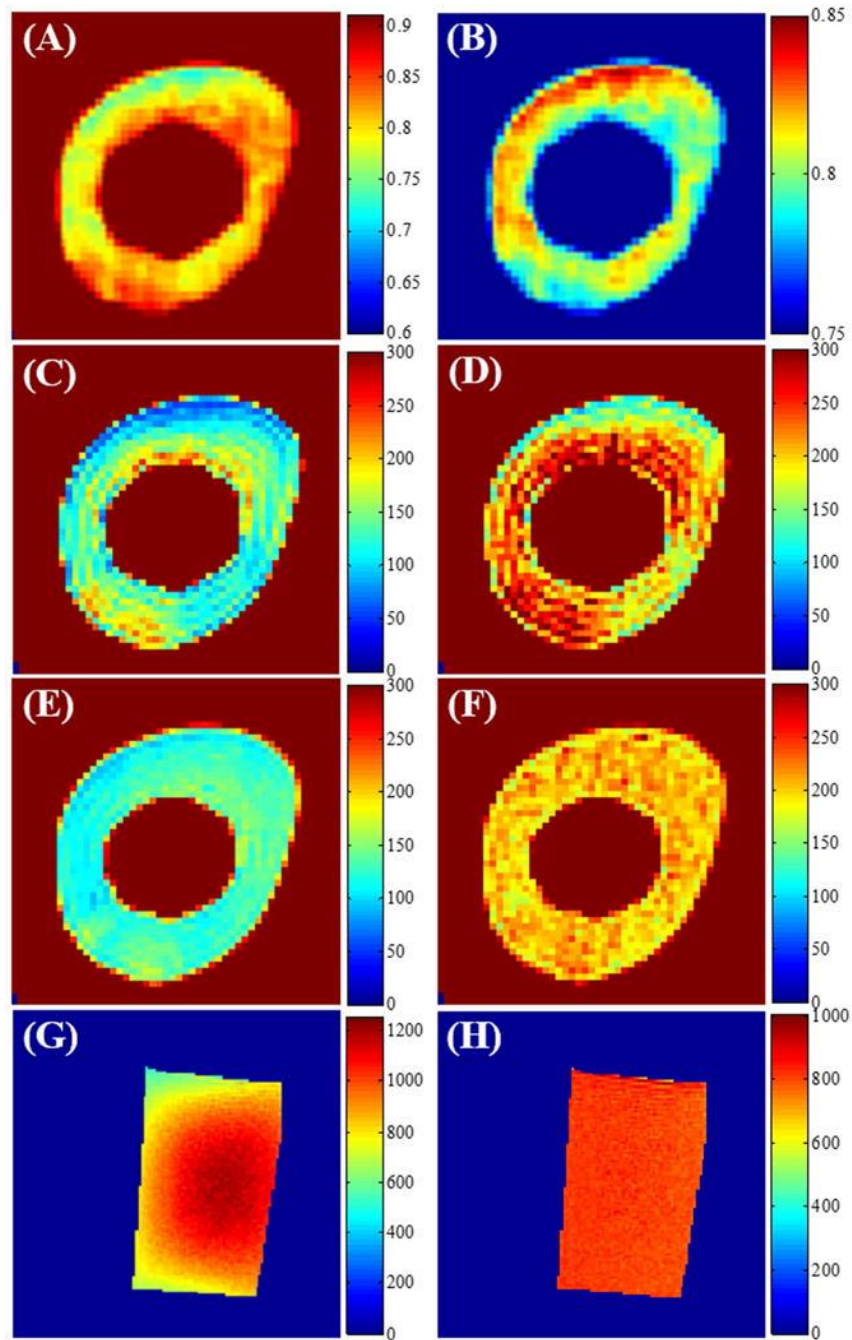


Figure 1.10. Example of T1-related maps of an agarose bone phantom.

The cortical bone section was stripped off with soft tissues and suspended within the agarose gel. T1 mappings used 3D UTE-Cones variable flip angle (VFA) and variable time-of-repetition (VTR) based methods (in units of ms). (a) B_{1s} field map; (b) f_z map; (c) T1 map (ms) using VFA without B_1 correction; (d) T1 map (ms) using VFA with B_1 correction; (e) T1 map (ms) using VTR without B_1 correction; and (f) T1 map (ms) using VTR with the actual flip angle imaging (AFI) correction. Another phantom just containing agarose was also used for T1 mappings. (g) T1 map (ms) using VTR without B_1 correction; and (h) T1 map (ms) using VTR with AFI- B_1 correction. Reprinted from (81) (DOI link: <https://doi.org/10.1002/mrm.27066>). Permission is granted by *John Wiley and Sons* for reuse in a thesis/dissertation.

1.2.3.2. T2* Relaxation Time Mapping

T2* mapping in UTE imaging can be realized by a variable TE method with a mono- or bi-exponential fitting (84,85). It is challenging to use UTE sequences to obtain T2 maps since some T2-mapping sequences need a long TE; for example, spin-echo sequences require the presence of a long inversion pulse within the TE. For short-T2 tissues, one can obtain the T2* by fitting the UTE signal collected with different TEs to a mono-exponential model (41). This method treats short-T2 tissues as one single compartment. However, it is likely more realistic to think short T2 tissues as being composed of long and short T2 components, e.g., the coexisting free water and water of the collagen in the meniscus. Since UTE sequences can simultaneously acquire adequate signals for both long and short T2 components, one can also fit a bi-exponential model to obtain estimates of two components, specifically the T2* times and fractions of each (86). Studies have demonstrated that the bi-exponential model can provide a superior fitting result as compared to the mono-exponential model (Figure 1.11), although a longer scan time is also required (85). However, it is unclear how many T2 components a tissue has, so even higher-order fitting might be required; for example, a tri-component model (87). With a higher order of fitting, more parameters are introduced. Therefore, to be able to estimate the parameters that determine the fitting model uniquely, one must sample a higher number of TEs (echoes), and the range of the TE sampling must sufficiently cover the range of possible T2* values in the examined tissue (87).

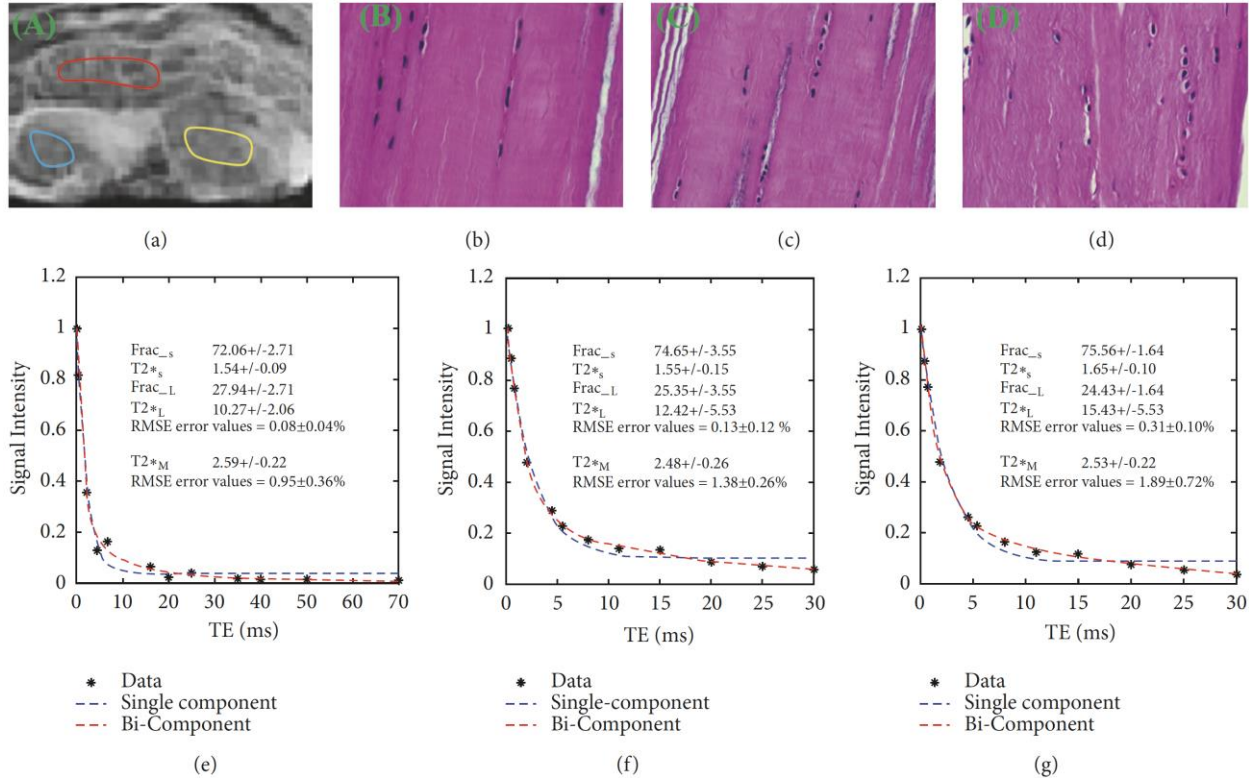


Figure 1.11. Example of the mono- and bi-component T2* fit.

(a) Region-of-interest (ROI): the red contour represents the patella tendon (PT) sample, the yellow contour stands for the posterior cruciate ligament (PCL) sample, and the blue contour delineates the anterior cruciate ligament (ACL) sample. Histology in (b) PT, (c) PCL, and (d) ACL. (e-g) show the raw data, single-, and bi-component fitting of PT (e), PCL (f), and ACL (g) using interleaved multi-echo UTE images. The bi-component model shows an overall better fitting than the single-component model. Reprinted from (85) (DOI link: <https://doi.org/10.1155/2019/8597423>). This open-access article, published by *Hindawi*, permits unrestricted use, distribution, and reproduction in any medium, under the license <https://creativecommons.org/licenses/by/4.0/>.

1.2.3.3. Magnetization Transfer Ratio (MTR)

In UTE imaging, MTR can also be obtained for short T2 tissues. MTR has been used by some quantitatively and by others as a different contrast mechanism to observe particular morphology since the calculated MTR values depend on specific parameters of MT pulses (9,88). As a result, it is difficult to compare MTR between studies. Majorly through a dipole-dipole coupling, the MT effect describes the cross-relaxation or spin exchange between a free (e.g., water) and a bound pool (e.g., macromolecules) (78). A regular RF excitation pulse can only select a narrow spectral band around the water proton's resonant frequency, while the macromolecules, possessing a broad spectral bandwidth, hardly respond to this on-resonance pulse. Though the signal from the bound pool is almost always undetectable, one can still assess the bound pool indirectly via the MT effect

by using an off-resonance pulse to saturate the bound pool exclusively. The MT effect can be evaluated by MTR, using two image sets (an MT-pulse-saturated one and an unsaturated one), as defined in the following:

$$MTR = \frac{M_0 - M_1}{M_0} \quad [1.9]$$

Where M_0 and M_1 are the images acquired without and with an off-resonance saturation pulse, respectively. The off-resonance pulse has little impact on the free pool, so the MT effect is barely observed in the tissues where only the free pool exists, for example, the fat or bone marrow. Therefore, one can use the MT difference contrast (i.e., $M_0 - M_1$) or MTR contrast to suppress the signal from free pools with long T2 (e.g., fat or water).

The generation of MTR contrast is subject to sequence settings. UTE sequences can help MT pulses effectively display MTR contrast for the short T2 tissues, such as cortical bone, as the saturated signal resulted from the MT effect in their free pools decays so fast from being detected by conventional sequences. An off-resonance pulse can affect the free pool in two ways, the direct saturation and indirect MT, and both effects are accounted for in the calculation of MTR jointly, i.e., we cannot distinguish between them (88). The direct saturation effect can be diminished by applying a lower flip angle and a higher frequency offset to the off-resonance pulse, which can lead to a true MTR. However, an off-resonance pulse with an overly-high frequency or/and overly-low flip angle might fail to perform a thorough saturation for the bound pool, resulting in a degraded MT effect (88). To sum up, although the MTR is dependent on both physical properties of tissues and the sequence settings, including the choice of frequency offsets and flip angles of MT pulses, MTR values can still serve as a quantification biomarker for a phenomenological measure (9). For example, the variation of the MTR values was used to study the depleted-collagen within the patellar cartilage as a function of cartilage depth (89). Another example used UTE sequences to report a pixel-wise MTR map to quantify the MT effects of *in vivo* human tibial cortical bone (Figure 1.12) (88).

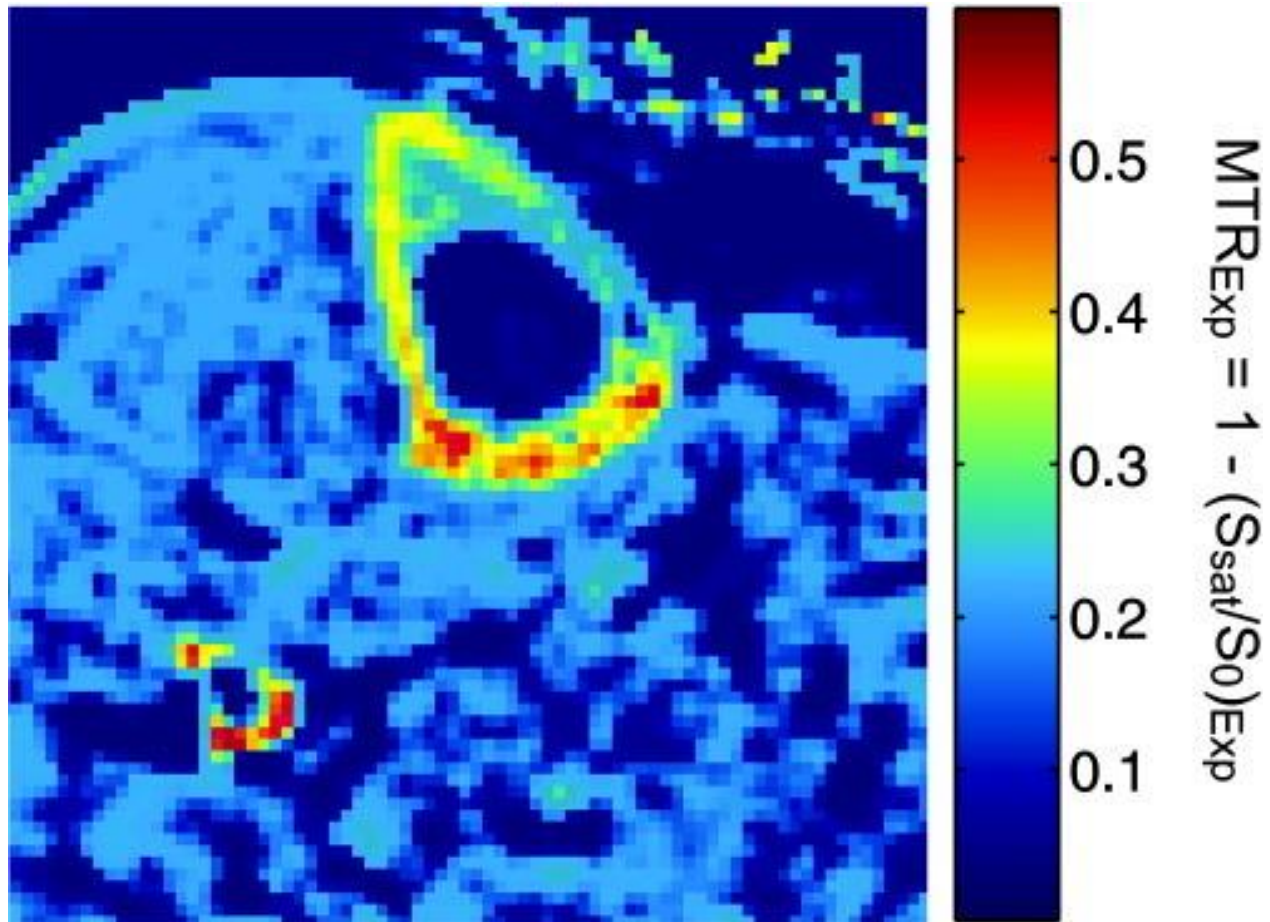


Figure 1.12. Example of a magnetization transfer ratio map of human tibial cortical bone *in vivo*.

The magnetization transfer (MT) pulse was set with an off-resonance frequency of 10 kHz and an MT pulse flip angle of 300° . Reprinted from (88) (DOI link: <https://doi.org/10.1002/mrm.21866>). Permission is granted by *John Wiley and Sons* for reuse in a thesis/dissertation.

1.2.3.4. *Quantitative Magnetization Transfer (QMT)*

Combined with UTE imaging, the QMT modelling (UTE-QMT) can provide enriched quantitative interpretations to short T2 tissues. Although UTE sequences cannot directly detect the signal of macromolecules, one can still use an MT pulse to probe macromolecules indirectly, as introduced above. By systematically adjusting an MT pulse's flip angle and frequency offset in a UTE sequence, one can further estimate additional MR properties from short T2 tissues with the help of the two-pool model, which will be covered in Chapter 3. These MR properties include the bound pool fraction (also known as a macromolecular fraction, MMF), T1 relaxation time of the free pool, T2 relaxation time of the free pool, T2 relaxation time of the bound pool, and the exchange rate between two pools (78,90,91). The UTE-QMT modelling can provide more informative analysis

for short T2 tissues than either T1 or T2* relaxation time mapping, as the former allows for an indirect quantitative assessment of the macromolecules in the bound pool. As an example, a study shows a significantly strong correlation ($R = -0.72$, $P < 0.01$) between the estimate of bound pool fraction and the bone porosity measured by micro-CT (which has been the gold standard for assessing porosity) (Figure 1.13) (92). In the same study, no significant correlation was found between the T2 relaxation time of the bound pool and the bone porosity. Despite being a relatively new technique, UTE-QMT imaging has demonstrated great potential in the quantitative assessment of some short T2 tissues, for example, the cortical bone and Achilles tendon (91–94). Further details of UTE-QMT mapping will be described in Chapter 3.

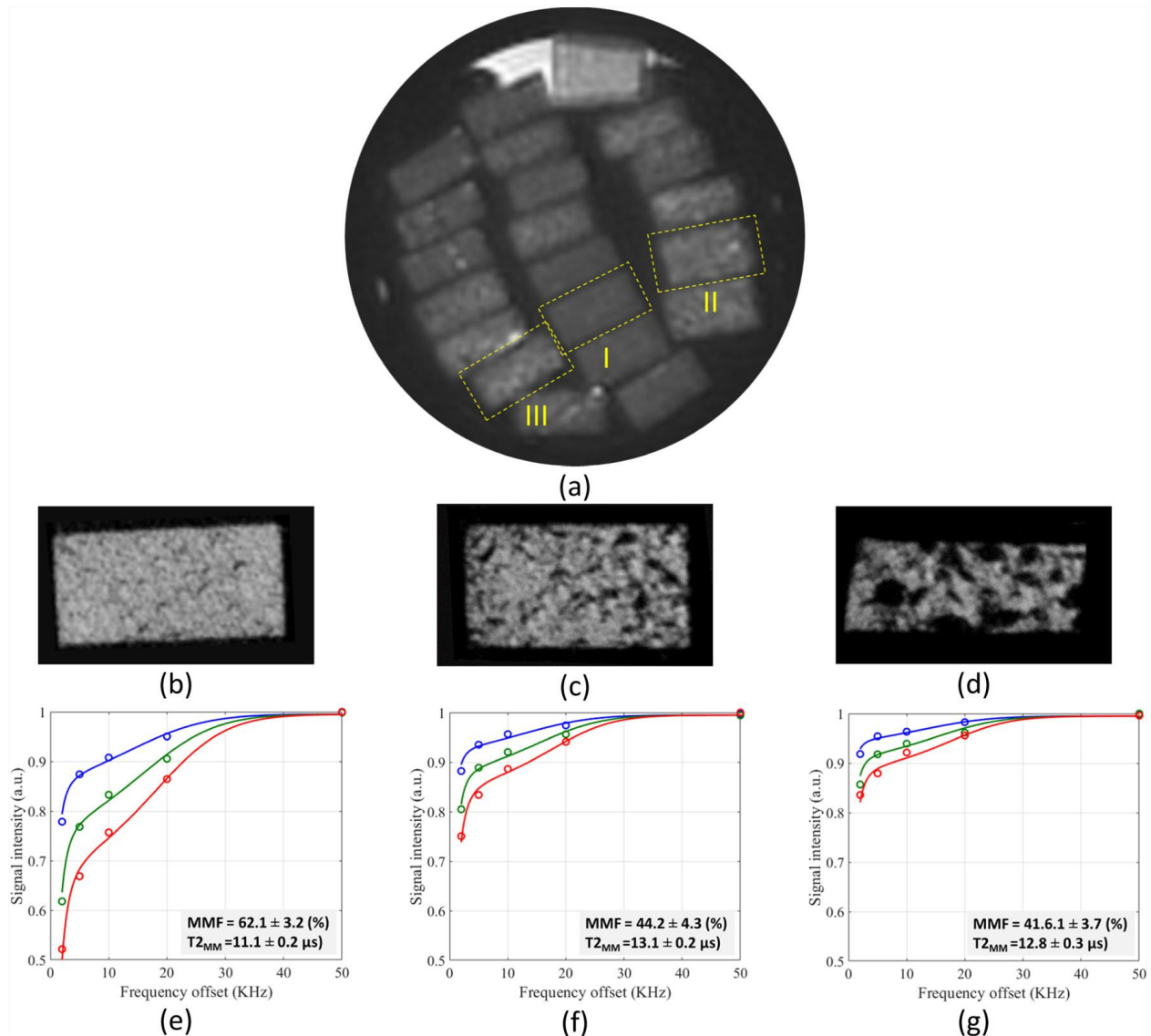


Figure 1.13. Example of the UTE-QMT modelling used in the porosity assessment of the bone.

Sample (I) is from a 47-year-old male donor with an average porosity of 5%; Sample (II) is from a 57-year-old female donor with an average porosity of 33%; Sample (III) is from a 91-year-old female donor with an average porosity of 53%. (a) UTE MR images with a TE of 0.032 ms; (b) μ CT images of Sample (I); (c) μ CT images of Sample (II); (d) μ CT images of Sample (III). (e) The two-pool MT modelling analysis of Sample (I); (f) the two-pool MT modelling analysis of Sample (II); (g) the two-pool MT modelling analysis of Sample (III). The MT pulses used three powers (400° in blue, 600° in green, and 800° in red) and five frequency offsets (2, 5, 10, 20, 50 kHz) for the modelling. MMF stands for macromolecular fraction, and $T2_{MM}$ denotes the T2 time of macromolecular. Reprinted from (92) (DOI link: <https://doi.org/10.1016/j.bonr.2019.100220>). Permission is not required for this non-commercial use (i.e., reuse in a thesis/dissertation). This article is published by Elsevier under the terms of <https://creativecommons.org/licenses/by-nc-nd/4.0/>.

1.2.3.5. Summary of Quantitative UTE Imaging

Preliminary results show that quantitative UTE MRI is promising for assessing tissue health and structure.

Summary of T1 relaxation mapping:

- For the UTE-QMT two-pool modelling, it is relatively unknown if it is feasible to use UTE-T1 relaxation mapping to help estimate the physical properties of the free and the bound pool.

Summary of T2* relaxation mapping:

- It is relatively unclear how many components (single or double) would be appropriate to consider for the T2* exponential fitting.

Summary of MTR mapping:

- It is unclear whether to consider MTR as a type of morphologic contrast or quantitative map since MTR is dependent on both sequence settings and tissue properties.
- The combination of the MTR method and UTE sequences has not been widely explored either for morphological visualization or quantitative assessment.

Summary of QMT mapping:

- There still have not been enough studies to verify the feasibility of QMT modelling using UTE sequences.
- The impacts of B1 correction and fitting lineshapes (Gaussian vs. Super-Lorentzian) on the UTE-QMT parameter estimations have not been thoroughly studied.

1.2.4. UTE Applications

As UTE sequences become further developed and disseminated, their clinical and research applications are being established. While there are many areas to explore, three currently important applications include the musculoskeletal system, radiation therapy, and lung disease. This section will give an overview of the UTE imaging in each of these particular applications.

1.2.4.1. The Musculoskeletal System

The musculoskeletal (MSK) system includes muscles, bones, and other connective joint tissues, such as, menisci, articular cartilage, tendons, and ligaments. These various tissues, working

coordinately, provide the necessary support to the structural integrity and movement of the body. Knee joints are a common example of the MSK system in the human body and are useful to study because they are often affected by disease and injury, and they contain many different tissues. The knee is comprised of the muscle, fat, bone, meniscus, cartilage, tendon, and ligament; the bone tissues (i.e., femur, tibia, and patella) mainly consist of the cortical bone, cancellous bone, and marrow (Figure 1.14). These knee tissues have widely different T2 relaxation times ranging from short to long. For example, the long-T2 tissues can include the muscle (T2 ~ 32-50 ms), fat (T2 ~ 133 ms), marrow (T2 ~ 133 ms), and superficial cartilage (T2 ~ 30-40 ms); the short-T2 tissues can include the cortical bone (T2 ~ 0.4-0.5 ms), meniscus (T2 ~ 5-8 ms), deep cartilage (T2 ~ 5-10 ms), tendon (T2 ~ 6 ms), and ligament (T2 ~ 4-10 ms) (5–8,10). The variety of the short-T2 and long-T2 tissues makes the knee an ideal joint for testing UTE sequences.

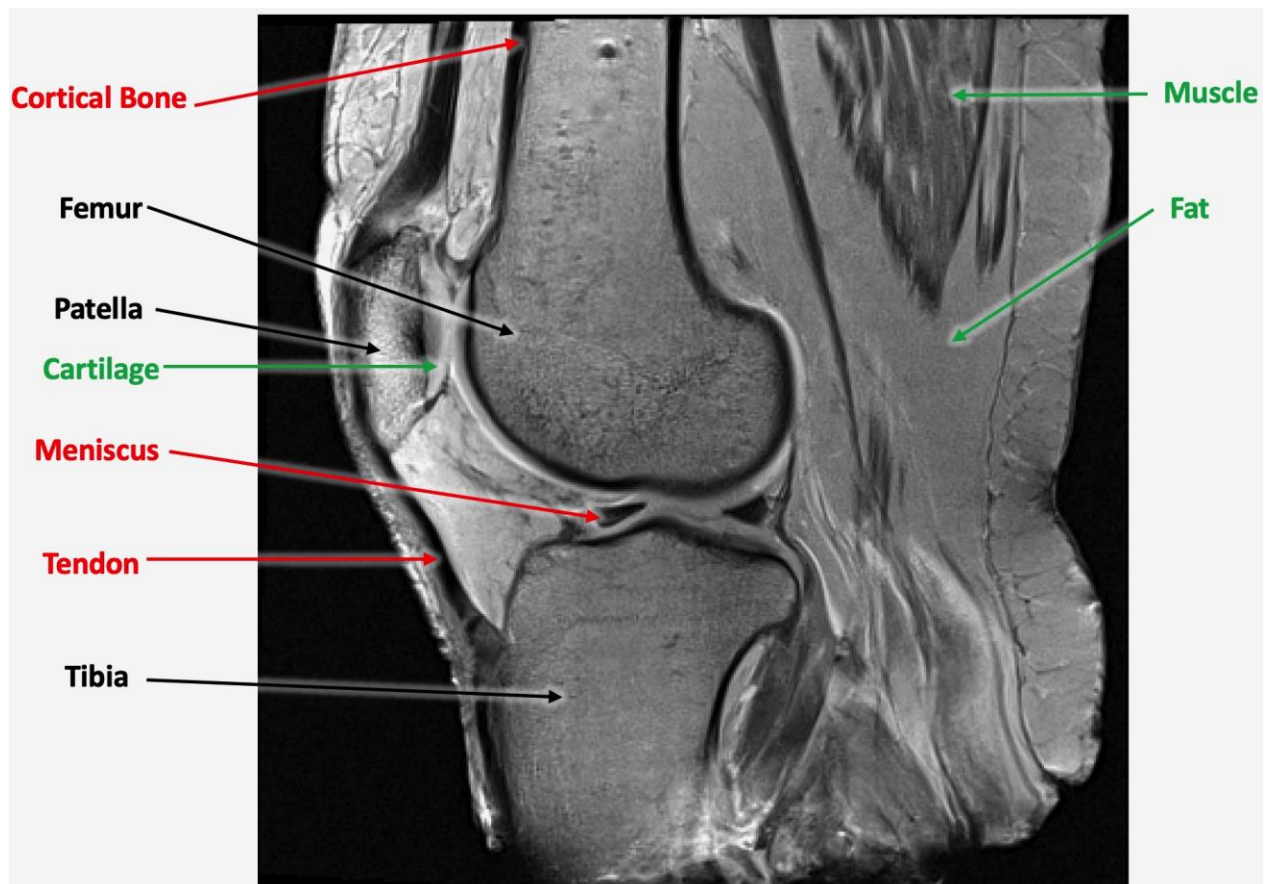


Figure 1.14. Knee anatomy illustrated using a sagittal MR image.

The red labels indicate the short-T2 tissues, and the green labels represent the long-T2 tissues.

Various UTE techniques have been introduced for imaging tissues of the musculoskeletal system, such as articular cartilage, meniscus, and cortical bone. Unlike muscle or fatty tissues enriched mainly with long-T2 water or fat, many MSK tissues also comprise short T2 components with some presence of long T2 components. These short T2 components typically include collagen, proteoglycan, or calcium hydroxyapatite; these components provide structural supports or other functional roles. The presence of short T2 components cause the tissues to have short overall T2 and T2* relaxation times (i.e., their signal decays more quickly than those of surrounding tissues such as muscle or marrow). Some MSK tissues consist of multiple components with differing T2 relaxation times due to their content and their organization (structure). For example, although the superficial and middle layers of cartilage is visible in conventional MR images, the deep layer of cartilage often produces a low intensity (dark region); this is due to differences in collagen arrangement and ratio of water content between layers. As another example, cortical bone is absent from conventional MR images due to its higher fraction of short T2 component (i.e., hydroxyapatite) and lower water content. Therefore, UTE sequences play an indispensable role in delineating morphological details of the short T2 species in MSK tissues. Besides the qualitative imaging, UTE sequences can also quantify the relaxation properties of short T2 components in MSK tissues. The qualitative and quantitative properties assessed by UTE might convey diagnostic and research information about MSK tissues relating to degeneration. This subsection will review three types of MSK tissues, including cartilage, meniscus, and cortical bone, as investigated by many UTE studies.

UTE sequences are fast becoming a powerful tool in the qualitative and quantitative imaging of articular cartilage (35,48,65,66,71,95). The articular cartilage is a connective tissue that coats the ends of knee bones to facilitate joint motion with a smooth, lubricated surface (96). For structure, the cartilage comprises four zones from the outer articular surface to the inner layer attached to the bone, and they are the superficial zone made of tangential collagen fibers, the middle zone made of random collagen fibers and proteoglycans, the deep zone made of radial collagen fibers, and the calcified zone anchoring the radial collagen fibers to the bone (Figure 1.15) (96). For composition, the cartilage is majorly composed of water, collagen, and proteoglycan; water constitutes up to 80% of the wet weight (96). The relative water concentration increases from ~65% at the deep layer to ~80% at the superficial layer, which might suggest the reason that the cartilage has a wide range

of T2 relaxation times from the deep zone to the superficial zone, from 5-10 ms to 30-40 ms (6,7,10,97). In fact, neither the deep layer of cartilage nor the calcified cartilage can supply sufficient signal on conventional MR images for assessment due to their short T2 relaxation times (4,98,99). However, the (sub-clinical) change of the deep cartilage matrix and the thickening of the calcified cartilage may suggest the early disease of knee osteoarthritis (OA) (98,100–102). UTE sequences can render high morphological contrast for both the deep cartilage and calcified cartilage by using the dual-echo subtraction method, saturation pulses, or/and inversion pulses to selectively suppress the long T2 signal from the water residing in the superficial layer and bone marrow fat enclosed in the subchondral bone (35,48,65,66,71,95,103). Additionally, UTE sequences can also evaluate cartilage quantitatively (35,65,66,76,87,104,105). Obtained with a variable TE UTE acquisition, T2* mapping analyzed with a mono-exponential model suggests a low T2* value in the deep layer of cartilage and the calcification part (76). As an improvement, the bi-exponential fitting can estimate the T2* values and fractions for both the long and short components in the cartilage (87,104,105). These quantitative properties have provided researchers more pathways to study the degeneration progressing in cartilage. For example, higher UTE-T2* values have been found for the deep layer of the cartilage in the anterior cruciate ligament (ACL) injured patients than what has been found in the uninjured volunteers (98,106). Another study suggests decreased UTE-T2* values in degenerate deep cartilage over the healthy controls (76). Although the results of these studies differed, so did the patient populations; as such, more work assessing UTE-T2* is required to understand the degeneration process in a disease-specific manner.

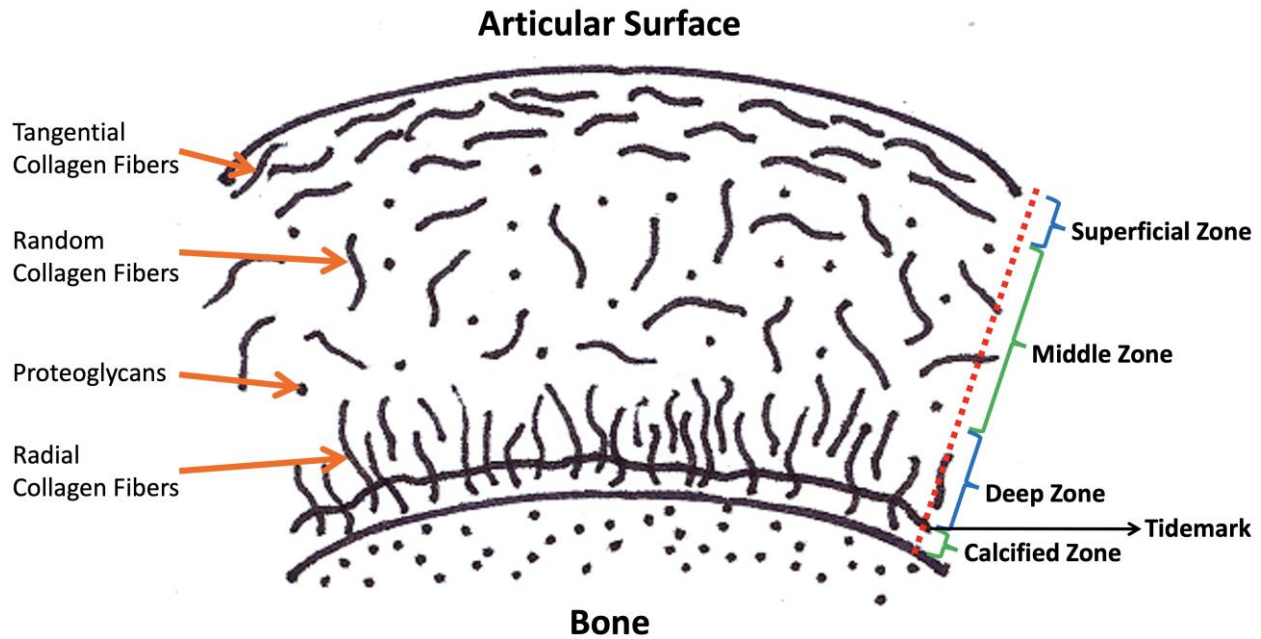


Figure 1.15. Structure of the articular cartilage.
 Courtesy of Dr. Emily J. McWalter. Adapted with permission.

UTE sequences are important for the qualitative and quantitative imaging of the meniscus. The meniscus, which sits between the femoral condyle and the tibia plateau, is another knee connective tissue comprised of two components (107). Both components of the meniscus appear as a wedge shape in the coronal cross-section and a semi-lunar shape in the axial cross-section (107). For function, the meniscus provides the knee load-bearing, load transmission, shock absorption, and lubrication and nutrition of articular cartilage (107). For structure, the meniscus mainly comprises proteoglycans, radial collagen, circumferential collagen, and random collagen; however, the inner and the outer region differ because the former has proteoglycans, while the latter is vascularized of blood vessels (Figure 1.16) (107). For composition, the meniscus is majorly composed of water (72%), collagen (21%), and proteoglycan (~5%) (107). The meniscus is considered a short-T2 tissue with a T2 relaxation time of 5-8 ms (7). UTE sequences can detect the signal from the short T2 components within the meniscus, optimizing the contrast of the meniscus tissues (Figure 1.17) (108). In meniscus imaging, some long T2 suppression techniques can aid UTE sequences to highlight any calcification which may occur with degeneration or disease (which has a short T2 property) (67,71). For quantitative evaluation in the meniscus, UTE sequences, performed with a variable TE acquisition, can generate T2* maps fitted by either the mono- or bi-exponential model (105,109,110). Some studies show a potential correlation between the variation of T2* and the

tissue degeneration or calcification in the meniscus (109,110). For example, compared to the healthy, significantly increased UTE-T2* values have been observed for the patients with both ACL tears and meniscal tears; moreover, significantly lower UTE-T2* values also found for the patients with only ACL tears than the patients with both ACL tears and meniscal tears (110). This latter finding is particularly important as it suggests that the UTE-T2* measure can detect changes to the meniscus even before a morphological change like a tear (i.e., sub-clinical degeneration) (110). Similarly, another study also suggests significantly higher T2* estimates, derived from both mono-component fit and bi-component fit, were found in the degenerative and tear menisci than the normal menisci (77).

Coronal Midslice Cross-Section

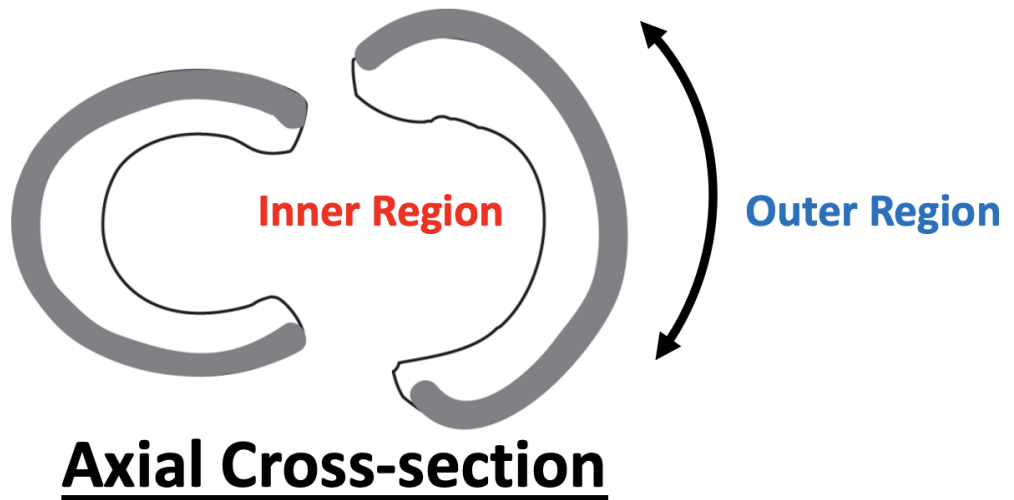
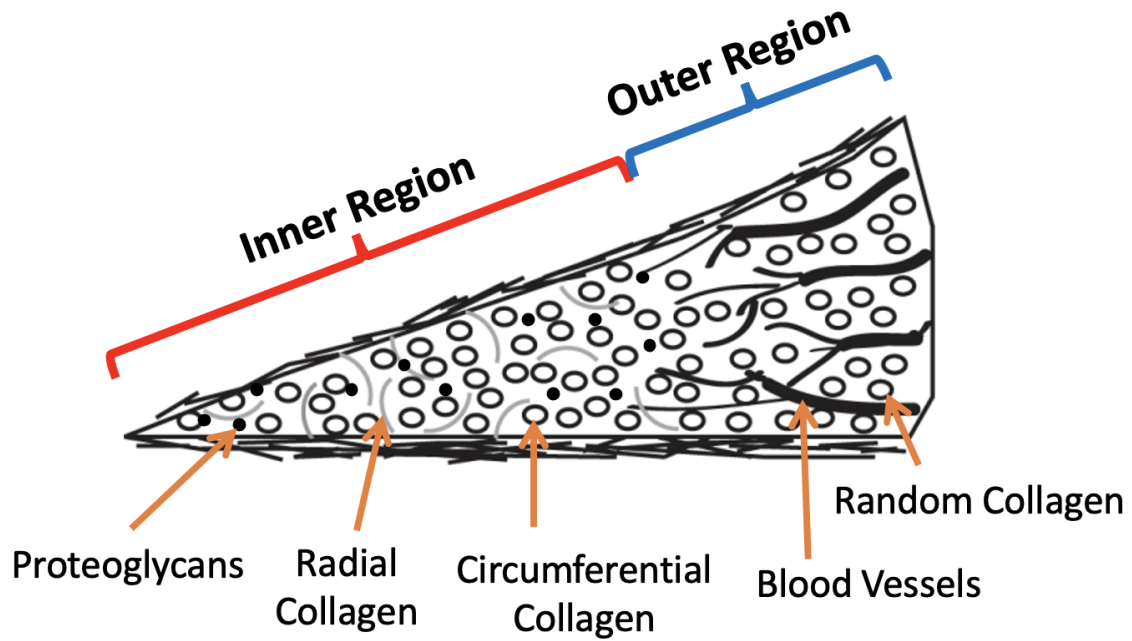


Figure 1.16. Structure of the meniscus.
Courtesy of Dr. Emily J. McWalter. Adapted with permission.

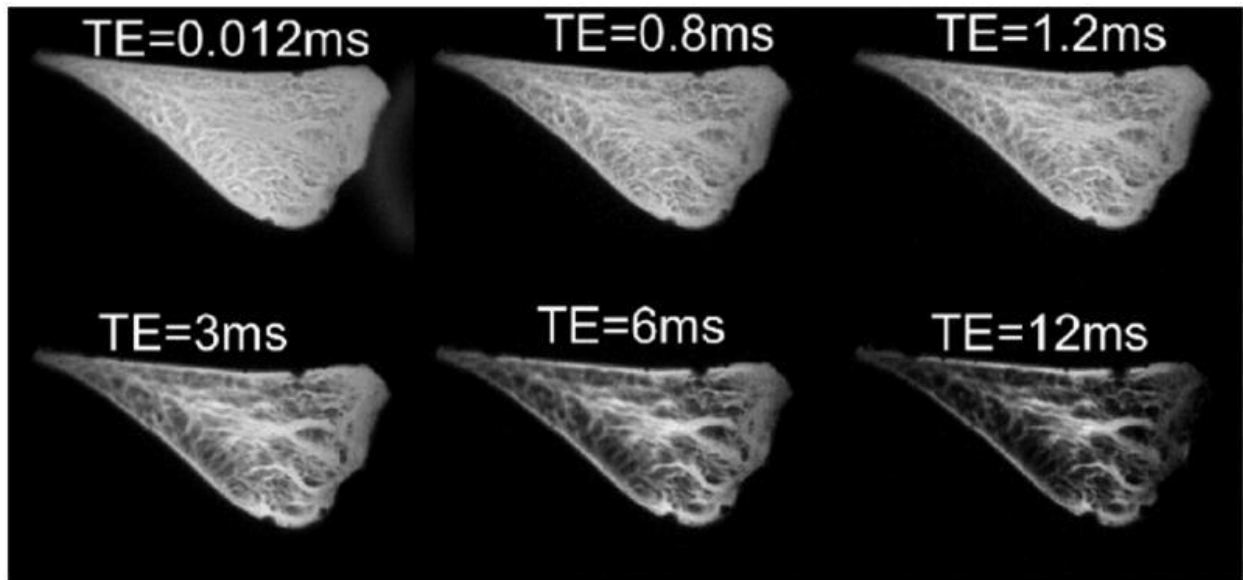


Figure 1.17. Menisci scanned by fat-saturated UTE-MRI with TE varying from 0.012 to 12 ms. Lower TEs present more enriched details on both the blood vessels and the collagen fibres in the meniscus. Reprinted from (108) (DOI link: <https://dx.doi.org/10.1097%2FRMR.0b013e31823cceb>). Permission is granted by *Wolters Kluwer Health, Inc.* for reuse in a thesis/dissertation.

From both qualitative and quantitative perspectives, the imaging of MSK tissues can benefit from the UTE sequences, especially for the cortical bone. Due to the sparse distribution of free water, the cortical bone carries a very short T₂ of ~0.4-0.5 ms (7), making it invisible from conventional MR images. However, the morphological contrast of the cortical bone can be well delineated by UTE sequences (20,66,70,79,111,112). For a better view of the cortical bone, some long T₂ suppression techniques, such as the dual-echo subtraction and water/fat saturation or inversion pulses, are usually required in the UTE acquisitions (66,67,70,74). The UTE-T₂* mapping with a mono- or bi-exponential analysis has also been used in cortical bone imaging (20,21,41,74,79,83,105). In addition to that, the QMT modelling implemented with UTE sequences can indirectly quantify the macromolecules-i.e., collagen matrix in the cortical bone, providing estimates of the fraction and T₂* of the macromolecules (92,93). These quantitative measures could be used for the study of osteoporosis (92). For example, a significant, negative correlation (i.e., -0.72) was found between the fraction of macromolecules and the porosity: a higher macromolecular fraction suggests a lower porosity (92).

UTE sequences have also been used to qualitatively and quantitatively characterize other MSK tissues, such as tendons, intervertebral disc, ligaments, temporomandibular joint, and entheses (21,31,65,74,85,108,113).

1.2.4.2. Radiation Treatment Planning

UTE sequences have demonstrated the potential for the generation of synthetic computed tomography (sCT) used in radiation treatment planning (RTP). Routinely, a radiation therapy workflow requires CT data for radiation dose calculation, which requires bone signal. Due to the lack of bone signal in conventional MR images, MRI cannot substitute for CT images in RTP, even though it has a better anatomical delineation for soft tissues and no ionizing radiation. However, UTE techniques can acquire adequate cortical bone signal and further enhance the bone contrast, for example, using the dual-echo subtraction method, which allows for the generation of sCT images (114). Some studies have shown the feasibility of sCT images for carrying out dose calculations comparable to authentic CT data's outcomes (114–116). Despite some challenges, such as slight geometric distortion, it is promising to use UTE sequences to achieve MR-only radiation therapy with the benefits of gaining well-delineated soft-tissue contrasts for better treatment contouring.

1.2.4.3. Other Applications

UTE sequences have been an indispensable method in lung imaging. Lungs cannot provide enough signal in conventional MR imaging due to their low distribution of protons and short T2 relaxation time. Therefore, UTE sequences serve as an imperative tool to rendering the structural image of the lung for the diagnosis of lung cancers or airway diseases (39,55,57,117,118).

1.2.4.4. Summary of UTE Applications

UTE is showing great promise in several important applications where short-T2 tissues are present.

- For morphological UTE imaging of knee joints, it is relatively unknown that if the various tissues (e.g., cortical bone or tendon) are feasible to be isolated by different long-T2 suppression techniques.
- Also, there has not been a comprehensive quantitative assessment of the meniscus using UTE sequences to map QMT parameters and T1 and T2* relaxation times.
- For synthetic CT generation for RTP, it is relatively unclear whether the cortical bone imaging is feasible to be improved by optimization of the trajectory and sampling parameters of UTE sequences.

1.2.5. Conclusion

UTE sequences have demonstrated their unique ability in the qualitative and quantitative imaging of short T2 tissues/components. Due to the difficulty of the short-T2 imaging using MRI, many UTE techniques need to be re-invented or improved for better performance, such as novel excitation pulses, preparation pulses, or non-Cartesian trajectories. However, the development of these UTE approaches has been hampered by the lack of high-quality product sequences, a lack of flexibility in the individual sequences (i.e., only one trajectory or pulse option available), the time and effort required to write new, all-encompassing sequences from scratch, and the uncertainty about the optimal parameters to use for a particular application or purpose.

1.3. Research Motivations and Thesis Objectives

After conducting a comprehensive literature review covering the UTE techniques, imaging methods, and applications, it is clear that there is no flexible UTE sequence that includes various acquisition techniques (e.g., RF pulses, trajectories, and long-T2 suppression techniques) to

facilitate direct comparisons between different approaches and for optimization for particular applications. Therefore, the following overarching research objective and sub-objectives were identified to fill the clear need in the literature:

Overarching Research Objective:

The overarching objective of this thesis is to develop a flexible, product-quality UTE sequence that incorporates various acquisition options which will allow us to directly compare sequence features and to optimize short T2 imaging for different applications.

Sub-objective 1: To develop a novel, robust, flexible UTE sequence that produces high-quality morphologic images with minimal artifacts; and this sequence can be used for various applications and includes choices of RF pulses, trajectories, dimension schemes (2D/3D), and long-T2 suppression methods.

Sub-objective 2: To evaluate the sequence with customized scan protocols for morphological and quantitative imaging in the knee.

Sub-objective 3: To assess the performance of the sequence for cortical bone imaging for synthetic CT generation.

Potential impact and contributions: This sequence will provide researchers and general MR users with the flexibility of switching between the various UTE imaging techniques and the ability to optimize sequence parameters that will result in an overall improvement of both morphologic imaging and quantitative mapping.

1.4. Thesis Organization

In this thesis, we designed three studies to achieve each sub-objective. The remainder of this thesis comprises the following chapters: Chapter 2 where the flexible UTE sequence is developed and evaluated under a series of conditions (Sub-objective 1); Chapter 3 where bovine knees are used to evaluate the flexible sequence in morphological and quantitative imaging (Sub-objective 2); Chapter 4 where the ability of the flexible sequence to image cortical bone is assessed for the

purpose of synthetic CT generation (Sub-objective 3); Chapter 5 where an integrated discussion considering all studies is presented.

Chapter 2 Design and development of a novel Flexible Ultra Short Echo time sequence (FUSE)

Synopsis: Ultrashort echo time (UTE) pulse sequences can capture the signal from short T2 tissues. Many UTE techniques have been developed for achieving an ultrashort TE (less than 0.1 ms) or enhancing the short-T2 contrast. However, these approaches have not been extensively compared directly due to the lack of a flexible UTE sequence that integrates the different approaches. Therefore, in this work, we developed a versatile UTE sequence, which creates high quality UTE images, can be used to directly compare UTE approaches and provides options for researchers and clinicians to choose the appropriate UTE imaging schemes that fit the particular application.

2.1. Introduction

Short T2 tissues are difficult to image using conventional MRI pulse sequences due to their short T2 relaxation times (10). Ultrashort echo time (UTE) techniques allow for rapid signal acquisition, delivering short-T2 contrast in MR images (10,15). Hallmark features of UTE techniques include the use of a half-Sinc (15) or rectangular radiofrequency (RF) excitation pulses (19,20), non-Cartesian (data-filling) trajectories (radial (14) and spiral (17,18)), 2-dimensional/3-dimensional (2D/3D) acquisition schemes (14,45,46,49), and long-T2 suppression techniques (68,72,73). However, these approaches and the resulting images have not been compared directly and evaluated systematically. Further, the impact of these parameters on image quality has not been assessed. For example, although short T2 tissues such as bone, meniscus, tendons, ligaments and deep layers of cartilage have been successfully visualized using UTE approaches (35,66,71,79,85,108), it is unclear what particular trajectories, pulses, and associated parameters are optimal for visualization and quantification. This is because there is no integrated UTE sequence that conveniently includes these options in one place for direct comparisons. Even though it may be possible to compare these features using different UTE sequences, the results would be

limited in that differences may be due to inherent differences in the sequence's configuration and settings as opposed to the features themselves. For example, for trajectory comparison, it is unreasonable to directly compare a 2D radial UTE sequence requiring 512 trajectory lines for acquisition with a 2D spiral UTE sequence that may only support up to 64 trajectory lines. There is also no direct comparison between the 3D half-Sinc pulse and the 3D rectangular pulse using the identical flip angle and other parameters for assessing their outcomes in terms of signal-to-noise ratio (SNR) and contrast. Therefore, in order to carry out these comparisons optimally, all features should be included in a single sequence.

Some factors have an imperative impact on the reconstruction of the UTE sequence and might need to be improved in order to obtain high-quality UTE images; density compensation is one particular area of importance. Unlike the Cartesian trajectory, the non-Cartesian ones cannot fill the sampled signal homogeneously in k-space. If a non-Cartesian trajectory is directly regridded to Cartesian k-space without penalties, the inner part will contribute more to signal information than the outer part (26). For example, both radial and spiral trajectories feature centre-out signal filling (spokes or interleaves), so the inner part in k-space is always sampled more heavily than the outer part. As a result, the centre component will be more pronounced in the subsequent reconstruction transform, producing low-frequency artifacts in the reconstructed image. The density compensation for the non-Cartesian trajectories can be carried out by density correction functions (DCF) (119,120). Derived from the geometry of the trajectories, analytical DCFs can execute simple and effective density correction for the various non-Cartesian trajectories (120–122). However, there might still be some room for them to be improved with a more accurate geometrical description for the trajectories.

The off-resonance artifact is another factor that is important to consider in UTE imaging but has yet to be methodically characterized with suitable remedies. The inhomogeneity of the main magnetic field and the susceptibility of imaged objects can cause off-resonance effects, leading to an erroneous phase accumulation for acquired MR signals (123,124). This error accumulation transforms into the off-resonance artifact in the reconstructed image. UTE sequences are particularly susceptible to the off-resonance artifact because they use centre-out trajectories that concentrate

the phase errors from all signal acquisitions on k-space's centre (which stores the most spectral energy of the image, i.e., the low-frequency component). The artifact can cause blurring in UTE images and worsen with increases in readout-gradient duration, e.g., long spiral gradients (125,126). Interestingly, the off-resonance artifact might manifest differently depending on UTE approach, such as choice of trajectory and acquisition dimensions (2D vs. 3D). Therefore, together with the comparison of UTE features, the resulting off-resonance effects must be characterized. In addition, since different characteristics of off-resonance artifacts have emerged, the corresponding suitable correction solutions also need to be explored and optimized.

To fill these gaps, we are proposing the development of a pulse sequence and reconstruction software that tackle these shortcomings highlighted. To this end, an entirely new Flexible Ultra Short Echo time sequence (or FUSE for short), including a reconstruction pipeline, was developed. The sequence comprises various acquisition options for radiofrequency (RF) pulses, trajectories, dimension schemes (2D/3D), and long-T2 suppression techniques. The reconstruction pipeline includes improved correction capabilities for k-space density compensation and the off-resonance artifact. Features of FUSE were then systematically evaluated by contrasting the methods for the k-space density correction and off-resonance artifact correction regarding the variation of the produced artifact and comparing the combinations of the various RF pulses and trajectories, 3D RF pulses with the shortest TEs, and long-T2 suppression techniques regarding the variation of the contrast and SNR.

2.2. Materials and Methods

This section details the development of the acquisition sequence and reconstruction pipeline, and it also proposes the evaluation method for the various UTE features.

2.2.1. Development of a Flexible Ultra Short Echo Time Sequence (FUSE)

A Flexible Ultra Short Echo time sequence (FUSE) was developed in this study for providing multiple acquisition features and their flexible combinations. The FUSE sequence was modified and developed from a standard gradient-recalled echo sequence (using a Cartesian trajectory). The

FUSE sequence was programmed and tested using a manufacturer's development platform (IDEA, Siemens Healthineers, Erlangen, Germany) and ported to a 3 Tesla system (PrismaFit, VE11C, Siemens Healthineers, Erlangen, Germany). The sequence was implemented with various RF excitation pulses, trajectories, dimensionalities, and long-T2 suppression techniques (in a total of thirteen possibilities, as shown in Figure 2.1). Many of these acquisition features were not available in IDEA by default and were designed from scratch for this sequence, specifically the 2D/3D half-Sinc pulse, 2D/3D half-Sinc pulse with the variable-rate selective excitation (VERSE) technique, 2D/3D radial trajectory, and 2D/3D spiral trajectory. These features, along with their settings, were designed to be readily changeable and user-configurable on the sequence's user interface. Also, one acquisition feature can be flexibly combined with another for meeting different imaging needs: for example, a fat-saturated 2D radial scan using a half-Sinc RF pulse can be easily switched to a water-saturated 3D Spiral-Cones scan using a rectangular RF pulse.

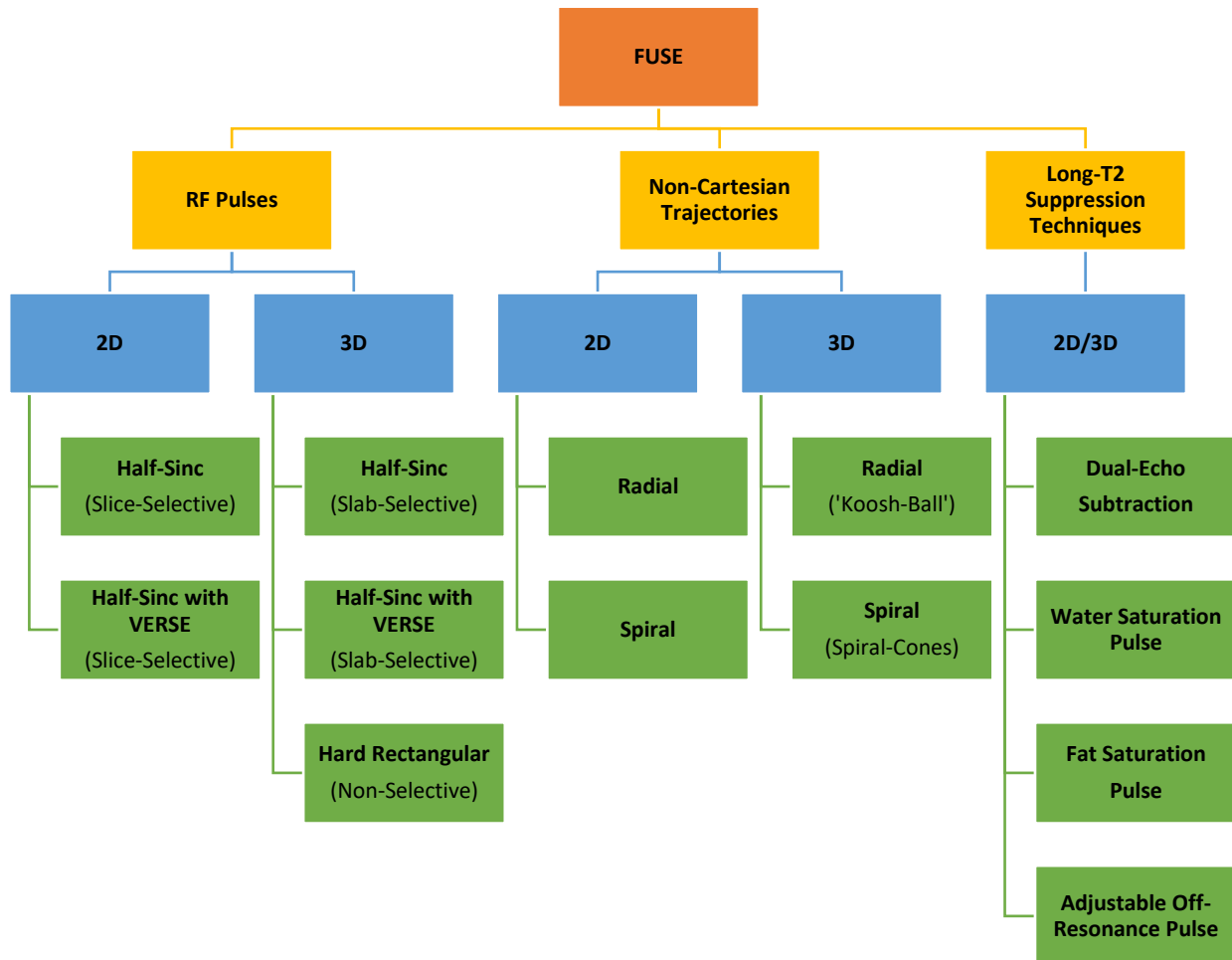


Figure 2.1. The feature tree of the FUSE sequence.

The yellow blocks represent three main FUSE scan functions provided with multiple acquisition options. The blue blocks indicate the available dimensionalities for each scan function. The green blocks layout the specific acquisition options available in different scan functions and dimensionalities. FUSE allows for flexible switching between and combining of these provided options.

2.2.1.1. RF Pulse Design

Three varieties of RF excitation pulses, including two half-Sinc types and one hard-rectangular type, were implemented in the FUSE sequence. The half-Sinc pulse divides the excitation process into two acquisition cycles to achieve an intact slice selection (14,15,29,38). In this process, two identical half pulses sequentially excite the target slice, with the second half requiring a reversed slice-selection gradient (opposite in polarity to the one used in the first cycle). As a result, the resulting echoes from two excitations need to be added to each other for a full acquisition. In this work, we customized the half-Sinc pulse by tailoring the first half of a full-Sinc RF pulse and its excitation was set to play out during the plateau of the slice-selection gradient. This excitation scheme can reduce the RF excitation time by half from the minimal TE, as compared to a conventional full-Sinc excitation (38). The sequence also incorporates the VERSE technique into the regular half-Sinc RF pulse, allowing for a further TE reduction (14–16,30). The half-Sinc pulse modified by VERSE can take advantage of both flat-top and ramp-down of a slice-selection gradient for excitation. In this case, the use of a refocusing gradient becomes unnecessary. As the VERSE-modified half-Sinc technique is not readily available in the development environment (i.e., IDEA), we designed our VERSE-modified half-Sinc pulse featuring a real-time adaptation to the protocol-driven variation of the gradient’s ramp-down. As an important improvement, we also extended both types of half-Sinc pulses to 3D. Additionally, a hard-rectangular RF pulse, exclusively for 3D UTE acquisition, was incorporated in the sequence. This pulse was used as a reference to help investigate whether the 3D versions of the half-Sinc pulse could serve as effective alternatives in the 3D UTE imaging.

2.2.1.2. Implementation of Multiple K-Space Trajectories

The ability to switch between different k-space trajectories was included in the FUSE sequence. This is a key feature that, to our knowledge, is currently not available in UTE sequences. FUSE employs four types of centre-out, non-cartesian k-space trajectories to transverse k-space, which are 2D radial, 2D spiral, 3D radial (“Koosh-Ball”), and 3D spiral (Spiral-Cones).

The 2D radial trajectory consists of multiple radial spokes, and the waveform of each corresponding readout gradient has a trapezoidal shape. The readout gradient between radial spokes varies as follows,

$$G_x = -G_{RD}\cos(\theta_i) \quad [2.1]$$

$$G_y = G_{RD}\sin(\theta_i) \quad [2.2]$$

where G_{RD} is the readout gradient for the radial line (RD); θ_i is the azimuth angle in the k_x - k_y plane within a range of $[0, 2\pi)$, and $i = 1, 2, 3 \dots, n$ (number of spokes); and G_x and G_y are the gradient components along the k_x and k_y axes.

A 2D spiral trajectory can be either a continuous spiral course or multiple spiral interleaves (that spread out radially around an origin) which covers k -space from the centre to the defined field-of-view (FOV). Our sequence utilizes an analytical method governed by the limits of both the gradient's slew rate and amplitude to approximate the 2D spiral's readout gradient (17,18). Also, the readout gradient can flexibly accommodate the acquisition changes and regenerate the waveform and amplitude on-the-fly. For an interleaved spiral trajectory (i.e., interleaved around the origin with an in-plane rotation angle, θ), the gradient variations, between different spiral interleaving trajectory lines (i.e., number of spiral lines), are defined by:

$$G_x = -G_{SPy}\sin(\theta_i) - G_{SPx}\cos(\theta_i) \quad [2.3]$$

$$G_y = -G_{SPy}\cos(\theta_i) + G_{SPx}\sin(\theta_i) \quad [2.4]$$

where G_{SPx} and G_{SPy} are the time-varying spiral components (SP) derived by the approximation in the k_x - k_y plane (17); θ_i is the azimuth angle in the k_x - k_y plane within a range of $[0, 2\pi)$, and $i = 1, 2, 3 \dots, n$ (number of interleaves); and G_x and G_y are the final gradient components resolved to the k_x and k_y axes, respectively.

Similar to the 2D radial trajectory, a 3D radial trajectory has spokes around k -space's origin, but the spokes simultaneously vary with azimuth and altitude angles in a 3D-space, forming a Koosh-Ball like space. The 3D radial adds another dimension of variation, the k_z -axis, for the readout gradients, which can be described as follows (40):

$$G_x = -G_{RD}\sin(\varphi_j)\cos(\theta_i) \quad [2.5]$$

$$G_y = G_{RD}\sin(\varphi_j)\sin(\theta_i) \quad [2.6]$$

$$G_z = -G_{RD}\cos(\varphi_j) \quad [2.7]$$

where G_{RD} is the constant readout gradient for the radial (RD); θ_i is the azimuth angle in the k_x - k_y plane within a range of $[0, 2\pi)$, and $i = 1, 2, 3 \dots, n$ (number of spokes); φ_j is the altitude angle

along the k_z -axis within a range of $[0, \pi)$, and $j = 1, 2, 3 \dots, m$ (number of cones); and G_x , G_y , and G_z are the resolved gradient components along the k_x , k_y , and k_z axes, respectively.

The implemented 3D spiral trajectory, Spiral-Cones, combines the features of both the spiral and radial trajectory. The Spiral-Cones trajectory uses a 2D spiral course in the k_x - k_y plane and follows a radial variation along the k_z -axis (127). This hybrid form adopts both the spiral (k_x and k_y axes) and trapezoid (k_z -axis) gradient waveforms to accomplish the data filling in 3D k -space, which can be described by the following equations:

$$G_x = -G_{SPY}\sin(\varphi_j)\sin(\theta_i) - G_{SPX}\sin(\varphi_j)\cos(\theta_i) \quad [2.8]$$

$$G_y = -G_{SPY}\sin(\varphi_j)\cos(\theta_i) + G_{SPX}\sin(\varphi_j)\sin(\theta_i) \quad [2.9]$$

$$G_z = -G_{RDZ}\cos(\varphi_j) \quad [2.10]$$

where G_{SPX} and G_{SPY} are the time-variable spiral components (SP) derived by the approximation in the k_x - k_y plane (17), and G_{RDZ} is the constant trapezoid component, i.e., radial readout gradient (RD), along the k_z -axis; θ_i is the azimuth angle in the k_x - k_y plane within a range of $[0, 2\pi)$, and $i = 1, 2, 3 \dots, n$ (number of interleaves); φ_j is the altitude angle along the k_z axis within a range of $[0, \pi)$, and $j = 1, 2, 3 \dots, m$ (number of cones); and G_x , G_y , and G_z are the final gradient components resolved to the k_x , k_y , and k_z axes, respectively.

These non-Cartesian trajectories can be used with the half-Sinc or rectangular RF pulse to effectively reduce the TE to an ultrashort interval. This interval spans from the end (half-Sinc) or middle (rectangular) of the RF pulse to the beginning of centre-out acquisition (radial or spiral trajectory). However, in this setup, the ultrashort TE is still constrained by the hardware capacity (the transmitter/receiver dead time) and the acquisition parameters. The latter might include the rectangular pulse's duration and the regular half-Sinc pulse's slice-selection gradient ramp-down time (non-VERSE modified).

2.2.1.3. Implementation of Various Long T2 Suppression Techniques

Various long-T2 suppression techniques were also implemented in FUSE for selectively suppressing long-T2 signals and enhancing short-T2 contrasts. Although an ultrashort acquisition can sufficiently capture the signal decay of short-T2 components, long-T2 components barely have

any signal decay during the same acquisition window. As a result, brightness of long-T2 species affects the dynamic range in the image and makes distinguishing between the intensity of short-T2 species difficult. Therefore, the long-T2 suppression techniques implemented here aim to minimize the long-T2 contrast while enhancing the short-T2 contrast.

The comprehensive long-T2 suppression capability in the sequence was carried out by four approaches, including the dual-echo subtraction, fat saturation, water saturation, and differenced MT contrast. The dual-echo subtraction method first required two individual scans set with an ultrashort (e.g., 0.14 ms) and a long TE (e.g., 2.46 ms) and then used the second image to subtract from the first image to obtain the difference image (67,68). Since the signal intensity varied more drastically between the two TEs for the short-T2 component than for the long-T2 component, this method offset the long-T2 contrast and emphasized the short-T2 one in the difference image. The fat saturation method adopted a non-selective Gauss-shaped preparation pulse with a centre frequency of -407 Hz and flip angle of 110° to suppress the fat signal exclusively before the UTE signal acquisition (67,73). Similarly, the water saturation method also used a non-selective Gauss-shaped preparation pulse with a centre frequency of 0 Hz and flip angle of 110° to diminish the water signal before the UTE signal acquisition (15). The differenced magnetization transfer (MT) contrast method first applied a Gauss-shaped saturation pulse with an off-resonance centre frequency (i.e., 1200 Hz) and a large flip angle (i.e., 500°) before the UTE signal acquisition and then used this saturated image to subtract from an unsaturated image to obtain the difference image (72,75,78). The MT method relies on a two-pool model theory where tissues comprise a free and a bound pool: the free pool is enriched with free protons (e.g., water), and the bound pool consists of restricted protons (possessing very short T2) (78). Since the off-resonance saturation works on the bound pool solely while sparing the free pool, the magnetization residing within the free pool can be transferred to the bound pool through the dipole-dipole effect. As a result, together with the UTE acquisitions, the subtraction step can visualize the MT effect between the two pools even in short-T2 species. However, the MT effect is near to nil for some long-T2 species where the bound pool is absent, for example, pure water or fat. Hence, this method can effectively suppress these single pool long-T2 species and enhance the short-T2 components with the difference MT contrast. These approaches are able to suppress different types of the long-T2 signal for various short-T2 contrast enhancement purposes.

2.2.2. UTE Reconstruction Pipeline

An offline UTE reconstruction pipeline based on the gridding algorithm was implemented (MATLAB, MathWorks, Natick, MA, USA) with an off-resonance artifact correction (123) in order to create high-quality UTE images (Figure 2.2). First, the pipeline corrects k-space trajectory error (a momentary lapse in time) for the raw data mapped in a non-Cartesian coordinate system. Second, the pipeline further compensates for the uneven density distribution of the raw data in k-space. Third, the gridding algorithm uses a Kaiser–Bessel window to convolute with each data point (acquired by the non-Cartesian trajectories) and assign (re-grid) them to their theoretical k-space locations in the Cartesian coordinate system (25,26). As further explanation, the pipeline can flexibly re-grid the data acquired by both the radial and spiral trajectories, including their 2D and 3D variants. Fourth, the reconstruction for re-gridded k-space data is accomplished by an inverse Fast Fourier Transform (iFFT) (25,26). Last, the pipeline integrates an automated deblurring algorithm, allowing for correction for the off-resonance artifact. Among all the processing steps, the gridding algorithm and iFFT (Steps 3 and 4) are usually recognized as routine methods for the UTE reconstruction. Instead, various correction methods regarding k-space trajectory's time-lapse and density and the off-resonance artifact (e.g., Steps 1, 2, and 5) weigh more importance on delivering a high-quality UTE reconstruction free of severe artifact and distortion. Hence, the technical details on the correction methods implemented in the developed pipeline will be elaborated in the following sections.

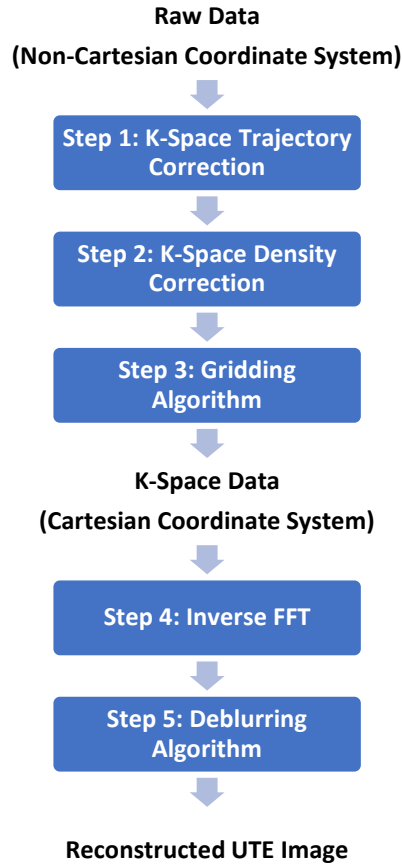


Figure 2.2. Proposed UTE reconstruction pipeline.

2.2.2.1. *K-Space Trajectory Correction*

The reconstruction pipeline corrects the non-Cartesian trajectory error introduced by the centre-out gradient's potential time-delay and specialized waveform. First, due to imperfections in the gradient, there is a momentary time lapse for the readout gradient generating the desired waveform. Conventional Cartesian trajectories bypass this issue because the acquisition does not begin until the readout gradient reaches the plateau, and it uses a pre-dephasing gradient to force the signal peak (gradient echo) to be at the centre of k-space. However, the non-Cartesian trajectories are sensitive to the gradient delay as the centre-out acquisition starts at the same time as the readout gradient and lacks the pre-dephasing gradient. Together, these two factors can cause a peak shift of k-space centre for the acquired Free induction Decay (FID) signal and can potentially lead to artifacts in the reconstructed images. Therefore, the drifted peak must be shifted back to the centre of k-space before the gridding process. In Step 1 of the pipeline, k-space trajectory correction (Figure 2.2), k-space shifting offset to compensate for the readout gradient delay was chosen

empirically based on the disappearance or reduction of artifact on the reconstructed images. The k-space trajectory correction also needs to account for the specialized waveforms of both the radial and the spiral trajectories. In the radial trajectory, the signal sampling usually starts from the ramp-up of the trapezoid gradient. The ramp-up region has a varying gradient amplitude but identical sampling intervals with the analog-to-digital converter (ADC). Therefore, the signal points within the ramp-up region must be re-projected in k-space via the following relationship:

$$k_{Rampup}(t) = \frac{\gamma}{2\pi} \int_0^t G \frac{t}{T_{Rampup}} dt, \quad 0 \leq t \leq T_{Rampup} \quad [2.11]$$

where k_{Rampup} is the re-projected k-space location within the ramp-up; γ is the gyromagnetic ratio; G is the amplitude of radial gradient's plateau; T_{Rampup} is the ramp-up duration of the radial gradient; t defines the time variable on the gradient ramp-up. For the spiral trajectory, due to the discrepancy between the gradient raster time (10 us in the Siemens systems) and the receiver's sampling interval (e.g., 7.5 us), the gradient waveform must be interpolated to the receiver's sampling interval to match the data-filling trajectory in k-space. In other words, the spiral gradient waveform cannot always retrieve actual k-space location for each acquired signal point because of this time discrepancy. Hence, for the k-space trajectory correction in the spiral, the reconstruction pipeline applies a B-spline interpolation function to the gradient waveform, using the receiver's time scale. This B-spline-interpolated spiral gradient waveform can describe the k-space location of each sampled data point more accurately.

2.2.2.2. *K-Space Density Correction*

The reconstruction pipeline employs adaptable density correction approaches for the different non-Cartesian trajectories. In Step 2 of the pipeline, k-space density correction (Figure 2.2), traditional and new analytical density correction functions (DCF) were used to compensate for the various uneven density patterns introduced by different non-Cartesian trajectories. The DCFs work as a weighting factor that can directly multiply with re-gridded k-space for the density compensation. The DCFs proposed here were derived analytically based on the geometry of each trajectory.

For 2D radial trajectories, the most common approach utilizes k_r , which stands for the k-space location of each point on the spokes, as an analytical DCF (120,128–130); however, here a more

suitable analytical form was proposed by considering the area difference between adjacent sampled points in k-space using the radial spoke's polar distance, k_r ,

$$DCF_{2DRD}(i) = \begin{cases} \frac{k_r(i)^2}{k_r(i)}, & i = 1 \\ \frac{k_r(i)^2 - k_r(i-1)^2}{k_r(i) - k_r(i-1)}, & 1 < i \leq N \end{cases} \quad [2.12]$$

where DCF_{2DRD} is the DCF (of each radial spoke) of the 2D radial trajectory; N , indexed by i , is the number of sampled points along each radial spoke in k-space.

As for the 2D spiral trajectory, an analytical DCF form was adopted, as detailed in (121),

$$DCF_{2DSP} = |\vec{k}_{int}| \cdot |\vec{g}_{int}| \cdot |\cos(\vec{g}_{int}, \vec{k}_{int})| \quad [2.13]$$

where DCF_{2DSP} is the DCF (of each spiral interleave) of the 2D spiral trajectory; \vec{k}_{int} is the k-space location of each spiral interleave; \vec{g}_{int} is each spiral interleaf's gradient waveform; and $(\vec{g}_{int}, \vec{k}_{int})$ is the angle between \vec{g}_{int} and \vec{k}_{int} .

For the 3D radial trajectory, although a common analytical DCF uses k_r^2 -i.e., the square of the k-space location for each sampled points along the spokes (39,122,131,132), in this work, a new approach was developed. The proposed DCF function was created using a differential volume element defined in the 3D polar coordinate system for k-space. The differential element can geometrically describe the density compensation factor via volume for each adjacent k-space element. In k-space, each radial spoke's polar distance, k_r , and altitude angle relative to the z-axis, φ , concurrently determined the differential volume element. The DCF was modified to the following piecewise format that was able to produce an improved compensation outcome,

$$DCF_{3DRD,j=1}(i) = \begin{cases} \frac{k_r(i)^3}{k_r(i)} \cdot \left| \cos\left(\varphi_j - \frac{\pi}{N_{angles}}\right) - \cos(\varphi_{j+1}) \right|, & i = 1 \\ \frac{k_r(i)^3 - k_r(i-1)^3}{k_r(i) - k_r(i-1)} \cdot \left| \cos\left(\varphi_j - \frac{\pi}{N_{angles}}\right) - \cos(\varphi_{j+1}) \right|, & 1 < i \leq N \end{cases} \quad [2.14]$$

$$\begin{aligned}
& DCF_{3DRD, 1 < j \leq N_{angles}}(i) \\
& = \begin{cases} \frac{k_r(i)^3}{k_r(i)} \cdot (\cos(\varphi_j) - \cos(\varphi_{j+1})), & i = 1 \\ \frac{k_r(i)^3 - k_r(i-1)^3}{k_r(i) - k_r(i-1)} \cdot (\cos(\varphi_j) - \cos(\varphi_{j+1})), & 1 < i \leq N \end{cases} \quad [2.15]
\end{aligned}$$

where j represents each sampled altitude angle relative to the k_z -axis, ranging from 1 to N_{angles} ; DCF_{3DRD} is the DCF (of each radial spoke) of the 3D radial trajectory; N , indexed by i , is the number of sampled points along each radial spoke in k -space; φ_j is the sampled altitude angle relative to k_z -axis, falling within a range between 0 and π , which also suggests that $\cos(\varphi_j) - \cos(\varphi_{j+1}) > 0$.

Lastly, for the 3D Spiral-Cones trajectory, a novel hybrid analytical DCF was proposed. This hybrid DCF combines the 2D spiral DCF described in Eq. [2.13] and the density compensation for the cone variations using the altitude angle relative to the z -axis, φ , defined in k -space. The DCF was formulated as follows,

$$\begin{aligned}
& DCF_{3DSP}(j) \\
& = \begin{cases} DCF_{2DSP} \cdot DCF_{cones} \cdot \left| \cos\left(\varphi_j - \frac{\pi}{N_{cones}}\right) - \cos(\varphi_{j+1}) \right|, & j = 1 \\ DCF_{2DSP} \cdot DCF_{cones} \cdot (\cos(\varphi_j) - \cos(\varphi_{j+1})), & 1 < j \leq N_{cones} \end{cases} \quad [2.16]
\end{aligned}$$

where $DCF_{2DSP}(i) = |k_{int}(i)| \cdot |g_{int}(i)| \cdot \left| \cos\left(\phi_{\vec{g}_{int}}(i) - \phi_{\vec{k}_{int}}(i)\right) \right|$
for $i \in [1, N]$, and

$$DCF_{cones}(i) = \begin{cases} \frac{k_r(i)^2}{k_r(i)}, & i = 1 \\ \frac{k_r(i)^2 - k_r(i-1)^2}{k_r(i) - k_r(i-1)}, & 1 < i \leq N \end{cases}$$

where, j indicates each cone of spiral along the k_z -axis, and it is indexed from 1 to N_{cones} ; DCF_{3DSP} is the DCF (of each spiral interleave) of the 3D spiral trajectory; φ_j (from 0 to π) is the altitude angle relative to k_z -axis; N , indexed with i , is the number of sampled points at each spiral interleave in k -space; k_{int} and g_{int} , respectively, are the 3D spiral trajectory's k -space location and gradient

waveform projected in the k_x - k_y plane; $\phi_{\vec{k}_{int}}$ and $\phi_{\vec{g}_{int}}$ are the angles of vectors \vec{k}_{int} and \vec{g}_{int} ; and k_r is the k-space location of the 3D spiral trajectory along the k_z -axis.

2.2.2.3. Automatic Off-Resonance Correction Algorithm

A 2D auto-deblurring algorithm was adopted in the reconstruction pipeline for the off-resonance artifact correction (123), and the algorithm was modified to improve the artifact correction in 3D. Off-resonance artifacts are commonly observed in the centre-out acquisitions performed by non-Cartesian trajectories due to magnetic field inhomogeneity and susceptibility. This artifact can drastically degrade the quality of UTE images by causing blurring around objects. A field map (B_0) can provide information regarding the local frequency variation (inhomogeneity) and help ease the off-resonance effect, but it requires a separate acquisition or map estimation (124–126,133,134). Therefore, for better efficiency, our pipeline used an automatic off-resonance artifact correction technique (auto-deblurring algorithm) that did not require a B_0 field map as a prior knowledge (123). In Step 5 of the pipeline (Figure 2.2), the automatic off-resonance correction algorithm followed the inverse FFT (of the re-gridded k-space data). This algorithm first used a series of frequency offsets to demodulate the reconstructed image (in complex form), producing a group of base images. Next, the algorithm applied a focusing criterion to determine the minimum blurring effect among those base images, pixel-by-pixel. In the final step, the pixels with the minimum blurring effect were automatically selected to compose a blurring-corrected image jointly (123). Although the algorithm was originally proposed for 2D non-Cartesian trajectories, this work extends it to 3D, allowing for off-resonance artifact correction in the 3D radial and Spiral-Cones trajectories. However, the auto-deblurring algorithm tailored for 3D can be very time-consuming since most modern systems collect MR data in a multi-channel fashion, and the correction is required for each channel. Our modified 3D method addressed this issue by estimating the field map from one channel to guide the demodulation and correction in the other channels. This modification can improve the processing efficiency.

2.2.3. Phantom Evaluation of the FUSE

To systematically test FUSE, we constructed a phantom containing rubber as the short-T2 component and water, grapeseed oil, and agar as varying long-T2 components (Figure 2.3.a and b).

As measured in the preliminary measurement, the hard rubber rod (Hard Multipurpose Neoprene Rubber Rod, 1" Diameter, 6" Long, 75A Durometer, McMASTER-CARR, Aurora, OH, USA) used in this work has a $T2^*$ value of ~ 0.25 ms. This $T2^*$ measurement is sufficiently short for us to evaluate the UTE techniques as other studies used rubber with a $T2^*$ of ~ 0.3 ms for mimicking short- $T2$ compartments (84,135). To assess the performance of the sequence, we systematically evaluated and compared:

- 1) the methods for k-space density correction;
- 2) the approaches for off-resonance artifact correction;
- 3) the combinations of the various RF pulses and trajectories;
- 4) 3D RF pulses with the shortest TEs; and
- 5) the long- $T2$ suppression techniques.

All the tests were carried out on a 3 Tesla MRI system (MAGNETOM PrismaFit, VE11C, Healthineers, Erlangen, Germany) using a 32-channel birdcage head coil, and the scan protocols are listed in Table 2.1. The parallel imaging was not used. Results were compared based on 1) empirical observation of the variation of the artifacts and 2) the Signal-to-Noise Ratio (SNR). The SNR values were calculated using a normal image and a pure noise image over the same region-of-interest (ROI) (136),

$$SNR = \frac{\text{mean}_{r \in \text{ROI}}(I_{\text{normal}}(r))}{\text{std.dev}_{r \in \text{ROI}}(I_{\text{noise}}(r))} \quad [2.17]$$

where I_{normal} is the normal image; I_{noise} is the pure noise image; r is the pixel location of the ROI.

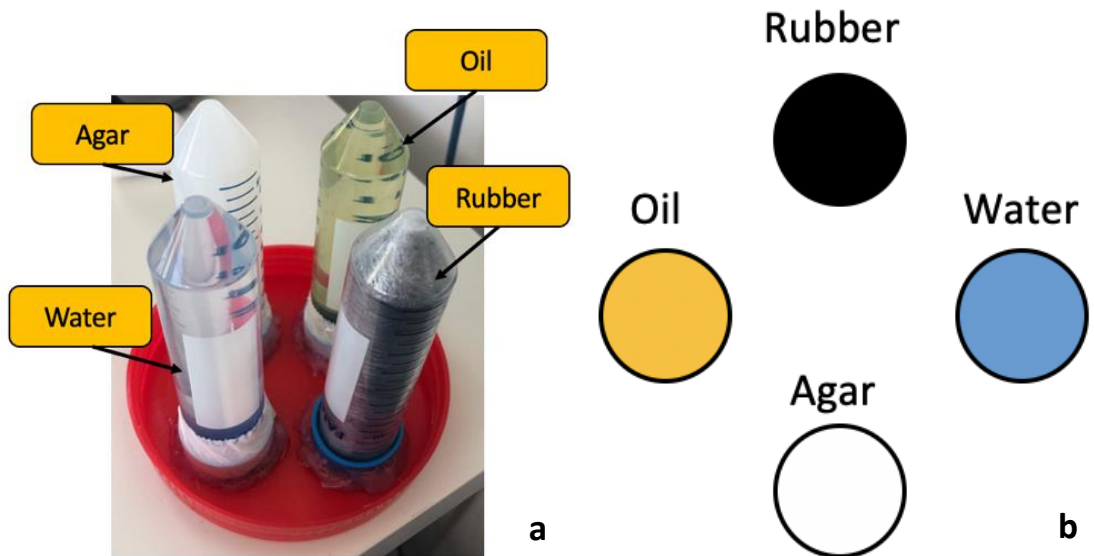


Figure 2.3. In-house short-T2 phantom.
(a) Picture of the phantom; (b) Axial schematic of the phantom.

Table 2.1. Scan parameters for the systematic evaluation of 1) the methods for k-space density correction (Experiment 1); 2) the approaches for off-resonance artifact correction (Experiment 2-4); 3) the combinations of the various RF pulses and trajectories (Experiment 5); 4) 3D RF pulses with the shortest TEs (Experiment 6); 5) the comprehensive long-T2 suppression techniques (Experiment 7).

Experiments	Trajectory	RF	Long-T2 suppression	FOV (mm)	Reconstruction Matrix	In-Plane Trajectory Lines	Out-of-Plane Cones	TE (ms)	TR (ms)	BWP (Hz)	Flip angle (°)	Slice Thickness (mm)	
1	Density Correction Evaluation	2D Radial	VHSP*	NO	180	256 ²	1024	N/A	0.02	70	260	25	5
		3D Radial	VHSP	NO	180	256 ³	256	128	0.02	11	410	25	0.7
		3D Spiral	VHSP	NO	180	256 ³	256	128	0.02	11	410	25	0.7
2	Deblurring Algorithm Assessment	2D Spiral	VHSP	NO	180	256 ²	512	N/A	0.02	70	260	25	5
		2D Radial	VHSP	NO	180	256 ²	1024	N/A	0.02	70	260	25	5
		3D Spiral	VHSP	NO	180	256 ³	256	128	0.02	11	410	25	0.7
	3D Radial	VHSP	NO	180	256 ³	256	128	0.02	11	410	25	0.7	
3	Elevation of Bandwidth-per-Pixel (BWP) for Off-Resonance Correction	2D Spiral	VHSP	NO	180	256 ²	32	N/A	0.02	70	210	25	5
											260		
											310		
											410		
											510		
610													
4	Increase of the Number of Spiral-Interleaves for Off-Resonance Correction	2D Spiral	VHSP	NO	180	256 ²	16	N/A	0.02	70	260	25	5
							32						
							64						
							128						
							256						
512													
5	Evaluation of RF/Trajectory Combinations	3D Spiral	RHSP*	NO	180	256 ³	256	128	0.06	11	410	25/0 [†]	0.7
			VHSP										
			RP*										
	3D Radial	RHSP	NO	180	256 ³	256	128	0.04/0.06	11	410	25/0 [†]	0.7	
	RP												
6	Evaluation of the RF Pulses with the Shortest TE	3D Spiral	RHSP	NO	180	256 ³	256	128	0.02/0.04/0.06	11	410	25	0.7
			VHSP	NO	180	256 ³	256	128	0.06	11	410	25	0.7
			RP	NO	180	256 ³	256	128	0.14/2.46	28	260	25/0 [†]	5
7	Comparison of Long-T2 Suppression Approaches	2D Spiral	RHSP	Dual Echo subtraction	180	256 ²	512	N/A	0.14	28	260	25	5
				Water-Saturation Pulse	180	256 ²	512	N/A	0.14	28	260	25	5
				Fat-Saturation Pulse	180	256 ²	512	N/A	0.14	28	260	25	5
				MT** Pulse (Flip angle-500°, Frequency offset-1200Hz, Duration-10.24 ms)	180	256 ²	512	N/A	0.14	28	260	25	5

*VHSP – Variable-rate selective excitation (VERSE) - modified Half-Sinc Pulse; RHSP – Regular Half-Sinc Pulse; RP – Rectangular Pulse.

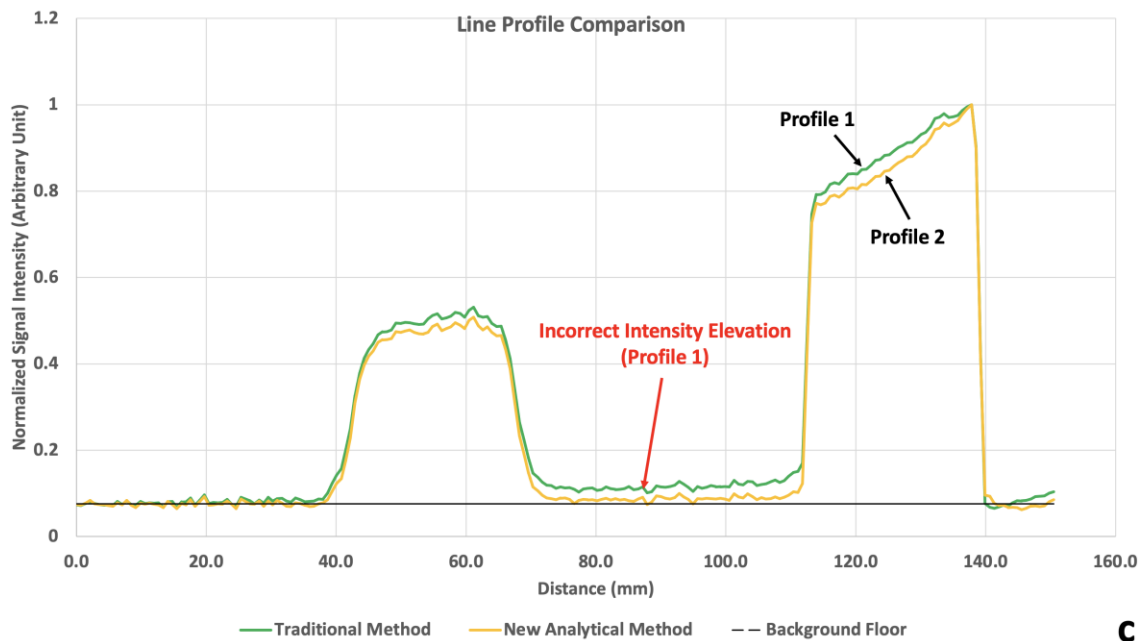
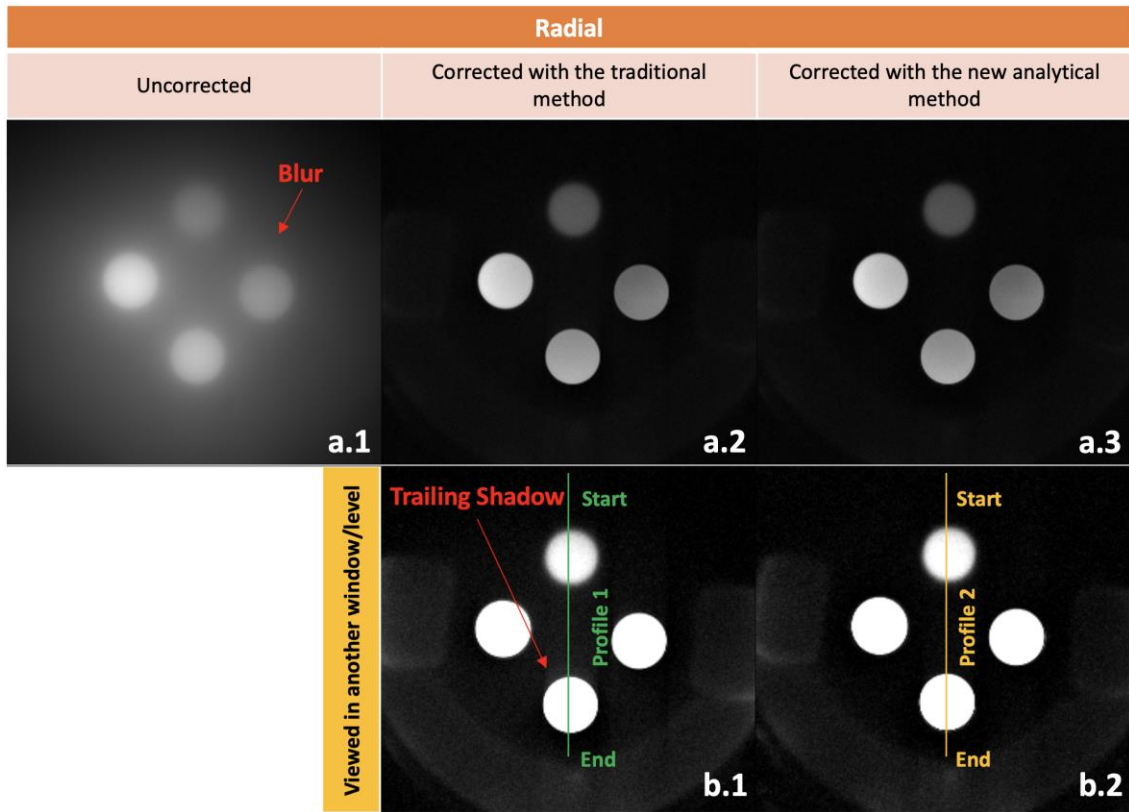
**MT – Magnetization Transfer.

†Noise Image (No RF; Flip Angle = 0°).

2.3. Results

2.3.1. Density Correction

The proposed new analytical method for density correction greatly reduces the artifacts in contrast to the traditional method. For the UTE images acquired with the 2D radial trajectory, both the traditional and new analytical density correction (DC) methods can effectively clean up the ‘blur’ artifact (red arrow) produced without the use of density correction (Figures 2.4.a.1-3). However, the results corrected by the traditional and new analytical methods present a slight difference where the traditional DC method reveals some more prominent artifacts formed as trailing shadows (red arrows in Figures 2.4.b.1-2). For closer observation, two profile lines were drawn (Figures 2.4.b.1-2). The comparison suggests that the traditional DC method (the dash-dotted line), in contrast to the new analytical DC method (the solid line), incorrectly elevates the image intensity between the two vials (80-100 mm) above the background floor (denoted by the dashed line), resulting in the trail-like artifact (Figure 2.4.c). For the 3D radial trajectory, without any correction, the image quality severely deteriorates with the ‘blur’ artifacts (dark blue arrows) covering most of the image detail (Figure 2.5.a.1). In the corrected cases, the proposed analytical DC function described by Eq. [2.14] and [2.15] demonstrate a superior correcting performance (Figure 2.5.a.3) as the traditional DCF (k_r^2) exhibits some artifacts (the red arrows in Figure 2.5.a.2) in the coronal and sagittal planes. The removal of the artifact is mainly due to the weighting factor associated with the altitude-angle, $(\cos(\varphi_j) - \cos(\varphi_{j+1}))$, described in Eq. [2.15]. This weighting factor was also implemented for the 3D spiral density correction since the Spiral-Cones trajectory used a similar radial-style acquisition approach along the k_z -axis. The Spiral-Cones DCF without the weighting factor (simply formulated as a product of the 2D spiral and 1D radial DCFs) produces an artifact pattern analogous to the artifact seen in the traditional 3D radial density correction (Figure 2.5.b.2 vs. Figure 2.5.a.2), even though the ‘blur’ artifact disappeared (as compared to Figure 2.5.b.1). However, the proposed DCF, applied with the weighting factor, can remove the artifact (Figure 2.5.b.2), proving its superiority in the Spiral-Cones density correction (Figure 2.5.b.3).



C

Figure 2.4. Comparison between the traditional and new analytical density correction functions.

The uneven intensity distribution improved with the traditional and new analytical density correction (Eq. [2.12]) functions in the 2D radial (a.1-3). The density-corrected results are viewed in another window and level, and trail-like artifact becomes visible in the traditional DC method (b.1) by contrast to the new DC method (b.2). The trail artifact emerged in the traditional DC method is further verified by the profile comparison (c).

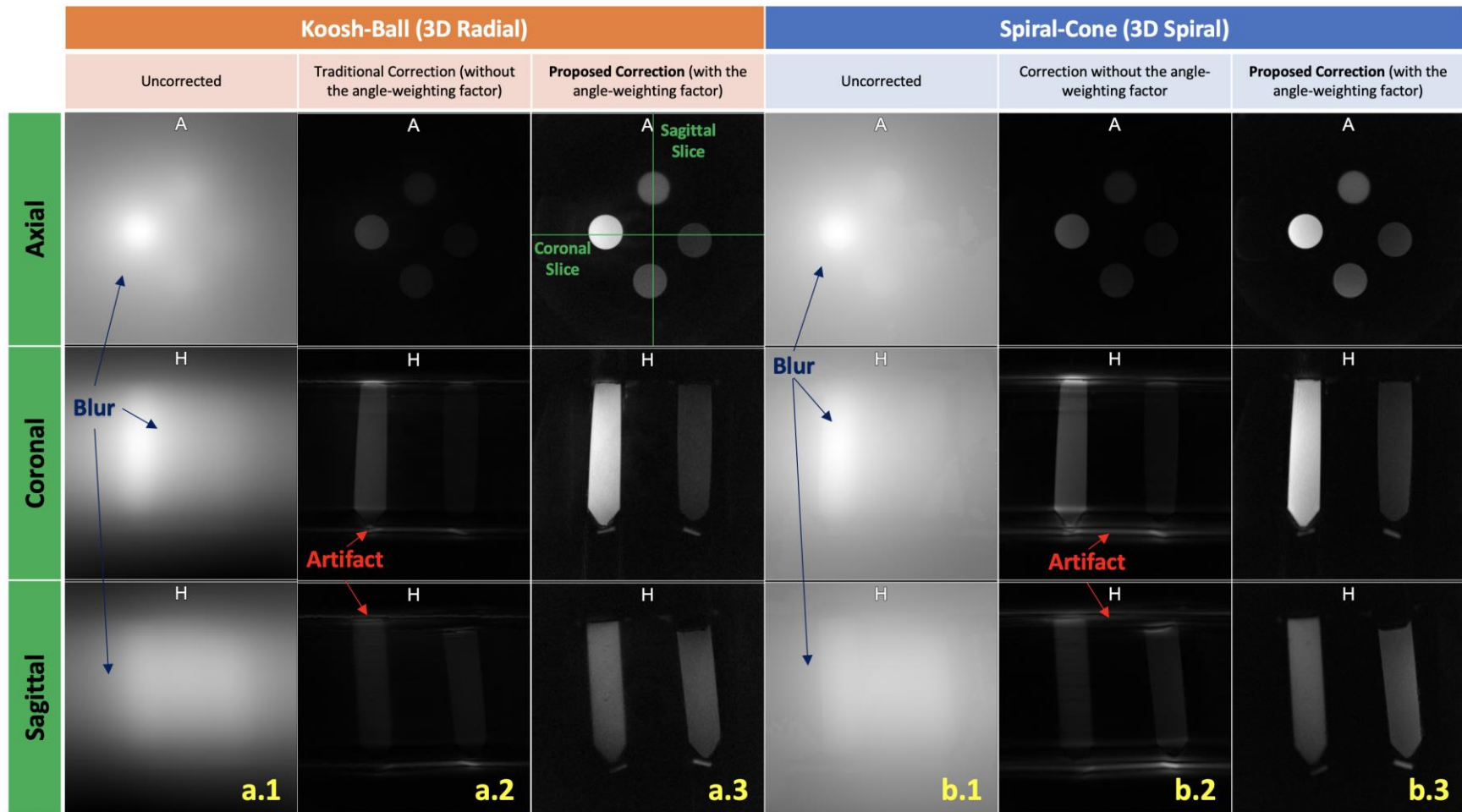


Figure 2.5. Comparison of the density correction techniques used in the 3D radial and spiral.

For the 3D radial, there includes an uncorrected case (a.1), correction using the traditional method (a.2), and correction using the proposed method (Eq. [2.14] and [2.15]) (a.3). For the 3D spiral, there includes an uncorrected case (b.1), correction without the angle-weighting factor (b.2), and the correction using the proposed method with the angle-weighting factor (Eq. [2.16]) (b.3). Beginning from the top and going clockwise, the vials contain rubber, water, agar and oil. The green lines indicate the slices of sagittal and coronal views shown below.

2.3.2. Off-Resonance Artifact Correction

The auto-deblurring algorithm applied in 2D and 3D can successfully suppress the off-resonance artifact, characterized by the blurry edges, in the spiral and radial trajectories (Figures 2.6 and 2.7). In the 2D acquisitions of spiral and radial, the ring-like off-resonance artifact mostly identified around the oil vial (red arrows) disappears after the algorithm processing (yellow arrows in Figures 2.6.a.1-4). Another improvement observed in the 2D radial is a sharper edge (yellow arrow) of the rubber rod. Even though the off-resonance artifact extends to more dimensions (highlighted by the red boxes) in the 3D acquisitions of both spiral and radial, the 3D de-blurring algorithm successfully reduced the artifact as highlighted by the green boxes (Figures 2.6.b.1-4). However, the off-resonance correction sometimes requires more than just the auto-deblurring algorithm, especially for the spiral trajectory with long-duration settings. Further, the algorithm demonstrated an acceptable efficacy with different bandwidth-per-pixel (BWP) and spiral interleaves (Figure 2.7). However, for those long-duration settings with lower BWPs or fewer spiral interleaves, the algorithm exhibits some artifacts (red arrows in Figures 2.7.b.1, b.2, d.1, and d.2). As a supplement to the analysis, this work also demonstrates that elevating BWP or increasing spiral interleaves without the auto-deblurring algorithm can still effectively alleviate the artifact (Figures 2.7.a.1-6 and c.1-6). By contrast, the latter approach seems to provide better suppression towards the off-resonance artifact, but neither the highest BWP nor the most spiral interleaves can solely eliminate the artifact completely. Hence, the auto-deblurring algorithm can serve as an effective complementary remedy to the settings with higher BWPs and more spiral interleaves, producing effective off-resonance correction (Figures 2.7.b.1-6 and d.1-6).

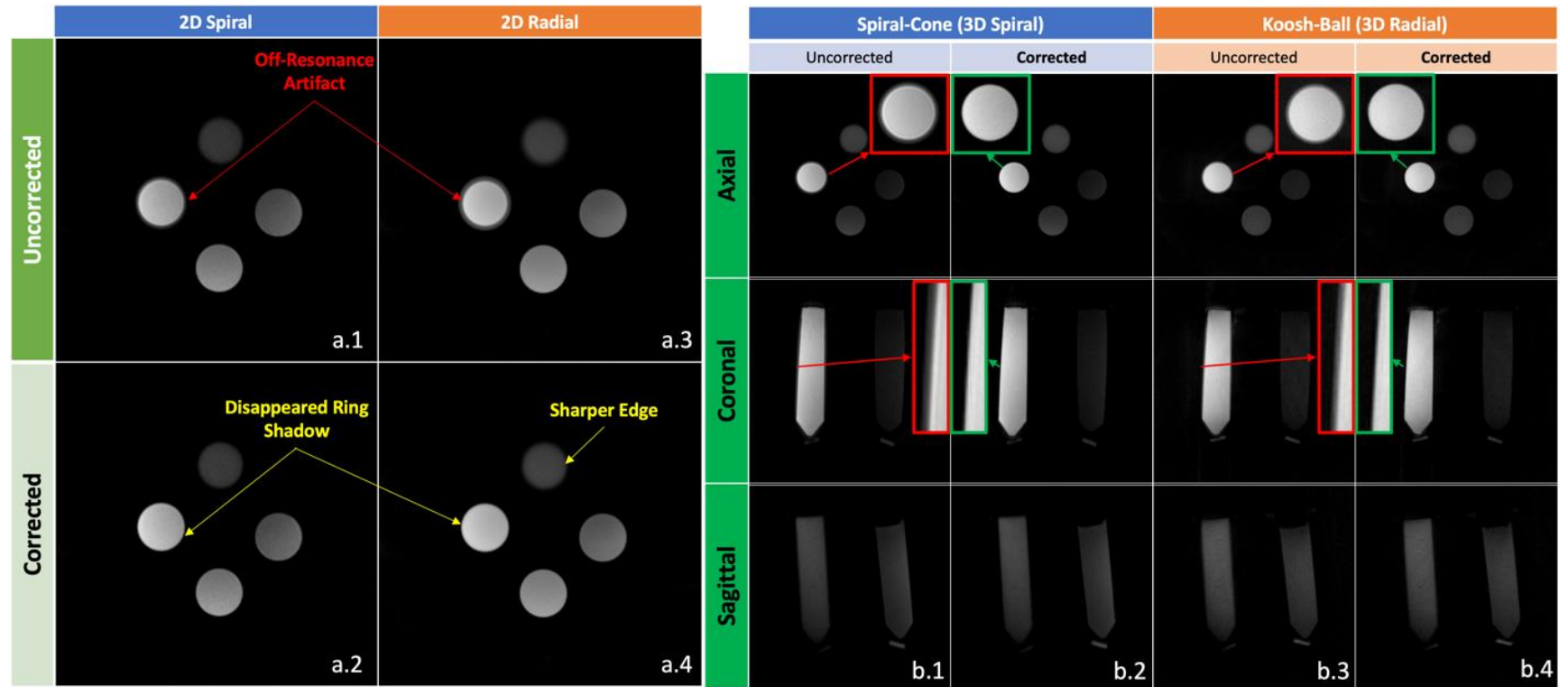


Figure 2.6. The off-resonance artifact improved with the deblurring algorithm.

The reduced artifacts are observed in the 2D Spiral (a.1-2), 2D Radial (a.3-4), 3D Spiral-Cones (b.1-2), and 3D Radial (“Koosh-Ball”) (b.3-4). The red and green enlargements in (b.1-4) highlight the comparison before and after the correction in 3D. Beginning from the top and going clockwise, the vials contain rubber, water, agar and oil.

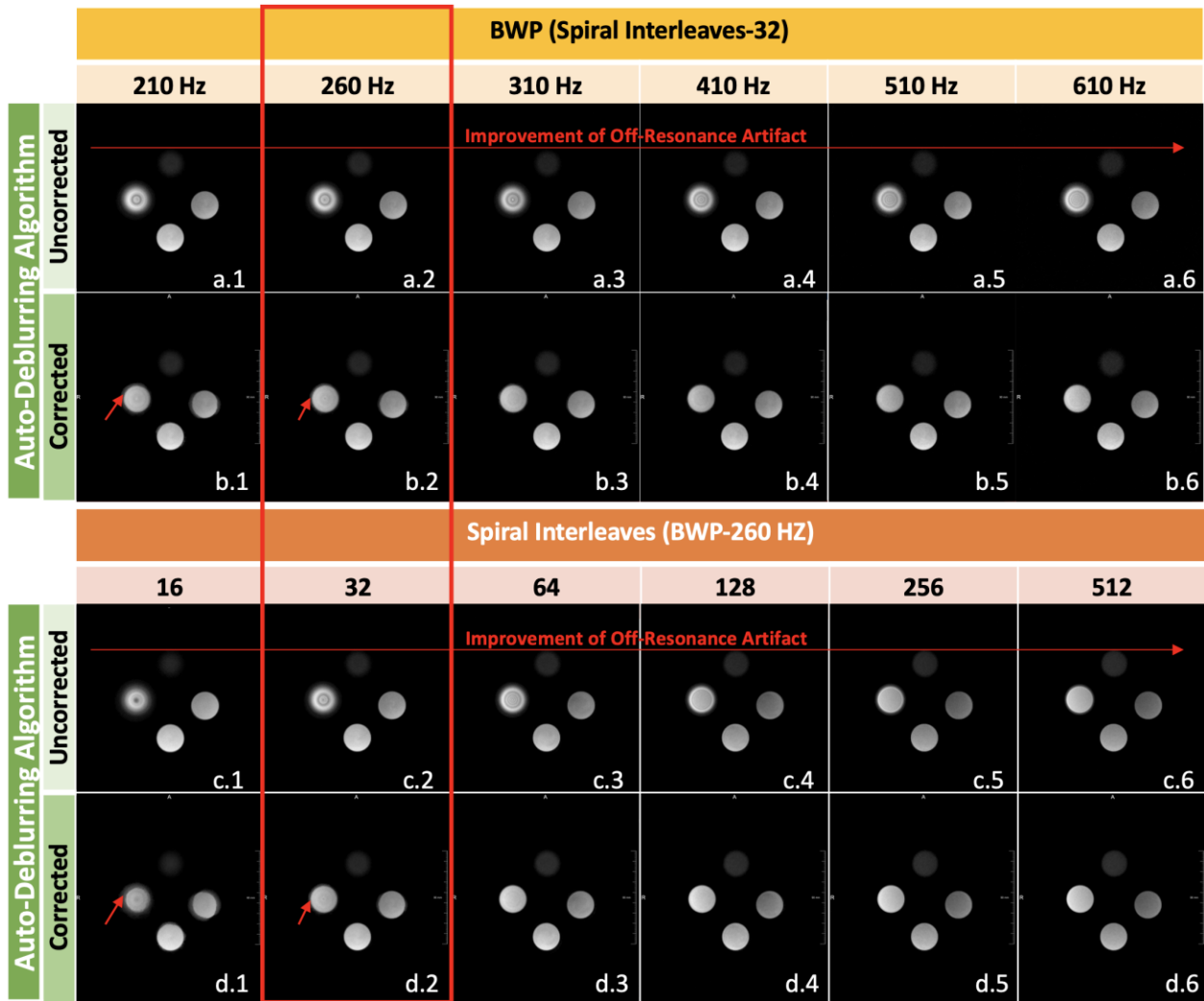


Figure 2.7. The off-resonance artifact improved with increases of the bandwidth-per-pixel (BWP) and spiral interleaves.

While increasing the BWP for 2D spiral acquisitions alleviated off-resonance artifact (a.1-6), using a deblurring correction in conjunction with increasing BWP did so more efficiently (b.1-6). Similar results were found for the 2D spiral acquisitions, for the uncorrected (c.1-6) and corrected (d.1-6) cases. The red box indicates the identical settings. The red arrows point at the imperfect off-resonance correction; and the red box encloses the identical settings. Beginning from the top and going clockwise, the vials contain rubber, water, agar and oi

2.3.3. Direct Comparison between Combinations of RF Pulses and Trajectories

In combination with different RF pulses, the spiral trajectory overall manifests a superior outcome compared to the radial trajectory, using the comparable scanning settings (Figure 2.8). The qualitative comparison suggests no visually evident difference between the corresponding spiral and radial trajectories with different RF selections (Figures 2.8.a.1-3 vs. a.4-6). The regular and the VERSE-modified half-Sinc pulses demonstrate more brightness than the rectangular pulse for the vials of oil, agar, and water for each trajectory regardless of the spiral (Figures 2.8.a.1-3) or the radial (Figures 2.8.a.4-6). In addition, a quantitative SNR comparison reveals that the scan with the regular half-Sinc pulse and the Spiral-Cones trajectory possesses the highest SNR for all the vials among all six combinations (Figure 2.8.b). The SNRs of water, agar, and oil were higher for the rectangular pulse than the regular or the VERSE-modified half-Sinc pulse for either of the trajectories (Figure 2.8.b). However, the SNR of the short-T2 component, rubber, was nearly retained at the same level for all three RF pulses in either the Spiral-Cones or the “Koosh-Ball” (Figure 2.8.b). Regarding the time-efficiency, both the regular and VERSE-modified half-Sinc pulses require double the scan time of the rectangular pulse for the same acquisition parameters (Figure 2.8).

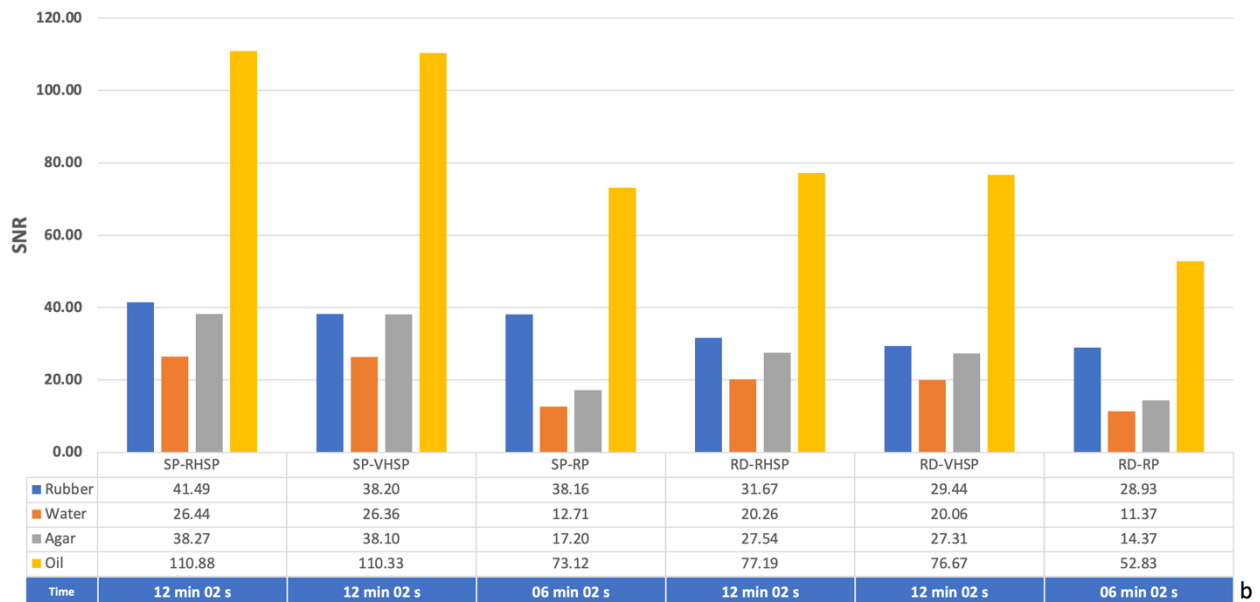
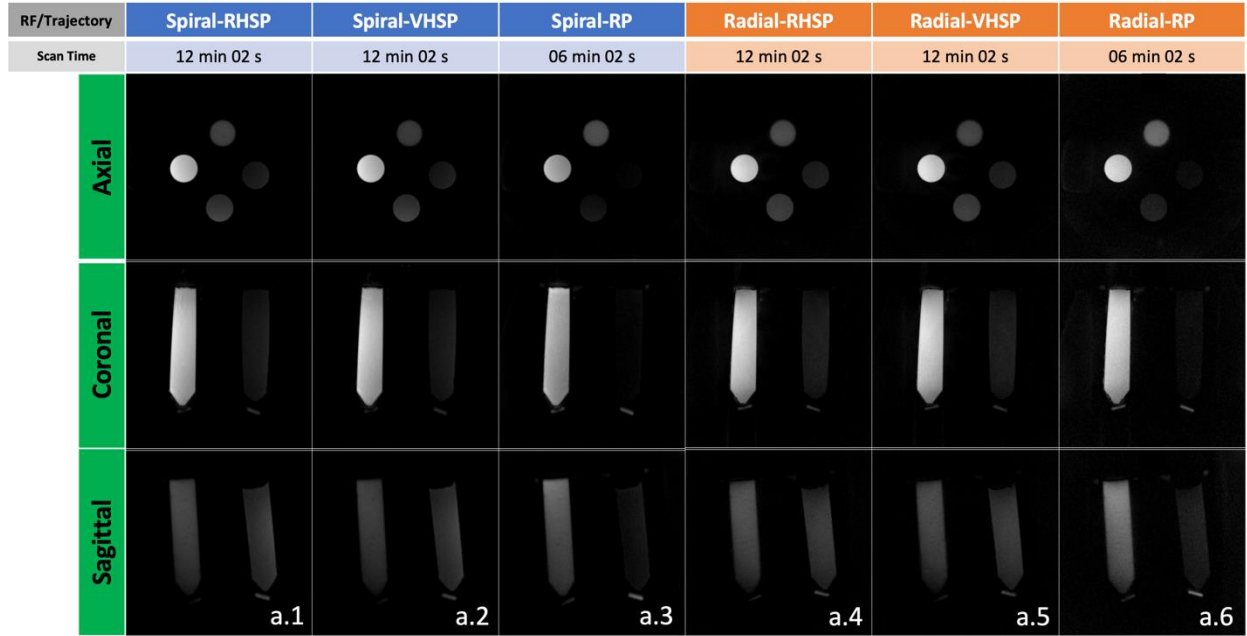


Figure 2.8. Qualitative and quantitative evaluations of the various combinations of the implemented RF pulses and trajectories.

Comparison of 3D radial and spiral trajectories among the regular half-Sinc pulse (RHSP) excitation, VERSE-modified half-Sinc pulse (VHSP) excitation, and the rectangular pulse (RP) excitation with matching scan parameters (a.1-6). SNR of the rubber (short T2 material) was generally higher for the spiral trajectories as compared to the radial trajectories (b). SP-spiral; and RD-radial. Beginning from the top and going clockwise, the vials contain rubber, water, agar and oil.

2.3.4. The Effect of Echo Time Minimization

Higher SNRs for the short-T2 component, rubber, can be achieved using half-Sinc pulses and shorter TE (Figure 2.9). The hard rectangular RF pulse allows for an ultrashort TE of 60 us while the regular half-Sinc pulse and its VERSE variant can achieve shorter TEs as of 40 and 20 us, respectively (red arrow Figure 2.9). However, the regular half-Sinc pulse (RHSP) (with 40 us) demonstrated the highest SNRs for all components among all three RF types using the earliest echo time of each, even though the VERSE-modified half-Sinc pulse (VHSP) was executed with a shorter TE of 20 us. When the TEs of all three pulses were set to 60 us, the RHSP still produced the highest SNRs for all components (the grey arrow in Figure 2.9). Furthermore, with the matching settings (TE of 60 us), the RHSP and VHSP yielded comparable SNR measurements for both the long-T2 (water, agar, and oil) and short-T2 (rubber) components. However, these half-Sinc pulses possess higher SNR measurements than the RP for the long T2-components while a similar SNR for the rubber. Also, decreasing the TE from 60 to 20 us using the VHSP barely impacted the SNR measurements for the long-T2 components (-0.54% to +0.24%) but improved the SNRs of rubber by 5% and 9.8% (blue arrow Figure 2.9).

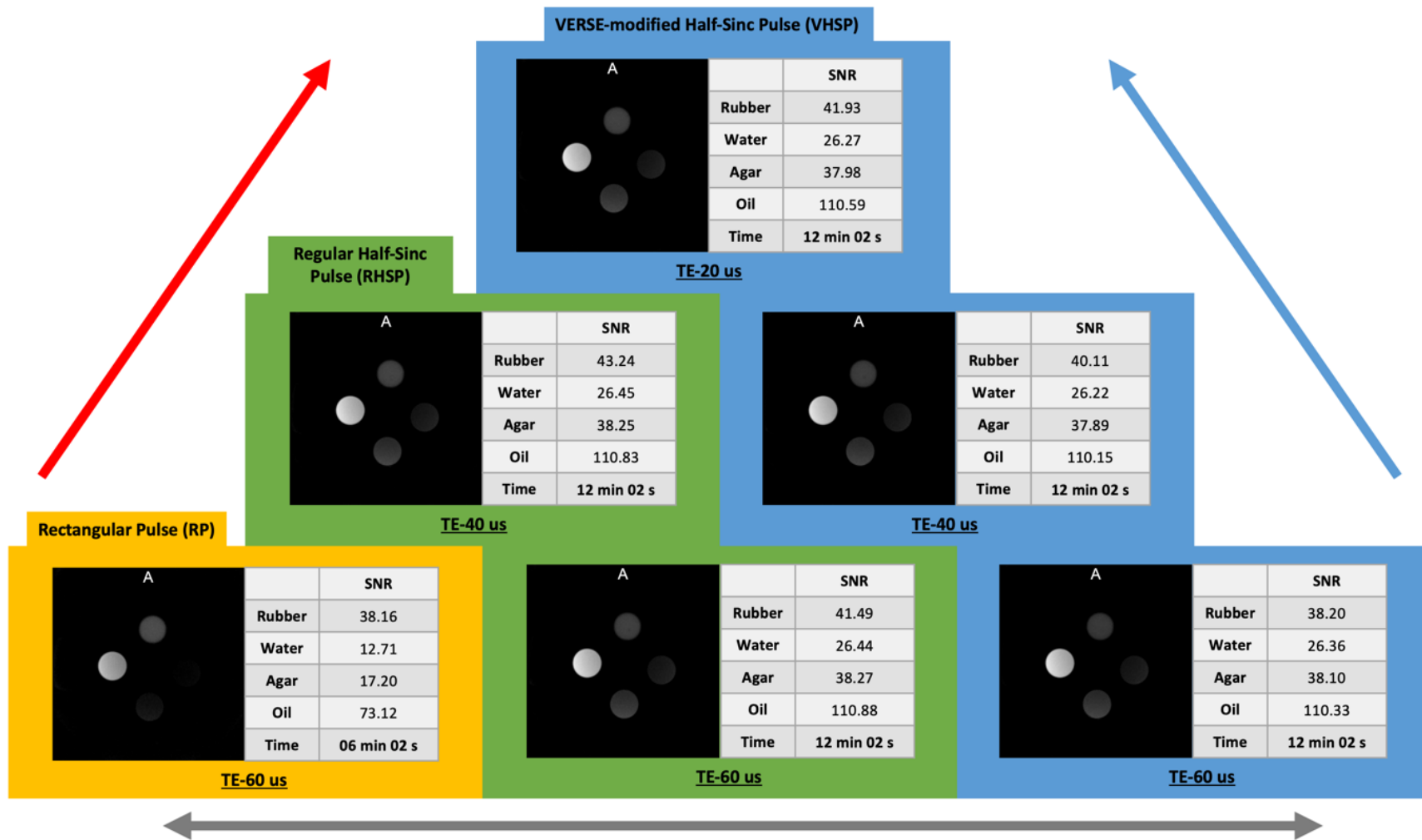


Figure 2.9. Comparison of the implemented RF excitation schemes including VERSE-modified half-Sinc pulse (VHSP), regular half-Sinc pulse (RHSP), and rectangular pulse (RP) with the TE variation.

The TE variation was compared between (different colors) and within (identical colors) pulses. The blue single-arrow directs the variation of image contrast and SNR using the VHSP pulse with a decrease of TE; the red single-arrow indicates the variation of image contrast and SNR using three different types of pulses with a decrease of TE; the grey double-arrow compares the image contrast and SNR among three types of pulses with an identical TE. Beginning from the top and going clockwise, the vials contain rubber, water, agar and oil.

2.3.5. Effective Long T2 Suppression Techniques

Satisfactory suppression results for different long-T2 materials can be achieved by selecting appropriate long-T2 suppression techniques (Figure 2.10). The dual-echo subtraction method (with two in-phase TEs) completely saturated the water and agar components but only partially suppressed the oil signal (Figures 2.10.a-c). Also, because the longer TE could not capture the rubber signal, the subtraction excluded the long-T2 contrast while enhancing the short-T2 contrast (rubber). The fat-saturation pulse drastically reduced the oil signal, but there was still some insignificant residual signal (Figure 2.10.d). In contrast to the unsaturated short-TE scan, we also observed signal reduction for the rubber, slight signal reduction for the agar, and no signal variation for the water. The water-saturation pulse successfully saturated the water and agar (water-based) without any residual but left the fat barely affected and the rubber partially saturated (Figure 2.10.e). The off-resonance saturation approach could completely suppress the water and oil signals yet only partially saturated the agar and rubber components due to their MT effects, as expected (Figures 2.10.f-h).

Supported by the SNR analysis, all the implemented suppression techniques demonstrate outstanding performance for their targeted long-T2 materials (Figure 2.10.i). To create a reference, we first estimated the background SNR as 8.6, determined by the signal void of rubber identified in the long-TE scan (Figure 2.10.b). For the rubber, the dual-echo subtraction demonstrated the maximized enhancement (highest SNR) across all applied techniques. In comparison, the off-resonance saturation method yielded the weakest enhancement for the rubber with the lowest SNR. Additionally, because the water and fat saturation pulses had partially saturated the rubber, the rubber contrast was compromised (reduced SNR). For the water, the dual-echo subtraction, water saturation pulse, and off-resonance saturation exhibited an excellent suppression capability since the observed SNRs were lower than the background SNR. By contrast, the fat-saturation pulse had nearly no impact on the SNR of water. Concerning the agar, both the dual-echo subtraction and water saturation pulse successfully minimized the SNR of agar below the background. However, the off-resonance saturation method could not suppress the agar signal thoroughly due to the agar's MT effect. Moreover, the fat-saturation pulse also led to a slightly reduced SNR for the agar. For the oil, all the applied techniques failed to deliver total signal suppression except the off-resonance saturation. In other words, only the off-resonance saturation returned a near-zero SNR for the oil.

Among the rest of the approaches, the fat saturation pulse with a lower SNR committed a superior oil suppression than the dual-echo subtraction and water saturation pulse. Among all the implemented techniques, the off-resonance saturation method is the only approach that can simultaneously saturate both the water and oil.

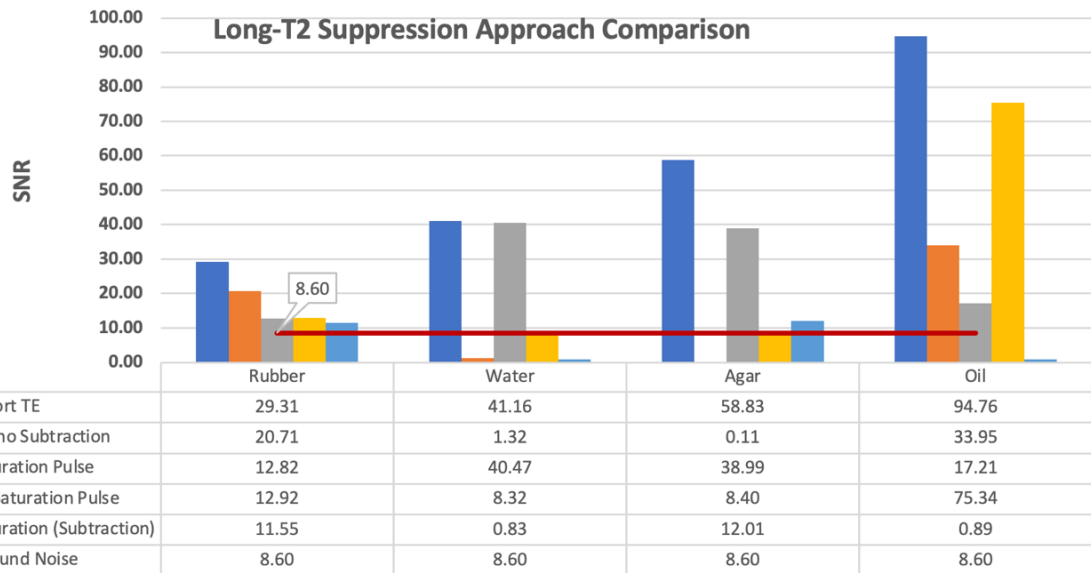
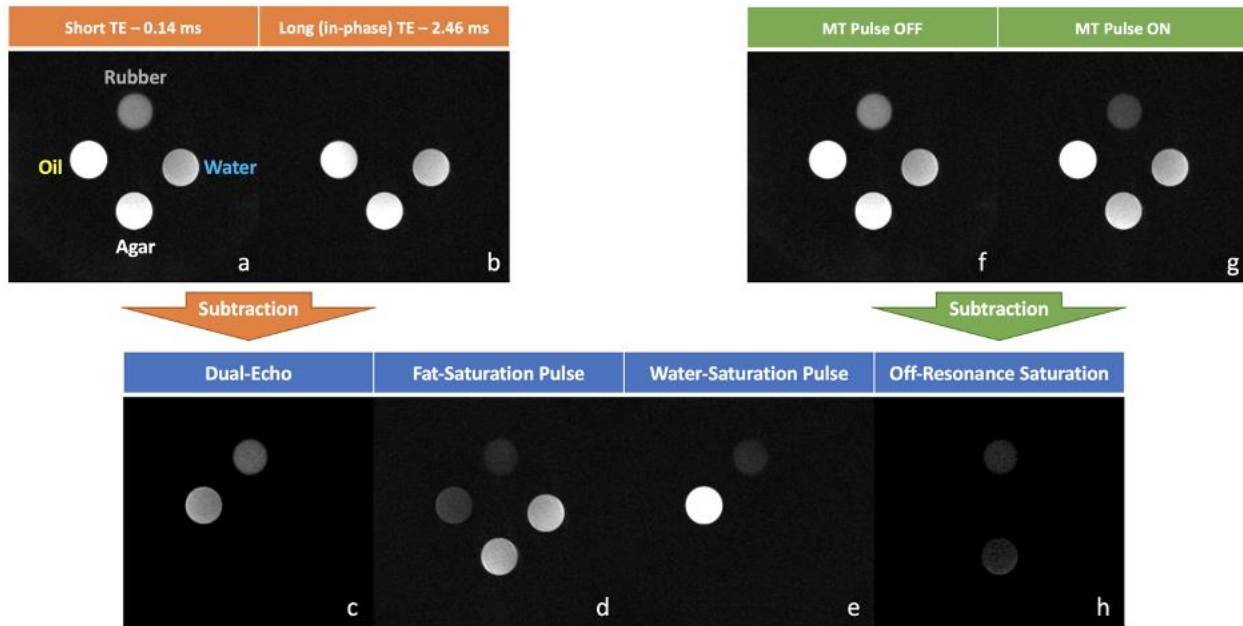


Figure 2.10. Direct qualitative and quantitative comparisons between the implemented long-T2 suppression techniques.

(a-h) Comparison of the implemented long-T2 suppression techniques including dual-echo subtraction, fat-saturation pulse, water-saturation pulse, and MT saturation, and (i) SNR comparison for different long-T2 suppression approaches. Dual echo subtraction can simultaneously suppress all long-T2 components while others can selectively suppress one or more particular long-T2 components. Beginning from the top and going clockwise, the vials contain rubber, water, agar and oil.

2.4. Discussion

Overall, the results in the study suggest that differing sequence acquisition approaches can improve the UTE images concerning the quality and SNR, and various correction methods are also indispensable for ameliorating the artifacts associated with the (non-Cartesian) UTE acquisitions. As a novelty, the developed UTE sequence includes flexibly user-configurable radiofrequency (RF) pulses, trajectories, dimension schemes (2D/3D), and long-T2 suppression methods, uniquely allowing for direct comparisons. In addition to the sequence, the specialized reconstruction pipeline can provide various novel correction methods compensating for the k-space trajectory errors, uneven the k-space density distribution, and off-resonance artifact. The developed sequence and reconstruction pipeline, through the systematic evaluation, not only provides high-quality UTE images but also renders optimized scanning guidance for different potential UTE applications, for example, musculoskeletal (MSK) and synthetic computed tomography (sCT) generation studies.

The analytical DCFs of the 2D radial, the 3D radial, and the 3D spiral trajectory were improved in this study. The traditional and proposed analytical DCFs can effectively compensate for the uneven data-filling data characterized by non-Cartesian trajectories, refining the image quality in the UTE reconstruction by removing the blurry artifact (Figures 2.4 and 2.5). Compared to the traditional analytical DCFs (120,131), the proposed analytical DCFs can provide a more geometrically correct density compensation model in k-space, which leads to a superior density correction with diminished artifacts (Figure 2.4.b.1 vs. Figure 2.4.b.2, Figure 2.5.a.2 vs. Figure 2.5.a.3, and Figure 2.5.b.2 vs. Figure 2.5.b.3). Besides, in practice, one may also adopt a numerical DCF to achieve a more optimized density correction with better-suppressed artifacts (58,131,137,138). However, the numerical DCF is estimated iteratively from a convergence model, which lacks computational simplicity comparing to the proposed analytical DCFs. Also, the numerical DCF might result in a downgraded sharpness for the image detail contrasting to the analytical form. Except for the correction methods executed in reconstruction as above, some groups used variable density gradients to achieve the density correction within the acquisition simultaneously (39,139). These variable density gradient techniques consider the density correction in the gradient design (generation) for an improved SNR efficiency or more optimized sampling pattern. However, compared to the analytical DCF in this work, the gradient design with the variable density incorporation is more subject to the hardware constraints, e.g., the maximums of gradient amplitude

and slew rate. In other words, the variable density gradient might require a much higher gradient strength or slew rate than the regular gradient for the same imaging settings, which limits the flexibility of the former's protocol adjustment. As another drawback, the variable density gradient requires a more complex formulation and calculation, which might be inefficient for the gradient generation and updating during the modifying of scan protocols in real-time.

This study has highlighted the importance of the auto-deblurring algorithm for improving the image quality with sharper edges by correcting the off-resonance artifact (Figure 2.6). The off-resonance artifact is often identified as the blurry shadows around the imaged objects (Figures 2.6.a.1, a.3, b.1, and b.3) in the acquisitions of non-Cartesian trajectories-e.g., the 2D/3D radial or spiral. To alleviate the artifact appearing in the 2D radial and spiral (Figures 2.6.a.3-4), we implemented an automatic deblurring algorithm proposed by *Noll et al.* (123). This auto-deblurring algorithm does not require an additional field map obtained by extra scans or estimation, contrasting with other off-resonance-correction algorithms (124–126,133,134). As a critical improvement, we re-developed the deblurring algorithm, proposed in 2D originally, in 3D to tackle the off-resonance artifact extending to the third dimension (Figures 2.6.b.1 and 3). This new development inherited the acquisition-efficient feature from its predecessor in 2D, where no field map is required. The new 3D deblurring algorithm can successfully eliminate the off-resonance artifact in both the 3D radial and spiral trajectories (Figures 2.6.b.2 and b.4). This result manifests the necessity and efficacy of the newly developed deblurring algorithm for correcting the off-resonance artifact in 3D.

The evaluation of FUSE shows that the optimization of UTE protocols can combine with the deblurring algorithm to collectively improve the off-resonance artifact occurring in the spiral acquisitions (Figure 2.7). To our knowledge, this study is the first to investigate and evaluate the performance of the combination of both approaches. Compared to the 2D radial trajectory, the 2D spiral usually has a longer gradient readout and can lead to a more severe off-resonance artifact. In this case, the auto-deblurring algorithm might not effectively fulfill the artifact correction. Therefore, we have explored other approaches that can productively alleviate the off-resonance artifact on the acquisition side, for example, the shortening of the spiral readout-gradient (Figure 2.7). In the exploration, we investigated and compared two remedies that can beneficially reduce

the spiral gradient's duration, specifically elevating the BWP for the receiver and increasing the number of spiral interleaves. The elevation of BWP can shrink the sampling interval (of the receiver), leading to a shorter readout-gradient duration, while the increase of the number of spiral interleaves can segment a long spiral readout-gradient into multiple interleaves with short durations. The experiment results suggest (Figures 2.7.a.1-6 and c.1-6) that both measures for shortening the spiral gradient can help alleviate the off-resonance artifact effectively, but the increase of the number of spiral interleaves seems to have a superior outcome. However, neither of the measures can solely eliminate the artifact without the deblurring algorithm. Also, successful off-resonance correction cannot merely rely on the deblurring algorithm as we also observed imperfect correction for the scans with the lower BWP settings or fewer spiral interleaves (red arrows in Figures 2.7.b.1, b.2, d.1, and d.2). These findings suggest that we might need to combine the acquisition adjustments with the deblurring algorithm to achieve a satisfying off-resonance correction, especially in the spiral UTE acquisitions (Figures 2.7.b.3-6 and d.3-6).

The combinations of different RF pulses and trajectories have not been directly compared before due to the lack of a proper UTE sequence integrated with these techniques; however, this study shows that these combinations using matching scan parameters can lead to dissimilar time efficiency and SNR results. In the experiments, all the RF/trajectories combinations can provide distortion-free and artifact-free images (Figures 2.8.a.1-6). However, in the SNR measurements, we have discovered differences between the various combinations. From the aspect of trajectory, the spiral trajectory's settings, taking all RF types into account, have demonstrated overall higher SNRs for all materials than their counterparts in the radial trajectory's settings. Given the numbers of the in-plane views and cones are identical for all scans here, the spiral's higher SNR measurements are likely because of its superior coverage for k-space (against the radial trajectory). However, this finding does not necessarily suggest that the spiral trajectory is always desirable in the UTE scans. Given the radial trajectory usually has a faster readout-gradient allowing for a shorter TR, it has more flexibility in terms of contrast manipulation and the potential for higher time efficiency. From the angle of RF pulse for evaluating the various combinations, in either the spiral or the radial trajectories, the RHSP and VHSP yielded similar SNR measurements but higher SNR measurements than the RP overall. This observation suggests each RF scheme can deliver a unique impact on the excitation outcome-i.e., SNR and contrast. One possible explanation is the

half-Sinc excitation scheme's (including the VERSE modification) actual (or delivered) flip angle might be different from the prescribed angle, which results in a variation in SNR and contrast compared to the matching RP setting. Another explanation might be that the addition of the FID signals from two half-Sinc excitations could reduce the noise collected in each receiver channel (given the noise here can be approximated to follow a Gaussian distribution). However, these deserve further investigation in future studies. The RP has been a more popular choice for performing 3D UTE scans (34,40,41,56,140,141), while the half-Sinc pulse is rarely adopted by 3D UTE sequences (37,142). This may be because the RP is easier to design and requires half the acquisition time than the half-pulse excitations if the same imaging parameters (e.g., total prescribed flip angle) are maintained.

The different pulse shapes and configurations can lead each implemented RF pulse to a unique minimum TE limit; however, switching the pulse type for a shorter minimum TE limit cannot guarantee a higher SNR output for the short-T2 component (Figure 2.9). Due to the lack of an integrated sequence, this was the first study to directly compare all three pulse types regarding the image contrast and SNR in the 3D UTE imaging. The RP's minimum TE is constrained by half of the pulse duration plus the switching time limit between the transmitter and receiver (Tx/Rx). In comparison, the RHSP does not need to contribute any pulse duration to TE since the half-pulse completes its excitation before time-zero (i.e., the starting of TE). However, the RHSP excitation scheme still needs to account for the ramp-down of slab-selection gradient plus the following refocusing gradient as a minimum in the TE calculation. This minimum TE calculation can also cover (overlap with) the system limit of Tx/Rx. As compared to the RHSP, the VHSP can exclude the ramp-down (integrated to the excitation process instead) and refocusing gradient from the TE contribution and further narrow down the minimum TE to the time limit between Tx and Rx. Using the matching scanning protocols (e.g., flip angles and resolution), the RHSP might have a shorter minimum TE (the ramp-down plus refocusing gradient) than the RP (where the minimum TE includes half of the pulse duration and the Tx/Rx limit). This is because the 3D RHSP excitation is usually associated with a low amplitude for the slab-selection gradient, which only demands relatively short gradient ramping-down and refocusing times. Compared to the RHSP, the VHSP further permits a smaller minimum TE due to the absence of the slab-selection ramp-down and refocusing gradient. Among all three RF types, the VHSP has the shortest minimum TE (i.e., 20

us) compared to the others with their minimum TEs (40 and 60 us). However, the VHSP with the shortest minimum TE does not necessarily produce the highest SNRs (red arrow in Figure 2.9), and the RHSP with a longer minimum TE leads to higher SNR measurements. As discussed in the previous section (also indicated by the grey arrow in Figure 2.9), this SNR divergence might be due to the variation between the actual and prescribed flip angles and suggest this flip angle variation has a greater influence on the SNR outcomes than the TE shortening. As for the overall SNR variation with shortening the TE for the VHSP excitation, the short-T2 component's (rubber) SNR can benefit a lot, while the SNR outcomes of the long-T2 components barely vary (blue arrow in Figure 2.9).

Lastly, the FUSE sequence can effectively suppress the signal for the various long-T2 components, providing enhanced contrast for the short-T2 component (Figure 2.10). Depending on the desired imaging goals, the sequence can either exclusively saturate a single long-T2 contrast using a water- or fat-saturation pulse or simultaneously suppress multiple long-T2 contrast types with a dual-echo subtraction or off-resonance saturation method. Compared with a similar study, this work has provided a more inclusive evaluation supplemented with SNR analyses for the long-T2 suppression techniques above (Figure 2.10.i) (72). In this work, we have demonstrated that it is feasible to use the developed sequence to manipulate (i.e., retain or suppress) different long-T2 contrast types. With this feature, this sequence can potentially adapt to various applications in short T2 imaging, depending on needs.

This study was the first to use an integrated sequence to compare across the widely adopted UTE techniques. As a strength, this study highlights the unique features of each technique through direct comparison. Since selecting appropriate UTE techniques and parameters is important for researchers to customize the scan protocols for different applications, this study provides systematic guidance. As another strength, this study also explores some new techniques for the direct comparison, i.e., the 3D half-Sinc pulses (including the VERSE modification), which have been ignored in many previous 3D UTE developments. One limitation of this study is that the types and relaxation properties of the materials used in the phantom might not be sufficient for the sequence evaluation. For example, only one short-T2 component, rubber, was constructed within the phantom for the assessment. Due to this, we were uncertain if the developed sequence would

be capable of imaging other short-T2 materials with different types or shorter T2 relaxation properties. However, a better phantom with more enriched short-T2 species could potentially address this issue. We could also image cadaver tissues, carry out biochemical or histology tests to further characterize their contents, and compare the obtained various tissue properties back to the UTE scans. As another limitation, although the various evaluation testing conducted in this study can be considered inclusive, there might still be some other evaluations necessary to be carried out for a particular application but absent from this study. For example, the optimal RF pulse (RP, RHSP, or VHSP) might need to be determined for the T1 relaxation time mapping in various knee joint tissues. For another limitation, we could also potentially include long-T2 inversion pulse techniques for conducting the long-T2 suppression, such as a fat-inversion or water-inversion pulse. As a result, we might need to expand or extend our sequence evaluation after investigating the developed sequence for specific applications, for example, MSK imaging or cortical bone imaging in sCT generation.

2.5. Conclusion

In this chapter, we presented a flexible, multi-purpose UTE sequence, which is entitled FUSE. The FUSE sequence is the first comprehensive sequence integrated with many versatile acquisition features, in a total of thirteen possibilities, including the adaptable RF pulses, trajectories, dimension schemes (2D/3D), and long-T2 suppression techniques. The sequence is also equipped with novel correction techniques in the reconstruction, specifically, improved analytical density correction functions and 3D auto-deblurring algorithm for tackling the off-resonance artifact. Together with the proposed reconstruction pipeline, the sequence not only provides high-quality short-T2 imaging but also direct comparison across different UTE approaches. Furthermore, this work enables customized scanning optimization through the direct technique and protocol comparison for various UTE applications.

Chapter 3 Morphological and quantitative musculoskeletal (MSK) imaging of the bovine knee using a novel flexible ultrashort echo time (FUSE) sequence

Synopsis: Joints in the musculoskeletal (MSK) system are challenging to image because several tissues have short T2 relaxation times. The FUSE sequence presents a unique opportunity to study joint tissues both qualitatively and quantitatively by exploiting the flexibility in parameter selection. There lacks an extensive study that evaluates different long-T2 suppression techniques that can provide various morphological contrasts in MSK tissues. Also, there has been no study on the exploration of combining the quantitative magnetization transfer (QMT) technique and 3D UTE using half-Sinc and Spiral-Cone acquisitions. In addition, the quantitative T1 and T2* relaxation time mapping using UTE sequences in MSK tissues deserve more investigation. QMRI of the meniscus was used an example in this study. Consequently, the purpose of this work is to evaluate a novel, user-configurable UTE sequence (i.e., FUSE) for morphological and quantitative imaging in the bovine knee.

3.1. Introduction

Compared to other imaging modalities, magnetic resonance imaging (MRI) can provide signal from soft tissues while delivering no ionizing radiation to patients. The superior contrast between soft tissues imaged by MRI is useful for the direct study of musculoskeletal (MSK) tissues non-invasively and allows for earlier diagnosis of diseases such as osteoarthritis (OA), when compared to standard radiography-based methods (143). OA is a degenerative joint disease that commonly affects the knee (144–148). For many years, OA was characterized as a disease of cartilage degeneration (149–153), but the contemporary view is that it involves changes to the whole knee joint. The importance of these other knee tissues, in particular the meniscus, in the OA disease process is becoming increasingly recognized (154–157). Some tissues in the knee joint have small T2 relaxation times ($T_2 < \sim 10$ ms), such that conventional MRI techniques are unable to obtain sufficient signals from them (3,4,10,11,24). These short-T2 tissues include menisci, tendons,

ligaments, and cortical bone, which exhibit dark or voided regions on the traditional MR images (66,71,79,85,108). The insufficient or non-existent signal in the knee joint restricts MRI from providing high-quality morphological contrast—for example, between the deep layer of cartilage and subchondral bone—or informative quantification for short-T2 components like those found in the meniscus (4,23,110,158). However, both the morphological and quantitative evaluation is essential for the early-OA detection to provide the tissue integrity delineation and biomarkers, respectively (98,99,106,109,110,158–163). As a solution to tackle these challenges, ultrashort echo time (UTE) sequences have been developed and employed for short-T2 tissue imaging over the last three decades (14,15,40,57,68,72,73,162,164). UTE sequences adopt a short radiofrequency (RF) excitation pulse and centre-out k-space acquisition to achieve an echo time (TE) of less than 100 μ s that can effectively capture the signal of short-T2 tissues (7).

In morphological UTE imaging of knee joints, selections of long-T2 suppression methods are essential for isolating signals from the various short-T2 tissues. Although UTE scans can effectively collect the signal from short-T2 tissues in the knee, it also obtains a barely decayed signal from tissues such as muscle or fat due to their long T2 relaxation times. Therefore, the strong long-T2 signal has always been an issue in UTE scans for obscuring the short-T2 contrast, as suggested by many studies (68,73,117,165). Researchers often use fat saturation (FS) pulses to primarily suppress the long-T2 signal from the knee's fat, bone marrow and potentially fatty infiltration into muscle (141,162,166). This measure can preserve and enhance other tissues such as cartilage or menisci for investigation. By comparison, the dual-echo method can simultaneously suppress all types of long-T2 tissues: this method can provide distinct contrast for the cortical bone tissue and the adjacent trabecular bone and articular cartilage (68,70). Also, the off-resonance saturation (OS) method, exploiting the magnetization transfer (MT) effect, can serve as another long-T2 suppression technique that has been shown to effectively enhance the patella tendon and meniscus (short-T2) contrast (72,75); but it needs further investigation due to the few studies in the knee. To date, there has not been a comprehensive study or flexible MRI sequence that evaluates these methods directly in whole knee UTE imaging. As such, it is not evident which technique is superior for enhancing a particular tissue type. For example, the OS-UTE might provide a more visible contrast for the cortical bone than the FS-UTE.

Quantitative MRI (QMRI) techniques can provide biomarkers for detecting the OA in the knee. It has been shown that increases in the common biomarkers, e.g., T2, T2*, and T1rho relaxation time, are associated with degenerative changes occurring in knee joints, which might suggest OA (110,167–171). It is believed that OA involves not only the pathological change of cartilage but also the degeneration and damage of the meniscus (157). Hence, for a better understanding of the onset of OA, more quantitative metrics of the meniscus are required. The quantitative magnetization transfer (QMT) technique that may fill this role because it probes the bound macromolecules in the tissue. It uses two-pool modelling to simulate tissues as the free (i.e., free proton) and bound (i.e., macromolecular) pool and estimate the macromolecular proton fraction and the T1 and T2 relaxation times in both pools, respectively (78,90,172). These parameters have been investigated for assessing the variation of some tissue properties. For example, a moderate positive correlation with statistical significance has been found between the macromolecular proton fraction and proteoglycan (PG) content in articular cartilage (173). As another example, the OA patients were observed with a significantly higher T2 relaxation time of the bound pool in patellar cartilage than the healthy volunteers (174). Studies investigating QMT in the meniscus have been limited a few existing works (175–178). Conventional QMT techniques use Fast Low Angle SHot (FLASH) sequences for data acquisitions, which are more suitable for estimating the two-pool parameters of long-T2 tissues (90,172–174). Compared to FLASH, UTE can be a better alternative in the QMT modelling to assess the two-pool information in both short and long tissues, but only a few studies explored the possibility of coupling the QMT and UTE (92,93,158,179). Since the meniscus possesses abundant short-T2 components residing with long-T2 components, QMT parameters using UTE (UTE-QMT) can serve as potential biomarkers for the early-OA detection in the meniscus. To our knowledge, there are relatively few studies that have looked at the QMT parameters using UTE (158). As such, the potential of UTE-QMT parameters deserves much more investigation, specifically on the impacts of different fitting lineshapes (e.g., Gaussian vs. Super-Lorentzian) and B1 corrections.

Besides the QMT parameters, there are other quantitative measures that are important in QMRI using UTE sequences, for example, the T1 and T2* relaxation times. Although it has not been shown with enough evidence that T1 estimation using UTE (UTE-T1) can be a biomarker for assessing OA in the meniscus, UTE-T1 is essential for helping deriving UTE-QMT parameters

(90,172). The impact of B1 correction on the variation of UTE-T1 estimate also needs more investigation. UTE-T2* is another of interest biomarker that can be used for assessing the meniscus. One can use a mono-exponential model to estimate the UTE-T2* parameter as a bulk metric or a bi-exponential model to estimate UTE-T2* parameters in long-T2 and short-T2 components separately. An increased bulk T2* relaxation time has been observed for the degenerative menisci over the asymptomatic menisci (110). Another study also suggests higher T2* estimates for both long and short components in the degenerative and torn menisci than the normal menisci (77). However, the differences between the mono-exponential and bi-exponential fit still need more verification (77,85,180–182).

It is relatively unknown whether the various knee joint tissues (e.g., the cortical bone or tendon) are feasible to be isolated by different long-T2 suppression techniques with morphological UTE imaging; also, no comprehensive quantitative assessment of the meniscus, using the UTE sequence, has been carried out for mapping QMT parameters and T1 and T2* relaxation times. In the morphological imaging of knee joints, the isolated contrasts between the tissues are very important for providing the well-delineated anatomical structure that might improve manual and automatic segmentation or potentially provide diagnostic information. With a flexible UTE sequence including multiple long-T2 suppression techniques, it might be possible to isolate the signals from the various knee joint tissues. Furthermore, UTE sequences can facilitate the quantitative evaluation of short-T2 tissues with ample signal. Hence, a comprehensive quantitative assessment of short-T2 tissues in the knee, using UTE sequences, is worthwhile to investigate for providing potential biomarkers that help detect early-stage OA. The QMRI mappings using UTE sequences are likely important in all short T2 tissues for OA, but for this work, the scope has been limited to a comprehensive study of the meniscus. This reason is that the meniscus is enriched with both long-T2 (e.g., water) and short-T2 (e.g., collagen) components, which necessitate a comprehensive quantitative assessment using UTE sequences. Besides, more evaluation for combining the UTE sequence and QMT modelling is needed due to the few existing studies (158). For potentially detecting early-stage OA in the knee, in this work, we are employing a novel in-house flexible UTE sequence (i.e., Flexible Ultra Short Echo time or FUSE for short) capable of providing multiple morphological contrasts and various quantitative biomarkers. The aims of this study are twofold:

- 1) To exploit the contrast capabilities of the FUSE sequence to create morphologic images that isolate signals from the various knee joint tissues.
- 2) To carry out a comprehensive quantitative assessment of the meniscus using the FUSE sequence to map QMT parameters and T1 and T2* relaxation times.

3.2. Materials and Methods

3.2.1. Bovine Specimen Study

Morphological and quantitative imaging experiments were carried out using six bovine stifle joints. The bovine stifle joint is similar to the human knee in terms of tissues and anatomy. In this study, the bovine stifle joints were used to mimic the human knee for evaluating the application of the sequence in qualitative and quantitative MSK imaging. To avoid confusion, we termed the bovine stifle joint as ‘knee’ for the following paragraphs. All the bovine stifle joint specimens were purchased from a local abattoir (Friesen Meat Processing Inc, Warman, SK, Canada), and they were thawed at least 24 hours before the MRI scans and scanned at room temperature. All data were acquired on a 3 Tesla MRI system (MAGNETOM PrismaFit, VE11C, Healthineers, Erlangen, Germany), using the novel FUSE sequence which allows for different morphological imaging mechanisms and various quantitative mappings. For data acquisition, a flexible 18-channel receiver-only body array coil combined with the built-in spine coil was used to accommodate the larger size of bovine stifle joints (as compared to human knees). Table 3.1 outlines all the scan parameters used for both morphologic and quantitative imaging. Different long T2 suppression techniques were used to create multiple morphological images (contrasts) for the whole knee of all specimens. For quantitative measurements of the meniscus, the menisci were manually segmented following a slice-by-slice method (MeVisLab, MeVis Medical Solutions AG, Bremen, Germany). With the segmented masks, all the quantitative maps for the menisci were produced using in-house software (MATLAB, MathWorks, Natick, MA, USA).

Table 3.1. Scan parameters for the morphological and quantitative imaging in the knee joint.

Experiments	Trajectory	RF*	FOV (mm)	Matrix	In-Plane Spiral-Interleaves	Cones	TE (ms)	TR (ms)	BWP (Hz)	Flip Angle** (°)	Slice Thickness (mm)	MT Pulse	
Fat Saturation UTE	3D Spiral	RP	260	256 ³	64	128	0.06	52	510	7	1.0	N/A	
Dual-Echo UTE	3D Spiral	RP	260	256 ³	64	128	0.06, 4.10	52	510	7	1.0	N/A	
MT-Off UTE	3D Spiral	RHSP	260	256 ³	64	128	0.04	34	510	7	1.0	N/A	
MT-On UTE	3D Spiral	RHSP	260	256 ³	64	128	0.04	34	510	7	1.0	Flip angle	426°
												Frequency offset	433 Hz
												Duration	10.24 ms
UTE-B1 Mapping (Dual-Angle)	2D Spiral	RHSP	260	64 ²	32	N/A	0.16	6000	590	60, 120	5.0	N/A	
UTE-T1 Mapping (Variable Flip Angle)	3D Spiral	RHSP	260	256 ³	64	128	0.04	15	510	30, 5, 10, 20	1.0	N/A	
UTE-QMT Mapping (2 Flip Angles × 5 Frequency Offsets)	3D Spiral	RHSP	260	256 ³	64	128	0.04	34	510	7	1.0	Flip angle	142, 426°
												Frequency offset	433, 1087, 2732, 6862, 17235 Hz
												Duration	10.24 ms
UTE-T2* Mapping (Variable TE Angle)	3D Spiral	RHSP	260	256 ³	64	128	0.06, 2.46, 4.10, 8.10, 12.10, 16.10, 32.00	52	510	7	1.0	N/A	

*RP – Rectangular Pulse; RHSP – Regular Half-Sinc Pulse.

**For RHSP, Flip Angle is set for per half-Sinc Pulse.

3.2.2. FUSE Sequence

A flexible UTE sequence, FUSE, was used for the MRI scans, allowing for different morphological imaging mechanisms and various quantitative mappings. The FUSE sequence was developed using a manufacturer's platform (IDEA, Siemens Healthineers, Erlangen, Germany). This sequence included multiple long-T2 suppression approaches, i.e., fat-saturation, dual-echo subtraction, and magnetization transfer (MT) saturation, for isolating the signal from the various knee joint tissues. Quantitative imaging functionalities were also enabled in the UTE sequence for quantifying the short-T2 tissues in the knee joint, including the B1, T1, T2*, and quantitative magnetization transfer (QMT) mapping. The UTE sequence utilized a rectangular or a half-Sinc pulse with a Spiral-Cones trajectory for both 3D qualitative and quantitative imaging. An in-house script written (MATLAB, MathWorks, Natick, MA, USA) to perform all UTE reconstruction offline. The reconstruction program adopted the gridding algorithm and was improved with the off-resonance correction algorithm (25,26,123). More technical details regarding the methods of morphological and quantitative imaging will be elaborated on in the following sections.

3.2.3. Morphological Imaging

The multi-contrast capability of the FUSE sequence was used for exploring and evaluating the morphological imaging methods and for isolating the contrast from the various knee joint tissues. The sequence includes three long-T2 suppression approaches, i.e., fat saturation, dual-echo subtraction, and off-resonance saturation. The fat saturation method was implemented with a Gaussian pulse and was placed before the RF excitation for every acquisition cycle in the pulse sequence. The employed dual-echo subtraction method used two separate scans set with an ultrashort and a slightly longer TE individually (i.e., 0.06 and 4.10 ms). We applied a linear-rescaling to the first echo or an exponential-rescaling to the second echo before the subtraction to produce different contrast types (70). The off-resonance saturation method involved two steps-i.e., the MT pulse saturation and MT contrast enhancement. The first step utilized a Gaussian off-resonance pulse with the flip angle and frequency offset fully adjustable (using a flip angle of 426° and a frequency offset of 433 Hz). The second step enhanced the MT contrast by subtracting the scan with the MT pulse from the one without the MT pulse. Additionally, the magnetization transfer ratio (MTR) image was derived by dividing this MT difference image by the MT-off image (Eq. 1.9).

3.2.4. Quantitative Imaging

With the FUSE sequence, four quantitative imaging methods were applied, including B1 mapping, T1 mapping, QMT mapping, and T2* mapping, to conduct a comprehensive quantitative assessment of the meniscus, which will be elaborated on below.

3.2.4.1. B1 Mapping

The B1 field inhomogeneity was estimated by the double-angle (DA) method voxel-wise and accounted for in the flip angle correction of the following T1 and QMT mappings (183–185). The DA method required two sets of UTE images set with different flip angles, α_1 and α_2 . While keeping other parameters identical for the UTE images, I_1 and I_2 , we forced the time-of-repetition (TR) to be sufficiently long ($TR \geq 5T_1$) and constrained $\alpha_2 = 2\alpha_1$ to estimate α_1 through the following relation,

$$\frac{I_1}{I_2} = \frac{A_0 * \left[\frac{1 - e^{-\frac{TR}{T_1}}}{1 - e^{-\frac{TR}{T_1}} * \cos(\alpha_1)} \right] * \sin(\alpha_1)}{A_0 * \left[\frac{1 - e^{-\frac{TR}{T_1}}}{1 - e^{-\frac{TR}{T_1}} * \cos(\alpha_2)} \right] * \sin(\alpha_2)} \quad [3.1]$$

$$\approx \frac{A_0 \sin(\alpha_1)}{A_0 \sin(\alpha_2)} = \frac{\sin(\alpha_1)}{2 \sin(\alpha_1) \cos(\alpha_1)} = \frac{1}{2 \cos(\alpha_1)}$$

where I_1 and I_2 are the two images; α_1 and α_2 are the two flip angles; A_0 is a constant parameter coupled by the proton density and T2 relaxation decay, and this parameter should be identical for the two acquisitions; the condition $TR \geq 5T_1$ drives the term e^{-TR/T_1} approaching zero; furthermore, the condition $\alpha_2 = 2\alpha_1$ simplifies the equation and gives $\alpha_1 = \cos^{-1}\left(\frac{S_2}{2S_1}\right)$. To retrieve the B1 correction map k , we first adopted a 2D acquisition protocol using a half-Sinc pulse excitation and spiral trajectory to acquire a coarse matrix of 64×64 (Table 3.1). Then, using the B-Spline approach, we interpolated the coarse matrix to a finer grid required by the correction in the T1 and QMT mappings. At last, we used the two interpolated B1 scans to measure actual flip angle α_1 using Eq. [3.1] and retrieved the B1 correction map k with the prescribed flip angle α_{1p} : $k = \alpha_1/\alpha_{1p}$.

3.2.4.2. *T1 Mapping*

The variable-flip-angle (VFA) method was implemented to estimate the longitudinal relaxation time T_1 , voxel-wise (186). We acquired data at different flip angles (i.e., 5° , 10° , 20° , 30°), using 3D isotropic UTE acquisitions with a half-Sinc excitation pulse and spiral-cone trajectory (Table 3.1). The data were then fitted using the following equation to estimate the relaxation time, T_1 , in a voxel-wise manner,

$$S = S_0 * \left[\frac{1 - e^{-\frac{TR}{T_1}}}{1 - e^{-\frac{TR}{T_1}} * \cos(a)} \right] * \sin(a) \quad [3.2]$$

Where S is the acquired data; S_0 is the initial signal intensity; TR and a are the time-of-repetition and flip angle of the scan protocols, respectively. In this work, we converted the fitting to a nonlinear least-squares minimization problem and solved it using the Levenberg-Marquardt algorithm. For better accuracy and efficiency, we initialized the parameter guesses (i.e., T_1 and S_0) with the estimating outcomes from the direct linearization of the Eq. [3.2] before the nonlinear fitting (187). As an option, we utilized the B1 correction map (k) described above to multiply with each nominal flip angle of the excitation pulse, voxel-wise, to address the potential B1 field inhomogeneity that might affect the accuracy of the VFA- T_1 mapping.

3.2.4.3. *Quantitative magnetization transfer (QMT) Mapping*

The two-pool model was adopted for quantifying the magnetization transfer effect between the bound and the free pool, voxel-wise (78). For capturing the magnetization transfer contrast, the sequence transmitted a Gaussian off-resonance pulse (also known as MT pulse) to irradiate the bound pool and then used a 3D half-Sinc excitation coupled with a Spiral-Cones trajectory to achieve the isotropic UTE scans (Table 3.1). The adopted 3D half-Sinc excitation is for a better slab selectivity, and the selected Spiral-Cones trajectory is for higher k-space-filling efficiency. This combination has also not been adopted by other studies. The Gaussian off-resonance pulse was repeated in every TR-cycle to approximate a continuous-wave bound pool irradiation (90). By systematically varying the MT pulse's power (i.e., the pulse's flip angle, not to be confused with the standard definition of flip angle) and frequency offset (Table 3.1), we quantified the magnetization transfer effect depicted by the various UTE scans into a Z-spectrum (90).

The Z-spectrum was modelled using the following mathematical description in a voxel-wise manner (90),

$$S = gM_0^a * \left[\frac{R_b \left(\frac{RM_0^a f}{R_a(1-f)} \right) + R_{RF_b} + R_b + RM_0^a}{\left(\frac{RM_0^a f}{R_a(1-f)} \right) (R_b + R_{RF_b}) + \left[1 + \left(\frac{\omega}{2\pi\Delta} \right)^2 \left(\frac{1}{R_a T_2^a} \right) \right] (R_{RF_b} + R_b + RM_0^a)} \right] \quad [3.3]$$

Where S is the acquired UTE-QMT image; a and b in all superscripts and subscripts denote the free and bound pools, respectively; ω is the amplitude of the MT pulse's saturating field; Δ is the MT pulse's off-resonance frequency offset; g is a system's signal-scaling constant; M_0^a is the initial magnetization in the free pool (before the MT saturation); f is the fraction of protons in the bound pool: that is, $f = M_0^b / (M_0^a + M_0^b)$ where M_0^b is the initial magnetization in the bound pool; R is the magnetization exchanging rate between the two pools; $R_a = 1/T_1^a$ and $R_b = 1/T_1^b$ are the longitudinal relaxation rates of the free and bound pools, respectively; T_1^a is the longitudinal relaxation time of the free pool; T_1^b is the longitudinal relaxation time of the bound pool; T_2^a is the transverse relaxation time of the free pool; and R_{RF_b} is the longitudinal magnetization loss rate of the bound pool because of the MT saturation or also known as the bound pool's RF absorption rate.

For specifying the bound pool's RF absorption rate, R_{RF_b} , both the Gaussian and Super-Lorentzian lineshapes were adopted using the following equations (172),

1) Gaussian:

$$R_{RF_b} = \omega^2 \sqrt{\frac{\pi}{2}} T_2^b \left(e^{-\frac{(-2\pi\Delta T_2^b)^2}{2}} \right) \quad [3.4]$$

Where T_2^b is the bound pool's transverse relaxation time; the other symbols share the same meaning as described in Eq. [3.3] above.

2) Super-Lorentzian:

$$R_{RF_b} = \omega^2 \pi \left[\int_0^{\frac{\pi}{2}} d\theta \sin \theta \sqrt{\frac{2}{\pi}} \frac{T_2^b}{|3 \cos^2 \theta - 1|} e^{-2 \left(\frac{2\pi\Delta T_2^b}{|3 \cos^2 \theta - 1|} \right)^2} \right] \quad [3.5]$$

Where θ represents the angle between the external magnetic field and orientation of molecular dipoles (172); the other symbols share the same meaning as described in equations [3.3] and [3.4] above. Both lineshape simulation approaches (Eqs. [3.4] and [3.5]) were investigated for deriving

T_2^b as both methods have been compared constantly for QMT studies without using UTE sequences (172,188). Supplying the UTE scans varied with ω and Δ , we were able to use Eqs. [3.3]-[3.5] to estimate the physical properties of the two pools and other parameters, including the free pool's longitudinal relaxation time T_1^a , free pool's transverse relaxation time T_2^a , bound pool's longitudinal relaxation time T_1^b , bound pool's transverse relaxation time T_2^b , bound pool's proton fraction f , magnetization exchanging rate between the two pools R , system's signal-scaling constant g , and free pool's initial magnetization M_0^a .

Since the sequence uses the repeated Gaussian MT pulse to approximate the continuous-wave off-resonance saturation to the bound pool, we specified the MT pulse's B1 amplitude ω with the continuous-wave-power-equivalent (CWPE) angular frequency ω_{CWPE} , using the following formula,

$$\omega = \omega_{CWPE} = \frac{\theta_{MT}\pi}{180^\circ p_1} \sqrt{\frac{p_2}{TR\tau}} \quad [3.6]$$

Where θ_{MT} is the MT pulse's nominal (prescribed) flip angle; τ is the MT pulse's duration; TR denotes the time-of-repetition; and $p_1(= 0.482)$ and $p_2(= 0.344)$ represent the geometric factors for simulating the Gaussian MT pulse to its rectangular pulse equivalent (90,172,189). As the model's inputs, the MT pulse's parameters, θ_{MT} , τ , and Δ were all directly amendable in the scan protocols.

We adopted a simplification procedure before the voxel-wise fitting of Eq. [3.3] (90,172). For simplifying the fitting process, six intermediate parameters, gM_0^a , R_b , RM_0^a , R_{RF_b} , $\frac{1}{R_a T_2^a}$, and $\frac{f}{R_a(1-f)}$, were used first to determine the model uniquely. Also, to improve the stability of the fitting, we pre-determined gM_0^a and R_b as constant parameters: we assigned the image without MT saturation to be gM_0^a and a fixed parameter 1 s to T_1^b (i.e., 1 s^{-1} to R_b since $R_b = 1/T_1^b$) as a common practice (172). Furthermore, we utilized the approximation defined in Eq. [3.4] or [3.5] to replace the estimation of R_{RF_b} and directly retrieved T_2^b from Eq. [3.3]. These simplification steps reduced the number of the intermediate parameters for estimation from six to four-i.e., RM_0^a , T_2^b , $\frac{1}{R_a T_2^a}$, and $\frac{f}{R_a(1-f)}$.

We first used the nonlinear least-squares method to estimate the simplified intermediate parameters (four) and then derived the final parameters from them, voxel-wise. The trust-region-reflective algorithm was used to solve the nonlinear least-squares minimization and estimate the intermediate parameters in a voxel-wise manner (190,191,191). To calculate the final parameters (T_1^a , T_2^a and f), we first decoupled R_a from the estimated intermediate parameters ($\frac{1}{R_a T_2^a}$ and $\frac{f}{R_a(1-f)}$) by applying the following equation (78,90),

$$R_a = \frac{R_{aobs}}{1 + \frac{\frac{RM_0^a f}{R_a(1-f)}(R_b - R_{aobs})}{R_b - R_{aobs} + RM_0^a}} \quad [3.7]$$

Where $R_{aobs} = 1/T_{1obs}$ is the longitudinal relaxation rate experimentally measured by separate VFA-T1 measurement; and other parameters are as described in Eq. [3.3]. Also, a secondary parameter RM_0^b was derived by the intermediate parameter RM_0^a through the following relation,

$$RM_0^b = kf = \frac{RM_0^a f}{1-f} \quad [3.8]$$

where RM_0^b describes the rate of the longitudinal magnetization exchange from the free pool to the bound pool; it also can be represented as kf according to the previous work (188,192). In the end, five final parameters were obtained as quantitative maps through the direct estimation and secondary derivation, including T_1^a , T_2^a , T_2^b , f , and kf .

As an option, we also utilized the B1 correction map (k) described above to multiply with each MT pulse's nominal flip angle, voxel-wise, to address the potential B1 field inhomogeneity that might affect the accuracy of the QMT mapping.

Last, four fitting approaches were investigated for the QMT mapping, including the uses of the Gaussian lineshape without B1 correction, Super-Lorentzian lineshape without B1 correction, Gaussian lineshape with B1 correction, and Super-Lorentzian lineshape with B1 correction.

3.2.4.4. T_2^* Mapping

The variable-time-of-echo (VTE) method was employed to estimate the transverse relaxation time T_2^* . We acquired data with a series of TEs, using 3D isotropic UTE acquisitions with a rectangular excitation pulse and spiral-cone trajectory (Table 3.1). The acquired data S was described using

the following mono-exponential model to provide an estimation for the bulk transverse relaxation time, $T2^*$, in a voxel-wise manner,

$$S = S_0 * e^{-\frac{TE}{T2^*}} \quad [3.9]$$

Where S is acquired signal; TE is the time-of-echo of the pulse sequence; and S_0 is the initial signal intensity; $T2^*$ is the bulk transverse relaxation time. In this mono-exponential model, we fit the data with a nonlinear least-squares method and used the Levenberg-Marquardt algorithm to search for the optimal $T2^*$ estimate. Also, we used the estimations (i.e., $T2^*$ and S_0) derived by the linearization of Eq. [3.9] to serve as the initial guesses for the nonlinear fitting. Compared to the expression Eq. [3.9], we also implemented a bi-exponential decay model that considered short and long T2 components residing in the tissue for a more sophisticated fitting in a voxel-wise manner,

$$S_N = \frac{M}{M_0^s + M_0^l} = Fs * e^{-\frac{TE}{T2_s^*}} + (1 - Fs) * e^{-\frac{TE}{T2_l^*}} \quad [3.10]$$

Where s and l in all superscripts and subscripts represent the short and the long T2 components, respectively; S_N stands for the observed signal normalized by the measured VTE magnetization (images) M , short T2 component's initial magnetization M_0^s , and long-T2 component's initial magnetization M_0^l ; $Fs = M_0^s / (M_0^s + M_0^l)$ is the fraction of the short-T2 component, which makes $Fl (= 1 - Fs)$ the fraction of the long-T2 component (i.e., $M_0^l / [M_0^s + M_0^l]$); $T2_s^*$ and $T2_l^*$ denote the T2* values for the short and the long T2 components, respectively; and TE is also the time-of-echo. The normalization to S_N requires extra knowledge of the total initial magnetization $M_0^s + M_0^l$, so we approximated $M_0^s + M_0^l$ with our ultrashort scan (e.g., $TE = 60 \mu s$) where all the magnetization components barely started decaying (105). With the model defined in Eq. [3.10], Fs , $T2_s^*$, and $T2_l^*$ were estimated by adjusting TE and providing S_N . To solve this bi-exponential model, we adopted the nonlinear least-squares method and accomplished the fitting with the trust-region-reflective algorithm.

3.2.5. Data Evaluation

We introduced the following index to evaluate the overall goodness of the voxel-wise nonlinear fit for the T1, QMT, and T2* mapping,

$$GoF = 1 - \frac{\|xref - x\|}{\|xref - mean(xref)\|} \quad [3.11]$$

Where GoF stands for the goodness-of-fit; $\|$ denotes the 2-norm, the Euclidean distance; x_{ref} is the reference data array from acquisition, and each element represents the average image intensity within the meniscus region; and x is the test data array from fitting, and each element represents the average image intensity within the meniscus region. GoF ranges from $-\infty$ to 1, corresponding to a poor fit to a perfect fit.

We removed the outliers in the statistical distribution plots of the quantitative estimations to retrieve reasonable means and standard deviations (Std. Dev.). We adopted the method of the interquartile range (IQR), trimming the distribution plots to a range of $[Q1 - 1.5 * IQR, Q3 + 1.5 * IQR]$ where $IQR = Q3 - Q1$, $Q1$ is the 25th percentile, and $Q3$ is the 75th percentile.

3.3. Results

3.3.1. Qualitative Imaging

Our novel FUSE sequence was able to create morphologic images that isolated the contrasts from the various knee joint tissues. As a reference, the image contrast acquired with a long TE (4.1 ms) returned signal voids or low image intensity for the short-T2 tissues, including the cortical bone, tendon, and meniscus, while retaining high image intensity for the long-T2 tissues, i.e., the bone marrow, fat, muscle, and cartilage (Figures 3.1.a.1 and b.1). The ultrashort TE scan acquired stronger signals from the cortical bone, tendon, and meniscus regions than the long TE one (Figures 3.1.a.2 and b.2). Also, the ultrashort TE scan enhanced the long-T2 tissues with much higher signal intensity than the short-T2 tissues: the cortical bone, lying between the marrow and muscle, presents a dimmed contrast (Figure 3.1.a.2). The dual-echo subtraction method heavily reduced the signal for the muscle and moderately suppressed the intensity for the marrow and fat (Figures 3.1.a.3 and b.3). Even though this subtraction enhances the tendon contrast, it does not create an explicit contrast between the cortical bone and marrow (Figure 3.1.a.3). The latter case also applies to the menisci and their surrounding tissue (Figures 3.1.b.3). Compared to the traditional dual-echo subtraction method ($C2-C1$), the linear rescaling of the first ultrashort echo resulted in improved suppression for nearly all long-T2 tissues in the subtracted result ($0.45 * C2 - C1$, Figures 3.1.a.4 and b.4). Comparatively, the exponentially-rescaled dual-echo subtraction approach better suppressed the long-T2 tissue signals and depicted the short-T2 details with a more distinct and smoother contrast ($C2 - C1^{2.0}$, Figures 3.1.a.5 and b.5). The ultrashort-TE scan with FS (FS-UTE) selectively

reduced the intensity for the fat and marrow yet exhibits a clear contrast for the meniscus and tendon (Figures 3.1.a.6 and b.6). However, the FS-UTE scan did not preserve a sufficient signal for the cortical bone and was unable to suppress the muscle signal effectively (Figure 3.1.a.6). The subtracted MT contrast demonstrates a similar contrast pattern with the FS-UTE result (Figures 3.1.a.7 and b.7). Compared to the subtracted MT contrast, the MTR contrast presents a bright delineation of the cortical bone (Figures 3.1.a.8 and b.8).

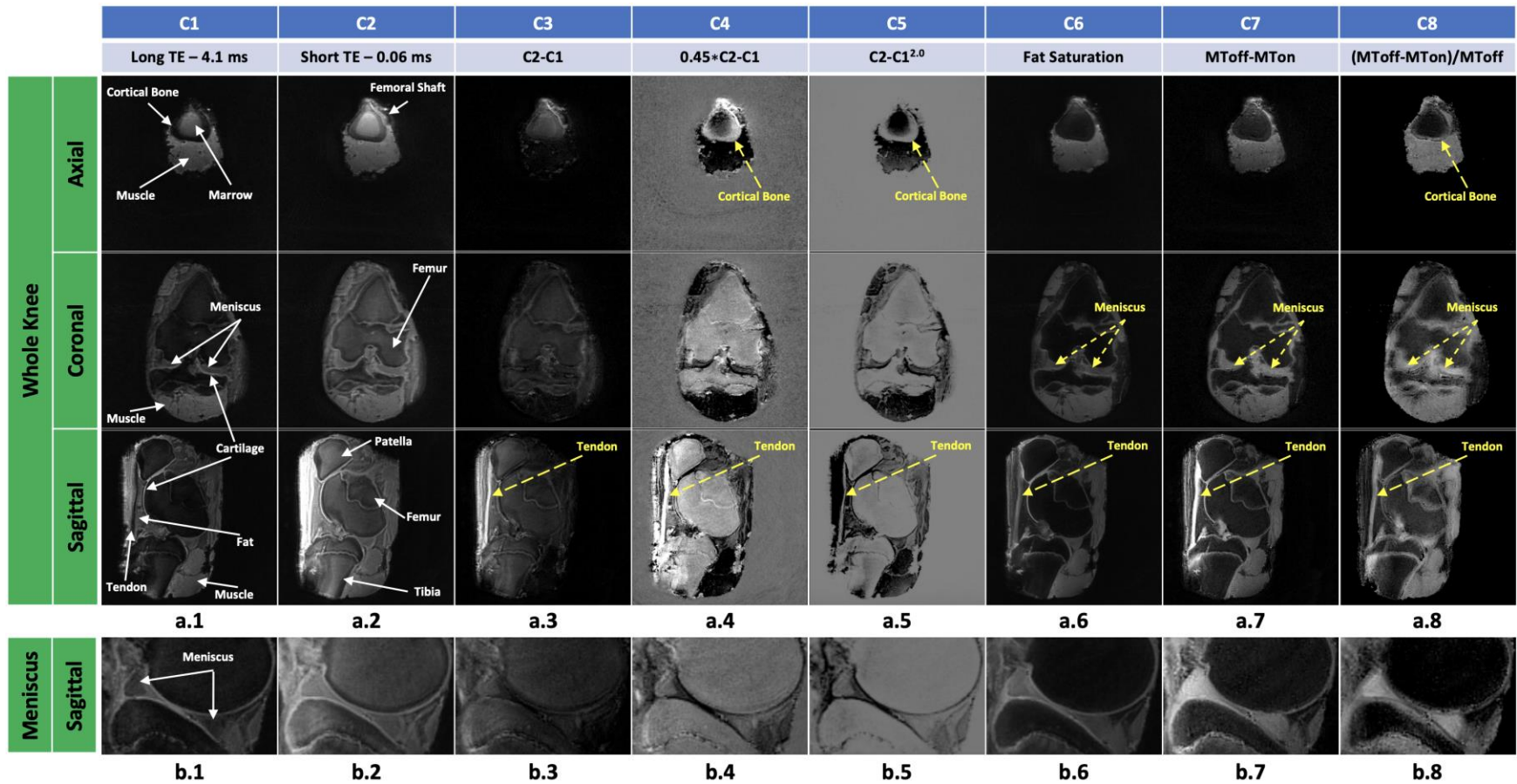


Figure 3.1. Multiple morphological contrasts generated by the FUSE sequence.

The figure shows an orthogonal view for the whole knee (a.1-8) and a sagittal enlargement for the meniscus (b.1-8). C1 (a.1 and b.1) is a long-TE reference scan representing the traditional MR technique where long-T2 tissues have a visible contrast and short-T2 tissues present a weak or voided signal. C2 (a.2 and b.2) is a UTE scan where both the long-T2 and short-T2 tissues demonstrate a visible contrast. For the various contrasts enabled by different long-T2 suppression techniques, there includes a dual-echo subtraction (a.3 and b.3), linearly-rescaled dual-echo subtraction (a.4 and b.4), exponentially-rescaled dual-echo subtraction (a.5 and b.5), fat-saturation UTE scan (a.6 and b.6), MT contrast (a.7 and b.7), and MTR contrast (a.8 and b.8). (The whole knee is presented with Specimen-S06, and the meniscus is presented with Specimen-S03)

3.3.2. T1 Mapping

Estimated by the VFA-T1 mapping technique using UTE (UTE-VFA-T1), the average T1 value of the meniscus across all specimens is 475.96 ± 56.57 ms with the B1 correction or 670.37 ± 90.53 ms without the B1 correction (Table 3.2). Overall, the B1 map does not exhibit drastic variation over the meniscus region (Figures 3.2.a). However, when accounting for the B1 map to calibrate the flip angles (defined in Eq. [3.1]), the T1 map presents different estimations (Figures 3.2.b.1 and b.2).

The T1 estimations corrected by the B1 map overall demonstrate a higher average GoF of 0.88 ± 0.01 for all the specimens than the uncorrected T1 estimations, although the latter case still returns only a slightly lower average GoF of 0.87 ± 0.01 (Table 3.2). The B1-corrected T1 maps have a lower inter-specimen mean of 475.96 ± 56.57 ms than the uncorrected T1 maps (670.37 ± 90.53 ms) (Table 3.2). The UTE sequence was able to contribute clear delineation and ample signal for the meniscus (Figure 3.3.a), and the data obtained by UTE scans can be well fitted by the VFA-T1 model (Eq. [3.2]) (Figure 3.3.b). Across all specimens, the distribution plots of the T1 estimations appear heterogeneous, spanning over a broad range (Figures 3.4.a and b). The inter-similarity and inter-variability between the specimens suggest that S03-S06 are more similar than S01 or S02 (Figures 3.4.a and b). The T1 map distributions for all specimens were smoothed and left-shifted due to the B1 correction (Figures 3.4.a and b).

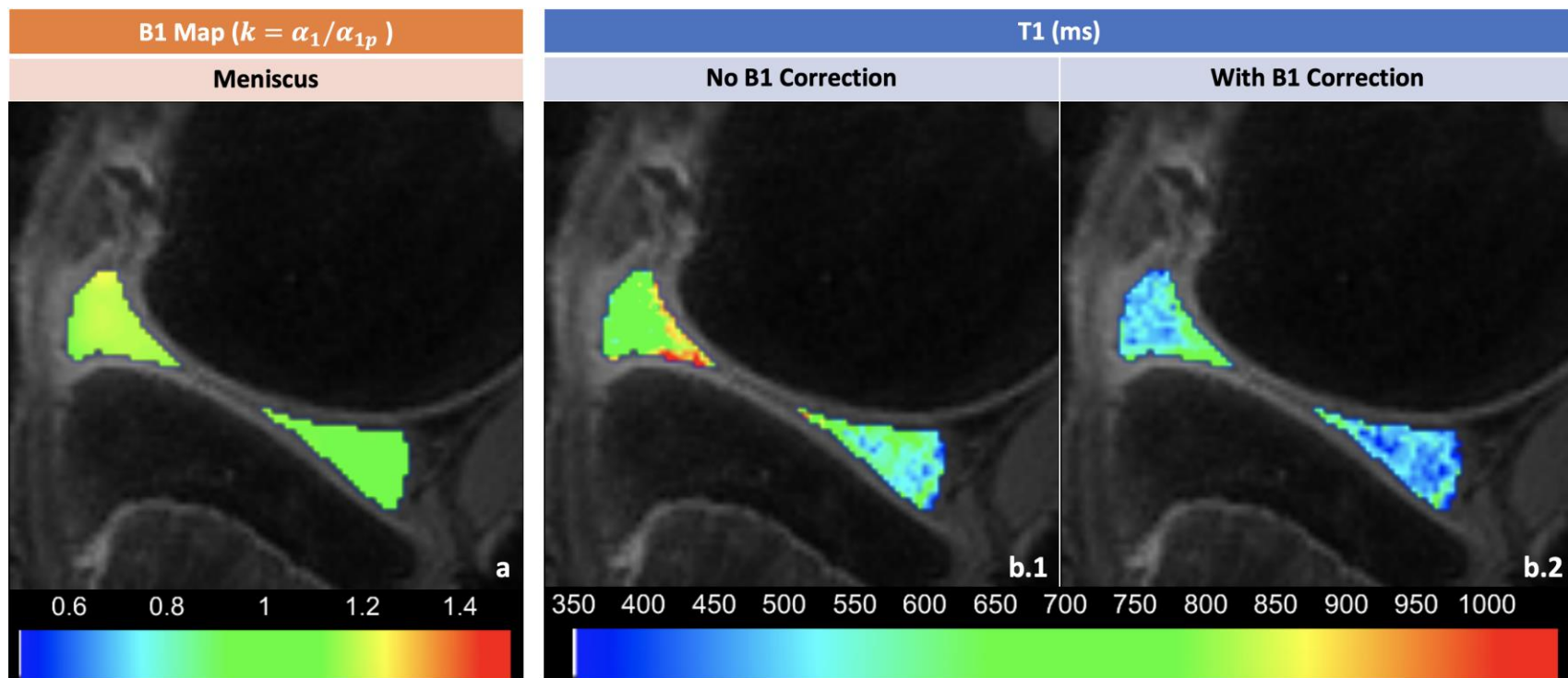


Figure 3.2. B1 map and T1 maps of the menisci.

The meniscus's B1 map overlaid on a fat-saturation UTE scan (**a**); the meniscus's T1 map without B1 correction (**b.1**); and the meniscus's T1 map corrected by the B1 map (**b.2**). (Illustrated with Specimen-S03).

Table 3.2. Statistic of the T1 maps without and with B1 correction for the intra- and inter-specimen in both menisci.

Specimen	T1 (ms)			T1 (ms) Corrected with B1			B1 Correction Factor	
	GoF	Mean	Std.Dev.	GoF	Mean	Std.Dev.	Mean	Std.Dev.
S01	0.90	504.21	73.08	0.90	382.07	51.47	1.14	0.02
S02	0.87	778.96	138.79	0.88	548.59	89.77	1.18	0.03
S03	0.86	682.97	150.30	0.87	514.22	96.90	1.15	0.05
S04	0.87	690.37	123.12	0.88	475.47	80.90	1.20	0.03
S05	0.87	664.06	114.30	0.88	480.09	76.66	1.17	0.03
S06	0.87	701.63	149.52	0.88	455.30	84.82	1.23	0.04
Average (n=6)	0.87	670.37		0.88	475.96		1.18	
Inter-Specimen Std.Dev.	0.01	90.54		0.01	56.57		0.03	

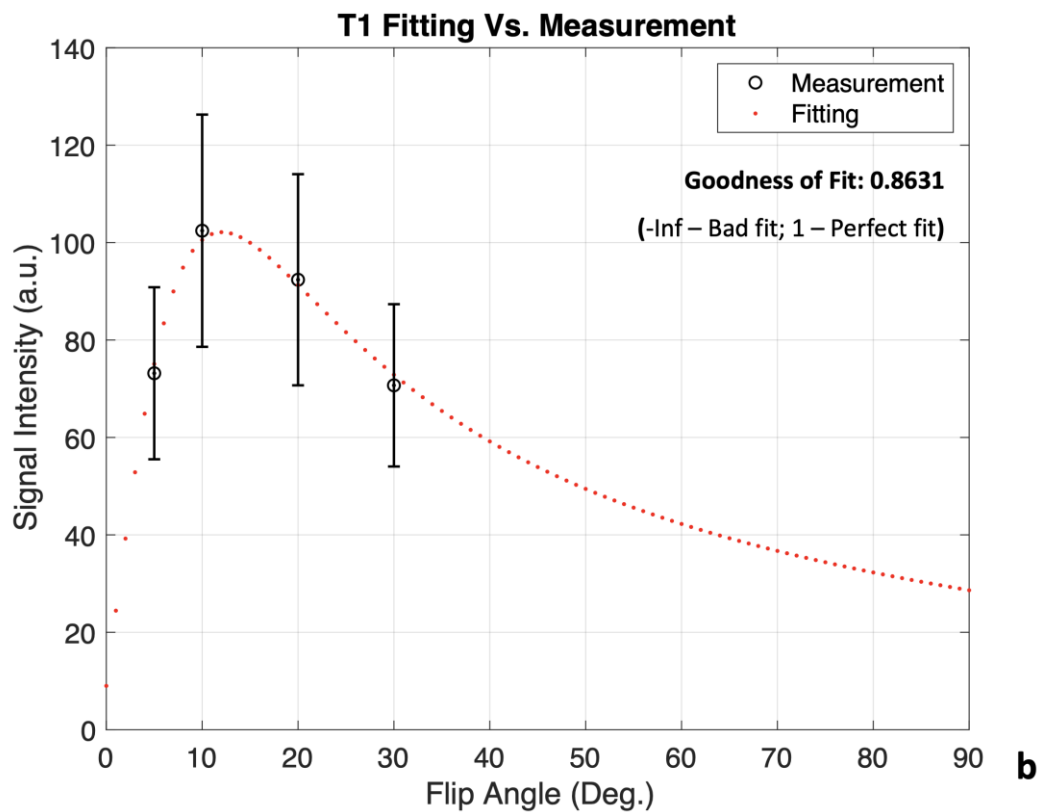
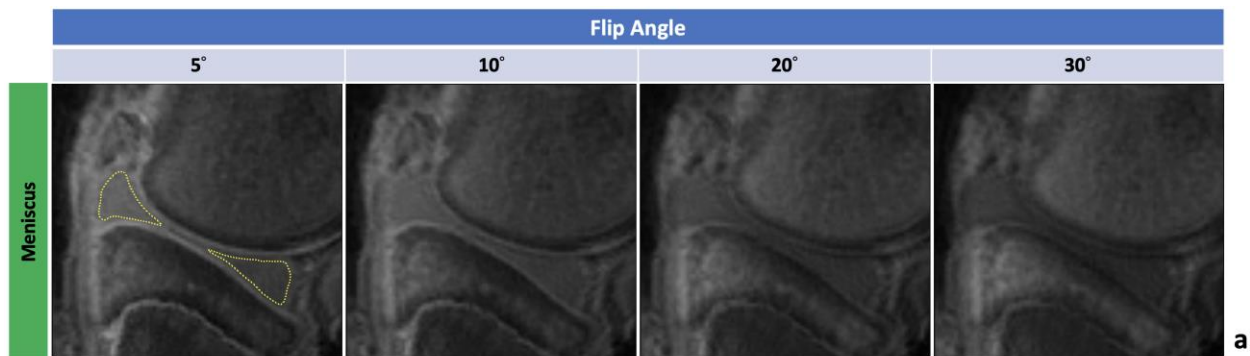


Figure 3.3. Signal measurements and T1 fitting of the menisci.

3D Half-Sinc Spiral-Cone UTE scans in the knee acquired with a variable flip angle (VFA) for T1 mapping (a). The yellow dotted line in (a) delineates the menisci on this exemplary slice. The T1 fitting result as opposed to VFA measurements for the menisci (b). The error bars in (b) represent the standard deviation for both entire menisci. (Illustrated with Specimen-S03).

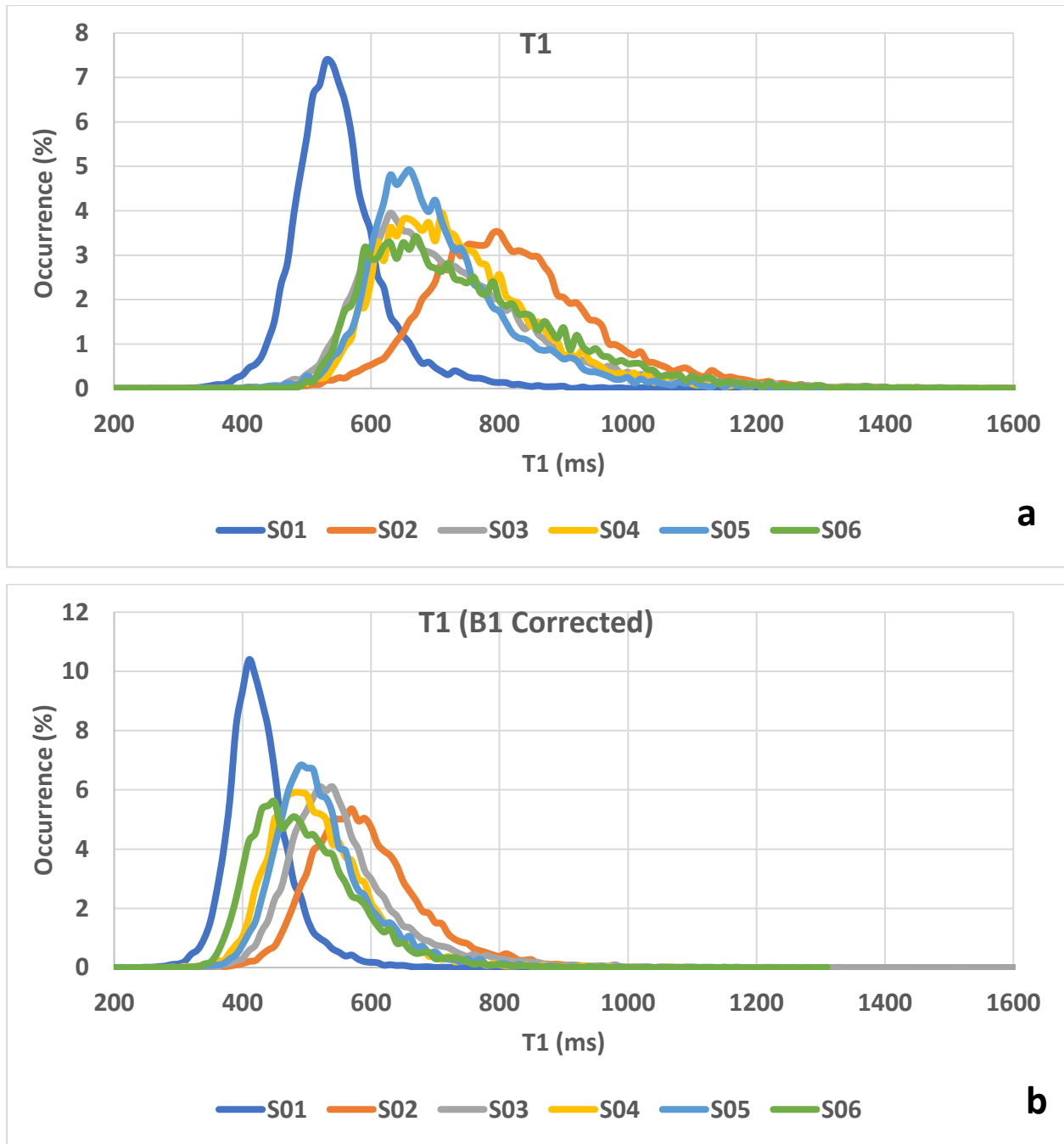


Figure 3.4. Distribution plots of the T1 maps for all meniscus specimens (S01-S06). Distribution plots of the T1 maps without (a) and with (b) the B1 correction for all meniscus specimens (S01-S06).

3.3.3. QMT Mapping

The QMT parameters of the meniscus across all specimens appear to vary with the selection of the fitting approach, e.g., the R_{RF_b} lineshape and B1 correction (Table 3.3). For both the Gaussian and the Super-Lorentzian lineshape, the B1 correction can create large relative average percentage deviations (i.e., $[(\text{Result}_{\text{B1}} - \text{Result}_{\text{noB1}})/\text{Result}_{\text{noB1}}] * 100\%$) across all specimens T_1^a , -34.2% (Gaussian) and -34.8% (Super-Lorentzian), and kf , 27.0% and 36.2%, while small relative T_2^b , 0.4% and -0.3%, f , -1.5% and -1.9%, and T_2^a , -6.0% and -6.8%, respectively. Likewise, regardless of the B1 correction, the lineshape factor can lead to comparatively large relative percentage deviations (i.e., $[(\text{Result}_{\text{Super-Lorentzian}} - \text{Result}_{\text{Gaussian}})/\text{Result}_{\text{Gaussian}}] * 100\%$) across all specimens T_2^b , -66.3% (with B1) and -66.5% (without B1), T_2^a , 21.2% and 20.1%, and f , 14.2% and 13.7%, while comparatively small relative T_1^a , -2.9% and -3.9%, and kf , 2.1% and 9.4%, respectively. The deviations were calculated using the averages of all specimens and derived for the non-B1 correction and B1 correction, respectively. The B1 correction has notable impact on the T_1^a maps, in contrast to the uncorrected results (Figure 3.5). Also T_2^b maps derived from the Gaussian lineshape are different from the Super-Lorentzian lineshape (Figure 3.5). However, the other parameters appear consistent for both lineshapes and regardless of the B1 correction (Figure 3.5). All four approaches, including two lineshapes paired with the B1 correction (on and off), create sufficiently good fittings supported by four GoF averages over 0.9 for all specimens (Table 3.3). The adjustable MT preparation pulses were able to suppress the meniscus signal at various levels (Figure 3.6.a). However, the UTE acquisitions can still guarantee sufficient signals obtained from the meniscus's short-T2 components after the MT irradiation. The Gaussian and the Super-Lorentzian lineshapes resulted in different fitting curves (Figures 3.6.b and c). Each QMT map's inter-specimen distributions manifest a close similarity in their shapes (Figure 3.7). However, the distribution plots of the T_2^b maps demonstrate more consistency between all specimens than the rest QMT parameters (Figure 3.7).

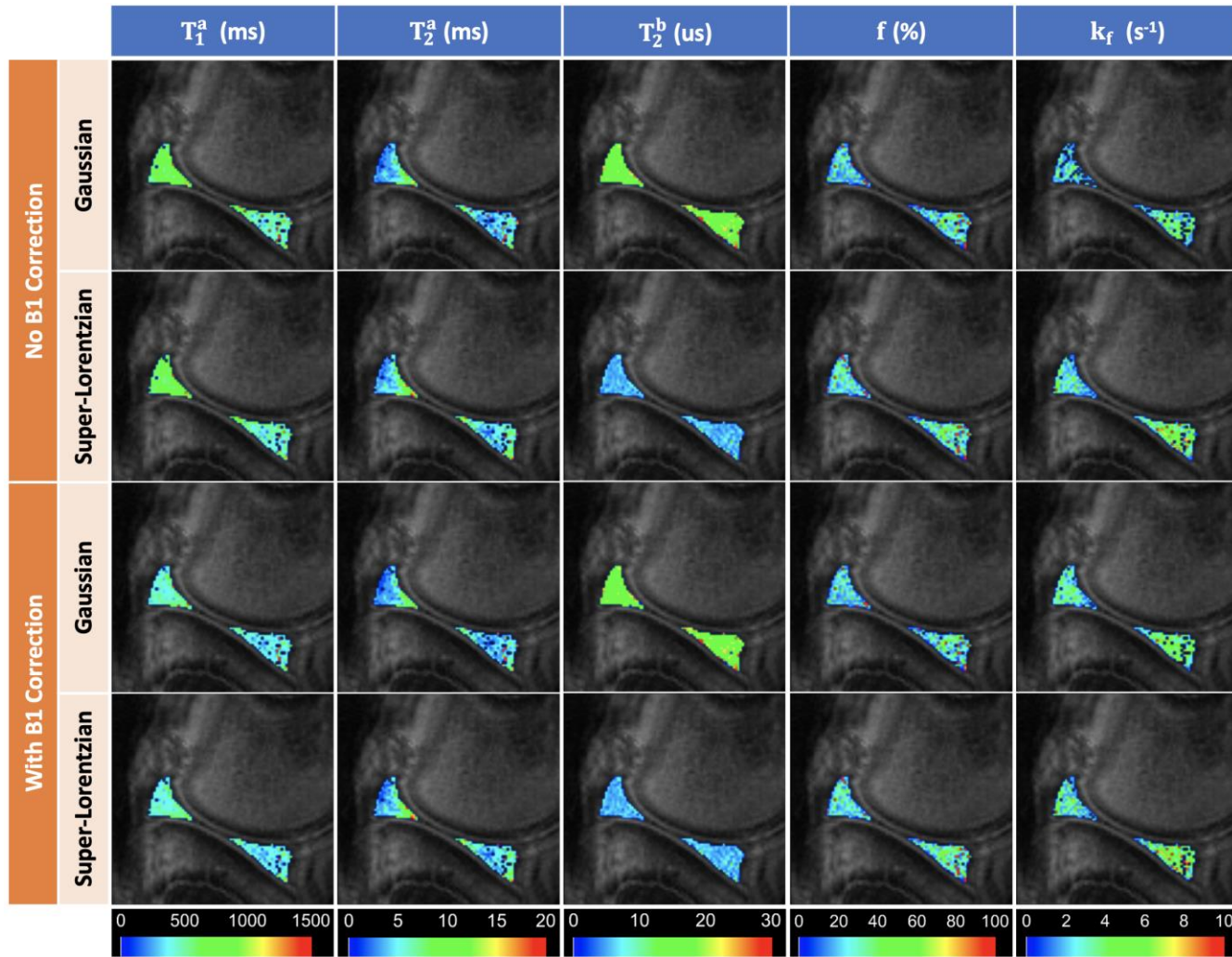
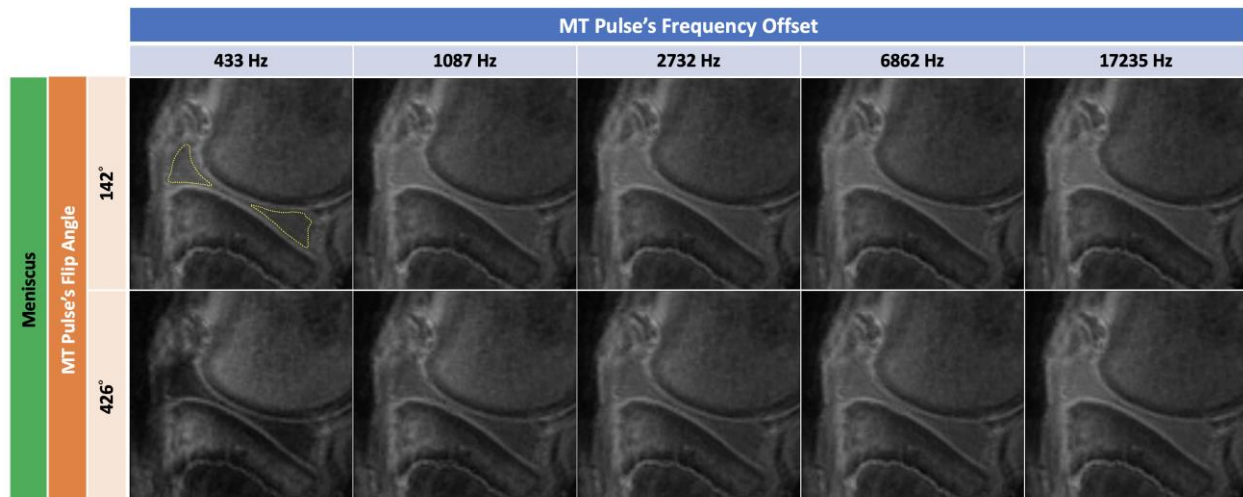


Figure 3.5. QMT maps of the menisci superimposed on an MT-weighted volume.

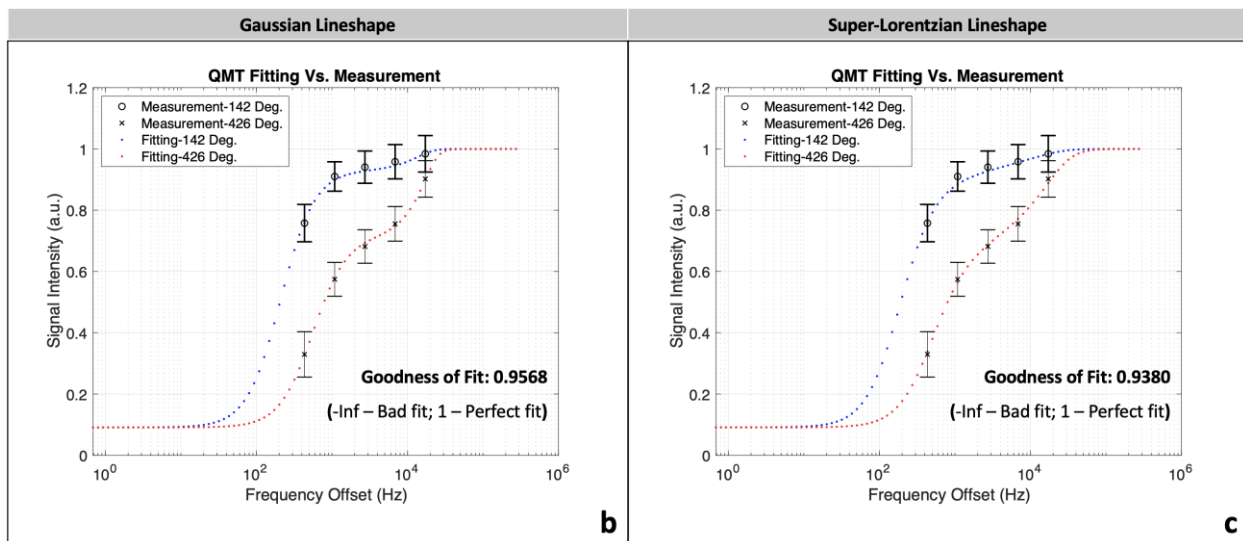
The QMT maps include five parameters, T_1^a , T_2^a , T_2^b , f , and k_f . Each parameter has four observations comprised of two lineshapes coupled with the toggles of B1 correction. (Illustrated with Specimen-S03).

Table 3.3. Descriptive statistics of the QMT maps using two lineshapes and with and without B1 correction for the intra- and inter-specimen in both menisci.

Specimen		S01	S02	S03	S04	S05	S06	Average (n=6)	Inter-Specimen Std.Dev.	
<i>GoF</i>	Gaussian	0.92	0.96	0.96	0.95	0.94	0.94	0.95	0.01	
	Super-Lorentzian	0.91	0.94	0.94	0.93	0.92	0.94	0.93	0.01	
	Gaussian (B1)	0.93	0.95	0.95	0.94	0.94	0.93	0.94	0.01	
	Super-Lorentzian (B1)	0.91	0.94	0.94	0.93	0.92	0.93	0.93	0.01	
T_1^a (ms)	Gaussian	Mean	412.28	721.82	605.90	608.11	584.53	622.90	592.59	100.61
		Std.Dev.	115.69	158.47	178.08	163.44	134.19	220.10		
	Super-Lorentzian	Mean	385.89	712.59	589.00	593.50	566.08	604.65	575.29	106.01
		Std.Dev.	169.37	163.49	174.27	159.67	141.54	212.92		
	Gaussian (B1)	Mean	293.77	475.53	426.88	386.37	398.07	359.25	389.98	61.58
		Std.Dev.	84.42	105.71	108.84	104.12	92.60	116.60		
	Super-Lorentzian (B1)	Mean	262.13	466.83	412.56	374.77	381.74	351.11	374.86	68.12
		Std.Dev.	111.55	105.67	109.35	103.81	98.94	115.36		
T_2^a (ms)	Gaussian	Mean	4.97	9.46	7.33	6.70	6.07	8.57	7.18	1.64
		Std.Dev.	2.56	3.85	3.59	3.01	2.63	4.01		
	Super-Lorentzian	Mean	5.66	11.80	8.74	8.21	7.13	10.69	8.71	2.26
		Std.Dev.	3.43	5.23	4.46	3.88	3.39	5.10		
	Gaussian (B1)	Mean	4.76	9.02	6.91	6.31	5.71	7.81	6.75	1.52
		Std.Dev.	2.54	3.77	3.36	2.93	2.50	3.72		
	Super-Lorentzian (B1)	Mean	5.23	11.09	8.33	7.54	6.68	9.79	8.11	2.12
		Std.Dev.	3.20	4.96	4.32	3.53	3.17	4.81		
T_2^b (us)	Gaussian	Mean	16.10	17.40	17.08	17.37	17.18	17.23	17.06	0.49
		Std.Dev.	2.00	2.13	2.18	2.37	2.57	2.64		
	Super-Lorentzian	Mean	5.40	5.88	5.66	5.95	5.86	5.77	5.75	0.20
		Std.Dev.	1.25	1.25	1.50	1.70	1.81	1.84		
	Gaussian (B1)	Mean	16.17	17.47	17.21	17.41	17.23	17.25	17.12	0.48
		Std.Dev.	2.00	2.13	2.37	2.25	2.59	2.69		
	Super-Lorentzian (B1)	Mean	5.35	5.89	5.66	5.95	5.85	5.73	5.74	0.22
		Std.Dev.	1.42	1.25	1.51	1.74	1.85	1.90		
<i>f</i> (%)	Gaussian	Mean	30.55	21.29	25.38	26.28	25.51	30.18	26.53	3.45
		Std.Dev.	18.28	10.52	14.41	14.54	14.87	20.77		
	Super-Lorentzian	Mean	38.40	23.69	28.41	29.57	30.18	31.60	30.31	4.80
		Std.Dev.	19.92	10.01	14.34	14.60	16.25	18.58		
	Gaussian (B1)	Mean	29.23	21.05	25.19	26.52	25.43	29.44	26.14	3.10
		Std.Dev.	16.13	9.04	13.22	13.23	13.38	17.89		
	Super-Lorentzian (B1)	Mean	36.81	23.68	27.97	29.44	29.19	31.22	29.72	4.299
		Std.Dev.	19.23	9.50	13.30	13.45	14.29	17.25		
<i>kf</i> (1/s)	Gaussian	Mean	2.59	2.47	2.92	3.37	3.06	2.95	2.89	0.33
		Std.Dev.	1.57	1.24	1.58	1.83	1.60	1.76		
	Super-Lorentzian	Mean	2.02	2.49	3.13	3.71	3.08	3.29	2.95	0.60
		Std.Dev.	1.26	1.24	1.77	2.14	1.71	2.01		
	Gaussian (B1)	Mean	3.14	3.10	3.57	4.38	3.75	4.11	3.68	0.51
		Std.Dev.	1.72	1.24	1.74	2.15	1.74	2.22		
	Super-Lorentzian (B1)	Mean	2.91	3.41	3.98	5.00	4.07	4.76	4.02	0.79
		Std.Dev.	1.79	1.39	1.99	2.56	1.99	2.61		



a



b

c

Figure 3.6. Signal measurements and QMT fittings of the menisci.

3D Half-Sinc Spiral-Cone UTE scans in the knee acquired with two MT flip angles and five MT frequency offsets for QMT mapping (a). The yellow dotted line in (a) delineates the menisci on this exemplary slice. The QMT fitting using the Gaussian lineshape versus the QMT measurements for both entire menisci (b). The QMT fitting using the Super-Lorentzian lineshape versus the QMT measurements for both entire menisci (c). The error bars in (b) and (c) represent the standard deviation measured for both entire menisci. The goodness of both fits is close to a perfect fit, 1. The fitting results illustrated here did not use the B1 correction. (Illustrated with Specimen-S03).

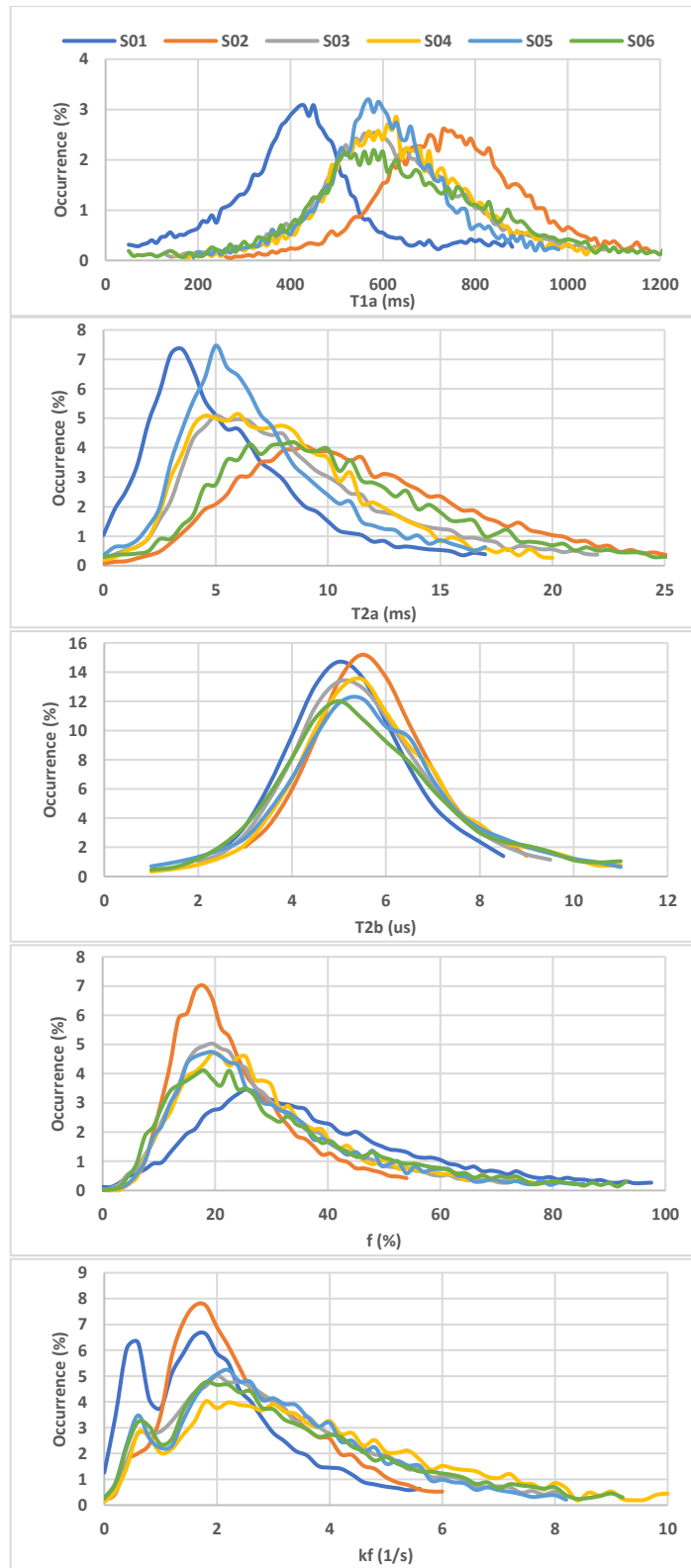


Figure 3.7. Distribution plots of the QMT maps for all meniscus specimens (S01-S06). The fitting results illustrated here used the Gaussian lineshape without the B1 correction.

3.3.4. T2* Mapping

With the VTE-T2* mapping technique using UTE (UTE-VTE-T2*), the mono-exponential fit derived average values (across all specimens) in the meniscus for $T2^*$ of 7.06 ± 1.55 ms, and the bi-exponential fit retrieved average values (across all specimens) in the meniscus for $T2_l^*$ of 10.00 ± 1.55 ms, $T2_s^*$ of 2.33 ± 0.46 ms, Fl of 52.19 ± 4.97 %, and Fs of 47.85 ± 4.96 % (Table 3.4). In the map of mono-exponential fit, the variation of $T2^*$ estimations within the meniscus region appeared smooth (Figure 3.8.a). Compared to the mono-exponential fitting, the bi-exponential fitting provides more parameters, including $T2_l^*$, $T2_s^*$, Fl , and Fs , and likely better represents the tissue properties (Figures 3.8.b.1-4). However, as a cost, the $T2_l^*$ map produced some sparsely scattered hotspots (i.e., overly high estimations), and the $T2_s^*$ map generated some zeros in the estimations (Figures 3.8.b.1 and b.2). The fraction maps seem to demonstrate more heterogeneity within the meniscus region than other parametric maps (Figures 3.8.b.3 and b.4). By contrast, the mono-exponential fit provides a higher overall average GoF than the bi-exponential fit (Table 3.4). The UTE scans from the ultrashort TE to the long TE were able to reflect a perceptible signal drop for the meniscus (Figures 3.9.a). The mono-exponential and the bi-exponential T2* models demonstrate different fitting curves, yet both return high GoF values (Figures 3.9.b and c). The distributions of $T2^*$ maps for all specimens overlap over a broad range of approximately 3-12 ms (Figure 3.10.a). Comparatively, the distributions of $T2_l^*$ maps for all specimens exhibit a more extensive overlapped range from 3-24 ms (Figure 3.10.b.1). For the distributions of $T2_s^*$ maps for all specimens, there is a narrow peak around the low $T2_s^*$ region (<1 ms) and a broader and flatter peak around the higher $T2_s^*$ region (≥ 1 ms and ≤ 5 ms) (Figure 3.10.b.2). The distributions of Fl maps for all specimens present two peaks around 10-20% and 80-90%, respectively, with a gradual incline in between (Figure 3.10.b.3). Likewise, the distributions of Fs maps for all specimens also manifest two peaks around 10-20% and 80-90%, respectively, with a gradual incline in between, however (Figure 3.10.b.4).

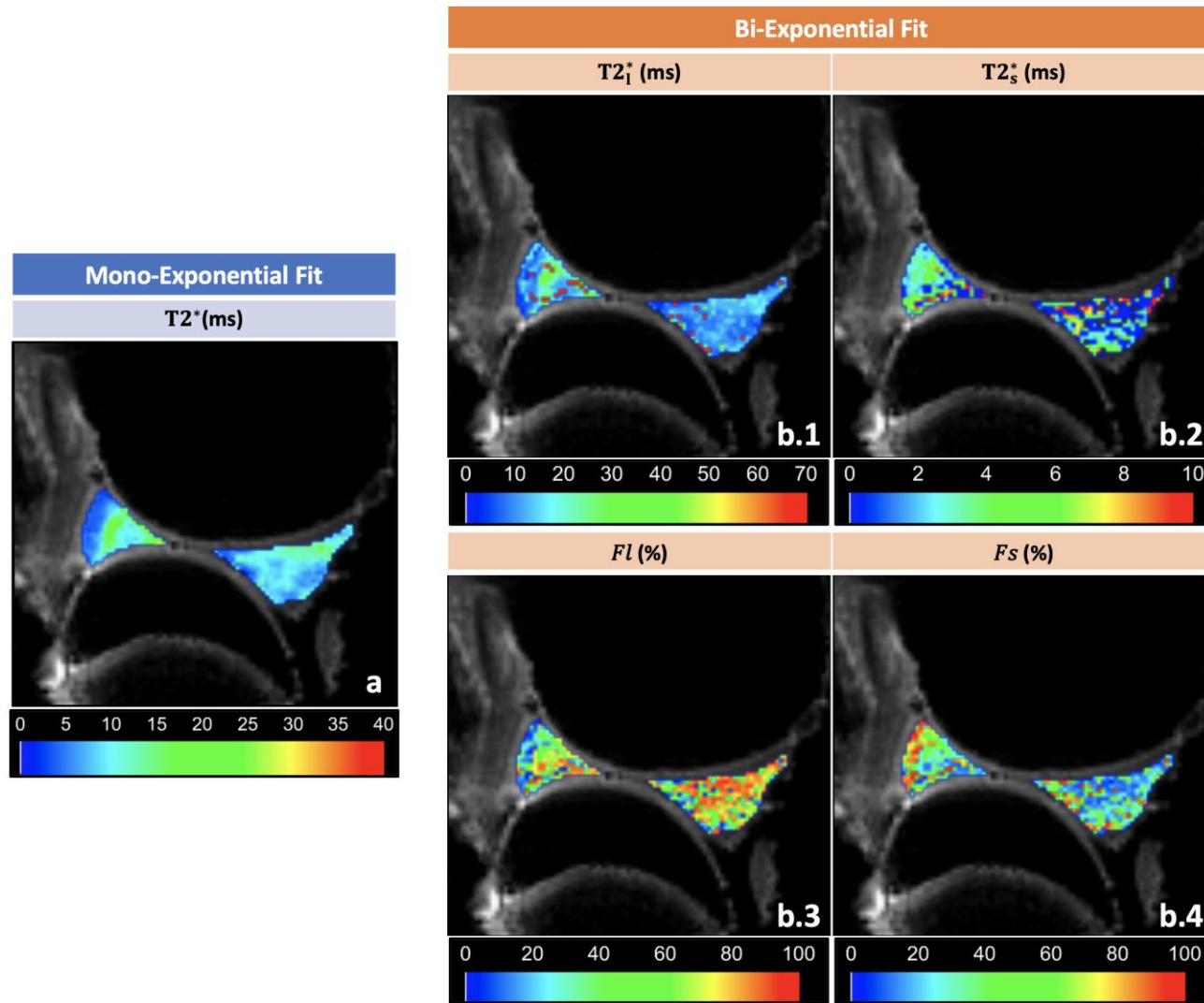


Figure 3.8. T2* maps of the menisci.

The meniscus's $T2^*$ map using the mono-exponential model overlaid on a fat-saturation (FS) UTE scan (a); the meniscus's $T2_i^*$, $T2_s^*$, Fl , and Fs maps using the bi-exponential model superimposed on an FS-UTE scan (b.1-4). (Illustrated with Specimen-S02).

Table 3.4. Statistic of the T2* maps using the mono-exponential fit and the T2l*, T2s*, Fl, and Fs maps using the bi-exponential fit for the intra- and inter-specimen in both menisci.

Specimen	Mono-Exponential Fit			Bi-Exponential Fit								
	GoF	T2* (ms)		GoF	T2 _l * (ms)		T2 _s * (ms)		Fl (%)		Fs (%)	
		Mean	Std.Dev.		Mean	Std.Dev.	Mean	Std.Dev.	Mean	Std.Dev.	Mean	Std.Dev.
S01	0.94	5.11	3.20	0.94	8.85	5.02	1.73	1.51	47.31	29.22	52.74	29.24
S02	0.97	8.22	3.01	0.94	10.91	4.57	2.89	2.78	54.87	30.83	45.15	30.84
S03	0.94	8.24	4.89	0.94	11.46	4.99	1.92	1.97	57.03	28.87	43.00	28.85
S04	0.97	6.25	2.48	0.94	8.81	4.40	2.38	2.36	50.01	31.13	50.01	31.14
S05	0.97	5.75	2.23	0.94	8.73	4.25	2.27	2.06	46.29	30.42	53.73	30.43
S06	0.96	8.80	3.99	0.94	11.23	4.99	2.78	3.12	57.60	29.26	42.46	29.25
Average (n=6)	0.96	7.06		0.94	10.00		2.33		52.19		47.85	
Inter-Specimen Std.Dev.	0.02	1.55		0.00	1.33		0.46		4.97		4.96	

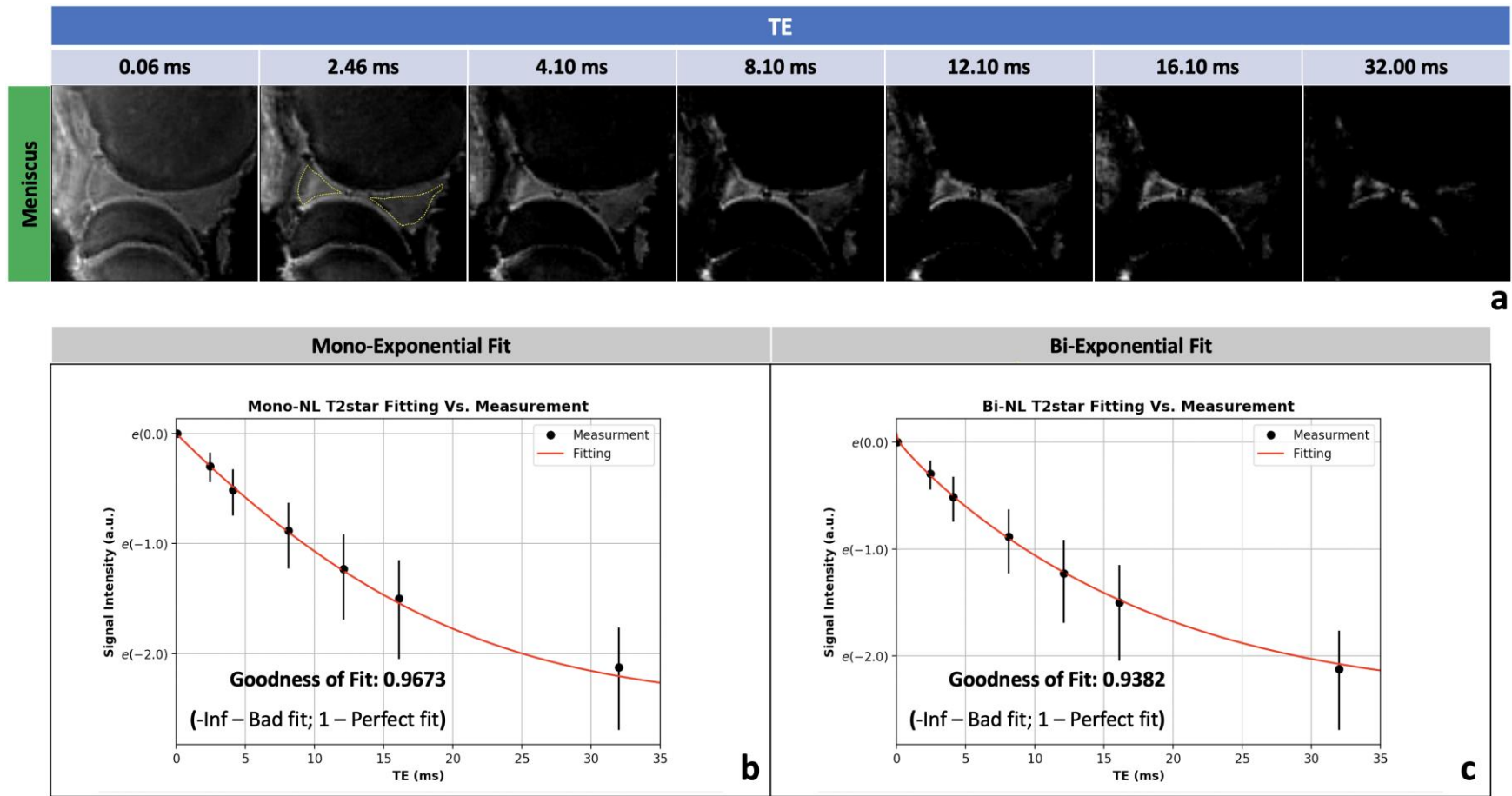


Figure 3.9. Signal measurements and T2* fitting of the menisci.

3D Rectangular Pulse Spiral-Cone UTE scans in the knee acquired with a variable TE (VTE) for T2* mapping (a). The yellow dotted line in (a) delineates the menisci on this exemplary slice. The T2* mapping can use two fitting methods, the mono-exponential (b) and the bi-exponential (c) models. The error bars in (b) and (c) represent the standard deviation for both entire menisci. The goodness of both fits is close to a perfect fit, 1. (Illustrated with Specimen-S02).

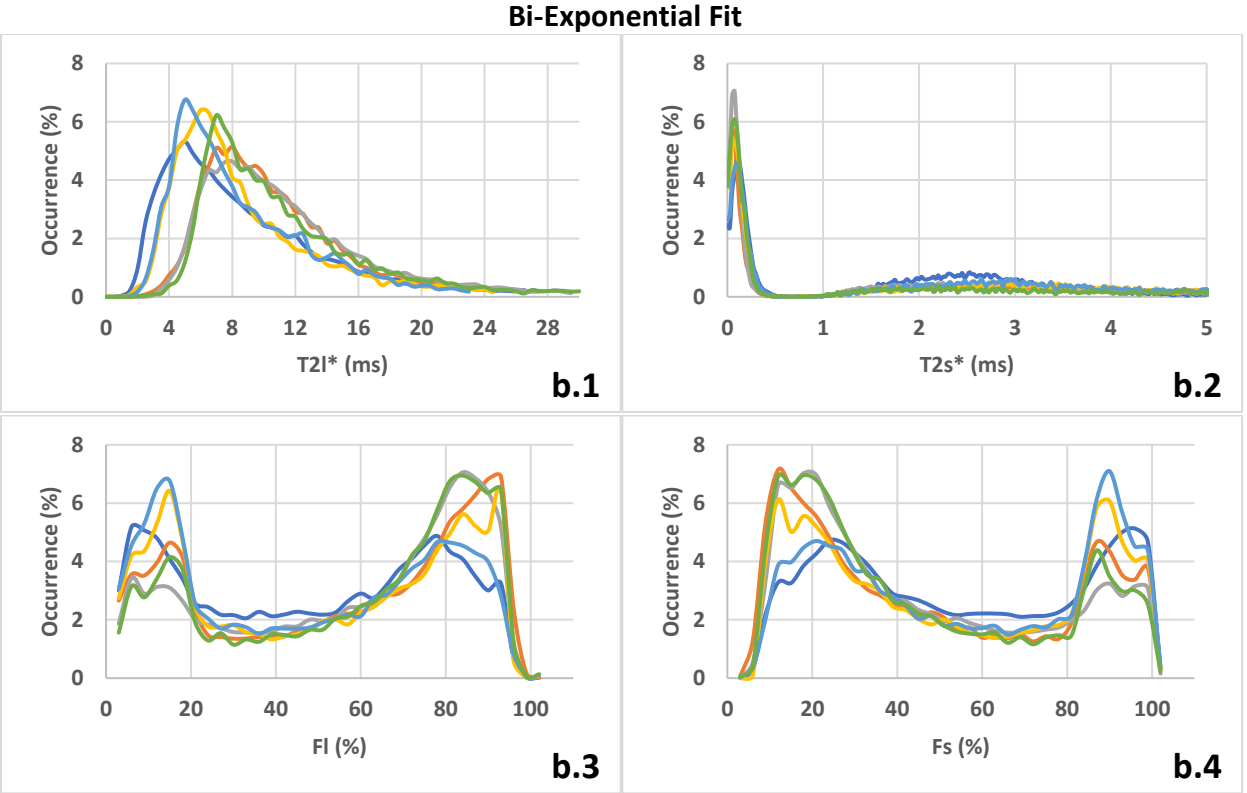
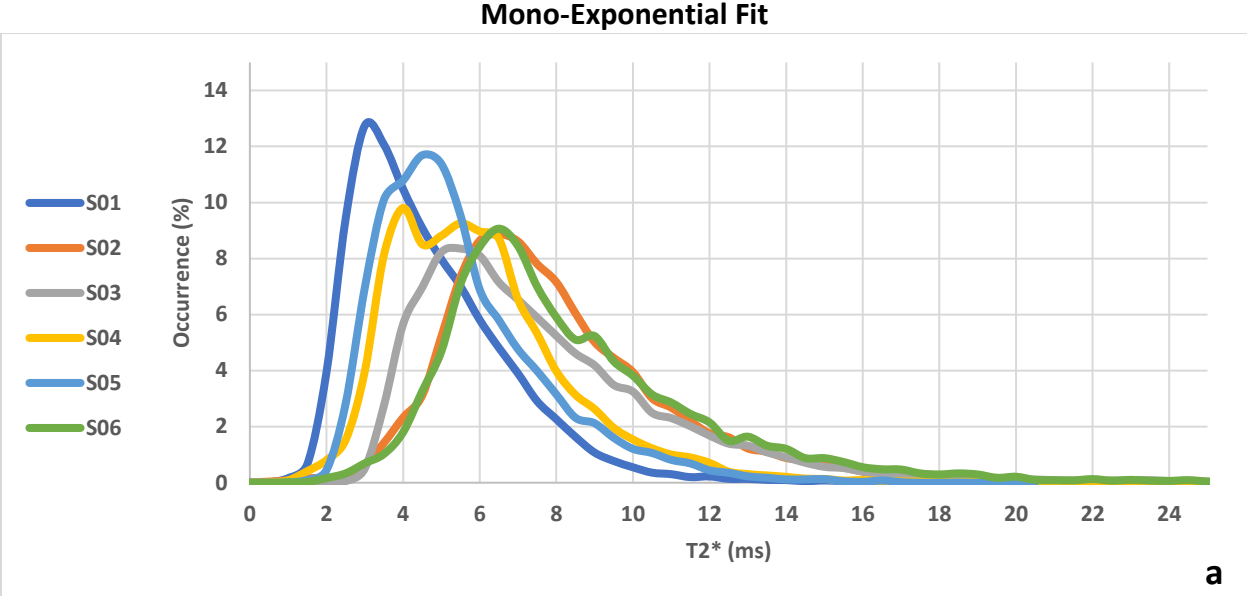


Figure 3.10. Distribution plots of the $T2^*$ maps for all meniscus specimens (S01-S06). The distribution plots of the $T2^*$ map using the mono-exponential fit (a) and the $T2_l^*$ (b.1), $T2_s^*$ (b.2), Fl (b.3), and Fs (b.4) maps using the bi-exponential fit for all meniscus specimens (S01-S06).

3.4. Discussion

Enabled by our FUSE sequence, the multi-contrast morphological imaging capability was exploited to isolate individual tissues in the knee joint, and comprehensive quantitative mappings were developed to assess the meniscus's T1 relaxation time, T2* relaxation time, and QMT parameters. To our knowledge, our results are amongst the first to explore the UTE-QMT parameter mapping in the meniscus (158). The importance of B1 correction was shown for the QMT modelling. This work also included the T1 and T2* mapping in addition to the QMT mapping to present an inclusive UTE quantitative assessment for the meniscus. The sequence also demonstrated flexibility in tailoring the parameters for the application. In summary, this work manifests the feasibilities of our novel FUSE sequence for isolating signals from the different knee joint tissues and for mapping various quantitative biomarkers in the meniscus.

With the long-T2 suppression techniques contained in our FUSE sequence, we can create various morphological contrasts to isolate individual short-T2 tissues from the knee joint (Figure 3.1). The fat saturation pulse, commonly used in MSK imaging, can provide an efficient (one scan required) signal suppression, specifically toward the fatty tissue (fat or marrow). In conjunction with the UTE acquisition, the FS-UTE scan is suitable for imaging the meniscus and tendon. However, the FS-UTE scan failed to create a sufficiently distinct contrast between the marrow and the cortical bone; they both appear as signal void (Figures 3.1.a.6 and b.6). The issue was because the frequency-based FS pulse could also directly saturate the cortical bone's signal due to its broad frequency spectrum (193). This observation agrees with the finding by Ma *et al.*, who showed that the FS-UTE scan might not be appropriate for imaging the cortical bone (141). Compared to the FS, the dual-echo subtraction requires two separate scans yet performs simultaneous suppression for multiple long-T2 tissue types. Given the assumption where the short-T2 signal decays drastically between two TEs while the long-T2 signal does not, the dual-echo subtraction should suppress all the long-T2 contrast and enhance the short-T2 contrast. As a result, the dual-echo subtraction technique successfully reduced the long-T2 intensity, including the fat, muscle, and marrow (Figures 3.1.a.3 and b.3). Although this technique also well isolated the tendon's contrast from its peripheral tissue, it did not present a clear delineation between the marrow and cortical bone or between the meniscus and cartilage due to insufficient suppression. To achieve a more intensive long-T2 suppression, we implemented linearly and exponentially rescaled subtraction

(70), respectively (Figures 3.1.a.4 and b.4 and Figures 3.1.a.5 and b.5). As compared to the unscaled method (Figures 3.1.a.3 and b.3), the rescaled results (Figures 3.1.a.4 & b.4 and Figures 3.1.a.5 and b.5) demonstrate more definite contrast enhancement for all short T2 tissues, especially for the cortical bone, as also suggested by Li *et al.* (70). Besides, the linear (Figures 3.1.a.4 and b.4) or exponential (Figures 3.1.a.5 and b.5) scaling factor can be further optimized in future work to accommodate other scanning parameters or selectively highlight different tissue-of-interest. The subtracted MT-UTE contrast (Figures 3.1.a.7 and b.7) achieved a successful signal suppression for the marrow and fat due to their lack of the MT effect (72). However, the MT-UTE contrast still preserved the muscle's and cartilage's signal because of the strong MT effect between their free (e.g., water) and bound (e.g., protein or collagen) pools (75). For the short-T2 tissues in the knee joint, the subtracted MT-UTE contrast can enhance the anatomical detail within the meniscus and tendon due to their large absolute amount of magnetization transfer. The reason is that the MT pulse should only saturate the bound-pool (e.g., macromolecules) according to the two-pool model (78,90), and the subtracted result (e.g., C7 in Figures 3.1.a.7 and b.7) lead to an effective elimination of the signal from the free-pool and signal boost for the bound-pool. In the knee joint particularly, the tissues, including the fat, marrow, and free water, cannot be reflected in the subtracted MT-UTE contrast due to their heavily-enriched free-pool over their barely-existent bound-pool (72,75). Although the subtracted MT-UTE contrast (Figures 3.1.a.7 and b.7) did not manifest the cortical bone, the UTE-MTR (Figures 3.1.a.8 and b.8) distinctly delineated the region of the cortical bone because of its high magnetization transfer ratio. Given that the cortical bone usually demonstrates low or zero signal intensity with the conventional sequence (FLASH), the UTE sequence is the only approach that allows for the MTR contrast in the cortical bone (Figures 3.1.a.8 and b.8). Our study found this combination could adequately create a noticeable morphological representation for the cortical bone and other short-T2 components, including the meniscus and tendon. There still is a limited number of studies around the combined use of the UTE and MT saturation (72,88), but this deserves more investigation.

This study has demonstrated the importance of the B1 correction for estimating the T1 relaxation times in the meniscus (Table 3.2). Before the T1 fitting, one can choose to use a B1 map to calibrate the flip angles that might deviate from their prescribed values due to the B1 field inhomogeneity to pursue a more accurate result. In this study, the average B1 correction factor measured in the

six meniscus samples (1.18 ± 0.03) is slightly higher than the reference of 1 (i.e., the ideal homogeneity). This increase in the B1 correction factors is possibly due to the generation of secondary B1 field components in the menisci, as suggested by a recent study (194). As a result, our higher average B1 value (greater than 1) led to a lower average T1 estimation (over six specimens) than the uncorrected case-i.e., 475.96 ± 56.57 ms vs. 670.37 ± 90.53 ms (Figure 3.2 and Table 3.2). Other studies have found similar results. For example, Ma *et al.* demonstrated reduced T1 values in menisci where the B1 scaling factors were higher than 1 (194); and Li *et al.* reported decreased T1 values in grey and white matter of the brain because the B1 scaling factors measured in both regions were above 1 (185). In this study, we collected 2D images to generate B1 maps and then interpolated the generated 2D B1 maps to 3D to match the T1 acquisitions for the correction. The reason is that the adopted DA method requires long TR, which is not time-efficient for 3D acquisitions. For example, species with a long T1 of around 1 s demand at least 5 s for the TR, which leads to an unbearably long scan time for a fully sampled 3D acquisition. As a better option, other studies suggest that the actual flip-angle imaging (AFI) can provide a fast 3D B1 mapping (81,195). However, we still need to verify the accuracy of the B1-corrected VFA-UTE T1 mapping method in future with more cadaver or *in vivo* studies in human menisci and other tissues.

With our FUSE sequence, the VFA technique was able to provide consistent T1 maps in the meniscus over all specimens. Our VFA-UTE-T1 estimation without the B1 correction (670.37 ± 90.53 ms) is comparable with another study that used a variable-TR method (the gold standard) without the B1 correction for the T1 fitting in bovine menisci (638 ± 42 ms) (196). Also, the overall inter-specimen consistency of the distribution plots suggests the robustness of our VFA-UTE-T1 mapping (Figure 3.4). Compared to other methods (80,196,197), the VFA fitting method uses a fixed TR without any additional time block for saturation or inversion recovery, which allows the minimal scan time permissible with the sequence. This feature makes it suitable for 3D volumetric T1 quantification. The VFA-UTE-T1 mapping has been implemented for investigating the T1 relaxation times in the various short-T2 knee joint tissues, including the meniscus (80,81,194). This study verified its feasibility in the meniscus with a comparable result to the literature and inter-specimen consistency.

In this work, we have demonstrated the feasibility of combining adjustable MT pulses and our UTE sequence to obtain 3D-isotropic QMT parameter maps via the two-pool modelling. While most QMT studies use an FLASH sequence (172–174,198), this study carried out the QMT studies with the UTE acquisitions. Compared to the FLASH-QMT, the UTE-QMT can directly probe the short-T2 tissues to retrieve the quantitative estimations of their physical properties. However, the UTE-QMT technique is still relatively new and needs more validation and exploration (93). As for the UTE sequences used for the QMT modelling, other studies have demonstrated their success with a 2D-radial sequence (93) and a 3D spiral-cone sequence with a rectangular RF excitation (92,158). Uniquely, we carried out the UTE-QMT modelling using a spiral-cone trajectory by combining it with a 3D half-Sinc excitation scheme. This particular combination has not been explored before in other QMT studies. Compared to the rectangular pulse (with a broad bandwidth), the 3D half-Sinc excitation in QMT scans can achieve a better slab selectivity and minimize its excitation to the bound pool after the off-resonance saturation. As for the trajectory, the 3D spiral-cone option can provide a higher k-space-filling efficiency (than the radial), which is essential to keep the specific absorption rate (SAR) of the QMT scans to a minimum. Since the SAR built up by the UTE-QMT protocol is mostly contributed by the high energy MT pulse required for every trajectory line (or every TR cycle), the spiral-cone with fewer spiral-interleaves would be an ideal choice over other options. Furthermore, the data required for our QMT fitting involve ten MT-UTE scans. Therefore, a highly efficient k-space-filling carried out by the spiral-cone trajectory can use fewer TR cycles to avoid the total SAR deposition exceeding the limit and ensure a fully sampled scan. This will be especially important for *in vivo* imaging. Therefore, we must optimize the scanning protocols for *in vivo* studies (174,177,199,200).

It was not clear what lineshape (Gaussian vs. Super-Lorentzian) should be used when carrying out QMT mapping in MSK tissues; here, we showed good fits for both. Some literature has suggested that the Super-Lorentzian lineshape can serve as a better fit for biological tissues (172). However, our results from the meniscus samples suggest that the Gaussian lineshape can provide slightly superior GoFs than the other (Table 3.3), even though they are both very good. Besides, the study analyzed the impact of the B1 correction and the lineshapes on the outcomes of the QMT mapping. The B1 correction seems to only create an evident difference on T_1^a and kf , while the lineshape factor has more influence on T_2^b , T_2^a , and f . This observation suggests that to obtain more accurate

QMT parameters, we must ensure the accuracy of the B1 mapping and have more evidence to support the decision of the superior lineshape. As suggested by the inter-specimen consistency (Figure 3.7 and Table 3.3), our UTE-QMT sequence has demonstrated its robustness with different lineshapes and the toggles of the B1 correction.

We have verified the capability of the $T2^*$ mapping using our UTE sequence. We observed an apparent signal decay (~25%) between 0.06 and 2.46 ms in the meniscus (Figure 3.10). This range is usually inaccessible to conventional sequences. For the evaluation of $T2^*$ mapping, this work examined mono-exponential and the bi-exponential models for the meniscus. The mono-exponential mapping provides an overall estimation of $T2^*$ for each pixel. By contrast, the bi-exponential mapping divides each pixel of tissue into two compartments (long and short) and estimates each's $T2^*$ value and fraction. As shown in our results (Table 3.4), both models can produce highly reliable fits (close to 1 regarding the GoFs). However, the mono-exponential model yields a better fit than the bi-exponential model in the meniscus. The potential reason might be that the specimens were stored in the freezer before the scans, and the ice crystals formed within the (meniscus) tissue damaged the cells (intracellular and extracellular structures), which might make the two-compartment modelling impractical. For a more reasonable comparison between the two models, further *in vivo* studies are needed. A study using porcine menisci also demonstrated comparable goodness-of-fit between the mono-exponential and the bi-exponential model (180). As opposed to our comparable fits in the meniscus between two models, some studies in the patella tendon have suggested the bi-exponential model can yield a much-improved fitting outcome than the mono-exponential model (85,181,182). Therefore, the decision on the better fit needs to include more tissue types for investigation and is likely tissue specific. Through the comparison, we can also observe that the results of the bi-exponential fit show an agreement with the $T2^*$ map estimated from the mono-exponential fit. For example, on the mono- $T2^*$ map (Figure 3.8.a), the left meniscus's outer region exhibits visually lower $T2^*$ values (blue) and corresponds to higher percentages on the Fs map (Figure 3.8.b.4). Also, the $T2_i^*$ map reflects lower values for this region than the inner part (Figure 3.8.b.1). Although the bi-exponential fit provides more parameters than the other, we observed some 'hotspots' (e.g., infinite values) (Figure 3.8.b.1) and impractical estimations of zeros (Figure 3.8.b.2) from its results, possibly, due to the ill numerical fitting. This observation might suggest the mono-exponential fit is more robust regarding providing less noisy

quantitative maps. As for the distribution plots of the two fits, the bi-exponential fit reveals two peaks for the $T2_s^*$, Fl , and Fs maps, comparing to the mono-exponential fit. As suggested by the $T2_s^*$ map, even though the narrow, spiking peak displays a large portion of $T2_s^*$ estimated within the range between 0 ms and 0.5 ms, the broad, lower distribution shape shows some $T2_s^*$ estimations falling between 1 ms and 5 ms. This pattern suggests that using the means and standard deviations alone might not be enough to summarize the statistics of the $T2_s^*$ maps, and a fit including more compartments might be more appropriate in this case. Additionally, the two peaks of Fs and Fl maps can unveil tissue heterogeneity where the long and short components predominantly occupy different regions. In future work, we can further increase the TE sampling to improve the fitting quality and enable a tri- or higher-order exponential fitting.

This work has shown the efficacy and adaptability of our FUSE sequence in both qualitative and quantitative imaging. For the qualitative and quantitative knee imaging, this work mainly uses a 3D spiral-cone trajectory with a half-Sinc or rectangular pulse. The versatility of RF pulses and trajectories of our sequence allows for further optimization on the time-efficiency, signal-to-noise ratio (SNR), SAR, or accuracy of quantification. In each pixel, the VFA-T1 and mono-exponential $T2^*$ mappings can provide an overall parameter estimation, while the QMT and bi-exponential $T2^*$ mappings can render more divided parametric details. However, due to the more parameters involved, the complexity and instability of the fitting system might also increase. This work also has limitations. Firstly, one specimen (S01) exhibits more inter-subject variation than others. The possible reason is that this specimen has been stored in the freezer for approximately two years before use, while other specimens were purchased mere days before scanning. Secondly, we need to include other assessment methods for the meniscus. For example, we could also use biochemical analysis, histology tests or bio-mechanical tests to validate the quantitative biomarkers estimated by our sequence. Thirdly, we carried out this study using bovine specimens, but we still need to evaluate our qualitative and quantitative imaging methods with human menisci (cadavers or *in vivo*) in future studies. Fourthly, we did not consider the temperature change for the specimens during the scans since the increase of temperatures can lead to a lower proton resonance frequency for water (while the temperature barely affects the resonance frequency of fat). However, the temperature factor can be considered for future studies. Lastly, all current UTE images were reconstructed offline, so we could not examine the image results in real-time while scanning. Also,

this process was time-consuming. Therefore, we will need to develop an integrated reconstruction program for online reconstruction. In the future, it would be very promising to use our UTE sequence as a non-invasive tool to assess OA in the knee with multiple types of morphologic images and various quantitative maps as biomarkers.

3.5. Conclusion

It is feasible to use our flexible UTE sequence, FUSE, to create morphologic images that isolate signals from the various knee joint tissues and carry out the mappings of QMT parameters and T1 and T2* relaxation times for the meniscus. Our UTE sequence has the potential to assess tissue health and OA in the knee with its versatile morphological and quantitative imaging capabilities.

Chapter 4 Improving cortical bone imaging using the FUSE sequence for optimal synthetic CT generation

Synopsis: Ultrashort echo time (UTE) pulse sequences are used in the generation of synthetic computed tomography (sCT) for magnetic resonance-only (MR-only) radiation treatment planning (RTP). This study aims to verify and optimize the use of an in-house flexible UTE sequence (named as Flexible Ultra Short Echo time or FUSE for short) for improved cortical bone imaging used in synthetic CT generation. For achieving improved cortical bone imaging, we first used a rubber phantom to investigate the optimal acquisition techniques and parameters of the FUSE sequence in terms of the variations of the produced artifacts, signal-to-noise (SNR) ratio, and timing. Then, using a human skull, we applied the optimized UTE acquisition techniques and parameters and verified the improved overall image quality of cortical bone in comparison to a product UTE sequence. Also, we compared and contrasted the images of the human skull collected using the FUSE and traditional CT. Last, we demonstrated the clinical feasibility of the sCT data generated using the FUSE sequence in RTP. Using CT and sCT data, two radiation treatment plans were created and produced comparable dose calculations with the mean dose less than 1% different.

4.1. Introduction

There is growing demand to perform MRI only radiation treatment planning (RTP) or to achieve better integration of MRI into the routine radiation therapy (RT) workflow that currently mainly relies on x-ray based Computed Tomography (CT) (201–203). In routine radiation treatment planning (RTP), CT images are used for contour delineations and dose calculations. MRI is well known to provide superior soft-tissue contrast to CT, providing more distinct delineation and various contrast types for many organs, soft tissues, and tumours. Hence, over the past two decades MR images have been increasingly used in RTP to provide more accurate tumour and organs-at-risk (OAR) delineations (204–207). However, when compared to the use of CT in radiation therapy, MRI has some drawbacks, specifically regarding its geometric fidelity and the inability to use

MRI for dose calculation. It's well documented that MRI suffers geometric distortion due to the imperfect linearity inherent to the gradient system, (208,209). However, with recent advancements in MRI protocols, clinicians can effectively eliminate distortion effects using scanner-embedded or in-house algorithms (210,211). As well, many institutions employ quality assurance (QA) phantoms and evaluation software to track and assess the system-specific distortion errors before deciding to introduce the associated MR images to RTP (212). With regard to the second drawback, it is well known that the image intensities of MRI are relative values and dependent on various scan settings. Based on this, MR images alone cannot provide meaningful information for dose calculation (207,213). Typically, MRI information is incorporated into treatment by using an image registration algorithm to match the MRI to the planning CT. The co-registration helps in improving the overall accuracy of gross tumour and OAR delineation. However, due to the co-registration between the two modalities, some unwanted systematic uncertainties are introduced (214–216). Therefore, MR-only workflows are appealing for their potential to bypass the requirement of image registration and, more importantly, provide better soft tissue delineation and potentially take advantage of advanced MRI methods (e.g., diffusion-weighted imaging, quantitative maps, MR spectroscopy, etc.).

Synthetic Computed Tomography (sCT) is an MRI-derived image that tries to closely mimic an actual CT image (217). Common approaches for the sCT generation include the atlas-based method, bulk density assignment, and voxel-based density assignment (116,217–220). The atlas-based method requires co-registered MR and CT atlases pre-constructed by multiple training datasets and which can then be used to generate the sCT image by non-rigidly registering the MR and the CT atlas to the target MR image (219). The atlas-based method can provide a reliable pseudo-CT estimation, although it might also introduce some systematic uncertainties resulting from the necessary deformable registration steps (219,221,222). This method requires the construction of well-trained MR and CT atlases, which may be resource intensive and time consuming. This factor may limit its widespread use in small to medium size radiation treatment facilities. In comparison, the other two approaches utilize a series of MR scans featuring various types of contrast as prerequisites before the sCT generation. For example, one can use T1-weighted images to manifest the bone marrow and white matter contrast, T2-weighted images to depict the water content and grey matter, and ultrashort echo time (UTE) sequences to detect the cortical bone signal. By

mathematically combining all these images together, one can resolve the bony anatomy missing in traditional MRI's. To go from the MRI, which now includes the bony information, researchers have been creative. One method uses a bulk density assignment technique. This technique relies heavily on segmentation methods to produce a label mask for each tissue type and assigns an appropriate Hounsfield unit (HU) to each label to compose the sCT image (217,218,223). Comparatively, voxel-based density assignment uses algorithms to classify each tissue type with a probability map (0 to 1) and then perform a sum of the probability maps weighted by different mass tissue densities. Investigations show that voxel-based density assignment can provide sCT images similar to genuine CT images (116,220). However, the choice of classification algorithms adds to the complexity of processing, which varies from the fuzzy c-means (FCM) clustering technique to the more advanced random forest-based method (115,116,220). Relatively, the bulk density assignment method is simpler since the probability maps are not required for the workflow. Studies suggest that the bulk density assignment approach with simple segmentation methods can provide sufficiently accurate dose calculation comparable to the genuine CT data (218,223).

One critical challenge of all sCT generation methods is the difficulty in obtaining adequate cortical bone signal in MR images. Viewing the cortical bone is vital for radiation treatments like stereotactic body radiation therapy (SBRT) of the spine, sarcomas and other bone metastasis (224). Unlike CT images, cortical bone appears as signal voids and exhibit nearly undifferentiated contrast with air in conventional MR images. This fact creates an obstacle for the segmentation or classification required in the sCT generation methods since the air and the bone map might not be accurately distinguished. An accurate bone delineation is essential for the generation of sCT images. Cortical bone has a short MRI T2 relaxation time ($\sim 0.4-0.5$ ms), which leads to a significant signal decay before the acquisition of conventional MR sequences starts (7,115). UTE sequences use specialized acquisition techniques to efficiently shorten the time-of-echo (TE) of the pulse sequence, in order to acquire signal sufficiently quickly so that the cortical bone can be directly imaged (14,15). By combining the superior soft-tissue contrast provided by the conventional sequences and the ability of cortical bone imaging using UTE sequences, MRI undoubtedly has great promise for sCT generation for radiation treatment application. However, the quality of the UTE images of cortical bone is paramount; as such, choice of acquisition techniques (e.g., trajectories) and parameters must be carefully selected. Also, the UTE scan protocol needs to be

optimized using a systematic approach in terms of the visibility of short-T2 contrast, elimination of artifact, signal-to-noise ratio (SNR), and time efficiency.

As described in Chapter 2, our novel Flexible Ultra Short Echo time (FUSE) sequence provides a unique opportunity to optimize cortical bone imaging for RTP. The FUSE sequence provides two types of acquisition trajectories, i.e., the radial and spiral, which allow for flexible changes for the sampling parameters, e.g., the configuration of trajectory lines. Therefore, the overall purpose of this study is to verify and optimize the use of the FUSE sequence to improve cortical bone imaging and provide clinically feasible synthetic CT images for RTP. The overall study purpose can be further divided into four specific objectives:

- 1) The first objective, using a rubber phantom, was to optimize the trajectories and associated sampling parameters of our FUSE sequence regarding the variation of the produced artifacts, SNR, and time efficiency.
- 2) The second objective, using a human skull (immersed in saline), was to apply the optimized trajectory and sampling scheme to evaluate the feasibility of the FUSE sequence for providing improved cortical bone imaging on the artifact reduction and better cortical bone contrast delineation in comparison to a commercially available UTE sequence.
- 3) The third objective was to perform a direct anatomical comparison, between images collected of the human skull collected using the FUSE and ones collected using traditional CT regarding.
- 4) Lastly, the fourth objective was to use the FUSE sequence to generate a radiation treatment plan using an sCT created by FUSE and assess its dosimetric equivalence to a plan created using a traditional CT image.

In this chapter we present data and results that demonstrate that overall improvements in UTE imaging, as seen by using our novel FUSE sequence, translate to improvements in applications for radiation treatment planning.

4.2. Materials and Methods

4.2.1. Phantom and Human Skull

In this study we employed two types of phantoms, an in-house phantom and a human skull (dried cadaver). The in-house phantom contains both a short-T2 component-i.e., rubber- and long-T2

components (i.e., water, oil, and agar). The in-house phantom was used to determine the optimal scan parameters, using FUSE, to enhance the contrast in cortical bone. As well, we sought to reduce prominent artifacts, increase overall SNR, and reduce scan time. The human skull is a dry human skull preserved for anatomical study and X-ray-based imaging. This particular human skull has not been imaged using MRI. It was provided free of charge by the Department of Human Anatomy and Cell Science, University of Manitoba (Winnipeg, MB, Canada). For MRI scans, the dry human skull was fully immersed in a saline solution (1 litre H₂O, 3.6 grams NaCl (225)) and fixed in a sealed container in order to minimize susceptibility artifacts. The bone part and the saline serve as the short-T₂ component and the long-T₂ component, respectively, to help evaluate the feasibility of the FUSE sequence on cortical bone imaging.

4.2.2. FUSE Sequence

As previously described, the FUSE sequence was developed to be used for a number of different applications. This includes, facilitating better sCT generation for radiation treatment planning (RTP). The sequence provides user-configurable acquisition options, for example, radial and spiral trajectories with an adaptable combination of in-plane and out-of-plane trajectory lines. The FUSE sequence was developed using a vendor-specific platform (IDEA, Siemens Healthineers, Erlangen, Germany). The image reconstruction for the FUSE sequence utilized the gridding algorithm, followed by the inverse Fast Fourier Transform (FFT) (25,26). All FUSE reconstruction was performed offline using in-house software (MATLAB, MathWorks, Natick, MA, USA).

4.2.3. MR and CT Image Acquisitions

We carried out MR scans for the phantoms using a 3 Tesla Siemens MR system (MAGNETOM PrismaFit, VE11C, Siemens Healthineers, Erlangen, Germany). For technical optimization of the FUSE sequence for use in cortical bone imaging, we used the in-house phantom to determine the optimal selections of the trajectory type, number of k-space in-plane trajectory lines, and number of k-space out-of-plane trajectory lines (i.e., cones) by considering the appearance of unwanted artifacts, SNR, and scan time (Table 4.1). The resultant visible artifact and relative artifact are evaluated using observational assessment and described qualitatively. The SNRs for the various settings were calculated using a normal image and a pure noise image over a region-of-interest (ROI) ([Eq. 2.17]) (136). For the phantom scans, a birdcage 32-channel head coil was used for the

data acquisition. To scan the human skull using the FUSE sequence, we applied the optimized acquisition scheme, including the choices of the trajectory type and the number of trajectory lines. To enhance the cortical bone contrast, we adopted the dual-echo subtraction technique (68,224). Using this technique, we acquired an ultrashort TE (0.06 ms) scan and a longer TE (2.46 ms) scan for offline subtraction (i.e., Echo_{0.06}-Echo_{2.46}) to generate a UTE difference image highlighting the bone contrast only (Table 4.2). To illustrate the improvement made by the FUSE, we collected images of the human skull using a commercially available sequence called Pointwise Encoding Time Reduction with Radial Acquisition (PETRA) for comparison. The scan protocols we used are shown in Table 4.2 (226). For demonstrating the signal voids observed in cortical bone using conventional sequences, we lastly collected T2-weighted images for the human skull using another commercially available sequence called, Sampling Perfection with Application optimized Contrasts using different flip angle Evolution (SPACE) (Table 4.2) (227). For all MR scans of the human skull, a flexible 18-channel receiver-only body array coil combined with the built-in spine coil was used to provide a total of 30 channels for the data acquisition.

We acquired a CT scan for the skull to act as the reference image. The skull was scanned on a Siemens CT scanner (SOMATOM Definition Edge, Siemens Healthineers, Erlangen, Germany). The scan used a head-first supine position with 120 kVp, 210 mA, 200 mm as field-of-view (FOV), 0.6 mm as slice thickness, 512×512×264 as the reconstructed matrix, and 0.39² mm² as the in-plane resolution.

Table 4.1. MRI scan parameters for the systematic optimization using the phantom.

Experiments	Trajectory	RF*	FOV (mm)	Matrix	Voxel Size (mm ² /mm ³)	In-Plane Acquisitions	Cones	TE (ms)	TR (ms)	BWP (Hz)	Flip Angle (°)	Slice Thickness (mm)
Systematic Optimization by Varying In-Plane Acquisitions	2D Spiral	RHSP	180	256 ²	0.70 ²	16, 32, 64, 128, 256, 512	N/A	0.14	56	260	25	5.0
	2D Radial											
Systematic Optimization by Varying Cones	3D Spiral	RP	180	256 ³	0.70 ³	128	8, 16, 32, 64, 128, 256, 512	0.06	11	510	7	0.7

***RP – Rectangular Pulse; RHSP – Regular Half-Sinc Pulse.**

Table 4.2. MRI scan parameters for the human skull.

Scans	Trajectory	RF*	FOV (mm)	Matrix	Voxel Size (mm ³)	In-Plane Acquisitions	Cones	TE (ms)	TR (ms)	BWP (Hz)	Flip Angle (°)	Slice Thickness (mm)	Total Acquisition
FUSE	3D Spiral	RP	220	256 ³	0.86 ³	256	256	0.06/2.46	12	410	25	0.86	13 min 08 s**
PETRA	Mix of 3D Radial and Cartesian	RP	260	320 ³	0.81 ³	N/A	N/A	0.07	3.32	400	6	0.81	05 min 55 s
T2-SPACE	3D Cartesian	Slab-Selective	220	256 ³	0.86 ³	N/A	N/A	408	3200	590	120	1.17	06 min 34 s

*RP – Rectangular Pulse;

**The scan time is for each scan.

4.2.4. Image processing and Evaluation

To compare images from the FUSE sequence and the CT imaging, we applied a series of image processing steps to the two datasets. These include, image registration, segmentation, and comparison of the geometric similarity. All the data was processed and analyzed using packaged software (MeVisLab, MeVis Medical Solutions AG, Bremen, Germany). As the first step, we performed a rigid registration of the CT images to UTE difference images. The registration process comprised of two parts, a manual and an automatic portion. The manual registration provided a crude initial estimate for the subsequent automatic registration to avoid convergence at a local minimum. The automatic registration, aiming to provide a more precise result, used an iterative algorithm based on the normalized mutual information (NMI) similarity measure between two datasets (228).

Next, we segmented the bone from both the UTE and CT images to assess similarity. We applied the FCM clustering method to extract the bone from the UTE difference images (220). The FCM processing used a two-classification setting with a fuzzy exponent of 1.6 to classify the skull bone as one cluster and the background as the other, generating probability maps for both (220). With a threshold above 0.5, a mask for the skull bone was segmented using the probability map. For the CT segmentation, we used a thresholding method. The CT scan of the skull was acquired in a dry condition (i.e., not in saline), so we used a threshold of -400 Hounsfield Unit (HU) (suggested by the literature) to define the ‘true’ air, discriminating the skull bone from the air on the CT images (220).

Last, we compared the geometric similarity between the two segmented masks. We conducted a visual inspection and calculated the Dice Similarity Coefficient (DSC) between the masks (229).

4.2.5. Dose Calculation Using Synthetic CT

To examine the feasibility of using the new UTE difference image for dose calculation, we seek to convert the UTE difference image to a sCT using a bulk density assignment technique. To do this, we imported the newly derived UTE difference image into the radiation treatment planning system (Eclipse Version 13.6, Varian Medical Systems, Pal Alto, USA). Since the morphology of the UTE bone is comparable to the CT images, we decided to convert the UTE image to a synthetic

CT by performing a simple bulk density assignment. In our treatment planning system, we used the complete histogram of the UTE difference image to create a contour of the bony anatomy. A Gaussian based smoothing algorithm was used to remove unwanted holes and bumps in the contour. After inspecting the contour, a bulk density assignment was applied to bony anatomy using a nominal value of 1196 HU (mass density 1.85 g/cm³). A simple two field 6 MV parallel opposed radiation treatment plan was created by an expert (medical physicist with greater than 10 years of experience), using dose fractionation of 2000 cGy in five fractions. For comparison, the same plan was generated using CT image of the same human skull. For both plans, minimum, maximum, and mean dose metrics were calculated and compared.

4.3. Results

4.3.1. Optimization of the Use of the FUSE Sequence

Overall, the spiral trajectory provides better-controlled artifacts and higher SNR than the radial trajectory when the same number of in-plane trajectory lines (e.g., 64-512) were used (Figure 4.1.a-e). A higher number of radial spokes (e.g., 128-512) decreased the under-sampling artifacts than fewer ones (e.g., 16-64) (Figure 4.1.a). Likewise, more spiral interleaves (e.g., 64-512) exhibit better suppressed off-resonance artifacts than fewer ones (e.g., 16 and 32) (Figure 4.1.a). Also, fewer spiral interleaves scans (e.g., 16-64) did not present the under-sampling artifact observed in the radial scans with the same number of radial spokes (Figure 4.1.a). The scan with 64 spiral interleaves did not show any under-sampling artifacts or off-resonance artifacts. The spiral scans demonstrate higher SNRs than the radial scans using the same number of in-plane trajectory lines (i.e., identical acquisition times) (Figures 4.1.b-e). More radial spokes improve SNRs for all testing components (i.e., rubber, agar, water, and oil) (Figures 4.1.b-e). More spiral interleaves show decreasing SNRs for the water and agar (Figures 4.1.c and d) but increasing SNRs for the oil and the rubber (Figures 4.1.b and e).

In the 3D Spiral-Cones scans, more out-of-plane trajectory lines (i.e., cones), associated with longer acquisition times, provide better-suppressed artifacts and higher SNRs than fewer cones (Figure 4.2.a-b). An insufficient cone number can lead to a drastic under-sampling artifact, and a two-fold increase of cones can effectively reduce the artifact at the cost of a doubled scan time (Figure 4.2.a). Increased cones can efficiently increase SNRs for all components (Figure 4.2.b),

although it is visually challenging to perceive any evident improvement from 128 to 512 cones (Figure 4.2.a).

Spiral Interleaves	16	32	64	128	256	512
Scan Time	03 s	05 s	09 s	16 s	30 s	59 s

Spiral						

Radial Spokes	16	32	64	128	256	512
Scan Time	03 s	05 s	09 s	16 s	30 s	59 s

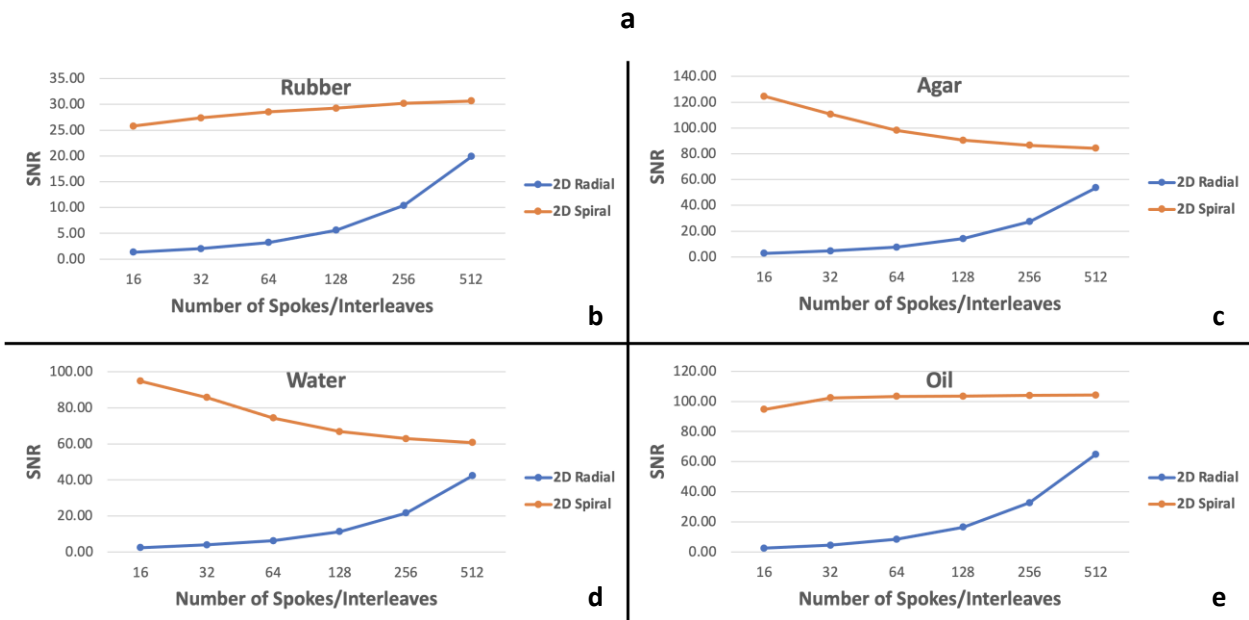
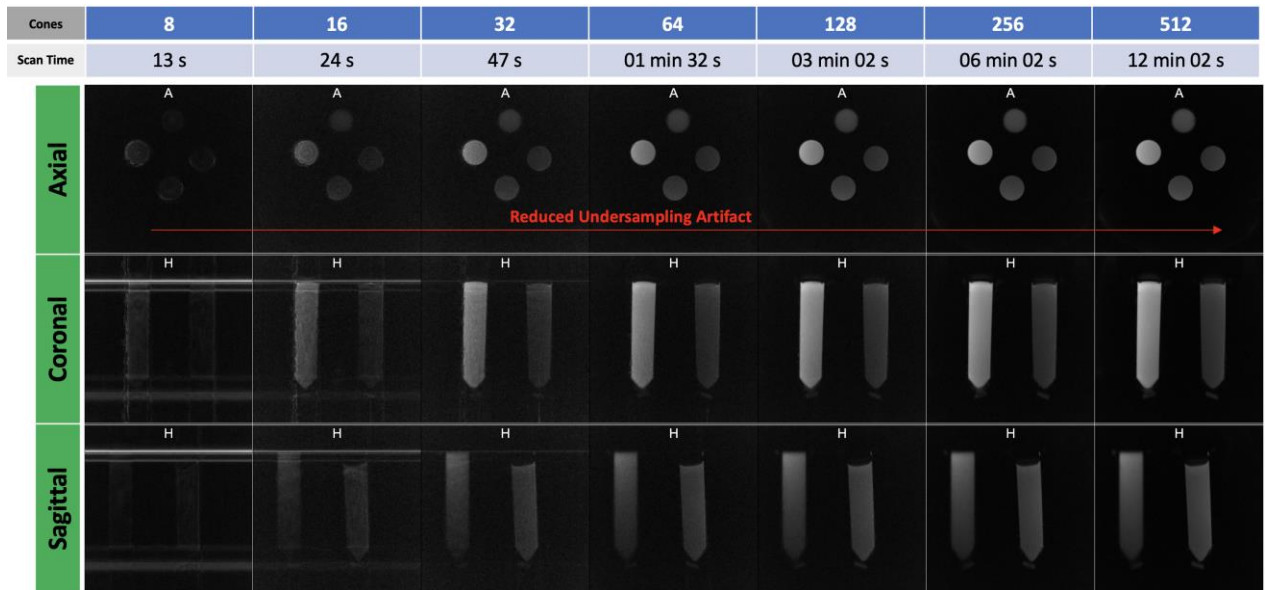
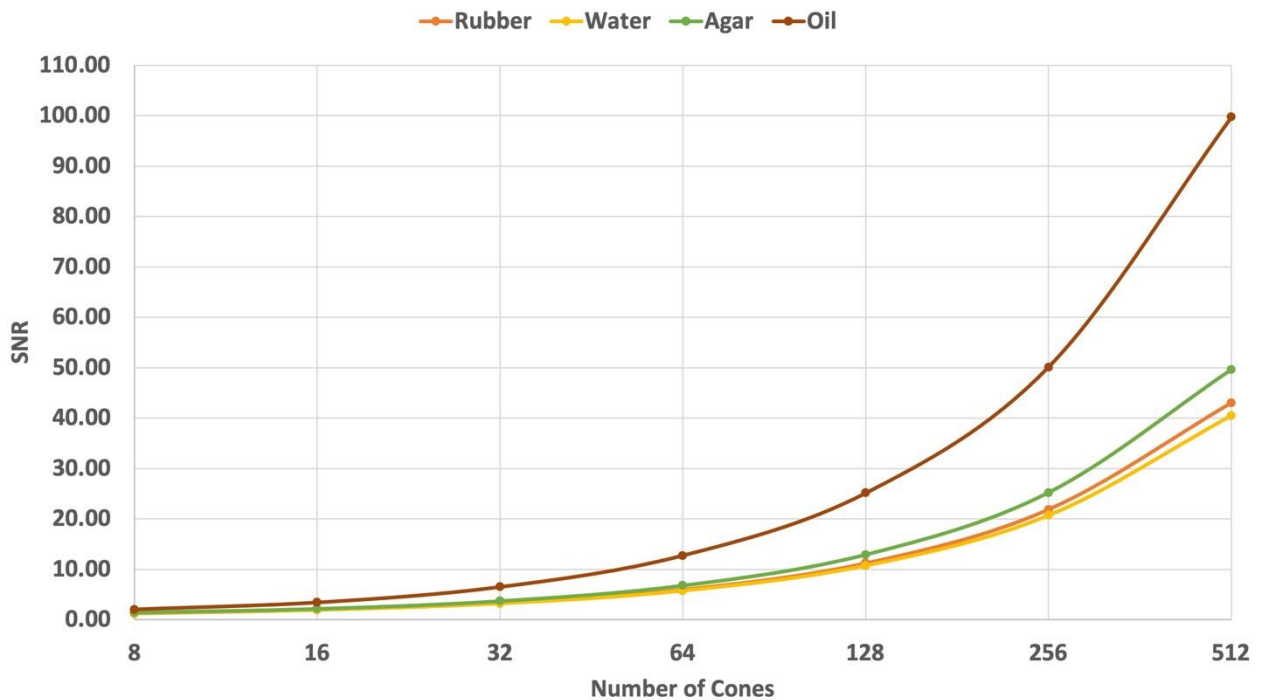


Figure 4.1. Variations of the artifacts, SNRs, and times with the increase of in-plane trajectory lines for the radial and spiral trajectory.

(a) The increase of in-plane acquisitions can effectively alleviate the off-resonance artifact for spiral acquisitions and reduce the under-sampling artifact for radial acquisitions. Also, the time consumption grows as the number of in-plane acquisitions multiplies. Beginning from the top and going clockwise, the vials contain rubber, water, agar, and oil. As the number of spokes/interleaves increases, (b) rubber shows slowly improved SNRs for the spiral acquisitions and rapidly enhanced SNRs for the radial acquisitions, (c) agar demonstrates declined SNRs for the spiral acquisitions and inclined SNRs for the radial acquisitions, (d) water presents similar SNR variations as (c) agar, and (e) oil exhibits similar SNR trends as (b) rubber. However, higher overall SNRs were still observed for all components scanned by the spiral trajectory.



a



b

Figure 4.2. Variations of the artifacts, SNRs, and times with the increase of out-of-plane trajectory lines for the Spiral-Cones trajectory.

(a) The increase of cones can minimize the under-sampling artifact for the 3D Spiral-Cones trajectory; and (b) the SNR measurements associated with the time consumption increase with the growth of cones for all components. Beginning from the top and going clockwise, the vials in the axial view contain rubber, water, agar, and oil.

4.3.2. Improved Cortical Bone Imaging Using the FUSE

With the optimized scan parameters (Table 4.2), the FUSE sequence used a scan with a TE of 0.06 ms to provide a well-defined delineation and enhanced contrast of the cortical bone using the dual-echo subtraction method (Figures 4.3.c and e). For reference, the T2-SPACE scan was not able to directly provide the bone signal, presenting a signal void for the cortical skull bone (Figure 4.3.a). Interestingly images acquired using the PETRA sequence displayed some major artifacts, which are absent from other scans (Figure 4.3.b). The PETRA was able to modestly capture the cortical bone signal but at the expense of very poor bone contrast compared to the FUSE-based ultrashort-TE scan and the subsequent difference image (i.e., the result of the dual-echo subtraction) (Figure 4.3.b vs. Figures 4.3.c and e). Although the long-TE scan (2.46 ms) using the FUSE sequence still present signal void for the cortical bone (Figure 4.3.d), the difference image (i.e., Echo_{0.06}-Echo_{2.46}) provides an enhanced contrast between the cortical bone and the cancellous bone (Figure 4.3.e).

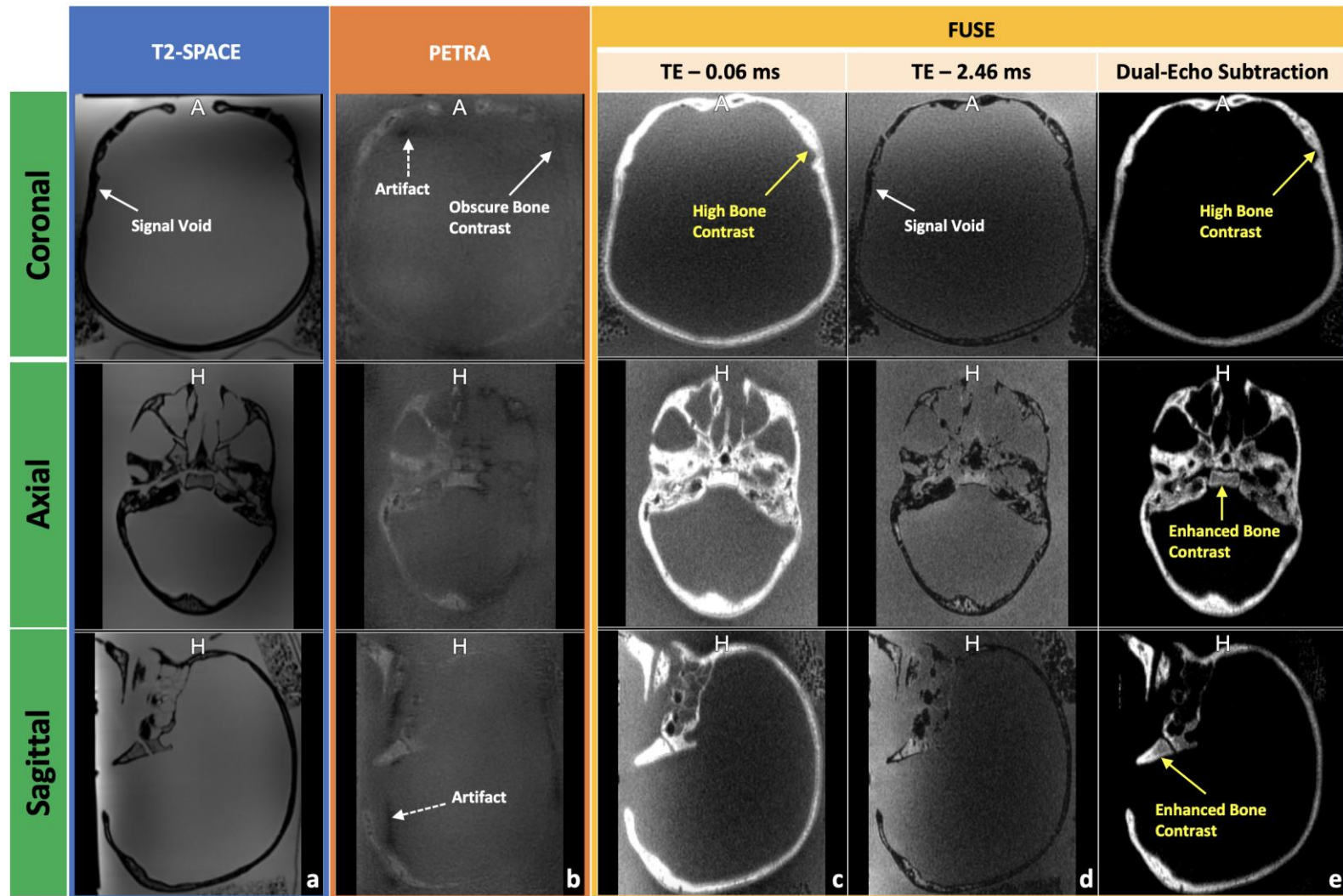


Figure 4.3. Comparison between T2-SPACE, PETRA, and FUSE.

The 3D volumes of the realistic skull phantom presented by (a) T2-weighted SPACE; (b) PETRA; (c) the first echo of the FUSE sequence (Spiral-Cones); (d) the second echo of the FUSE sequence (Spiral-Cones); and (e) the difference image using the first echo minus the second echo. For better visualization, (c-e) use the same window and level settings.

4.3.3. Morphological Comparison between the FUSE and CT

The FUSE sequence was able to delineate the human skull's morphology, and the end result was comparable to CT. After the registration, both the FUSE difference and CT showed a match of the geometry for the skull bone (Figure 4.4.a). Compared to the CT, the FUSE difference image also provided a well-defined cortical bone contrast, showing structural and anatomical details (the yellow boxes in Figure 4.4.b and c). In the 3D rendering results, the FUSE sequence demonstrates the integrity of the skull bone comparable to CT (Figure 4.4.d). After the segmentations, the mask produced by the FUSE difference image shows an acceptable structure similarity with the CT mask with a DSC value of 0.72 (Figure 4.5.a-c).

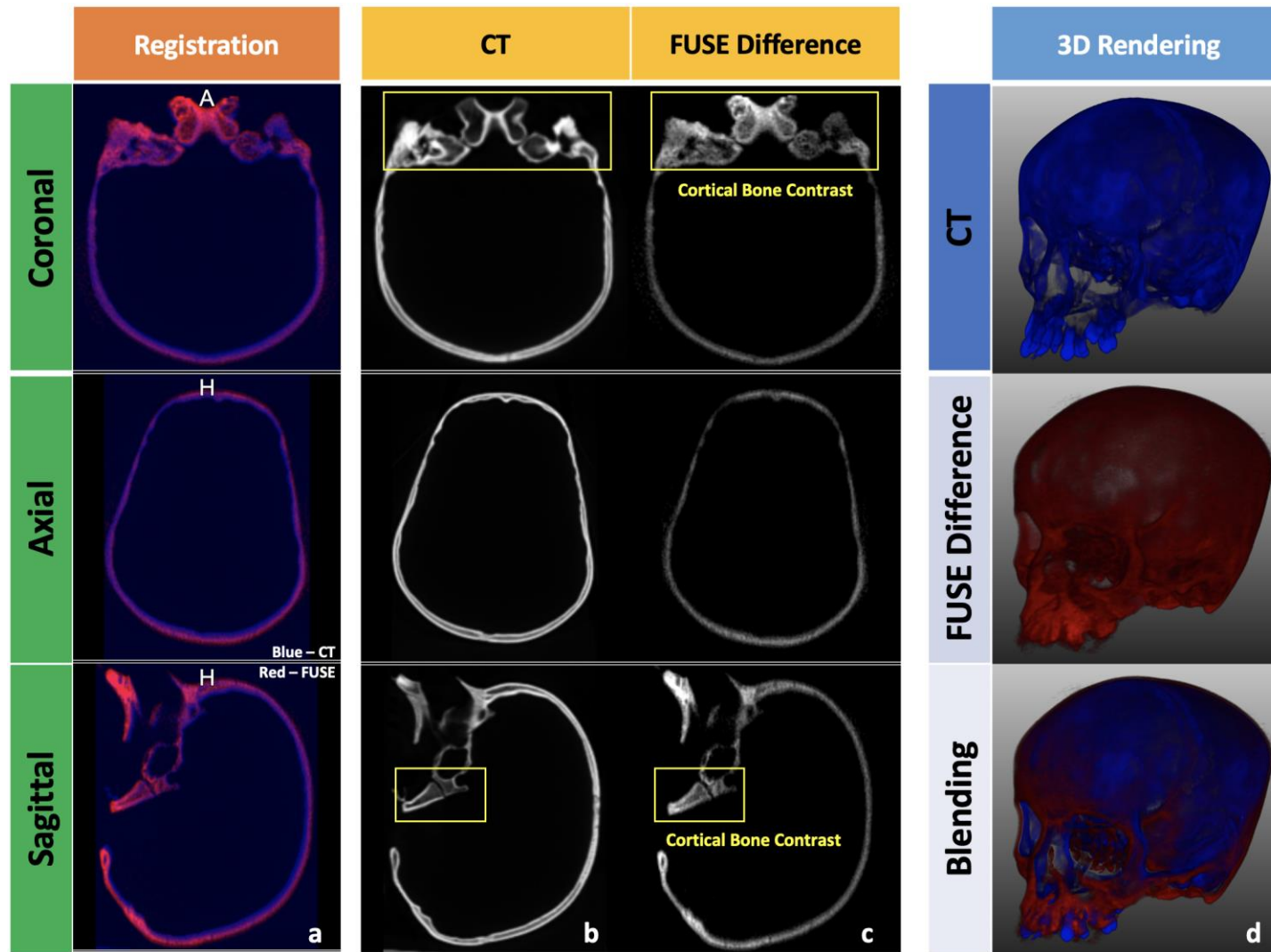


Figure 4.4. Comparison between CT and FUSE.

(a) The co-registered outcome between the CT and the FUSE difference volume; (b) the CT volume; (c) the FUSE difference volume; and (d) the 3D rendering volumes of CT, the FUSE difference, and the blending result. The yellow boxes manifest the cortical bone contrast delineated by two modalities.

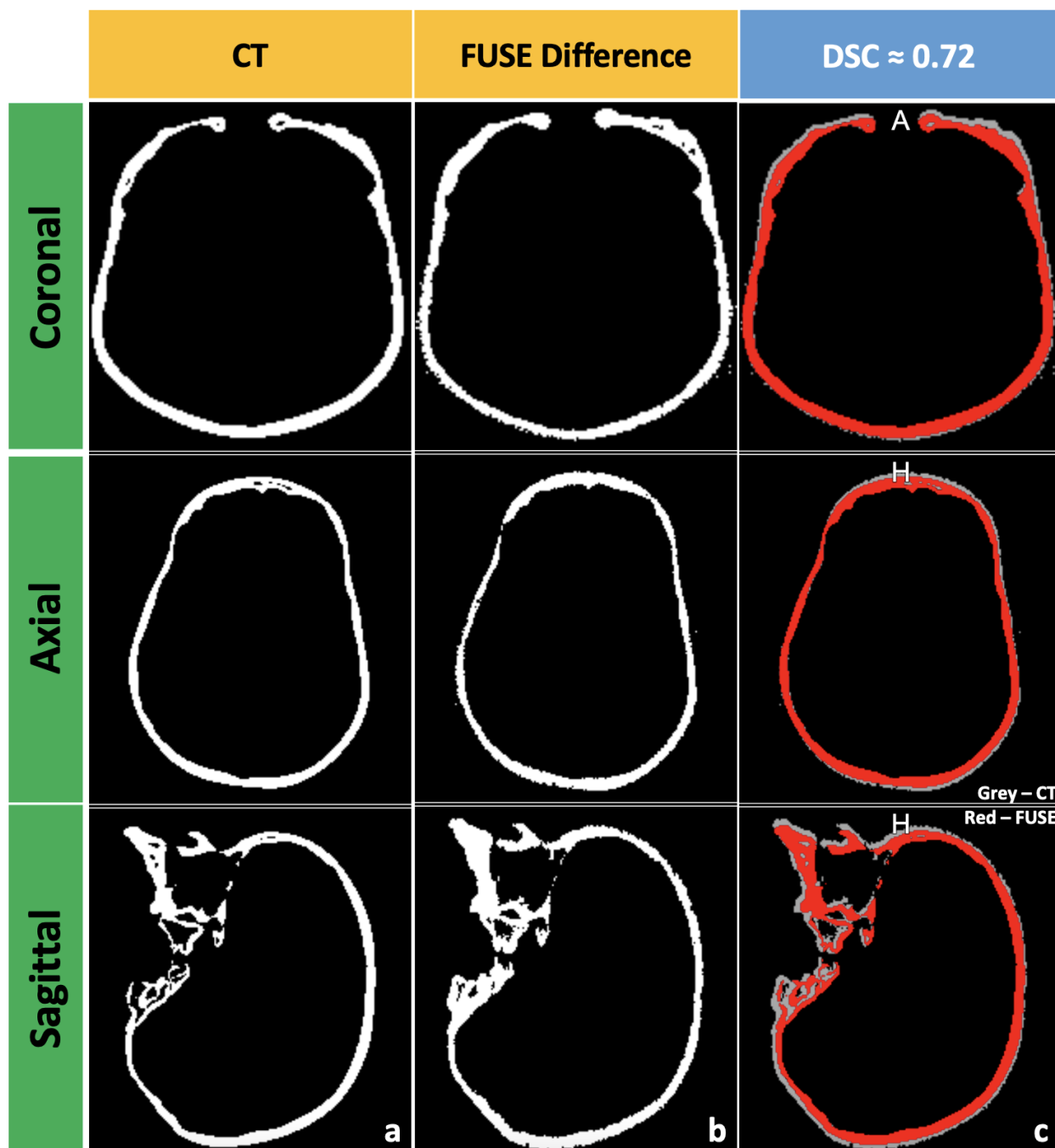


Figure 4.5. Geometrical evaluation between CT and FUSE.

(a) The skull bone mask segmented from the CT volume; (b) the skull bone mask segmented from the FUSE difference volume; (c) the FUSE difference volume superimposed on the CT volume, demonstrating a geometrical similarity with a DSC value around 0.72.

4.3.4. Dose Calculation Results

To demonstrate clinical feasibility, we compare dose distributions calculated using two different imaging data sets, namely the MRI derived sCT and the traditional CT. The comparison between two plans, one created using a synthetic CT derived from our FUSE sequence and one using the standard CT imaging, is shown in Figure 4.6. For the plan created using the synthetic CT we calculated the minimum, maximum, and mean dose to be 1284 cGy, 2181cGy, and 2004cGy, respectively. Similarly, for the plan created using the CT image we calculated the minimum, maximum, and mean dose to be 1344 cGy, 2186cGy, and 2002cGy, respectively. Comparatively the two plans are clinically identical. The mean dose is less than 0.1% different, and dose profiles as seen in Figure 4.6 B, demonstrate very good agreement.

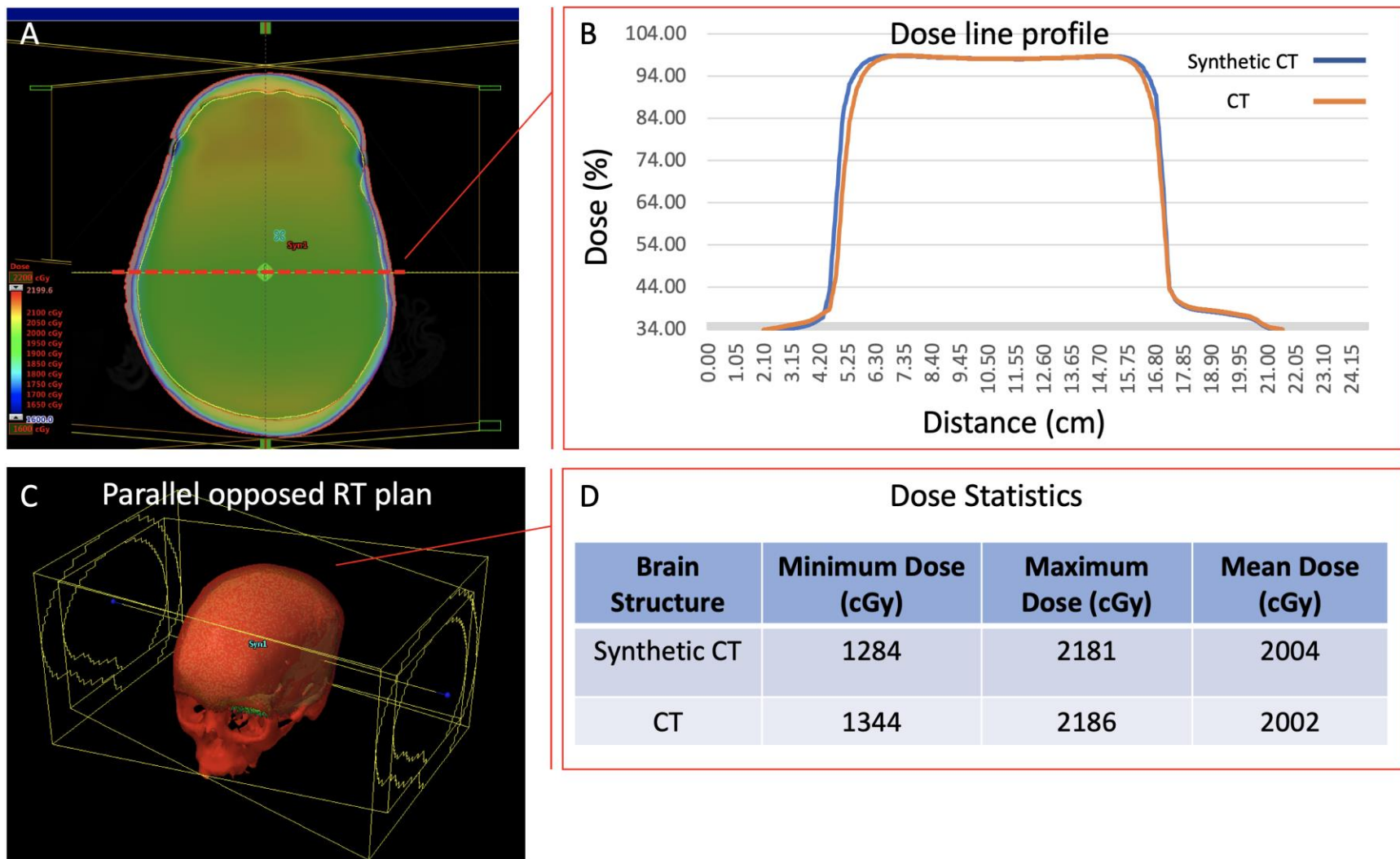


Figure 4.6. Comparison of the dose calculation between two radiation treatment plans using CT and FUSE-derived sCT.

In (A), we present the isodose distribution generated using our newly derived Synthetic CT. In (B) the plot the dose line profile through the center of the human skull for both radiation treatment plans. Both plans followed a simple parallel opposed geometry, utilizing a 6 MV radiation beam as seen in (C). The dose statistics are presented in (D).

4.4. Discussion

Overall, the results in this work show that the FUSE sequence could provide high SNR and artifact-free scans for cortical bone imaging. We were able to use the FUSE sequence to obtain bone images with comparable anatomical details to CT. We also demonstrated the feasibility of the FUSE sequence for sCT generation, and for RTP, the FUSE-derived sCT was able to provide clinically equivalent dosimetry to the true CT.

The spiral trajectory of our FUSE sequence provides demonstrable higher SNR and better artifact reduction than the radial trajectory. As well, we determined more out-of-plane trajectory lines (i.e., cones) are crucial for the Spiral-Cones trajectory for eliminating the artifact, while improving SNR. Compared to the spiral trajectory, the radial trajectory is less vulnerable to the off-resonance artifact due to its shorter activation of ADC within each TR. However, the spiral trajectory is more robust to the under-sampling artifact and able to provide overall higher SNR. This is because the radial trajectory has more efficient k-space coverage (Figures 4.1.a-e). Also, more spiral interleaves can effectively reduce the off-resonance artifact with a shorter ADC activation over each TR cycle, especially for the materials with a chemical shift (e.g., oil or rubber). The off-resonance artifact reduction is the cause of the increase in SNRs of the oil and rubber (Figures 4.1.b and e). On the other hand, more spiral interleaves can also decrease the SNRs of the on-resonance materials (i.e., the water and agar). One possible explanation for this may be that more spiral interleaves can reduce k-space's filling density. Also, by increasing the scanning time this becomes a non-negligible factor as the in-plane spiral interleaves multiply. Using the in-house phantom, the optimization of the use of the FUSE sequence directed us to choose the spiral trajectory for the bone imaging in the synthetic CT generation. However, we must also consider the trade-off between the time, reduction of the artifact, and SNR when selecting the spiral's imaging parameters: better-controlled artifacts and higher SNRs suggest longer scan times. For 3D bone imaging, we also studied the impact of the variation of the out-of-plane trajectory lines (i.e., cones) and discovered that sufficient cone numbers are crucial to the artifact reduction and improvement of SNR (Figures 4.2.a-b). The optimal use of our FUSE sequence is essential for the bone imaging that is used for synthetic CT generation. To our knowledge this has not been extensively studied until now, due to the lack of user-configurable UTE sequence like FUSE.

In comparison to the commercial UTE sequence, PETRA, we were able to use the FUSE sequence with the Spiral-Cones trajectory and optimized sampling scheme to provide an improved bone contrast. The bone contrast ordinarily appears as a signal void in the routine MRI, such as the T2-weighted image produced by the T2-SPACE sequence (Figure 4.3.a). Although the bone delineation can be indirectly retrieved by the inverting of intensities (dark to bright) occasionally, this approach cannot effectively differentiate the bone from the air (230,231). The contrast created by this approach contains both air and bone and can potentially bring errors to the synthetic CT generation. Therefore, a direct imaging method is more desirable for a more accurate representation of bone, which was clearly demonstrated by FUSE. Compared to the PETRA scan, the UTE scan using FUSE exhibits a higher contrast between the bone and the background without artifacts (Figure 4.3.b vs. Figure 4.3.c). One possible explanation is that the FUSE sequence uses a Spiral-Cones trajectory, which could provide higher SNR and reduced artifacts than the hybrid Cartesian-Radial trajectory used by the PETRA sequence. Also, many scan parameters of the PETRA sequence are not configurable and inherently restrict its use. In stark contrast, our FUSE sequence provides more flexibility on the parameter's optimization, e.g., change the Spiral-Cones trajectory's in-plane spiral interleaves or out-of-plane cones, for a higher bone contrast without artifacts.

The dual-echo subtraction technique enabled by the FUSE sequence can enhance the cortical bone contrast for the synthetic CT generation. In a single UTE scan, the acquired MR signal is mixed from the long-T2 (e.g., water or fat) and short-T2 tissues (e.g., bone), and the long-T2 signals could considerably diminish the signal from the bone. Therefore, it was necessary for us to apply the dual-echo subtraction for our FUSE sequence to enhance the cortical bone contrast since a high dynamic range of the bony tissue is key to the optimal generation of synthetic CT (Figure 4.3.e) (115,224). In our study, due to the significantly fast decay in the bone against the much slower decay in the saline (i.e., background), the subtraction can preserve most of the bone signal while diminishing the saline's signal, allowing for an enhanced bone contrast (i.e., a high dynamic range). The dual-echo subtraction method has also been adopted in other synthetic CT studies for its efficacy and simplicity (115,220,224).

The CT scan of the skull bone verified the feasibility of the FUSE sequence for providing comparable bone contrast. As a geometric reference, the CT scan can help us examine any critical distortion of the bone delineation exhibited by our FUSE sequence. Rigid registration is required for the comparison between the FUSE difference image and CT image, even though registration is unnecessary for sCT generation. To refrain the FUSE difference image from interpolation (introduced from the registration), we registered the CT image to the FUSE difference image rigidly (115). As a result, our FUSE difference image provides an overall comparable geometry to the CT data (Figure 4.4.a). After comparing the segmented masks, we found a DSC of 0.72 between both modalities (Figure 4.5.a-c). Our DSC result is slightly lower than a similar study where a DSC of 0.81 was reported (115). Our lower DSC was possibly due to imperfect segmentation, imperfect registration, or MR distortion error. Although the FUSE difference image was able to demonstrate the cortical bone contrast, the presented anatomical details look slightly different from the CT result (the yellow boxes in Figure 4.4.b and c). One possible explanation is that these two imaging modalities have different contrast mechanisms.

It is feasible to use the FUSE sequence to generate the sCT data for the skull bone and apply the sCT data in RTP to produce equivalent dosimetry to the authentic CT data. The dose calculations between the two plans are comparable (i.e., the difference of mean dose is less than 1%), which suggests the FUSE-based synthetic CT data is clinically equivalent to traditional CT (Figure 4.6). Other studies also demonstrated similar dose calculation results between traditional CT and sCT using the bulk density assignment (218,220).

One major limitation of this study was that we did not explore other long-T2 suppression techniques, which might better isolate the cortical bone signal. Another limitation was that we did not perform any geometric distortion correction to our FUSE images. However, this problem still deserves some investigation and could potentially improve the fidelity of the MR-derived CT data. For another limitation, we were unable to include more realistic head anatomy, for example, water, white matter, or grey matter, to evaluate the feasibility of our FUSE sequence for sCT generation.

In future work, we want to explore other long-T2 suppression techniques, which can provide a better delineation for the cortical bone. Also, we want to introduce a geometric distortion correction

function to our FUSE sequence. Last, we will investigate the feasibility of our FUSE sequence for providing the synthetic CT data for *in vivo* cases.

4.5. Conclusion

The spiral trajectory of our FUSE sequence is superior to the radial trajectory for providing a higher SNR efficiency and better artifact control. We used the Spiral-Cones trajectory and the dual-echo subtraction method, obtaining an enhanced cortical bone contrast in the FUSE difference image. The FUSE difference image and CT image demonstrated a DSC of 0.72 for the geometric similarity. The FUSE-based sCT and authentic CT data were respectively used to create radiation treatment plans, showing comparable dosimetry: the dose differences of minimum, maximum, and mean between the two modalities are less than 4.7%, 0.2%, and 0.1%, respectively. In summary, we have shown the feasibility and potential of our FUSE sequence for generating the sCT data that is clinically equivalent to the traditional CT for RTP.

Chapter 5 Integrated Discussions and Future Considerations

Synopsis: This chapter discusses the totality of this work from an overall point of view. The first section summarizes the findings of each chapter. In the second section, the three studies (Chapters 2-4) are discussed altogether. The third section details our contribution from development to evaluation to application. Lastly, we propose specific future directions for expanding our work.

5.1. Summary of Findings

Ultrashort echo time (UTE) sequences can provide direct anatomical detail for short T2 tissues that appear as signal voids on conventional magnetic resonance (MR) images. However, it is unclear what particular UTE techniques and associated parameters are optimal for visualization and quantification for different applications. For example, differing approaches might be necessary to obtain a high-resolution image of skull cortical bone morphology for radiation treatment planning versus to carry out a quantitative T2* relaxation time assessment in the meniscus. The reason for this is that there lacks a sequence that allows for systematic evaluation regarding image quality (producing or diminishing of artifact), signal-to-noise (SNR) ratio and other features particular to the specific application. Therefore, this work proposed a novel Flexible Ultra Short Echo time pulse sequence (i.e., FUSE) featuring thirteen user-configurable acquisition techniques enabled with flexible changes of parameters. We evaluated the application of FUSE in musculoskeletal (MSK) imaging and synthetic computed tomography (sCT) generation. The main findings of this thesis are summarized as follows:

- **The improvement of UTE images can be achieved by optimizing aspects of both acquisition and reconstruction.** The direct comparisons using the FUSE sequence demonstrated that different choices of the acquisition techniques (e.g., the RF pulses, trajectories, and long-T2 suppression techniques) present a varied impact on the reduction

of artifacts, SNR, and contrast enhancement. Also, with a proper adjustment for the various acquisition parameters, the UTE images can be improved with reduced artifacts, higher SNRs, and short-T2 contrast enhancements. As a result of the reconstruction development, we discovered that the novel density correction and the customized off-resonance correction implemented in the reconstruction pipeline could effectively improve the image quality by compensating the artifact. As the novelties of this work, this thesis presents,

- 1) flexible UTE acquisition variations for direct comparisons (FUSE sequence),
- 2) 3D half-Sinc excitations available with the 3D radial ('Koosh-Ball') and 3D Spiral-Cones trajectory,
- 3) new forms of analytic density correction functions for the 2D radial, 3D radial, and 3D spiral trajectory, and
- 4) an extended 3D deblurring algorithm for the correction of the off-resonance artifact.

This chapter conveyed valuable information and guidance on selecting appropriate UTE techniques and parameters for the subsequent MSK and sCT studies.

- **The FUSE sequence can provide superior contrast between short and long T2 tissues in the knee and multi-parametric quantitative mapping of the meniscus, including T1 relaxation time, T2* relaxation time, and QMT parameters.** Both qualitative and quantitative properties of the short T2 tissues are essential for the early assessment of MSK tissue degeneration, in diseases such as knee OA. However, properly retrieving of this information needs specialized UTE techniques, such as the various long-T2 suppression techniques or quantitative magnetization transfer (QMT) modelling using the Spiral-Cones acquisitions. The results of Chapter 3 showed it was feasible to adapt our equipped long-T2 suppression techniques to different short T2 tissues in the knee for the best visualization. Particularly, the magnetization transfer (MT) pulse and FUSE sequence can effectively isolate the cortical bone signal in the magnetization transfer ratio (MTR) image while other long-T2 suppression techniques cannot. Also, our UTE sequence was able to provide robust quantitative imaging methods, including the QMT modelling, T1-mapping, and T2* mapping. As a cutting-edge technique, the combination of the MT pulse (adjustable with the power and frequency offset) and our newly developed UTE acquisition scheme, utilizing a 3D half-Sinc excitation with a Spiral-Cones trajectory, was able to estimate QMT

parameters; we used the meniscus as a model to demonstrate the feasibility. This chapter demonstrated great promise to extend our UTE sequence to *in vivo* studies of healthy and diseased joints and to other short T2 tissues in the knee.

- **The FUSE sequence successfully delineated bone contrast in a manner comparable to CTs, demonstrating the potential for improved synthetic CT generation for RTP.** High-quality UTE images lay the foundation for sCT generation, but the techniques and protocols for cortical bone imaging require systematic optimization of parameters to reduce artifacts, increase SNR, and minimizing time. The results of Chapter 4 showed that the image artifact, SNR, and imaging time were highly dependent on the choice of trajectory and the acquisition parameters-e.g., the numbers of the in-plane trajectory lines or out-of-plane trajectory lines (cones). Most commercially available UTE sequences are not equipped with this flexibility making direct bone imaging for sCT untenable. After understanding the variation, we customized the scan parameters for visualizing the skull bone, and the UTE bone contrast was assessed to be similar to the CT image. This chapter presented the great potential to use the FUSE sequence to develop the MR-only radiation therapy (RT) workflow for use in the routine clinic, which will benefit both patients and clinicians by minimizing assessment time and data processing, respectively.

5.2. General Discussion

5.2.1. Why is UTE important?

Short-T2 tissues, including MSK tissues and cortical bone, are an essential subset of the human body and develop diseases (e.g., OA in the knee) or represent necessary information for treatments (e.g., imaging of cortical bone for MR-only radiation treatment planning, RTP). However, obtaining high-quality MR images of short-T2 tissues for visualization and quantification is always a challenging task. One major setback is that conventional MR techniques cannot provide enough signal for the short-T2 tissues, although these techniques are superior to other modalities like CT for the imaging of soft tissues. The root cause is that some short-T2 tissues have an extremely short T2 (less than 1 ms), which leads to a significantly rapid signal decay before the acquisition. Therefore, researchers have developed UTE pulse sequences to achieve an early signal acquisition for the short-T2 tissues. With numerous UTE techniques developed, many applications, varying

from the MSK tissues to the cortical bone in RTP to imaging the lung, benefit from the visualization and quantification in the short-T2 tissues for providing both research and theranostic information (57,106,232). As demonstrated in Chapter 3, UTE can generate various morphological contrasts in the whole knee, especially for the meniscus, tendon, and cortical bone. Also, UTE allows for quantitative assessment of the T1-mapping, T2*-mapping, and QMT modelling in short-T2 tissues like the meniscus. As another example of the application, in Chapter 4, UTE presents a clear delineation of the skull, including the cortical bone, and exhibits its potential of use in MR-only RTP. In summary, UTE, as a specialized MRI pulse sequence, uncovers the imaging domain of short-T2 tissues, which is not accessible by conventional MRI pulse sequence.

5.2.2. What makes our UTE pulse sequence different?

Our FUSE sequence provides flexible combinations of various acquisition techniques (e.g., RF pulses, trajectories, and long-T2 suppression techniques), allowing for optimizing the use of the sequence for different applications. Researchers usually develop or utilize a single-function UTE sequence, e.g., one half-Sinc pulse with one 2D radial trajectory or one 3D rectangular pulse with one 3D spiral trajectory. They then use it for all the group's work because that is all that is available, not because it is the best approach for the application. However, various UTE techniques have not been compared directly, and the optimal scan functions and parameters used under different scenarios have not been comprehensively investigated. For example, when we approached the UTE-QMT portion of the MSK study in Chapter 3 our questions include what techniques and parameters were required to ensure a well-sampled acquisition while retaining minimal RF energy deposition from the high-power magnetization transfer (MT) pulse recurring in each acquiring cycle for multiple scans. In Chapter 4 we had to determine the best trajectory and associated parameters to produce the artifact-free and both SNR- and time-efficient images demanded in sCT generation. To answer these questions with valid evidence, researchers need a sequence that has the capability to compare different UTE techniques head-to-head with varying parameters for evaluation. Our sequence meets this need. Specifically, our sequence provides flexible scan combinations, including the options of half-Sinc and rectangular RF pulse, radial and spiral trajectory, 2D/3D dimension, and multiple long-T2 suppression techniques. The evaluation results in Chapter 2 showed that that spiral interleaves as few as 64 could sufficiently produce a fully sampled scan, and high bandwidth and auto-deblurring algorithm would effectively improve image

quality by repressing the off-resonance artifact. These results informed our design of the UTE-QMT protocols in Chapter 3; specifically, that the RF deposition could exceed the SAR limit as the number of spiral interleaves mounted, and the fat (widely distributed in the knee) could lead to the off-resonance artifact. Further, the evaluation results in Chapter 4 suggested that the spiral trajectory was more suitable in sCT generation for providing better control of artifact with more SNR- and time-efficient short-T2 imaging than the radial trajectory. Thus, what we learned in Chapter 2 is instrumental in informing our work and also the work of others in the field in terms of the trade-offs between different UTE parameters. No other study has made this important comparison to date. Likewise, we also characterized other UTE techniques and the associated parameters in Chapter 2, and the outcomes provided us instructive guidance for the applications in Chapters 3 and 4. In summary, what makes our FUSE sequence different is its flexibility for the scan customization for a particular application, for example, cortical bone imaging using MTR contrast.

5.2.3. How can we take advantage of our flexible UTE sequence?

Our sequence provides flexibility by varying the UTE acquisition techniques and parameters, which can support many applications. For qualitative imaging, we enabled multiple long-T2 suppression techniques for the sequence, including the dual-echo subtraction, water/fat saturation pulse, and MT pulse, which could produce various morphological contrasts by selectively targeting specified long-T2 materials while highlighting other short-T2 and long-T2 components. In Chapter 2, we evaluated the suppression performance of each technique on various materials, i.e., rubber (short-T2), water, grapeseed oil, and agar. Knowing their characteristics of suppression and enhancement, we further applied and evaluated these techniques for whole knee imaging in Chapter 3. Understanding that the knee is an integrated MSK system comprised of many different types of long-T2 (e.g., muscle, marrow, or fat) and short-T2 tissues (e.g., tendon, meniscus, or cortical bone), we found that the contrast enhancement for each short-T2 tissue type varied between these techniques. Thus, parameter choice may differ depending on the tissue of interest. Moreover, in Chapter 4, we adopted the dual-echo subtraction technique and successfully extracted the cortical bone contrast from the long-T2 background-i.e., saline water. These techniques make our sequence a multi-contrast imaging tool that allows for specific short-T2 tissue enhancement. There are infinite possibilities of how contrast can be scaled and combined to highlight and suppress various

signals acquired using our sequence. Also, our evaluations show that our sequence is promising for utilization in other potential short T2 imaging. Quantitative-imaging-wise, besides the regular T1 and T2* mapping achieved by the variable-flip-angle (VFA) and variable-time-of-echo (VTE) method, the adjustable MT pulse also grants our UTE sequence the capability of QMT modelling (this combination is still a relatively new quantification attempt with only one other group in the world doing UTE-QMT (179)). In Chapter 3, we demonstrated that all these techniques could estimate the intrinsic MR properties of the meniscus, providing enriched quantitative information, especially the UTE-QMT mapping. These estimated property parameters can potentially serve as biomarkers, which we can use to characterize both healthy tissues and the disease or degeneration specifically happening within short-T2 tissues, similar to the successful quantitative mapping work that has been done in articular cartilage using cartesian sequences (106,173,174). To sum up, using our FUSE sequence, we can compare different acquisition techniques with matching parameters (e.g., the spiral and the radial trajectory with the same in-plane trajectory lines) to determine the optimal acquisition scheme and parameters for a particular application.

5.3. Scientific Contributions

This thesis centered around our novel FUSE sequence from development to evaluation to application; many contributions were made in terms of these three aspects:

For the novelties about the development detailed in Chapter 2,

1. We developed a pulse sequence that included variable options for the RF pulse, trajectory, dimension scheme (2D/3D), and long-T2 suppression method, allowing for direct comparisons between varying acquisitions.
2. We implemented a 3D half-Sinc RF pulse with and without a variable-rate selective excitation (VERSE) modification; these 3D half-sinc pulses can be flexibly combined with the 3D radial ('koosh-ball') and 3D Spiral-Cones trajectory.
3. We proposed new forms of analytic density correction functions for the 2D radial, 3D radial, and 3D spiral trajectory, which all showed improved performance.
4. We mathematically re-derived in three dimensions the auto-deblurring algorithm, which has never been done before (the original algorithm was proposed in 2D (123)).

For the novelties regarding the evaluation detailed in Chapter 2,

1. We compared three pathways for correcting the off-resonance artifact in spiral scans, including multiplying the spiral interleaves during the acquisition, increasing bandwidth during the acquisition, and turning on the auto-deblurring correction algorithm during the reconstruction. We discovered that increasing either the bandwidth or the spiral interleaves could effectively suppress the off-resonance artifact. Also, we found that introducing the auto-deblurring correction algorithm to either of two methods can help eliminate the artifact, which would be a better option over others. For example, in our studies, at least 410 Hz for the bandwidth-per-pixel or 128 spiral interleaves was required to obtain an artifact-free image if the auto-deblurring correction algorithm was also on. (These settings are subject to changes of other scan parameters, for example, the field-of-view). However, determining the best approach for correcting the off-resonance artifact in spiral scans still needs more quantification. In addition, we also found that increases of both bandwidth and spiral interleaves simultaneously were not possible due to the system's limitations.
2. We discussed the optimal combination of the RF pulse and the trajectory from the viewpoints of contrast, SNR, and time efficiency; this evaluation is novel majorly because the 3D half-Sinc pulses (including the VERSE modification) have not been evaluated between themselves or against the rectangular pulse when combining with different 3D trajectories. With matchable scan settings, we were able to show that the combinations between the Spiral-Cones trajectory and all the 3D RF pulses present better SNRs than the combinations using the 3D radial trajectory.
3. We showed that the VERSE-modified 3D half-Sinc pulse allowed for an absolute, shorter minimal TE than the rectangular pulse and regular 3D half-Sinc pulse. The reason was that the VERSE-modified half-Sinc pulse's duration was not counted in the minimal TE calculation, and this pulse itself also does not require the refocusing gradient. Also, we found that the regular and the VERSE-modified 3D half-Sinc pulse can provide comparable outcomes in terms of contrast and SNR; this comparison has not been carried out before to the best of our knowledge. Last, prescribed with the same RF flip angles for each intact RF pulse (i.e., the flip angle for two half-Sinc pulses is equal to the one for one rectangular pulse), the two 3D half-Sinc pulses (including the VERSE modification) present a different

contrast than the rectangular pulse. This observation was found in our study, and it deserves further investigation.

4. Using the VERSE-modified 3D half-Sinc pulse, we presented the shortest minimal TE of 20 us enabled by our FUSE sequence, which is also the Siemens system's permissible TE limitation.
5. We comprehensively compared the various long-T2 suppression techniques implemented in our FUSE sequence in terms of the enhanced contrast and SNR. In comparison to other common long-T2 suppression techniques, including the dual-echo subtraction, fat-saturation pulse, and water-saturation pulse, the results showed that the MT saturation provided by the UTE sequence was able to achieve an almost complete suppression for the water and oil. The produced MT contrast using UTE is unusual but will be very useful in knee imaging for suppressing the enriched fat signal (as an alternative to the commonly used fat-saturation pulse).

For the novelties exhibited by the applications detailed in Chapters 3 and 4,

1. A comprehensive comparison has not been assessed among various long-T2 suppression methods directly before (Chapter 3). We utilized the various long-T2 suppression techniques in our FUSE sequence to create morphologic images that isolate signals from the different knee joint tissues. As enlightened by Chapter 2, we used our FUSE sequence with the MT-saturation to scan the whole knee and showed that this method could exclusively isolate the cortical bone signal in the MTR contrast.
2. We developed UTE-QMT protocols using a novel combination of 3D half-Sinc pulse excitation and Spiral-Cones trajectory to quantify menisci as other studies mainly used 3D rectangular pulse excitation with Spiral-Cones trajectory for 3D UTE-QMT modelling (92,158). Also, we studied the impacts of the absorption lineshape (Gaussian vs. Super-Lorentzian) and B1 correction on the outcomes of the UTE-QMT fitting (Chapter 3). and
3. To develop optimal UTE protocols for cortical bone imaging in sCT generation, we used the FUSE sequence to carry out a systematic evaluation that used the trajectory types and their parameters for acquisition sampling as the controlled variables to assess the variation of artifact, SNR, and time consumption. This work demonstrated that the treatment plans using true CT and FUSE-derived sCT data produced similar dosimetric results (Chapter 4).

5.4. Overall Strengths and Limitations

The specific strengths and limitations of this work have been detailed in each chapter. Therefore, this section primarily focuses on the strengths and limitations from an overall point of view.

5.4.1. Strengths

The major strength of this thesis is that I have spent several years developing a sophisticated working MRI pulse sequence (i.e., FUSE). The development of the sequence and its reconstruction pipeline required me to practically use physical principles and convert mathematic expressions into practical biomedical engineering solutions. This means I needed to understand the theories of the various UTE techniques and be able to implement them through programming and make sure they could return expected results. Also, I needed to ensure the programmed sequence complied meeting hardware conditions and passed safety tests since we never want to cause danger to patients or/and damage the equipment. Gathering from all the experiments performed, we are certain that our sequence meets all system safety standards. Besides these, we are confident in our results for generally providing comparable, if not superior, results with a packaged Siemens UTE sequence.

5.4.2. Limitations and Challenges

One major limitation that played a factor through the course of performing my research was that due to the COVID-19 pandemic. The pandemic presented challenges to performing human studies. For example, I was not able to scan human knee cadavers as planned because I did not have access to these resources during this unprecedented period. To overcome this crisis, we had to make some necessary compromises for my research without undermining the quality of this work. Therefore, we switched to the bovine stifle joint samples, which can provide realistic tissue properties for carrying on my imaging tests. This change of plan was not ideal but helped me finish my thesis.

Another challenge was that the 3 Tesla scanner previously available for my research became unavailable due to tightening hospital resources. This change led me to collect data at the Hospital for Sick Children in Toronto.

Another limitation was that a single-set offline reconstruction for the FUSE sequence could take hours to finish. As my computer for the sequence development does not have the computational power that the scanner has, I spent many months obtaining all my results for one experiment. I chose to develop my reconstruction pipeline on my computer instead of using the inline reconstruction development software is because I needed to implement many investigational techniques, including my novel regridding approach and off-resonance correction algorithm. This option was efficient for the development but not for the data collection. For example, the reconstruction time for one dataset can be up to 8 hours on a laptop.

5.5. Future Work

Ultimately, we aim to translate our FUSE sequence into *in vivo* clinical applications with a broader scope, ranging from MSK imaging to sCT generation to proton lung imaging. However, before that, there are still some aspects of the work that we would like to improve upon:

1. Our current FUSE sequence uses offline reconstruction, which is workable and sufficient for research. However, in an *in vivo* clinical environment, we would prefer an inline, on-scanner reconstruction that allows for a real-time image examination. This scenario is

crucial for facilitating the clinical workflow in terms of time-saving where clinicians do not need to wait for the raw MR data to be ported offline and reconstructed later.

2. We also want to explore other reconstruction methods like NUFFT for the FUSE sequence and contrast it with the current gridding-based reconstruction algorithm. We might want to retain multiple reconstruction methods for users to achieve customized or optimal reconstruction results (for a specific application).
3. We could also make our FUSE sequence compatible with higher field strengths, for example, 7 Tesla, since our current FUSE sequence was developed on a 3 Tesla system. 7 Tesla systems are becoming more feasible in a research or clinical setting. The higher field strength means a stronger signal, so the imaging of short T2 tissues using the FUSE sequence could really benefit from gaining the stronger signal enabled by the 7 Tesla system.
4. Since our FUSE sequence uses non-Cartesian trajectories for 2D and 3D acquisitions, we will need to evaluate the potential geometric distortion introduced by the different trajectories and develop the corresponding correction algorithms. The distortion assessment is essential for sCT generation using UTE sequences to assist a safe and effective MR-only radiation therapy delivery.
5. For *in vivo* applications, clinicians and researchers always appreciate efficient scans, including UTE acquisitions. Therefore, we could explore the parallel imaging or the compressed sensing technique for implementation in our FUSE sequence for better efficiency (233,234). These acceleration techniques could potentially shorten the entire scan time of the quantitative imaging whose fitting models require multiple sampling (i.e., acquisition sets), especially for 3D *in vivo* quantification involving the QMT or the VTE-T2* modelling.
6. Last, although the centre-out non-Cartesian trajectories (like the 2D/3D radial and spiral in our sequence) are relatively insensitive to motion (comparing to the Cartesian trajectory), their motion sensitivity deserves more investigation for application in proton lung imaging. To compensate for the motion introduced by breathing, we will need to develop the gating or navigator technique suitable for our sequence.

5.6. Conclusion

The FUSE is the first UTE sequence that provides robust, flexible acquisition options from the various RF pulses to trajectories to long-T2 suppression techniques. In this work, we have demonstrated that it was feasible to employ the FUSE sequence to create morphological images that isolate signals from the various tissues in the knee. We have also shown that it was feasible to utilize the FUSE sequence to provide a comprehensive quantitative evaluation for the meniscus, including the biomarkers of UTE-T1, UTE-T2*, and the various UTE-QMT parameters. Last, we applied the FUSE sequence for the skull bone imaging and were able to generate the sCT data. The generated sCT data using the FUSE was able to provide dosimetric equivalence to the 'true' CT data, proving the FUSE's clinical feasibility in radiation treatment planning.

In this thesis, a flexible, product-quality UTE sequence that incorporated various acquisition options was developed, which allowed us to directly compare sequence features and optimize short T2 imaging methods for different applications.

References

1. Suetens P. *Fundamentals of Medical Imaging*. Cambridge University Press; 2009. 265 p.
2. Chavhan GB, Babyn PS, Thomas B, Shroff MM, Haacke EM. Principles, Techniques, and Applications of T2*-based MR Imaging and Its Special Applications. *RadioGraphics*. 2009 Sep 1;29(5):1433–49.
3. Du J, Takahashi AM, Chung CB. Ultrashort TE spectroscopic imaging (UTESI): Application to the imaging of short T2 relaxation tissues in the musculoskeletal system. *J Magn Reson Imaging*. 2009;29(2):412–21.
4. Chang EY, Du J, Chung CB. UTE imaging in the musculoskeletal system. *J Magn Reson Imaging*. 2015 Apr;41(4):870–83.
5. Gold GE, Han E, Stainsby J, Wright G, Brittain J, Beaulieu C. Musculoskeletal MRI at 3.0 T: relaxation times and image contrast. *AJR Am J Roentgenol*. 2004 Aug;183(2):343–51.
6. Stanisz GJ, Odrobina EE, Pun J, Escaravage M, Graham SJ, Bronskill MJ, et al. T1, T2 relaxation and magnetization transfer in tissue at 3T. *Magn Reson Med*. 2005 Sep;54(3):507–12.
7. Robson MD, Bydder GM. Clinical ultrashort echo time imaging of bone and other connective tissues. *NMR Biomed*. 2006 Nov 1;19(7):765–80.
8. Chaudhari AS, Sveinsson B, Moran CJ, McWalter EJ, Johnson EM, Zhang T, et al. Imaging and T2 relaxometry of short-T2 connective tissues in the knee using ultrashort echo-time double-echo steady-state (UTEDESS). *Magn Reson Med*. 2017 Jan 1;n/a-n/a.
9. Henkelman RM, Stanisz GJ, Graham SJ. Magnetization transfer in MRI: A review. *NMR Biomed*. 2001;14(2):57–64.
10. Bydder GM. The Agfa Mayneord lecture: MRI of short and ultrashort T2 and T2* components of tissues, fluids and materials using clinical systems. *Br J Radiol*. 2011 Dec;84(1008):1067–82.
11. Weiger M, Pruessmann KP. Short-T2 MRI: Principles and recent advances. *Prog Nucl Magn Reson Spectrosc*. 2019 Oct 1;114–115:237–70.
12. Robson MD, Gatehouse PD, Bydder M, Bydder GM. Magnetic Resonance: An Introduction to Ultrashort TE (UTE) Imaging. *J Comput Assist Tomogr*. 2003;27(6):825–46.
13. Qian Y, Williams AA, Chu CR, Boada FE. Repeatability of ultrashort echo time-based two-component T2* measurements on cartilages in human knee at 3 T. *Magn Reson Med*. 2013;69(6):1564–71.
14. Bergin CJ, Pauly JM, Macovski A. Lung parenchyma: Projection reconstruction MR imaging. *Radiology*. 1991;

15. Gold GE, Pauly JM, Macovski A, Herfkens RJ. MR Spectroscopic imaging of collagen: Tendons and knee menisci. *Magn Reson Med.* 1995;34(5):647–54.
16. Conolly S, Nishimura D, Macovski A, Glover G. Variable-rate selective excitation. *J Magn Reson* 1969. 1988;78(3):440–58.
17. Glover GH. Simple analytic spiral K-space algorithm. *Magn Reson Med.* 1999;42(2):412–5.
18. Cline HE, Zong X, Gai N. Design of a logarithmic k-space spiral trajectory. *Magn Reson Med.* 2001;46(6):1130–5.
19. Rahmer J, Börnert P, Groen J, Bos C. Three-dimensional radial ultrashort echo-time imaging with T2 adapted sampling. *Magn Reson Med.* 2006;55(5):1075–82.
20. Li S, Chang EY, Bae WC, Chung CB, Hua Y, Zhou Y, et al. The effect of excitation and preparation pulses on nonslice selective 2D UTE bicomponent analysis of bound and free water in cortical bone at 3T. *Med Phys.* 2014;41(2):1–9.
21. Ma YJ, Chang EY, Bydder GM, Du J. Can ultrashort-TE (UTE) MRI sequences on a 3-T clinical scanner detect signal directly from collagen protons: freeze–dry and D2O exchange studies of cortical bone and Achilles tendon specimens. *NMR Biomed.* 2016;29(7):912–7.
22. Abbasi-Rad S, Rad HS. Quantification of human cortical Bone Bound and Free Water in Vivo with Ultrashort echo Time MR imaging: A Model-based Approach. *Radiology.* 2017;283(3):862–74.
23. Gatehouse PD, Bydder GM. Magnetic Resonance Imaging of Short T2 Components in Tissue. *Clin Radiol.* 2003 Jan 1;58(1):1–19.
24. Mastrogiacomo S, Dou W, Jansen JA, Walboomers XF. Magnetic Resonance Imaging of Hard Tissues and Hard Tissue Engineered Bio-substitutes. *Mol Imaging Biol.* 2019 Dec 1;21(6):1003–19.
25. O’Sullivan JD. Fast Sinc Function Gridding Algorithm for Fourier Inversion in Computer Tomography. *IEEE Trans Med Imaging.* 1985;MI-4(4):200–7.
26. Jackson JI, Meyer CH, Nishimura DG, Macovski A. Selection of a Convolution Function for Fourier Inversion Using Gridding. *IEEE Trans Med Imaging.* 1991;10(3):473–8.
27. Pauly JM. Gridding & the NUFFT for Non-Cartesian Image Reconstruction. *ISMRM Educ Course Image Reconstr.* 2012;20:4–6.
28. Pauly J, Nishimura D, Macovski A. A k-space analysis of small-tip-angle excitation. *J Magn Reson* 1969. 1989 Jan 1;81(1):43–56.

29. Wansapura JP, Daniel BL, Pauly J, Butts K. Temperature mapping of frozen tissue using eddy current compensated half excitation RF pulses. *Magn Reson Med.* 2001;46(5):985–92.
30. Hargreaves BA, Cunningham CH, Nishimura DG, Conolly SM. Variable-rate selective excitation for rapid MRI sequences. *Magn Reson Med.* 2004;52(3):590–7.
31. Du J, Pak BC, Znamirovski R, Statum S, Takahashi A, Chung CB, et al. Magic angle effect in magnetic resonance imaging of the Achilles tendon and enthesis. *Magn Reson Imaging.* 2009;27(4):557–64.
32. Du J, Ma G, Li S, Carl M, Szeverenyi NM, VandenBerg S, et al. Ultrashort echo time (UTE) magnetic resonance imaging of the short T2 components in white matter of the brain using a clinical 3T scanner. *NeuroImage.* 2014 Feb;87(1):32–41.
33. Rettenmeier C, Stenger VA. Radiofrequency phase encoded half-pulses in simultaneous multislice ultrashort echo time imaging. *Magn Reson Med.* 2019;81(6):3720–33.
34. Techawiboonwong A, Song HK, Wehrli FW. In vivo MRI of submillisecond T2 species with two-dimensional and three-dimensional radial sequences and applications to the measurement of cortical bone water. *NMR Biomed.* 2008 Jan;21(1):59–70.
35. Du J, Carl M, Bae WC, Statum S, Chang EY, Bydder GM, et al. Dual inversion recovery ultrashort echo time (DIR-UTE) imaging and quantification of the zone of calcified cartilage (ZCC). *Osteoarthritis Cartilage.* 2013 Jan;21(1):77–85.
36. Konstandin S, Schad LR. Two-dimensional radial sodium heart MRI using variable-rate selective excitation and retrospective electrocardiogram gating with golden angle increments. *Magn Reson Med.* 2013;70(3):791–9.
37. Rad HS, Lam SCB, Magland JF, Ong H, Li C, Song HK, et al. Quantifying cortical bone water in vivo by three-dimensional ultra-short echo-time MRI. *NMR Biomed.* 2011 Aug;24(7):855–64.
38. Takizawa M, Hanada H, Oka K, Takahashi T, Yamamoto E, Fujii M. A Robust Ultrashort TE (UTE) imaging method with corrected k-space trajectory by using parametric multiple function model of gradient waveform. *IEEE Trans Med Imaging.* 2013;32(2):306–16.
39. Johnson KM, Fain SB, Schiebler ML, Nagle S. Optimized 3D ultrashort echo time pulmonary MRI. *Magn Reson Med.* 2013;70(5):1241–50.
40. Herrmann KH, Krämer M, Reichenbach JR. Time efficient 3D radial UTE sampling with fully automatic delay compensation on a clinical 3T MR scanner. *PLoS ONE.* 2016;11(3):1–16.
41. Nazaran A, Carl M, Ma Y, Jerban S, Zhu Y, Lu X, et al. Three-dimensional adiabatic inversion recovery prepared ultrashort echo time cones (3D IR-UTE-Cones) imaging of cortical bone in the hip. *Magn Reson Imaging.* 2017;44:60–4.

42. Lauterbur PC. Image formation by induced local interactions: Examples employing nuclear magnetic resonance. *Nature*. 1973;
43. Riemer F, Solanky BS, Stehning C, Clemence M, Wheeler-Kingshott CAM, Golay X. Sodium (^{23}Na) ultra-short echo time imaging in the human brain using a 3D-Cones trajectory. *Magn Reson Mater Phys Biol Med*. 2014;27(1):35–46.
44. Glover GH, Pauly JM. Projection Reconstruction Techniques for Reduction of Motion Effects in MRI. *Magn Reson Med*. 1992;
45. Glover GH, Pauly JM, Bradshaw KM. Boron-11 imaging with a three-dimensional reconstruction method. *J Magn Reson Imaging*. 1992;
46. Spielman DM, Pauly JM, Meyer CH. Magnetic resonance fluoroscopy using spirals with variable sampling densities. *Magn Reson Med*. 1995;34(3):388–94.
47. Kim DH, Adalsteinsson E, Spielman DM. Simple analytic variable density spiral design. *Magn Reson Med*. 2003;50(1):214–9.
48. Du J, Bydder M, Takahashi AM, Chung CB. Two-dimensional ultrashort echo time imaging using a spiral trajectory. *Magn Reson Imaging*. 2008;26(3):304–12.
49. Irrarrazabal P, Nishimura DG. Fast Three Dimensional Magnetic Resonance Imaging. *Magn Reson Med*. 1995;
50. Gurney PT, Hargreaves BA, Nishimura DG. Design and analysis of a practical 3D cones trajectory. *Magn Reson Med*. 2006;55(3):575–82.
51. Qian Y, Boada FE. Acquisition-weighted stack of spirals for fast high-resolution three-dimensional ultra-short echo time MR imaging. *Magn Reson Med*. 2008;60(1):135–45.
52. Boada FE, Gillen JS, Shen GX, Chang SY, Thulborn KR. Fast three dimensional sodium imaging. *Magn Reson Med*. 1997;37(5):706–15.
53. Pipe JG, Zwart NR, Aboussouan EA, Robison RK, Devaraj A, Johnson KO. A new design and rationale for 3D orthogonally oversampled k-space trajectories. *Magn Reson Med*. 2011;66(5):1303–11.
54. Kumar S, Rai R, Stemmer A, Josan S, Holloway L, Vinod S, et al. Feasibility of free breathing Lung MRi for Radiotherapy using non-Cartesian k-space acquisition schemes. *Br J Radiol*. 2017;90(1080):1–10.
55. Dournes G, Yazbek J, Benhassen W, Benlala I, Blanchard E, Truchetet ME, et al. 3D ultrashort echo time MRI of the lung using stack-of-spirals and spherical k-Space coverages: Evaluation in healthy volunteers and parenchymal diseases. *J Magn Reson Imaging*. 2018;48(6):1489–97.

56. Robison RK, Anderson AG, Pipe JG. Three-dimensional ultrashort echo-time imaging using a FLORET trajectory. *Magn Reson Med.* 2017;78(3):1038–49.
57. Willmerring MM, Robison RK, Wang H, Pipe JG, Woods JC. Implementation of the FLORET UTE sequence for lung imaging. *Magn Reson Med.* 2019;82(3):1091–100.
58. Zwart NR, Johnson KO, Pipe JG. Efficient sample density estimation by combining gridding and an optimized kernel. *Magn Reson Med.* 2012;67(3):701–10.
59. Dutt A, Rokhlin V. Fast Fourier Transforms for Nonequispaced Data. *SIAM J Sci Comput.* 1993;14(6):1368–93.
60. Sarty GE, Bennett R, Cox RW. Direct reconstruction of non-Cartesian k-space data using a nonuniform fast Fourier transform. *Magn Reson Med.* 2001 May;45(5):908–15.
61. Motaal AG, Noorman N, de Graaf WL, Hoerr V, Florack LMJ, Nicolay K, et al. Functional imaging of murine hearts using accelerated self-gated UTE cine MRI. *Int J Cardiovasc Imaging.* 2014;31(1):83–94.
62. Chen L, Liu D, Zhang J, Xie B, Zhou X, Grimm R, et al. Free-breathing dynamic contrast-enhanced MRI for assessment of pulmonary lesions using golden-angle radial sparse parallel imaging. *J Magn Reson Imaging.* 2018 Aug;48(2):459–68.
63. Zhang J, Feng L, Otazo R, Kim SG. Rapid dynamic contrast-enhanced MRI for small animals at 7T using 3D ultra-short echo time and golden-angle radial sparse parallel MRI. *Magn Reson Med.* 2019;81(1):140–52.
64. Siriwanarangsun P, Statum S, Biswas R, Bae WC, Chung CB. Ultrashort time to echo magnetic resonance techniques for the musculoskeletal system. *Quant Imaging Med Surg.* 2016;6(6):731–43.
65. Bae WC, Biswas R, Chen K, Chang EY, Chung CB. UTE MRI of the Osteochondral Junction. *Curr Radiol Rep.* 2014;2(2).
66. Du J, Takahashi AM, Bae WC, Chung CB, Bydder GM. Dual inversion recovery, ultrashort echo time (DIR UTE) imaging: Creating high contrast for short-T2 species. *Magn Reson Med.* 2010;63(2):447–55.
67. Du J, Bydder M, Takahashi AM, Carl M, Chung CB, Bydder GM. Short T2 contrast with three-dimensional ultrashort echo time imaging. *Magn Reson Imaging.* 2011 May;29(4):470–82.
68. Li C, Magland JF, Rad HS, Song HK, Wehrli FW. Comparison of optimized soft-tissue suppression schemes for ultrashort echo time MRI. *Magn Reson Med.* 2012;68(3):680–9.
69. Rahmer J, Blume U, Börnert P. Selective 3D ultrashort TE imaging: Comparison of “dual-echo” acquisition and magnetization preparation for improving short-T2 contrast. *Magn Reson Mater Phys Biol Med.* 2007;20(2):83–92.

70. Li S, Huang X, Li G, Zhang Y, Li Z, Liu L, et al. Exponential subtraction in 3D ultrashort echo time imaging to visualize short T2 tissues in tibia. *Acta Radiol.* 2019;
71. Lee YH, Kim S, Song HT, Kim IS, Suh JS. Weighted subtraction in 3D ultrashort echo time (UTE) imaging for visualization of short T2 tissues of the knee. *Acta Radiol.* 2014;55(4):454–61.
72. Du J, Takahashi AM, Bydder M, Chung CB, Bydder GM. Ultrashort TE imaging with off-resonance saturation contrast (UTE-OSC). *Magn Reson Med.* 2009;62(2):527–31.
73. Larson PEZ, Gurney PT, Nayak K, Gold GE, Pauly JM, Nishimura DG. Designing long-T2 suppression pulses for ultrashort echo time imaging. *Magn Reson Med.* 2006;56(1):94–103.
74. Ma YJ, Zhu Y, Lu X, Carl M, Chang EY, Du J. Short T2 imaging using a 3D double adiabatic inversion recovery prepared ultrashort echo time cones (3D DIR-UTE-Cones) sequence. *Magn Reson Med.* 2018;79(5):2555–63.
75. Carl M, Ma Y, Du J. Theoretical analysis and optimization of ultrashort echo time (UTE) imaging contrast with off-resonance saturation. *Magn Reson Imaging.* 2018 Jul;50(5):12–6.
76. Williams A, Qian Y, Bear D, Chu CR. Assessing degeneration of human articular cartilage with ultra-short echo time (UTE) T2* mapping. *Osteoarthritis Cartilage.* 2010;18(4):539–46.
77. Juras V, Apprich S, Zbýň Š, Zak L, Deligianni X, Szomolanyi P, et al. Quantitative MRI analysis of menisci using biexponential T2* fitting with a variable echo time sequence. *Magn Reson Med.* 2014;71(3):1015–23.
78. Henkelman RM, Huang X, Xiang Q -S, Stanisz GJ, Swanson SD, Bronskill MJ. Quantitative interpretation of magnetization transfer. *Magn Reson Med.* 1993;29(6):759–66.
79. Du J, Carl M, Bydder M, Takahashi A, Chung CB, Bydder GM. Qualitative and quantitative ultrashort echo time (UTE) imaging of cortical bone. *J Magn Reson.* 2010;207(2):304–11.
80. Wright P, Jellus V, McGonagle D, Robson M, Ridgeway J, Hodgson R. Comparison of two ultrashort echo time sequences for the quantification of T1 within phantom and human Achilles tendon at 3 T. *Magn Reson Med.* 2012;68(4):1279–84.
81. Ma Y-J, Lu X, Carl M, Zhu Y, Szeverenyi NM, Bydder GM, et al. Accurate T1 mapping of short T2 tissues using a three-dimensional ultrashort echo time cones actual flip angle imaging-variable repetition time (3D UTE-Cones AFI-VTR) method. *Magn Reson Med.* 2018 Aug;80(2):598–608.

82. Tyler DJ, Robson MD, Henkelman RM, Young IR, Bydder GM. Magnetic resonance imaging with ultrashort TE (UTE) PULSE sequences: Technical considerations. *J Magn Reson Imaging*. 2007;25(2):279–89.
83. Chen J, Chang EY, Carl M, Ma Y, Shao H, Chen B, et al. Measurement of bound and pore water T1 relaxation times in cortical bone using three-dimensional ultrashort echo time cones sequences. *Magn Reson Med*. 2017 Jun;77(6):2136–45.
84. Chang EY, Du J, Iwasaki K, Biswas R, Statum S, He Q, et al. Single- and Bi-component T2* analysis of tendon before and during tensile loading, using UTE sequences. *J Magn Reson Imaging*. 2015;42(1):114–20.
85. Liu J, Nazaran A, Ma Y, Chen H, Zhu Y, Du J, et al. Single- and Bicomponent Analyses of T2 Relaxation in Knee Tendon and Ligament by Using 3D Ultrashort Echo Time Cones (UTE Cones) Magnetic Resonance Imaging. *BioMed Res Int*. 2019;2019.
86. C. A. Araujo E, Azzabou N, Vignaud A, Guillot G, Carlier PG. Quantitative ultrashort TE imaging of the short-T2 components in skeletal muscle using an extended echo-subtraction method. *Magn Reson Med*. 2017;78(3):997–1008.
87. Qian Y, Williams AA, Chu CR, Boada FE. Multicomponent T2* mapping of knee cartilage: Technical feasibility ex vivo. *Magn Reson Med*. 2010;64(5):1427–32.
88. Springer F, Martirosian P, Machann J, Schwenger NF, Claussen CD, Schick F. Magnetization transfer contrast imaging in bovine and human cortical bone applying an ultrashort echo time sequence at 3 Tesla. *Magn Reson Med*. 2009;61(5):1040–9.
89. Regatte RR, Akella SVS, Reddy R. Depth-dependent proton magnetization transfer in articular cartilage. *J Magn Reson Imaging*. 2005;22(2):318–23.
90. Ramani A, Dalton C, Miller DH, Tofts PS, Barker GJ. Precise estimate of fundamental in-vivo MT parameters in human brain in clinically feasible times. *Magn Reson Imaging*. 2002;20(10):721–31.
91. Hodgson RJ, Evans R, Wright P, Grainger AJ, O’connor PJ, Helliwell P, et al. Quantitative magnetization transfer ultrashort echo time imaging of the Achilles tendon. *Magn Reson Med*. 2011;65(5):1372–6.
92. Jerban S, Ma Y, Dorthe EW, Kakos L, Le N, Alenezi S, et al. Assessing cortical bone mechanical properties using collagen proton fraction from ultrashort echo time magnetization transfer (UTE-MT) MRI modeling. *Bone Rep*. 2019;11(July):100220.
93. Ma YJ, Tadros A, Du J, Chang EY. Quantitative two-dimensional ultrashort echo time magnetization transfer (2D UTE-MT) imaging of cortical bone. *Magn Reson Med*. 2018;79(4):1941–9.

94. Ma YJ, Chang EY, Carl M, Du J. Quantitative magnetization transfer ultrashort echo time imaging using a time-efficient 3D multispoke Cones sequence. *Magn Reson Med.* 2018;79(2):692–700.
95. Bae WC, Dwek JR, Znamirovski R, Statum SM, Hermida JC, D’Lima DD, et al. Ultrashort echo time MR imaging of osteochondral junction of the knee at 3 T: Identification of anatomic structures contributing to signal intensity. *Radiology.* 2010;254(3):837–45.
96. Sophia Fox AJ, Bedi A, Rodeo SA. The Basic Science of Articular Cartilage. *Sports Health.* 2009 Nov;1(6):461–8.
97. Buckwalter JAMD++, Mankin HJMD. Instructional Course Lectures, The American Academy of Orthopaedic Surgeons - Articular Cartilage. Part I: Tissue Design and Chondrocyte-Matrix Interactions*+. [Miscellaneous Article]. *J Bone.* 1997 Apr;79(4):600–11.
98. Williams AA, Titchenal MR, Do BH, Guha A, Chu CR. MRI UTE-T2* shows high incidence of cartilage subsurface matrix changes 2 years after ACL reconstruction. *J Orthop Res.* 2019;37(2):370–7.
99. Chu CR, Williams AA, West RV, Qian Y, Fu FH, Do BH, et al. Quantitative Magnetic Resonance Imaging UTE-T2* Mapping of Cartilage and Meniscus Healing After Anatomic Anterior Cruciate Ligament Reconstruction. *Am J Sports Med.* 2014 Aug;42(8):1847–56.
100. Boyde A, Riggs CM, Bushby AJ, McDermott B, Pinchbeck GL, Clegg PD. Cartilage damage involving extrusion of mineralisable matrix from the articular calcified cartilage and subchondral bone. *Eur Cell Mater.* 2011 May 28;21:470–8; discussion 478.
101. Miller LM, Novatt JT, Hamerman D, Carlson CS. Alterations in mineral composition observed in osteoarthritic joints of cynomolgus monkeys. *Bone.* 2004 Aug 1;35(2):498–506.
102. Hwang J, Bae WC, Shieu W, Lewis CW, Bugbee WD, Sah RL. Increased hydraulic conductance of human articular cartilage and subchondral bone plate with progression of osteoarthritis. *Arthritis Rheum.* 2008 Dec;58(12):3831–42.
103. Goto H, Fujii M, Iwama Y, Aoyama N, Ohno Y, Sugimura K. Magnetic resonance imaging (MRI) of articular cartilage of the knee using ultrashort echo time (uTE) sequences with spiral acquisition. *J Med Imaging Radiat Oncol.* 2012;56(3):318–23.
104. Shao H, Chang EY, Pauli C, Zanganeh S, Bae W, Chung CB, et al. UTE bi-component analysis of T2* relaxation in articular cartilage. *Osteoarthritis Cartilage.* 2016;24(2):364–73.
105. Du J, Diaz E, Carl M, Bae W, Chung CB, Bydder GM. Ultrashort echo time imaging with bicomponent analysis. *Magn Reson Med.* 2012;67(3):645–9.

106. Titchenal MR, Williams AA, Chehab EF, Asay JL, Dragoo JL, Gold GE, et al. Cartilage Subsurface Changes to Magnetic Resonance Imaging UTE-T2* 2 Years After Anterior Cruciate Ligament Reconstruction Correlate With Walking Mechanics Associated With Knee Osteoarthritis. *Am J Sports Med.* 2018;46(3):565–72.
107. Makris EA, Hadidi P, Athanasiou KA. The knee meniscus: structure-function, pathophysiology, current repair techniques, and prospects for regeneration. *Biomaterials.* 2011 Oct;32(30):7411–31.
108. Bae W, Du J, Bydder G, Chung C. Conventional and Ultrashort MRI of Articular Cartilage, Meniscus and intervertebral disc. *Top Magn Reson Imaging.* 2010;21(5):275–89.
109. Yi J, Han Lee Y, Song HT, Suh JS. Comparison of T2* mapping between regular echo time and ultrashort echo time with 3D cones at 3 tesla for knee meniscus. *Med U S.* 2018;97(48).
110. Williams A, Qian Y, Golla S, Chu CR. UTE-T2* mapping detects sub-clinical meniscus injury after anterior cruciate ligament tear. *Osteoarthritis Cartilage.* 2012 Jun;20(6):486–94.
111. Ma L, Meng Q, Chen Y, Zhang Z, Sun H, Deng D. Preliminary use of a double-echo pulse sequence with 3D ultrashort echo time in the MRI of bones and joints. *Exp Ther Med.* 2013;5(5):1471–5.
112. Techawiboonwong A, Hee KS, Leonard MB, Wehrli FW. Cortical bone water: In vivo quantification with ultrashort echo-time MR imaging. *Radiology.* 2008;248(3):824–33.
113. Sanal HT, Bae WC, Pauli C, Du J, Statum S, Znamirovski R, et al. Magnetic resonance imaging of the temporomandibular joint disc: feasibility of novel quantitative magnetic resonance evaluation using histologic and biomechanical reference standards. *J Orofac Pain.* 2011;25(4):345–53.
114. Price RG, Kim JP, Zheng W, Chetty IJ, Glide-Hurst C. Image Guided Radiation Therapy Using Synthetic Computed Tomography Images in Brain Cancer. *Int J Radiat Oncol.* 2016 Jul;95(4):1281–9.
115. Soliman AS, Burns L, Owrangi A, Lee Y, Song WY, Stanisiz G, et al. A realistic phantom for validating MRI-based synthetic CT images of the human skull: *Med Phys.* 2017;44(9):4687–94.
116. Lei Y, Harms J, Wang T, Tian S, Zhou J, Shu H-K, et al. MRI-based synthetic CT generation using semantic random forest with iterative refinement. *Phys Med Biol.* 2019 Apr 5;64(8):085001.
117. Gai ND, Malayeri AA, Bluemke DA. Long T2 suppression in native lung 3-D imaging using k-space reordered inversion recovery dual-echo ultrashort echo time MRI. *Magn Reson Mater Phys Biol Med.* 2017;30(4):387–95.

118. Lederlin M, Crémillieux Y. Three-dimensional assessment of lung tissue density using a clinical ultrashort echo time at 3 tesla: A feasibility study in healthy subjects. *J Magn Reson Imaging*. 2014;40(4):839–47.
119. Meyer CH, Hu BS, Nishimura DG, Macovski A. Fast Spiral Coronary Artery Imaging. *Magn Reson Med*. 1992;28(2):202–13.
120. Joseph PM. Sampling errors in projection reconstruction MRI. *Magn Reson Med*. 1998 Sep;40(3):460–6.
121. Hoge RD, Kwan RKS, Pike GB. Density compensation functions for spiral MRI. *Magn Reson Med*. 1997;38(1):117–28.
122. Nagel AM, Laun FB, Weber M-A, Matthies C, Semmler W, Schad LR. Sodium MRI using a density-adapted 3D radial acquisition technique. *Magn Reson Med*. 2009;62(6):1565–73.
123. Noll DC, Pauly JM, Meyer CH, Nishimura DG, Macovskj A. Deblurring for non-2D fourier transform magnetic resonance imaging. *Magn Reson Med*. 1992;25(2):319–33.
124. Schomberg H. Off-resonance correction of MR images. *IEEE Trans Med Imaging*. 1999 Jun;18(6):481–95.
125. Noll DC, Meyer CH, Member S, Pauly JM, Nishimura DG, Macovski A. A Homogeneity Correction Method for Magnetic Resonance Imaging with Time-Varying Gradients. 1991;I(4).
126. Chen W, Meyer CH. Semiautomatic off-resonance correction in spiral imaging. *Magn Reson Med*. 2008;59(5):1212–9.
127. Setoi A, Kose K. 3D cones acquisition of human extremity imaging using a 1.5T superconducting magnet and an unshielded gradient coil set. *Magn Reson Med Sci*. 2019;18(1):88–95.
128. Ramachandran GN, Lakshminarayanan AV. Three-dimensional reconstruction from radiographs and electron micrographs: application of convolutions instead of Fourier transforms. *Proc Natl Acad Sci U S A*. 1971;68(9):2236–40.
129. Winkelmann S, Schaeffter T, Koehler T, Eggers H, Doessel O. An optimal radial profile order based on the golden ratio for time-resolved MRI. *IEEE Trans Med Imaging*. 2007;26(1):68–76.
130. Chan RW, Ramsay EA, Cheung EY, Plewes DB. The influence of radial undersampling schemes on compressed sensing reconstruction in breast MRI. *Magn Reson Med*. 2012;67(2):363–77.
131. Robertson SH, Virgincar RS, He M, Freeman MS, Kaushik SS, Driehuys B. Optimizing 3D noncartesian gridding reconstruction for hyperpolarized ^{129}Xe MRI-focus on preclinical applications. *Concepts Magn Reson Part A*. 2015;44(4):190–202.

132. Hemberger KRF, Jakob PM, Breuer FA. Multiparametric oxygen-enhanced functional lung imaging in 3D. *Magn Reson Mater Phys Biol Med*. 2015;28(3):217–26.
133. Fessler JA, Sangwoo Lee, Olafsson VT, Shi HR, Noll DC. Toeplitz-based iterative image reconstruction for MRI with correction for magnetic field inhomogeneity. *IEEE Trans Signal Process*. 2005 Sep;53(9):3393–402.
134. Lin W, Huang F, Simonotto E, Duensing GR, Reykowski A. Off-resonance artifacts correction with convolution in k-space (ORACLE). *Magn Reson Med*. 2012;67(6):1547–55.
135. He Q, Ma Y, Fan S, Shao H, Sheth V, Bydder GM, et al. Direct Magnitude and Phase Imaging of Myelin Using Ultrashort Echo Time (UTE) Pulse Sequences: a Feasibility Study. *Magn Reson Imaging*. 2017 Jun;39:194–9.
136. Dietrich O, Raya JG, Reeder SB, Reiser MF, Schoenberg SO. Measurement of signal-to-noise ratios in MR images: influence of multichannel coils, parallel imaging, and reconstruction filters. *J Magn Reson Imaging JMRI*. 2007 Aug;26(2):375–85.
137. Pipe JG, Menon P. Sampling density compensation in MRI: rationale and an iterative numerical solution. *Magn Reson Med*. 1999 Jan;41(1):179–86.
138. Pipe JG. Reconstructing MR images from undersampled data: data-weighting considerations. *Magn Reson Med*. 2000 Jun;43(6):867–75.
139. Lazarus C, Weiss P, Chauffert N, Mauconduit F, El Gueddari L, Destrieux C, et al. SPARKLING: variable-density k-space filling curves for accelerated T₂*-weighted MRI. *Magn Reson Med*. 2019;81(6):3643–61.
140. Guo J, Cao X, Cleveland ZI, Woods JC. Murine pulmonary imaging at 7T: T₂* and T₁ with anisotropic UTE. *Magn Reson Med*. 2018 Apr;79(4):2254–64.
141. Ma Y, Jerban S, Jang H, Chang EY, Du J. Fat suppression for ultrashort echo time imaging using a novel soft-hard composite radiofrequency pulse. *Magn Reson Med*. 2019 Dec;82(6):2178–87.
142. Abbasi-Rad S, Saligheh Rad H. Quantification of Human Cortical Bone Bound and Free Water in Vivo with Ultrashort Echo Time MR Imaging: A Model-based Approach. *Radiology*. 2017 Jan 4;283(3):862–72.
143. Hayashi D, Roemer FW, Guermazi A. Imaging for osteoarthritis. *Ann Phys Rehabil Med*. 2016 Jun 1;59(3):161–9.
144. Felson DT. Clinical practice. Osteoarthritis of the knee. *N Engl J Med*. 2006 Feb 23;354(8):841–8.
145. Hunter DJ, Lo GH. The Management of Osteoarthritis: An Overview and Call to Appropriate Conservative Treatment. *Med Clin North Am*. 2009 Jan 1;93(1):127–43.

146. Felson DT. Identifying Different Osteoarthritis Phenotypes through Epidemiology. *Osteoarthr Cartil OARS Osteoarthr Res Soc.* 2010 May;18(5):601–4.
147. Bierma-Zeinstra SM, Verhagen AP. Osteoarthritis subpopulations and implications for clinical trial design. *Arthritis Res Ther.* 2011;13(2):213.
148. Dell’Isola A, Allan R, Smith SL, Marreiros SSP, Steultjens M. Identification of clinical phenotypes in knee osteoarthritis: a systematic review of the literature. *BMC Musculoskelet Disord.* 2016 Oct 12;17(1):425.
149. McAlindon TE, Nuite M, Krishnan N, Ruthazer R, Price LL, Burstein D, et al. Change in knee osteoarthritis cartilage detected by delayed gadolinium enhanced magnetic resonance imaging following treatment with collagen hydrolysate: a pilot randomized controlled trial. *Osteoarthritis Cartilage.* 2011 Apr 1;19(4):399–405.
150. Kaukinen P, Podlipská J, Guerhazi A, Niinimäki J, Lehenkari P, Roemer FW, et al. Magnetic resonance imaging (MRI)-defined cartilage degeneration and joint pain are associated with poor physical function in knee osteoarthritis – the Oulu Knee Osteoarthritis study. *Osteoarthritis Cartilage.* 2017 Nov 1;25(11):1829–40.
151. Hirvasniemi J, Thevenot J, Multanen J, Haapea M, Heinonen A, Nieminen MT, et al. Association between radiography-based subchondral bone structure and MRI-based cartilage composition in postmenopausal women with mild osteoarthritis. *Osteoarthritis Cartilage.* 2017 Dec 1;25(12):2039–46.
152. Link TM, Li X. Establishing compositional MRI of cartilage as a biomarker for clinical practice. *Osteoarthritis Cartilage.* 2018 Sep 1;26(9):1137–9.
153. Tjörnstrand J, Neuman P, Svensson J, Lundin B, Dahlberg LE, Tiderius CJ. Osteoarthritis development related to cartilage quality-the prognostic value of dGEMRIC after anterior cruciate ligament injury. *Osteoarthritis Cartilage.* 2019 Nov 1;27(11):1647–52.
154. Hunter DJ, Guerhazi A, Lo GH, Grainger AJ, Conaghan PG, Boudreau RM, et al. Evolution of semiquantitative whole joint assessment of knee OA: MOAKS (MRI Osteoarthritis Knee Score). *Osteoarthr Cartil OARS Osteoarthr Res Soc.* 2011 Aug;19(8):990–1002.
155. Eijgenraam SM, Bovendeert FAT, Verschueren J, van Tiel J, Bastiaansen-Jenniskens YM, Westorp MA, et al. T2 mapping of the meniscus is a biomarker for early osteoarthritis. *Eur Radiol.* 2019;29(10):5664–72.
156. Ikuta F, Takahashi K, Hashimoto S, Mochizuki Y, Yuzawa Y, Inanami H, et al. Effect of physical therapy on early knee osteoarthritis with medial meniscal posterior tear assessed by MRI T2 mapping and 3D-to-2D registration technique: A prospective intervention study. *Mod Rheumatol.* 2020 Jul 3;30(4):738–47.
157. Nebelung S, Dötsch L, Shah D, Abrar DB, Linka K, Knobe M, et al. Functional MRI Mapping of Human Meniscus Functionality and its Relation to Degeneration. *Sci Rep*

- [Internet]. 2020 Feb 12 [cited 2021 May 9];10. Available from:
<https://www.ncbi.nlm.nih.gov/pmc/articles/PMC7016001/>
158. Jerban S, Kasibhatla A, Ma Y, Wu M, Chen Y, Guo T, et al. Detecting Articular Cartilage and Meniscus Deformation Effects Using Magnetization Transfer Ultrashort Echo Time (MT-UTE) Modeling during Mechanical Load Application: Ex Vivo Feasibility Study. *CARTILAGE*. 2020 Dec 8;1947603520976771.
 159. Rahmer J, Börnert P, Dries SPM. Assessment of anterior cruciate ligament reconstruction using 3D ultrashort echo-time MR imaging. *J Magn Reson Imaging*. 2009 Feb 1;29(2):443–8.
 160. Lee YH, Suh J-S, Grodzki D. Ultrashort echo (UTE) versus pointwise encoding time reduction with radial acquisition (PETRA) sequences at 3 Tesla for knee meniscus: A comparative study. *Magn Reson Imaging*. 2016 Feb 1;34(2):75–80.
 161. Williams AA, Titchenal MR, Andriacchi TP, Chu CR. MRI UTE-T2* profile characteristics correlate to walking mechanics and patient reported outcomes 2 years after ACL reconstruction. *Osteoarthritis Cartilage*. 2018;26(4):569–79.
 162. Cai Z, Wei Z, Wu M, Jerban S, Jang H, Li S, et al. Knee osteochondral junction imaging using a fast 3D T1-weighted ultrashort echo time cones sequence at 3T. *Magn Reson Imaging*. 2020 Nov 1;73:76–83.
 163. Williams AA, Erhart-Hledik JC, Asay JL, Mahtani GB, Titchenal MR, Lutz AM, et al. Patient-Reported Outcomes and Knee Mechanics Correlate With Patellofemoral Deep Cartilage UTE-T2* 2 Years After Anterior Cruciate Ligament Reconstruction. *Am J Sports Med*. 2021 Mar 1;49(3):675–83.
 164. Ma Y-J, Jang H, Wei Z, Cai Z, Xue Y, Lee RR, et al. Myelin Imaging in Human Brain Using a Short Repetition Time Adiabatic Inversion Recovery Prepared Ultrashort Echo Time (STAIR-UTE) MRI Sequence in Multiple Sclerosis. *Radiology* [Internet]. 2020 Aug 11 [cited 2021 May 9]; Available from:
<https://pubs.rsna.org/doi/abs/10.1148/radiol.2020200425>
 165. Robson MD, Gatehouse PD, So PW, Bell JD, Bydder GM. Contrast enhancement of short T2 tissues using ultrashort TE (UTE) pulse sequences. *Clin Radiol*. 2004 Aug 1;59(8):720–6.
 166. Han M, Larson PEZ, Liu J, Krug R. Depiction of Achilles Tendon Microstructure In-Vivo Using High-Resolution 3D Ultrashort Echo-Time MRI at 7T. *Invest Radiol*. 2014 May;49(5):339–45.
 167. Dunn TC, Lu Y, Jin H, Ries MD, Majumdar S. T2 Relaxation Time of Cartilage at MR Imaging: Comparison with Severity of Knee Osteoarthritis. *Radiology*. 2004 Aug;232(2):592–8.

168. Rauscher I, Stahl R, Cheng J, Li X, Huber MB, Luke A, et al. Meniscal Measurements of T1 ρ and T2 at MR Imaging in Healthy Subjects and Patients with Osteoarthritis. *Radiology*. 2008 Nov;249(2):591–600.
169. Wang L, Chang G, Xu J, Vieira RLR, Krasnokutsky S, Abramson S, et al. T1rho MRI of Menisci and Cartilage in Patients with Osteoarthritis at 3T. *Eur J Radiol*. 2012 Sep;81(9):2329–36.
170. Son M, Goodman SB, Chen W, Hargreaves BA, Gold GE, Levenston ME. Regional Variation in T1 ρ and T2 Times in Osteoarthritic Human Menisci: Correlation with Mechanical Properties and Matrix Composition. *Osteoarthr Cartil OARS Osteoarthr Res Soc*. 2013 Jun;21(6):796–805.
171. Guerhazi A, Alizai H, Crema MD, Trattnig S, Regatte RR, Roemer FW. Compositional MRI techniques for evaluation of cartilage degeneration in osteoarthritis. *Osteoarthritis Cartilage*. 2015 Oct 1;23(10):1639–53.
172. Sinclair CDJ, Samson RS, Thomas DL, Weiskopf N, Lutti A, Thornton JS, et al. Quantitative magnetization transfer in in vivo healthy human skeletal muscle at 3 T. *Magn Reson Med*. 2010;64(6):1739–48.
173. Stikov N, Keenan KE, Pauly JM, Smith RL, Dougherty RF, Gold GE. Cross-relaxation imaging of human articular cartilage. *Magn Reson Med*. 2011;66(3):725–34.
174. Sritanyaratana N, Samsonov A, Mossahebi P, Wilson JJ, Block WF, Kijowski R. Cross-relaxation imaging of human patellar cartilage in vivo at 3.0T. *Osteoarthritis Cartilage*. 2014;22(10):1568–76.
175. Simard M. Quantitative Magnetization Transfer Evaluation of the Knee Joint in Magnetic Resonance Imaging. McGill University; 2016.
176. Berryman B. Predicting Meniscus Mechanical Properties using Quantitative Magnetization Transfer Magnetic Resonance Imaging. University of Saskatchewan; 2020.
177. Mostafavi F, Cui L, Berryman B, Levesque IR, McWalter EJ. Quantitative Magnetization Transfer in the Knee Meniscus: Minimizing Data Collection Protocols. In: ISMRM. 2021.
178. Olsen KD, Cui L, Berryman BE, Levesque IR, McWalter EJ. Quantitative Magnetization Transfer MRI of the Knee Meniscus: Correlations with Biochemistry and Histology. In: ISMRM. 2021.
179. Ma Y-J, Chang EY, Carl M, Du J. Quantitative magnetization transfer ultrashort echo time imaging using a time-efficient 3D multispoke Cones sequence. *Magn Reson Med*. 2018 Feb;79(2):692–700.
180. Kirsch S, Kreinest M, Reisig G, Schwarz MLR, Ströbel P, Schad LR. In vitro mapping of 1H ultrashort T2* and T2 of porcine menisci. *NMR Biomed*. 2013 Sep 1;26(9):1167–75.

181. Juras V, Apprich S, Szomolanyi P, Bieri O, Deligianni X, Trattnig S. Bi-exponential T2* analysis of healthy and diseased Achilles tendons: an in vivo preliminary magnetic resonance study and correlation with clinical score. *Eur Radiol.* 2013;23(10):2814–22.
182. Kijowski R, Wilson JJ, Liu F. Bicomponent ultrashort echo time T2* analysis for assessment of patients with patellar tendinopathy. *J Magn Reson Imaging.* 2017;46(5):1441–7.
183. Insko EK, Bolinger L. Mapping of the Radiofrequency Field. *J Magn Reson A.* 1993 Jun 1;103(1):82–5.
184. Balezeau F, Eliat P-A, Cayamo AB, Saint-Jalmes H. Mapping of low flip angles in magnetic resonance. *Phys Med Biol.* 2011 Oct;56(20):6635–47.
185. Li ZF, Zhao W, Qi TF, Gao C, Gu Q, Zhao JS, et al. A simple B1 correction method for dynamic contrast-enhanced MRI. *Phys Med Biol.* 2018;63(16).
186. Fram EK, Herfkens RJ, Johnson GA, Glover GH, Karis JP, Shimakawa A, et al. Rapid calculation of T1 using variable flip angle gradient refocused imaging. *Magn Reson Imaging.* 1987;5(3):201–8.
187. Deoni SCL, Peters TM, Rutt BK. High-resolution T1 and T2 mapping of the brain in a clinically acceptable time with DESPOT1 and DESPOT2. *Magn Reson Med.* 2005;53(1):237–41.
188. Sled JG, Bruce Pike G. Quantitative imaging of magnetization transfer exchange and relaxation properties in vivo using MRI. *Magn Reson Med.* 2001;46(5):923–31.
189. Berry I, Barker GJ, Barkhof F, Campi A, Dousset V, Franconi J-M, et al. A multicenter measurement of magnetization transfer ratio in normal white matter. *J Magn Reson Imaging.* 1999;9(3):441–6.
190. Coleman TF, Li Y. An Interior Trust Region Approach for Nonlinear Minimization Subject to Bounds. *SIAM J Optim.* 1996 May;6(2):418–45.
191. Coleman T, li Y. On the Convergence of Reflective Newton Methods for Large-Scale Nonlinear Minimization Subject to Bounds. *Math Program.* 1994 Oct 1;67:189–224.
192. Tozer D, Ramani A, Barker GJ, Davies GR, Miller DH, Tofts PS. Quantitative magnetization transfer mapping of bound protons in multiple sclerosis. *Magn Reson Med.* 2003;50(1):83–91.
193. Jerban S, Chang DG, Ma Y, Jang H, Chang EY, Du J. An Update in Qualitative Imaging of Bone Using Ultrashort Echo Time Magnetic Resonance. *Front Endocrinol [Internet].* 2020 [cited 2021 Apr 9];11. Available from: <https://www.frontiersin.org/articles/10.3389/fendo.2020.555756/full>

194. Ma Y-J, Zhao W, Wan L, Guo T, Searleman A, Jang H, et al. Whole knee joint T1 values measured in vivo at 3T by combined 3D ultrashort echo time cones actual flip angle and variable flip angle methods. *Magn Reson Med*. 2019 Mar;81(3):1634–44.
195. Byra M, Wu M, Zhang X, Jang H, Ma Y-J, Chang EY, et al. Knee menisci segmentation and relaxometry of 3D ultrashort echo time cones MR imaging using attention U-Net with transfer learning. *Magn Reson Med*. 2020 Mar;83(3):1109–22.
196. Ma Y, Carl M, Shao H, Tadros AS, Chang EY, Du J. Three-dimensional Ultrashort Echo Time Cones T1 ρ (3D UTE-Cones-T1 ρ) Imaging. *NMR Biomed [Internet]*. 2017 Jun [cited 2021 Apr 5];30(6). Available from: <https://www.ncbi.nlm.nih.gov/pmc/articles/PMC5505275/>
197. Du J, Sheth V, He Q, Carl M, Chen J, Corey-Bloom J, et al. Measurement of T1 of the ultrashort T2* components in white matter of the brain at 3T. *PloS One*. 2014;9(8):e103296.
198. Bajd F, Škrlep M, Čandek-Potokar M, Vidmar J, Serša I. Application of quantitative magnetization transfer magnetic resonance imaging for characterization of dry-cured hams. *Meat Sci*. 2016;122:109–18.
199. Levesque IR, Sled JG, Narayanan S, Giacomini PS, Ribeiro LT, Arnold DL, et al. Reproducibility of quantitative magnetization-transfer imaging parameters from repeated measurements. *Magn Reson Med*. 2010;64(2):391–400.
200. Levesque IR, Sled JG, Pike GB. Iterative optimization method for design of quantitative magnetization transfer imaging experiments. *Magn Reson Med*. 2011;66(3):635–43.
201. Hoffmann A, Oborn B, Moteabbed M, Yan S, Bortfeld T, Knopf A, et al. MR-guided proton therapy: a review and a preview. *Radiat Oncol Lond Engl*. 2020 May 29;15:129.
202. Chandarana H, Wang H, Tijssen RHN, Das IJ. Emerging Role of MRI in Radiation Therapy. *J Magn Reson Imaging JMRI*. 2018 Dec;48(6):1468–78.
203. Owrangi AM, Greer PB, Glide-Hurst CK. MRI-only treatment planning: benefits and challenges. *Phys Med Biol*. 2018 Feb 26;63(5):05TR01.
204. Chin S, Eccles CL, McWilliam A, Chuter R, Walker E, Whitehurst P, et al. Magnetic resonance-guided radiation therapy: A review. *J Med Imaging Radiat Oncol*. 2020;64(1):163–77.
205. Llorente R, Spieler BO, Victoria J, Takita C, Yechieli R, Ford JC, et al. MRI-guided stereotactic ablative radiation therapy of spinal bone metastases: a preliminary experience. *Br J Radiol*. 2020 Jan;93(1105):20190655.
206. Salembier C, Villeirs G, De Bari B, Hoskin P, Pieters BR, Van Vulpen M, et al. ESTRO ACROP consensus guideline on CT- and MRI-based target volume delineation for primary radiation therapy of localized prostate cancer. *Radiother Oncol*. 2018 Apr;127(1):49–61.

207. Khoo VS, Dearnaley DP, Finnigan DJ, Padhani A, Tanner SF, Leach MO. Magnetic resonance imaging (MRI): considerations and applications in radiotherapy treatment planning. *Radiother Oncol J Eur Soc Ther Radiol Oncol*. 1997 Jan;42(1):1–15.
208. Baldwin LN, Wachowicz K, Thomas SD, Rivest R, Fallone BG. Characterization, prediction, and correction of geometric distortion in 3T MR images: Characterization of geometric distortion in 3 T MR images. *Med Phys*. 2007 Jan 8;34(2):388–99.
209. Walker A, Liney G, Metcalfe P, Holloway L. MRI distortion: Considerations for MRI based radiotherapy treatment planning. *Australas Phys Eng Sci Med*. 2014;37(1):103–13.
210. Wang D, Doddrell DM, Cowin G. A novel phantom and method for comprehensive 3-dimensional measurement and correction of geometric distortion in magnetic resonance imaging. *Magn Reson Imaging*. 2004;22(4):529–42.
211. Crijs SPM, Raaymakers BW, Lagendijk JJW. Real-time correction of magnetic field inhomogeneity-induced image distortions for MRI-guided conventional and proton radiotherapy. *Phys Med Biol*. 2011;56(1):289–97.
212. Price RG, Knight RA, Hwang KP, Bayram E, Nejad-Davarani SP, Glide-Hurst CK. Optimization of a novel large field of view distortion phantom for MR-only treatment planning. *J Appl Clin Med Phys*. 2017;18(4):51–61.
213. Skrzyński W, Ziełńska-Dąbrowska S, Wachowicz M, Ślusarczyk-Kacprzyk W, Kukołowicz PF, Bulski W. Computed Tomography as a Source of Electron Density Information for Radiation Treatment Planning. *Strahlenther Onkol*. 2010 Jun;186(6):327–33.
214. Kessler ML. Image registration and data fusion in radiation therapy. *Br J Radiol*. 2006 Sep;79 Spec No 1:S99-108.
215. Nyholm T, Nyberg M, Karlsson MG, Karlsson M. Systematisation of spatial uncertainties for comparison between a MR and a CT-based radiotherapy workflow for prostate treatments. *Radiat Oncol*. 2009 Nov 17;4(1):54.
216. Ulin K, Urie MM, Cherlow JM. Results of a Multi-Institutional Benchmark Test for Cranial CT/MR Image Registration. *Int J Radiat Oncol Biol Phys*. 2010 Aug 1;77(5):1584–9.
217. Stanescu T, Jans H-S, Pervez N, Stavrev P, Fallone BG. A study on the magnetic resonance imaging (MRI)-based radiation treatment planning of intracranial lesions. *Phys Med Biol*. 2008 Jul 7;53(13):3579–93.
218. Jonsson JH, Karlsson MG, Karlsson M, Nyholm T. Treatment planning using MRI data: an analysis of the dose calculation accuracy for different treatment regions. *Radiat Oncol Lond Engl*. 2010 Jun 30;5:62.
219. Dowling JA, Lambert J, Parker J, Salvado O, Fripp J, Capp A, et al. An Atlas-Based Electron Density Mapping Method for Magnetic Resonance Imaging (MRI)-Alone

- Treatment Planning and Adaptive MRI-Based Prostate Radiation Therapy. *Int J Radiat Oncol*. 2012 May 1;83(1):e5–11.
220. Hsu S, Cao Y, Balter J. MO-G-BRA-02: Investigation of a Method for Generating Synthetic CT Models from MRI Scans for Radiation Therapy. *Med Phys*. 2012;39(6):3881.
221. Uh J, Merchant TE, Li Y, Li X, Hua C. MRI-based treatment planning with pseudo CT generated through atlas registration. *Med Phys*. 2014 May;41(5):051711.
222. Sjölund J, Forsberg D, Andersson M, Knutsson H. Generating patient specific pseudo-CT of the head from MR using atlas-based regression. *Phys Med Biol*. 2015 Jan;60(2):825–39.
223. Karotki A, Mah K, Meijer G, Meltner M. Comparison of bulk electron density and voxel-based electron density treatment planning. *J Appl Clin Med Phys*. 2011 Nov 15;12(4):97–104.
224. Yang Y, Cao M, Kaprealian T, Sheng K, Gao Y, Han F, et al. Accuracy of UTE-MRI-based patient setup for brain cancer radiation therapy. *Med Phys*. 2016 Jan 1;43(1):262–7.
225. Jackson E, Bronskill M, Drost D, Och J, Pooley R, Sobol W, et al. Acceptance Testing and Quality Assurance Procedures for Magnetic Resonance Imaging Facilities [Internet]. AAPM; 2010 Dec [cited 2021 Jul 18]. Available from: <https://www.aapm.org/pubs/reports/detail.asp?docid=101>
226. Grodzki DM, Jakob PM, Heismann B. Ultrashort echo time imaging using pointwise encoding time reduction with radial acquisition (PETRA). *Magn Reson Med*. 2012;67(2):510–8.
227. Mugler JP. Optimized three-dimensional fast-spin-echo MRI. *J Magn Reson Imaging*. 2014;39(4):745–67.
228. Boehler T, van Straaten D, Wirtz S, Peitgen HO. A robust and extendible framework for medical image registration focused on rapid clinical application deployment. *Comput Biol Med*. 2011;41(6):340–9.
229. Dice LR. Measures of the Amount of Ecologic Association Between Species. *Ecology*. 1945;26(3):297–302.
230. Korhonen J, Kapanen M, Keyriläinen J, Seppälä T, Tenhunen M. A dual model HU conversion from MRI intensity values within and outside of bone segment for MRI-based radiotherapy treatment planning of prostate cancer. *Med Phys*. 2014;41(1):011704.
231. Kim J, Glide-Hurst C, Doemer A, Wen N, Movsas B, Chetty IJ. Implementation of a novel algorithm for generating synthetic CT images from magnetic resonance imaging data sets for prostate cancer radiation therapy. *Int J Radiat Oncol Biol Phys*. 2015 Jan 1;91(1):39–47.

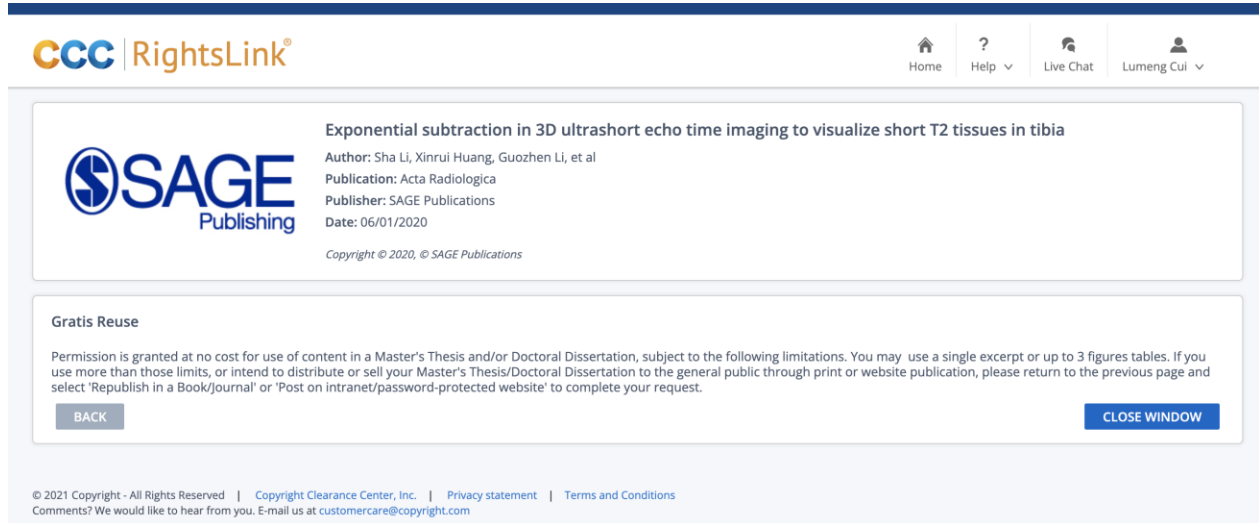
232. Wu H, Zhong Y, Nie Q, Chen W, Guo L, Yang X, et al. Feasibility of three-dimensional ultrashort echo time magnetic resonance imaging at 1.5 T for the diagnosis of skull fractures. *Eur Radiol.* 2016 Jan 1;26(1):138–46.
233. Feng L, Grimm R, Block KT, Chandarana H, Kim S, Xu J, et al. Golden-angle radial sparse parallel MRI: combination of compressed sensing, parallel imaging, and golden-angle radial sampling for fast and flexible dynamic volumetric MRI. *Magn Reson Med.* 2014 Sep;72(3):707–17.
234. Roy CW, Seed M, Kingdom JC, Macgowan CK. Motion compensated cine CMR of the fetal heart using radial undersampling and compressed sensing. *J Cardiovasc Magn Reson.* 2017;19(1):1–14.

Appendix A

Copyright Permissions

Copyright Permissions are attached in the following pages

Figure 1.6:



The screenshot displays the CCC RightsLink interface. At the top left is the logo for CCC | RightsLink. On the top right, there are navigation links: Home, Help, Live Chat, and a user profile for Lumeng Cui. The main content area features the SAGE Publishing logo on the left and the following text on the right:

Exponential subtraction in 3D ultrashort echo time imaging to visualize short T2 tissues in tibia
Author: Sha Li, Xinrui Huang, Guozhen Li, et al
Publication: Acta Radiologica
Publisher: SAGE Publications
Date: 06/01/2020
Copyright © 2020, © SAGE Publications

Below this, a section titled "Gratis Reuse" contains the following text:

Permission is granted at no cost for use of content in a Master's Thesis and/or Doctoral Dissertation, subject to the following limitations. You may use a single excerpt or up to 3 figures tables. If you use more than those limits, or intend to distribute or sell your Master's Thesis/Doctoral Dissertation to the general public through print or website publication, please return to the previous page and select 'Republish in a Book/Journal' or 'Post on intranet/password-protected website' to complete your request.

At the bottom of this section are two buttons: "BACK" and "CLOSE WINDOW".

At the very bottom of the page, there is a footer with the following text:

© 2021 Copyright - All Rights Reserved | Copyright Clearance Center, Inc. | Privacy statement | Terms and Conditions
Comments? We would like to hear from you. E-mail us at customercare@copyright.com

Figure 1.7:

10/13/21, 3:18 AM

Manage Account



Order Number: 1154103

Order Date: 13 Oct 2021

Payment Information

Lumeng Cui
lumeng.cui@usask.ca
Payment method: Invoice

Billing Address:
Lumeng Cui
3006-1331 Georgia St W
Vancouver, BC V6E 4P1
Canada

+1 (306) 371-2301
lumeng.cui@usask.ca

Customer Location:
Lumeng Cui
3006-1331 Georgia St W
Vancouver, BC V6E 4P1
Canada

Order Details

1. Magnetic resonance in medicine : official journal of the Society of Magnetic Resonance in Medicine

Billing Status:
Open

Article: Comparison of optimized soft-tissue suppression schemes for ultrashort echo time MRI.

Order License ID	1154103-1	Type of use	Republish in a thesis/dissertation
Order detail status	Completed	Publisher	JOHN/WILEY & SONS, INC.
Project name	ROBUST MAGNETIC RESONANCE IMAGING OF SHORT T2 TISSUES	Portion	Chart/graph/table/figure
ISSN	0740-3194		

0.00 CAD
Republication Permission

LICENSED CONTENT

Publication Title	Magnetic resonance in medicine : official journal of the Society of Magnetic Resonance in Medicine	Rightsholder	John Wiley & Sons - Books
		Publication Type	Journal
		Start Page	680
Article Title	Comparison of optimized soft-tissue suppression schemes for ultrashort echo time MRI.	End Page	689
		Issue	3
		Volume	68
Author/Editor	SOCIETY OF MAGNETIC RESONANCE IN MEDICINE (U.S.)		
Date	12/31/1983		

Language English
Country United States of America

REQUEST DETAILS

Portion Type	Chart/graph/table/figure	Distribution	Canada
Number of charts / graphs / tables / figures requested	1	Translation	Original language of publication
Format (select all that apply)	Print,Electronic	Copies for the disabled?	No
Who will republish the content?	Not-for-profit entity	Minor editing privileges?	No
Duration of Use	Life of current and all future editions	Incidental promotional use?	No
Lifetime Unit Quantity	Up to 499	Currency	CAD
Rights Requested	Main product		

NEW WORK DETAILS

Title	ROBUST MAGNETIC RESONANCE IMAGING OF SHORT T2 TISSUES	Institution name	University of Saskatchewan
Instructor name	Emily McWalter	Expected presentation date	2021-12-15

ADDITIONAL DETAILS

The requesting person / organization to appear on the license Lumeng Cui

REUSE CONTENT DETAILS

Title, description or numeric reference of the portion(s)	Figure 6	Title of the article/chapter the portion is from	Comparison of optimized soft-tissue suppression schemes for ultrashort echo time MRI.
Editor of portion(s)	Li, Cheng; Magland, Jeremy F.; Rad, Hamidreza Saligheh; Song, Hee Kwon; Wehrli, Felix W.	Author of portion(s)	Li, Cheng; Magland, Jeremy F.; Rad, Hamidreza Saligheh; Song, Hee Kwon; Wehrli, Felix W.
Volume of serial or monograph	68	Publication date of portion	2012-08-31
Page or page range of portion	680-689		

John Wiley & Sons - Books Terms and Conditions

No right, license or interest to any trademark, trade name, service mark or other branding ("Marks") of WILEY or its licensors is granted hereunder, and you agree that you shall not assert any such right, license or interest with respect thereto. You may not alter, remove or suppress in any manner any copyright, trademark or other notices displayed by the Wiley material. This Agreement will be void if the Type of Use, Format, Circulation, or Requestor Type was misrepresented during the licensing process. In no instance may the total amount of Wiley Materials used in any Main Product, Compilation or Collective work comprise more than 5% (if figures/tables) or 15% (if full articles/chapters) of the (entirety of the) Main Product, Compilation or Collective Work. Some titles may be available under an Open Access license. It is the Licensors' responsibility to identify the type of Open Access license on which the requested material was published, and comply fully with the terms of that license for the type of use specified Further details can be found on Wiley Online Library <http://olabout.wiley.com/WileyCDA/Section/id-410895.html>.

Total Items	1	Subtotal:	0.00 CAD
		Order Total:	0.00 CAD

Figure 1.8:

10/13/21, 3:26 AM

Manage Account



Order Number: 1154105

Order Date: 13 Oct 2021

Payment Information

Lumeng Cui
lumeng.cui@usask.ca
Payment method: Invoice

Billing Address:
Lumeng Cui
3006-1331 Georgia St W
Vancouver, BC V6E 4P1
Canada

+1 (306) 371-2301
lumeng.cui@usask.ca

Customer Location:
Lumeng Cui
3006-1331 Georgia St W
Vancouver, BC V6E 4P1
Canada

Order Details

1. Osteoarthritis and cartilage

Billing Status:
Open

Article: Dual inversion recovery ultrashort echo time (DIR-UTE) imaging and quantification of the zone of calcified cartilage (ZCC).

Order License ID	1154105-1	Type of use	Republish in a thesis/dissertation
Order detail status	Completed	Publisher	W.B./SAUNDERS CO. LTD.
Project name	ROBUST MAGNETIC RESONANCE IMAGING OF SHORT T2 TISSUES	Portion	Chart/graph/table/figure
ISSN	1063-4584		
			0.00 CAD
			Republication Permission

LICENSED CONTENT

Publication Title	Osteoarthritis and cartilage	Rightsholder	Elsevier Science & Technology Journals
Article Title	Dual inversion recovery ultrashort echo time (DIR-UTE) imaging and quantification of the zone of calcified cartilage (ZCC).	Publication Type	Journal
		Start Page	77
		End Page	85
		Issue	1
		Volume	21
Author/Editor	OSTEOARTHRITIS RESEARCH SOCIETY.		
Date	12/31/1992		
Language	English		
Country	United Kingdom of Great Britain and Northern Ireland		

REQUEST DETAILS

Portion Type	Chart/graph/table/figure	Distribution	Canada
Number of charts / graphs / tables / figures requested	1	Translation	Original language of publication
Format (select all that apply)	Print,Electronic	Copies for the disabled?	No
Who will republish the content?	Not-for-profit entity	Minor editing privileges?	Yes
Duration of Use	Life of current edition	Incidental promotional use?	No
Lifetime Unit Quantity	Up to 499	Currency	CAD
Rights Requested	Main product		

NEW WORK DETAILS

Title	ROBUST MAGNETIC RESONANCE IMAGING OF SHORT T2 TISSUES	Institution name	University of Saskatchewan
Instructor name	Emily McWalter	Expected presentation date	2021-12-15

ADDITIONAL DETAILS

The requesting person / organization to appear on the license	Lumeng Cui
--	------------

REUSE CONTENT DETAILS

Title, description or numeric reference of the portion(s)	Figure 3	Title of the article/chapter the portion is from	Dual inversion recovery ultrashort echo time (DIR-UTE) imaging and quantification of the zone of calcified cartilage (ZCC).
Editor of portion(s)	Du, J.; Carl, M.; Bae, W.C.; Statum, S.; Chang, E.Y.; Bydder, G.M.; Chung, C.B.	Author of portion(s)	Du, J.; Carl, M.; Bae, W.C.; Statum, S.; Chang, E.Y.; Bydder, G.M.; Chung, C.B.
Volume of serial or monograph	21		
Page or page range of portion	77-85	Issue, if republishing an article from a serial	1
		Publication date of portion	2012-12-31

Elsevier Science & Technology Journals Terms and Conditions

Elsevier publishes Open Access articles in both its Open Access journals and via its Open Access articles option in subscription journals, for which an author selects a user license permitting certain types of reuse without permission. Before proceeding please check if the article is Open Access on <http://www.sciencedirect.com> and refer to the user license for the individual article. Any reuse not included in the user license terms will require permission. You must always fully and appropriately credit the author and source. If any part of the material to be used (for example, figures) has appeared in the Elsevier publication for which you are seeking permission, with credit or acknowledgement to another source it is the responsibility of the user to ensure their reuse complies with the terms and conditions determined by the rights holder. Please contact permissions@elsevier.com with any queries.

Total Items 1

Subtotal: 0.00 CAD

Order Total: 0.00 CAD

Figure 1.9:

10/13/21, 3:28 AM

Manage Account



Order Number: 1154100

Order Date: 13 Oct 2021

Payment Information

Lumeng Cui
lumeng.cui@usask.ca
Payment method: Invoice

Billing Address:
Lumeng Cui
3006-1331 Georgia St W
Vancouver, BC V6E 4P1
Canada

+1 (306) 371-2301
lumeng.cui@usask.ca

Customer Location:
Lumeng Cui
3006-1331 Georgia St W
Vancouver, BC V6E 4P1
Canada

Order Details

1. Magnetic resonance in medicine : official journal of the Society of Magnetic Resonance in Medicine

Billing Status:
Open

Article: Ultrashort TE imaging with off-resonance saturation contrast (UTE-OSC).

Order License ID	1154100-1	Type of use	Republish in a thesis/dissertation
Order detail status	Completed	Publisher	JOHN/WILEY & SONS, INC.
Project name	ROBUST MAGNETIC RESONANCE IMAGING OF SHORT T2 TISSUES	Portion	Chart/graph/table/figure
ISSN	0740-3194		e

0.00 CAD
Republication Permission

LICENSED CONTENT

Publication Title	Magnetic resonance in medicine : official journal of the Society of Magnetic Resonance in Medicine	Rightsholder	John Wiley & Sons - Books
Article Title	Ultrashort TE imaging with off-resonance saturation contrast (UTE-OSC).	Publication Type	Journal
Author/Editor	SOCIETY OF MAGNETIC RESONANCE IN MEDICINE (U.S.)	Start Page	527
Date	12/31/1983	End Page	531
Language	English	Issue	2
		Volume	62

Country United States of America

REQUEST DETAILS

Portion Type	Chart/graph/table/figure	Distribution	Canada
Number of charts / graphs / tables / figures requested	1	Translation	Original language of publication
Format (select all that apply)	Print,Electronic	Copies for the disabled?	No
Who will republish the content?	Not-for-profit entity	Minor editing privileges?	Yes
Duration of Use	Life of current and all future editions	Incidental promotional use?	No
Lifetime Unit Quantity	Up to 499	Currency	CAD
Rights Requested	Main product		

NEW WORK DETAILS

Title	ROBUST MAGNETIC RESONANCE IMAGING OF SHORT T2 TISSUES	Institution name	University of Saskatchewan
Instructor name	Emily McWalter	Expected presentation date	2021-12-15

ADDITIONAL DETAILS

The requesting person / organization to appear on the license Lumeng Cui

REUSE CONTENT DETAILS

Title, description or numeric reference of the portion(s)	Figure 3	Title of the article/chapter the portion is from	Ultrashort TE imaging with off-resonance saturation contrast (UTE-OSC).
Editor of portion(s)	Du, Jiang; Takahashi, Atsushi M.; Bydder, Mark; Chung, Christine B.; Bydder, Graeme M.	Author of portion(s)	Du, Jiang; Takahashi, Atsushi M.; Bydder, Mark; Chung, Christine B.; Bydder, Graeme M.
Volume of serial or monograph	62	Publication date of portion	2009-07-31
Page or page range of portion	527-531		

John Wiley & Sons - Books Terms and Conditions

No right, license or interest to any trademark, trade name, service mark or other branding ("Marks") of WILEY or its licensors is granted hereunder, and you agree that you shall not assert any such right, license or interest with respect thereto. You may not alter, remove or suppress in any manner any copyright, trademark or other notices displayed by the Wiley material. This Agreement will be void if the Type of Use, Format, Circulation, or Requestor Type was misrepresented during the licensing process. In no instance may the total amount of Wiley Materials used in any Main Product, Compilation or Collective work comprise more than 5% (if figures/tables) or 15% (if full articles/chapters) of the (entirety of the) Main Product, Compilation or Collective Work. Some titles may be available under an Open Access license. It is the Licensors' responsibility to identify the type of Open Access license on which the requested material was published, and comply fully with the terms of that license for the type of use specified Further details can be found on Wiley Online Library <http://olabout.wiley.com/WileyCDA/Section/id-410895.html>.

Total Items	1	Subtotal:	0.00 CAD
		Order Total:	0.00 CAD

Figure 1.10:

10/13/21, 3:31 AM

Manage Account



Order Number: 1154107

Order Date: 13 Oct 2021

Payment Information

Lumeng Cui
lumeng.cui@usask.ca
Payment method: Invoice

Billing Address:
Lumeng Cui
3006-1331 Georgia St W
Vancouver, BC V6E 4P1
Canada

+1 (306) 371-2301
lumeng.cui@usask.ca

Customer Location:
Lumeng Cui
3006-1331 Georgia St W
Vancouver, BC V6E 4P1
Canada

Order Details

1. Magnetic resonance in medicine : official journal of the Society of Magnetic Resonance in Medicine

Billing Status:
Open

Article: Accurate T1 mapping of short T2 tissues using a three-dimensional ultrashort echo time cones actual flip angle imaging-variable repetition time (3D UTE-Cones AFI-VTR) method.

Order License ID	1154107-1	Type of use	Republish in a thesis/dissertation
Order detail status	Completed	Publisher	JOHN/WILEY & SONS, INC.
Project name	ROBUST MAGNETIC RESONANCE IMAGING OF SHORT T2 TISSUES	Portion	Chart/graph/table/figure
ISSN	0740-3194		

0.00 CAD
Republication Permission

LICENSED CONTENT

Publication Title	Magnetic resonance in medicine : official journal of the Society of Magnetic Resonance in Medicine	Rightsholder	John Wiley & Sons - Books
		Publication Type	Journal
		Start Page	598
Article Title	Accurate T1 mapping of short T2 tissues using a three-dimensional ultrashort echo time cones actual flip angle imaging-variable repetition time (3D UTE-Cones AFI-VTR) method.	End Page	608
		Issue	2
		Volume	80

Author/Editor SOCIETY OF MAGNETIC
RESONANCE IN
MEDICINE (U.S.)

Date 12/31/1983

Language English

Country United States of
America

REQUEST DETAILS

Portion Type	Chart/graph/table/figure	Distribution	Canada
Number of charts / graphs / tables / figures requested	1	Translation	Original language of publication
Format (select all that apply)	Print,Electronic	Copies for the disabled?	No
Who will republish the content?	Not-for-profit entity	Minor editing privileges?	Yes
Duration of Use	Life of current and all future editions	Incidental promotional use?	No
Lifetime Unit Quantity	Up to 499	Currency	CAD
Rights Requested	Main product		

NEW WORK DETAILS

Title	ROBUST MAGNETIC RESONANCE IMAGING OF SHORT T2 TISSUES	Institution name	University of Saskatchewan
Instructor name	Emily McWalter	Expected presentation date	2021-12-15

ADDITIONAL DETAILS

The requesting person / organization to appear on the license Lumeng Cui

REUSE CONTENT DETAILS

Title, description or numeric reference of the portion(s)	Figure 5	Title of the article/chapter the portion is from	Accurate T1 mapping of short T2 tissues using a three-dimensional ultrashort echo time cones actual flip angle imaging-variable repetition time (3D UTE-Cones AFI-VTR) method.
Editor of portion(s)	Bydder, Graeme M; Carl, Michael; Chang, Eric Y; Du, Jiang; Lu, Xing; Ma, Ya-Jun; Szeverenyi, Nikolaus M; Zhu, Yanchun	Author of portion(s)	Bydder, Graeme M; Carl, Michael; Chang, Eric Y; Du, Jiang; Lu, Xing; Ma, Ya-Jun; Szeverenyi, Nikolaus M; Zhu, Yanchun
Volume of serial or monograph	80		
Page or page range of portion	598-608		

Publication date of portion 2018-07-31

John Wiley & Sons - Books Terms and Conditions

No right, license or interest to any trademark, trade name, service mark or other branding ("Marks") of WILEY or its licensors is granted hereunder, and you agree that you shall not assert any such right, license or interest with respect thereto. You may not alter, remove or suppress in any manner any copyright, trademark or other notices displayed by the Wiley material. This Agreement will be void if the Type of Use, Format, Circulation, or Requestor Type was misrepresented during the licensing process. In no instance may the total amount of Wiley Materials used in any Main Product, Compilation or Collective work comprise more than 5% (if figures/tables) or 15% (if full articles/chapters) of the (entirety of the) Main Product, Compilation or Collective Work. Some titles may be available under an Open Access license. It is the Licensors' responsibility to identify the type of Open Access license on which the requested material was published, and comply fully with the terms of that license for the type of use specified Further details can be found on Wiley Online Library <http://olabout.wiley.com/WileyCDA/Section/id-410895.html>.

Total Items 1

Subtotal: 0.00 CAD
Order Total: 0.00 CAD

Figure 1.12:

10/13/21, 3:33 AM

Manage Account



Order Number: 1154109

Order Date: 13 Oct 2021

Payment Information

Lumeng Cui
lumeng.cui@usask.ca
Payment method: Invoice

Billing Address:
Lumeng Cui
3006-1331 Georgia St W
Vancouver, BC V6E 4P1
Canada

+1 (306) 371-2301
lumeng.cui@usask.ca

Customer Location:
Lumeng Cui
3006-1331 Georgia St W
Vancouver, BC V6E 4P1
Canada

Order Details

1. Magnetic resonance in medicine : official journal of the Society of Magnetic Resonance in Medicine

Billing Status:
Open

Article: Magnetization transfer contrast imaging in bovine and human cortical bone applying an ultrashort echo time sequence at 3 Tesla.

Order License ID	1154109-1	Type of use	Republish in a thesis/dissertation
Order detail status	Completed	Publisher	JOHN/WILEY & SONS, INC.
Project name	ROBUST MAGNETIC RESONANCE IMAGING OF SHORT T2 TISSUES	Portion	Chart/graph/table/figure
ISSN	0740-3194		

0.00 CAD
Republication Permission

LICENSED CONTENT

Publication Title	Magnetic resonance in medicine : official journal of the Society of Magnetic Resonance in Medicine	Rightsholder	John Wiley & Sons - Books
		Publication Type	Journal
		Start Page	1040
Article Title	Magnetization transfer contrast imaging in bovine and human cortical bone applying an ultrashort echo time sequence at 3 Tesla.	End Page	1048
		Issue	5
		Volume	61
Author/Editor	SOCIETY OF MAGNETIC RESONANCE IN MEDICINE (U.S.)		
Date	12/31/1983		

Language English
Country United States of America

REQUEST DETAILS

Portion Type	Chart/graph/table/figure	Distribution	Canada
Number of charts / graphs / tables / figures requested	1	Translation	Original language of publication
Format (select all that apply)	Print,Electronic	Copies for the disabled?	No
Who will republish the content?	Not-for-profit entity	Minor editing privileges?	Yes
Duration of Use	Life of current and all future editions	Incidental promotional use?	No
Lifetime Unit Quantity	Up to 499	Currency	CAD
Rights Requested	Main product		

NEW WORK DETAILS

Title	ROBUST MAGNETIC RESONANCE IMAGING OF SHORT T2 TISSUES	Institution name	University of Saskatchewan
Instructor name	Emily McWalter	Expected presentation date	2021-12-15

ADDITIONAL DETAILS

The requesting person / organization to appear on the license Lumeng Cui

REUSE CONTENT DETAILS

Title, description or numeric reference of the portion(s)	Figure 7	Title of the article/chapter the portion is from	Magnetization transfer contrast imaging in bovine and human cortical bone applying an ultrashort echo time sequence at 3 Tesla.
Editor of portion(s)	Springer, Fabian; Martirosian, Petros; Machann, Jürgen; Schwenzer, Nina F.; Claussen, Claus D.; Schick, Fritz	Author of portion(s)	Springer, Fabian; Martirosian, Petros; Machann, Jürgen; Schwenzer, Nina F.; Claussen, Claus D.; Schick, Fritz
Volume of serial or monograph	61		
Page or page range of portion	1040-1048	Publication date of portion	2009-04-30

John Wiley & Sons - Books Terms and Conditions

No right, license or interest to any trademark, trade name, service mark or other branding ("Marks") of WILEY or its licensors is granted hereunder, and you agree that you shall not assert any such right, license or interest with respect thereto. You may not alter, remove or suppress in any manner any copyright, trademark or other notices displayed by the Wiley material. This Agreement will be void if the Type of Use, Format, Circulation, or Requestor Type was misrepresented during the licensing process. In no instance may the total amount of Wiley Materials used in any Main Product, Compilation or Collective work comprise more than 5% (if figures/tables) or 15% (if full articles/chapters) of the (entirety of the) Main Product, Compilation or Collective Work. Some titles may be available under an Open Access license. It is the Licensors' responsibility to identify the type of Open Access license on which the requested material was published, and comply fully with the terms of that license for the type of use specified Further details can be found on Wiley Online Library <http://olabout.wiley.com/WileyCDA/Section/id-410895.html>.

Total Items 1

Subtotal: 0.00 CAD

Order Total: 0.00 CAD